RECRYSTALLISATION AND STRUCTURE OF MECHANICALLY ALLOYED STEELS

By
Tung-Sheng Chou
Darwin College

Department of Materials Science and Metallurgy
Pembroke Street
Cambridge
CB2 3QZ

A dissertation submitted for the fulfilment
of the Degree of Doctor of Philosophy
at the University of Cambridge
February 1994

To the memory of my mother

&

Dedicated to my father, my wife, and

my children, Hsi-Kai and Chia-Ying

PREFACE

The investigation described herein was carried out under the supervision of Dr. H.K.D.H. Bhadeshia at the Department of Materials Science and Metallurgy, Cambridge, between April 1991 and February 1994.

Except where acknowledgement and reference to previous work is made, this work is, to the best of my knowledge, original and carried out without collaboration. Neither this, nor any substantially similar dissertation has been submitted for any degree, diploma or qualification at any other university.

This dissertation contains less than 60,000 words.

Tung–Sheng Chou

February 1994

ACKNOWLEDGEMENTS

I would like to thank Professor C. J. Humphreys for the provision of laboratory facilities in the Department of Materials Science and Metallurgy at the University of Cambridge. I would like to express my gratitude to my supervisor, Dr. Harry Bhadeshia, for his guidance, support, and constant encouragement not only on my research work but also on my life and my family.

Thanks are also extended to the group leader of JRDC, Dr. H. Harada, for his assistance with the operation of Atom Probe. Particular thanks to Mr. K. Murakami and Dr. Wei Sha for very helpful discussions of this work.

I am grateful to the members of the PT group for their advice and entertainment.

Finally, I would like to thank my sponsors, China Steel Corporation (ROC), for their financial support.

NOMENCLATURE AND ABBREVIATIONS

A	Activation energy
APFIM	Atom probe field ion microscopy
b	Burgers vector
b.c.c.	Body centred cubic
C_o	The number of collected ions per sampling block
C_1	Constant
χ^2	Chi-squared value to judge the significance of clustering
CSL	Coincidence site lattice
D	Kinetic strength
D_b	Diameter of billet
D_E	Critical kinetic strength to complete recrystallisation
δ	Jumping distance of atoms across the boundary
Δt	Annealing time
ΔG	Effective driving force for recrystallisation
ΔG_D	Stored energy in materials due to dislocations
ΔG_P	Particles pinning force
ΔG_S	Stored energy in materials due to grain boundaries
e_i	Expected number estimated from the binomial distribution
$\dot{\varepsilon}$	Strain rate
ϵ_c	Critical strain for the start of dynamic recrystallisation
ϵ_p	Peak strain of stress/strain curve for the dynamic recrystallisation
ϵ_x	Equivalent strain required to recrystallise a significant fraction of the material
ξ	Fractional amount of transformation
f	Volume fraction of particle
f.c.c.	Face centred cubic
FIM	Field ion microscopy
G	Shear modulus
HIP	Hot isostatic processing
HV	Vickers hardness
L	Mean grain intercept
MA	Mechanical alloying
MeMeC	Metal-metal-composite
MTDATA	Thermodynamic phase stability calculations package
N	The number of collected ions per sampling block
N_N	The fixed number of nuclei available per unit volume at the start of recrystallisation
$N_{X,Y,Z}$	The number density of particles on the plane normal to the X, Y, and Z directions
ν	Atomic jump frequency across the boundary
ODS	Oxide dispersion strengthening
o_i	Observed frequency of blocks of a specified element
P_{AA}	Probability of finding A-A bonds
P_{AB}	Probability of finding A-B or B-A bonds
P_{BB}	Probability of finding B-B bonds
Q	Activation energy for the transfer of atom across the boundary

R	Universal gas constant
ρ	Dislocation density
R_o	Extrusion ratio
r_o	Mean particle radius
SEM	Scanning electron microscope
Σ	Coincidence-site-lattice parameter
σ	Stress
σ_d	Standard deviation of the statistical fluctuations
σ_o	Grain boundary energy per unit area
T	Absolute temperature
t	Heat-treatment time of isothermal treatment
T_E	Effective temperature to complete recrystallisation for isothermal annealing
TEM	Transmission electron microscope
θ	Rotation angle
T_m	Melting temperature
T_s	The starting temperature of recrystallisation
T_f	The finishing temperature of recrystallisation
T_{s_1}	The start of $\alpha \rightarrow \gamma$ transformation
T_{f_1}	The finish of $\alpha \rightarrow \gamma$ transformation
T_{s_2}	The start of $\gamma \rightarrow \delta$ transformation
T_{f_2}	The finish of $\gamma \rightarrow \delta$ transformation
T_t	The transition from the $\alpha \rightarrow \gamma$ to $\gamma \rightarrow \delta$ transformation
V	Grain boundary velocity during recrystallisation
v	Ram speed of extrusion
V_M	Molar volume of matrix metal
V_V	Molar volume of oxide particles
$V_{X,Y,Z}$	The grain boundary velocity along the X, Y, Z directions
ND	Normal direction
RD	Rolling direction
TD	Transverse direction
ϕ_1, ϕ, ϕ_2	Three Euler angles
ϕ, θ, ψ	Another set of Euler angles

CONTENTS

CHAPTER ONE

INTRODUCTION

1.1 BACKGROUNG TO PROJECT

Conventional nickel-base superalloys are limited in high temperature strength by the stability of γ' (Benjamin, 1970). To improve the high temperature strength a more stable species of particles has to be incorporated into the alloy matrix. A suitable dispersoid is yttrium oxide, a readily available compound having many times the stability of γ' (Ubhi *et al.*, 1981). To further enhance the dispersoid strengthening effect requires a finely dispersed particle distribution. Normal powder blending does not achieve the required fine dispersion, and melting causes the oxides to form an immiscible slag. On the other hand, the development of the mechanical alloying technique provides an economical and commercially feasible method of incorporating a refractory oxide into a superalloy matrix. From the initial laboratory success (Benjamin, 1970), well-controlled production operations and techniques have been developed to form and fabricate the alloys into useful components.

The mechanically alloyed metals have a submicrometre grain structure, the accompanying high hardness is undoubtedly not suitable for engineering application, hence recrystallisation heat treatment is always needed. The distinction of the recrystallised mechanically alloyed metals have a columnar structure along the the working direction, which is beneficial to provide a better creep property (Benjamin and Bomford, 1974).

Many mechanical alloyed metals are now commercially available, but steels produced using this method show particular promise in a variety of applications. The ferritic compositions can provide a significant strength to weight advantage over nickel based alloys, and lower thermal expansion coefficient which should be beneficial to thermal fatigue life. *MA956*, for example, is a chromium–rich ferritic stainless steel containing some eight atomic percent of aluminium forced into solution as an aid to oxidation resistance, together with a dispersion of yttrium oxide particles for creep resistance (Hack, 1984; Sundaresan *et al.*, 1987). Also, the void swelling resistance in ferritic metals, such as *MA957*, is superior to that in austenitic metals in nuclear reaction applications (Asano *et al.*, 1988; Little *et al.*, 1991). Thus, iron base ferritic mechanically alloyed steels are selected to be investigated in this study.

1.2 SCOPE AND AIM OF PROJECT

Mechanically alloyed oxide dispersion strengthened stainless steels usually tend to recrystallise into columnar grains, a microstructure ideal for certain creep applications. In other circumstances, *e.g.* for tubular applications, equiaxed grain structures are desired to improve the mechanical properties along the transverse directions as well. Furthermore, it is noticed that mechanically alloyed ODS materials have the exceptionally high recrystallisation temperature, exceeds 0.9 T_m (T_m is the melting temperature) for both steels and nickel-base alloys when they are produced by the mechanical alloying methods. Conventional alloys recrystallise during heating at around 0.6 T_m. Even there have been many studies of the recrystallisation behaviour of ODS alloys during the past two decades, many of them directed at explaining the exceptionally high recrystallisation temperature (around 0.9 of the melting temperature) of these alloys. However, a reasonable to explain the distinct recrystallisation behaviours is still unavailable. The aim of the work is thus put on the establishing of grain controlling and to investigate the factors affect the onset of recrystallisation. The relative experimental techniques required to meet the scope and aim of the project are concluded in Figure 1.1.

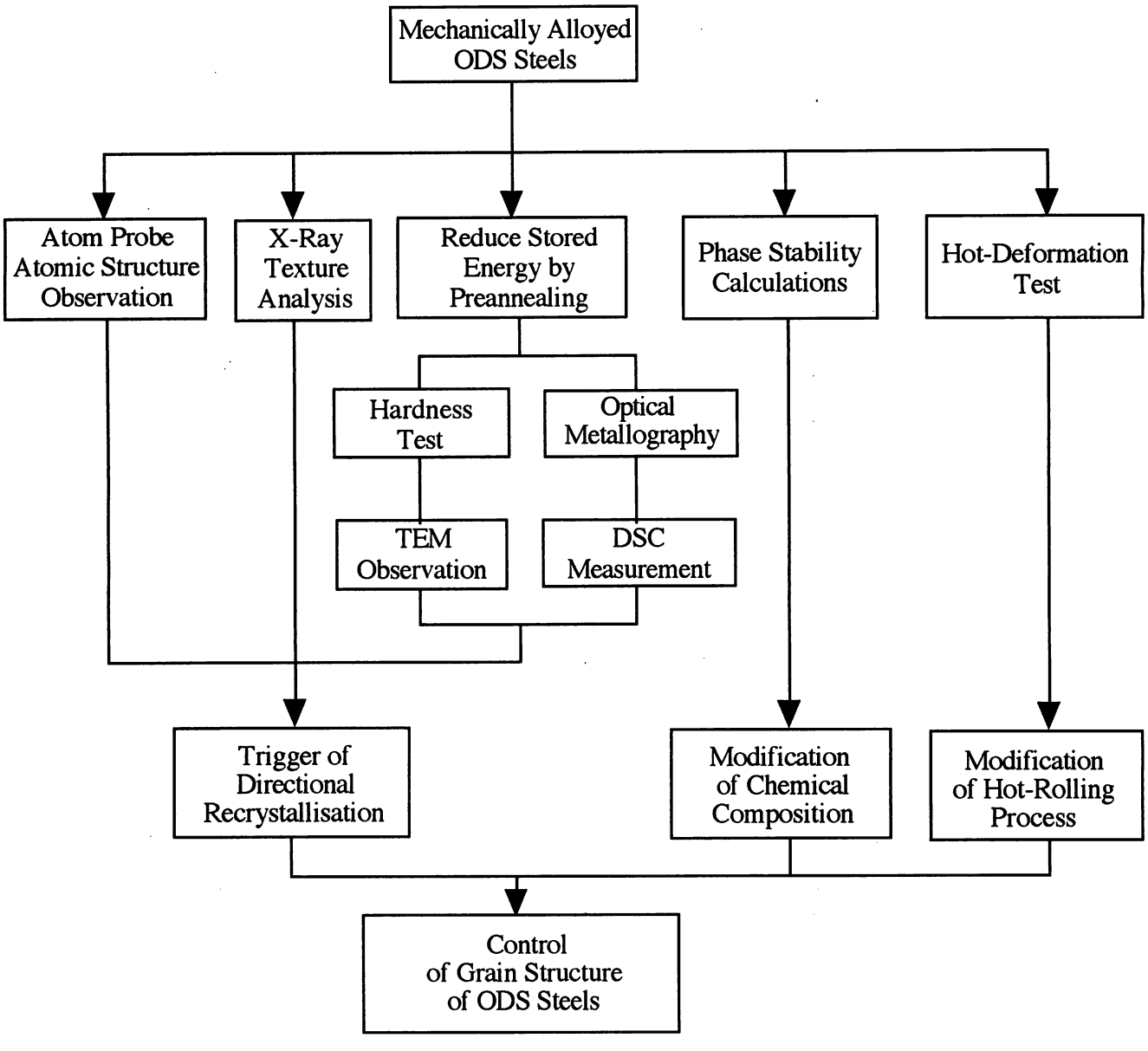

Figure 1.1 Flow chart of experimental procedures.

CHAPTER TWO

METALLURGICAL PHENOMENA IN MECHANICALLY ALLOYED STEELS

2.1 INTRODUCTION

The study of high energy ball milling has led to an intense interest in its use as a nonequilibrium processing tool. It has been realised that mechanical alloying can be used to synthesize metastable alloys and microstructures, like other nonequilibrium processing methods such as rapid solidification and physical vapor deposition. However, the precursor phase in the case of mechanical alloying is typically a crystalline solid, rather than liquid or vapour. The thermodynamic and kinetic factors which govern metastable phase formation can therefore be very different.

Two of the most important alloy systems to emerge from the mechanical alloying process are based on iron and nickel (Koch, 1990). In this chapter, the development of strong alloys by mechanical alloying, their recrystallisation behaviour, production, and applications are reviewed.

2.2 MECHANICAL ALLOYING PROCESS

Mechanical alloying is a dry, high-energy milling process that produces metal powders with controlled, extremely fine microstructures. The powders are produced in high-energy attrition mills or special large-ball mills. Typically, a mixture of commercially available metal powders (or master alloy powders), and a very fine refractory oxide powder is charged into the grinding mill. The resultant alloy has properties unattainable by conventional alloying methods (Benjamin and Volin, 1974). The mechanical alloying (MA) process includes high-energy milling and consolidation as discussed below.

2.2.1 High-Energy Milling

Mechanical alloying makes possible the combination of dispersion, solid-solution, and precipitation strengthening by mixing all the constituents in powder form ever more intimately until the formation of a true alloy powder leaving only the oxides dispersed in the solid solution (Gilman & Benjamin, 1983). Mixing is achieved by dry high-energy ball milling, under

conditions such that powders are not only fragmented but also rewelded together – a process prevented in conventional ball milling by the use of liquids and surfactants.

Throughout the period in which mechanical alloying was being developed, high-energy milling was performed in attritors, in which the ball charge is stirred vigorously with rotating paddles. The first commercial production used attritors able to process up to 34 kg of powder per charge. In the latest production units, up to 1 ton of powder is processed in a 2 meter diameter mill containing more than a million balls which weigh a total of around 10 tons (Fleetwood, 1986).

The charge is a blend of elemental and prealloyed powders, at least one of which is a ductile material, and a crushed master alloy containing intermetallic compounds of the most reactive elements. For example, titanium and aluminum are added as a Ni–Ti–Al alloy, which has much lower reactivity than elemental titanium or aluminum. To provide a dispersed phase in nickel- and iron-base alloys, fine inert oxides such as Y_2O_3 can be included in the charge.

The alloy can be considered to evolve in three stages, as shown in Figures 2.1~3 (Sundaresan and Froes, 1987). Initially, during an intense cold welding period, layered composite particulates of the starting constituents form. Then, during a rapid fracturing period, the repeated break-up and cold welding leads to ever finer composite particles. At this stage, convoluted lamellae can be observed within the particles, along with the beginnings of dissolution and solid solution formation. Next, in a moderate cold welding period, lamellae get finer and more convoluted, with lamellar spacings of less than one micrometre. The compositions of the individual particles converge to the blend chemistry, although the oxide dispersoids remain as such.

2.2.2 Consolidation and Microstructure Control

Oxide dispersion strengthened powders do not densify on simple sintering, and the high hardness of MA powder prevents cold pressing. The powders discharged from the mill must therefore be consolidated by a combination of high temperature and pressure: hot compaction plus hot extrusion, hot extrusion in a can, or hot isostatic pressing. By the time processing has been completed, the particles have an extremely deformed metastable microstructure, which can contain dispersoids (Figure 2.4).

Extrusion of canned powder is generally preferred for the consolidation process, being the cheapest process and able to provide anisotropic microstructures with good properties. High-temperature soaking before hot consolidation may complete homogenisation by diffusion. In the majority of production routes, the extruded bar is an intermediate stage which is normally

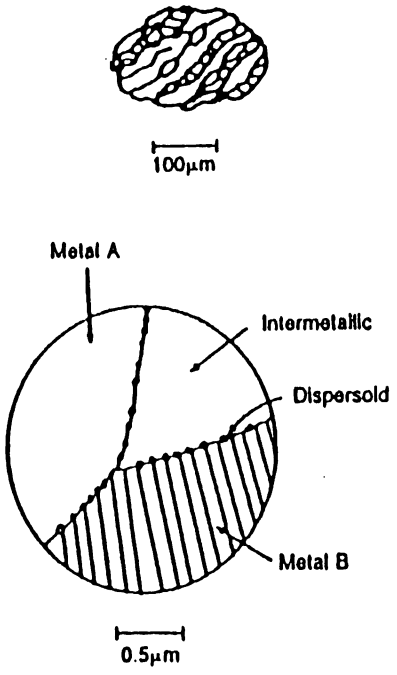

Figure 2.1: The first stage of MA processing — intense cold welding (Sundaresan and Froes, 1987).

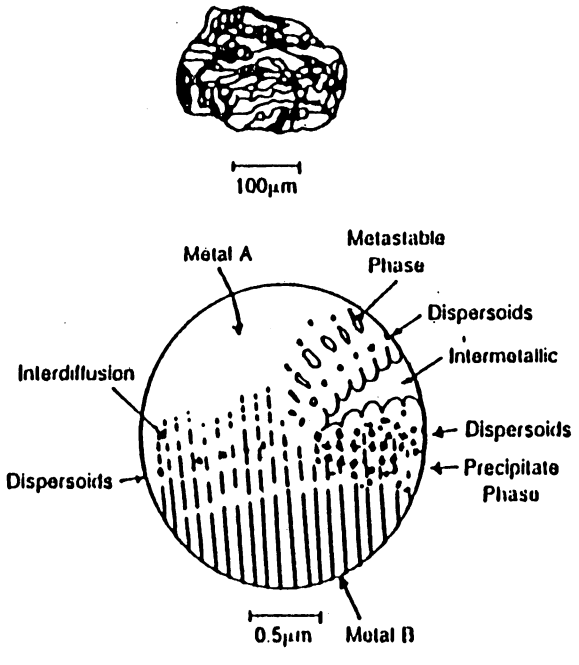

Figure 2.2: The intermediate stage of MA processing — rapid fracturing (Sundaresan and Froes, 1987).

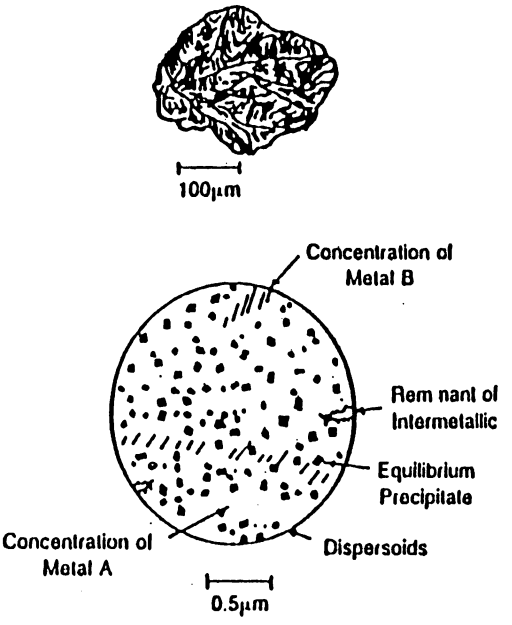

Figure 2.3: The final stage of MA processing — moderate cold welding (Sundaresan and Froes, 1987).

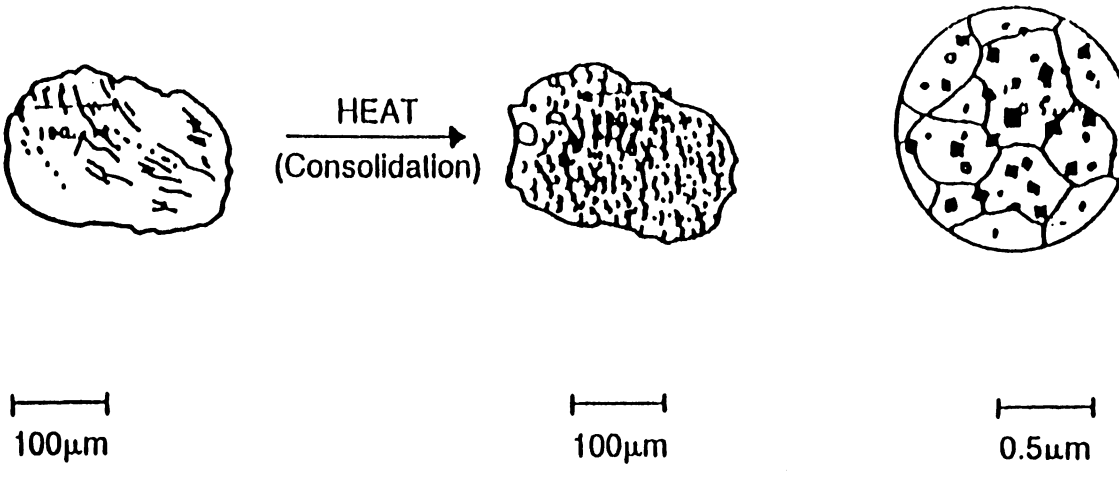

Figure 2.4: Completion of MA processing — steady state. Extremely deformed structure — lamellae no longer optically resolvable, metastable structure with dispersoids. Fine grain size. Equilibrium distribution of dispersoids (Sundaresan and Froes, 1987).

followed by hot rolling. This is a highly controlled operation which is ideal for optimizing the stored energy and can be used also to control texture (Hack, 1984). Any further processing after extrusion, therefore, must be carefully controlled to generate the optimum grain structure for particular applications.

Following hot rolling, most products are ready for recrystallisation heat treatment. One obvious exception is Incoloy *MA956* intended for cold drawn wire, cold rolled sheet, and even foil. Other exceptions are forging stock and products for hot fabrication, which generally respond more readily to deformation in the ultrafine grained condition. As with hot rolled products, the major operation is the recrystallisation heat treatment.

There are two microstructures which are needed for commercial exploitation:

(i) fine equiaxed grains, giving the best room–temperature strength, fatigue strength, and workability (*e.g.* for subsequent forging);

(ii) coarse elongated grains, giving good high–temperature stress–rupture strength and thermal–fatigue resistance.

The fine–grained condition exists in extruded material (although the scale is submicrometre), whereas the coarse elongated grains are developed by recrystallisation of material thermomechanically processed to produce a high level of stored energy. The later depends on the whole thermomechanical processing history of the material. For some special applications, an equiaxed fine grained structure in the tens of micrometre range is desired to improve the isotropy of mechanical properties.

Dieter (1976) found that there is only a limited combination of extrusion ratios and extrusion temperatures if coarse recrystallised grains are ultimately required to improve the rupture strength of the material. Figure 2.5 shows how the extrusion-press behaviour interacts with the rupture strength of *MA753* [1] at 1311 K for 1000 h. On the other hand, work carried out at Kramer (1977) revealed that increased consolidation temperatures simply cause an increase in the as-extruded grain size. Moreover, a significant increase in the as-consolidated grain size can be obtained by HIP (hot isostatic pressing) in *MA738* [2] alloy. The different grain sizes obtained by HIP and extrusion are shown in Figure 2.6.

With the assumption that strain rate is the important variable controlling the recrystallisation response, the relation between the strain rate $\dot{\varepsilon}$ and the other extrusion variables can be expressed by (Dieter, 1976):

---

[1] Nickel-base superalloy, 20 Cr–1.5 Al–2.3 Ti–1.4 Y_2O_3 (wt.%).

[2] *INCONEL 738* + Y_2O_3, (15.8 Cr–3.4 Al–8.4 Co–59.7 Ni + Y_2O_3, wt.%).

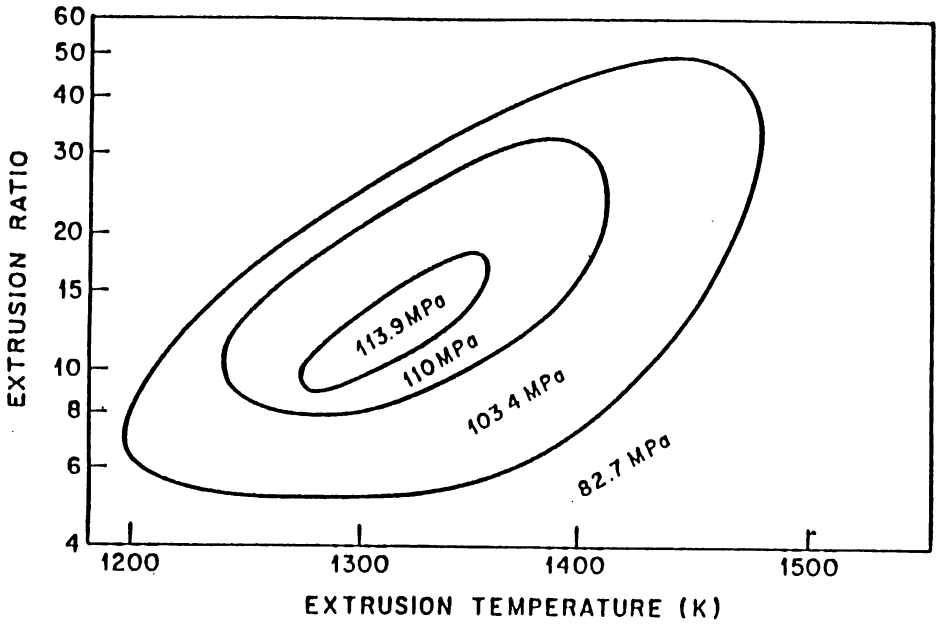

Figure 2.5: Rupture strength response of *MA 753* as a function of the extrusion conditions; the 1000 h rupture strength at 1311 K is indicated (Morse and Benjamin, 1976).

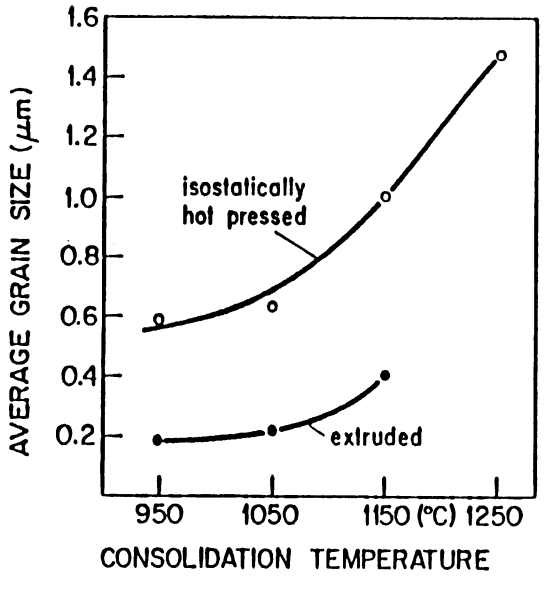

Figure 2.6: Comparison of grain sizes obtained in *MA 738* after hot isostatic pressing and after extrusion as a function of compacting temperature (Kramer, 1977).

$$\dot{\varepsilon} = \frac{6\ v\ \ln\ R_o}{D_b} \tag{2.1}$$

where v is the ram speed at a given temperature, R_o is the extrusion ratio and D_b is the billet diameter. A large diameter billet must therefore be processed at significantly higher ram speeds for a given temperature in order to obtain the same strain rate. Unfortunately, most commercial extrusion presses are incapable of delivering such high speeds at these extrusion conditions. The typical upper limit for extruded cross-sections of more complex ODS alloys is 20–30 cm^2 (Singer and Gessinger, 1982).

2.3 THE HEAT TREATMENT OF MECHANICALLY ALLOYED METALS

The recrystallisation behaviour of mechanically alloyed ODS metals differs from conventional materials because the recrystallisation occurs at very high temperatures, and once it is stimulated can be completed very rapidly. Therefore, grain-size and grain-shape control is more difficult to achieve for mechanically alloyed materials. There are three types of experiments commonly used to study the recrystallisation behaviour:

(1) isothermal annealing;

(2) annealing in a stationary thermal gradient;

(3) annealing in a moving thermal gradient.

Isothermal annealing is a very convenient method to investigate recrystallisation and grain growth as a function of material-processing parameters such as extrusion temperature, extrusion ratio and ram speed. This approach has been used to investigate the recrystallisation behaviour of *MA738* as function of the heat treatment temperature. Figure 2.7 illustrates the effects of annealing temperature and extrusion ratio. It is found that an increase in temperature causes an increase in the grain diameter and grain aspect ratio. However, there is not a linear relationship between the temperature and these two parameters. A peak occurs for both the grain diameter and the grain aspect ratio as a function of the annealing temperature.

Annealing in a stationary temperature gradient is frequently used to determine the appropriate temperature for grain coarsening. An extruded bar several centimetres long is placed into the temperature zone of a resistance-heated furnace. The purpose of the temperature gradient is mainly to provide a range of temperatures so that heating of just one specimen will allow the determination of the recrystallisation temperature.

Annealing in a moving temperature gradient can in principle produce larger and more elongated grains than isothermal annealing. Because of the gradient, nucleation starts at one end of the specimen. As the hot zone moves through the specimen, so these grains grow and

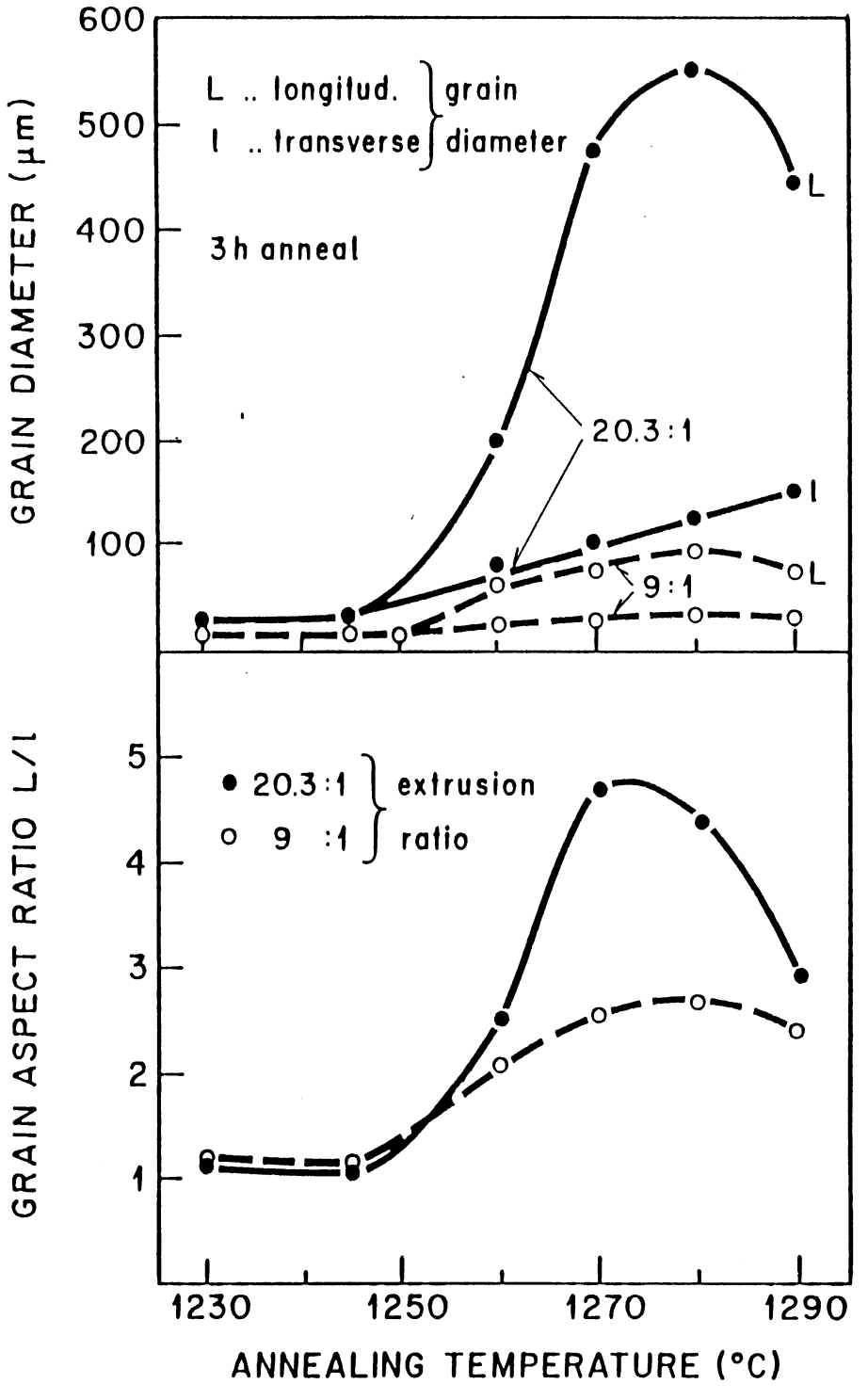

Figure 2.7: Grain size of *MA 738* in the longitudinal and transverse directions (top) and grain aspect ratio (bottom) as a function of temperature (Gessinger, 1976).

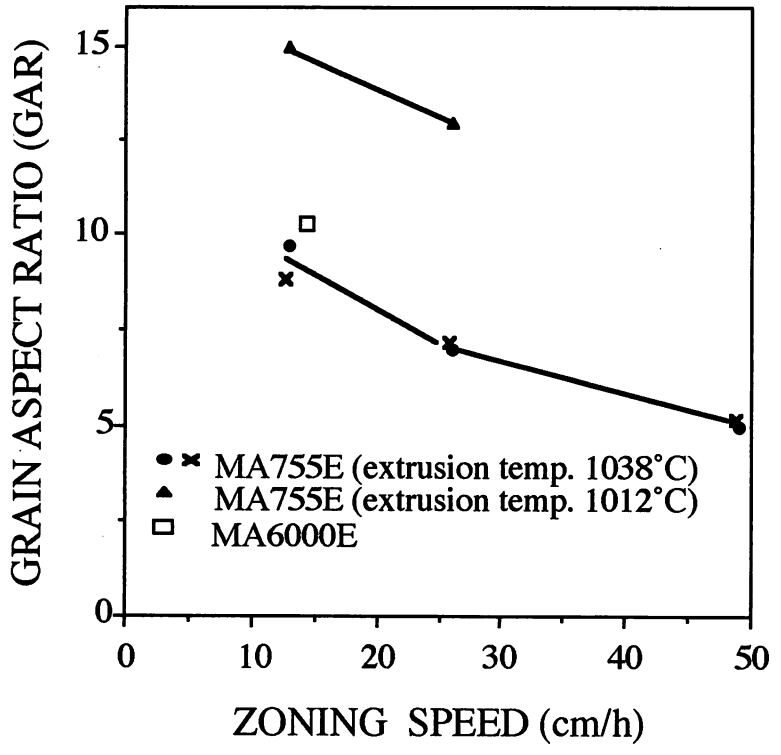

Figure 2.8: Effect of zone annealing speed on the grain aspect ratio (Cairns *et al.*, 1975).

a recrystallisation front develops. It is clear that the gradient should be as large as possible to decrease the probability of nucleation of new grains as much as possible. The recrystallised grain size decreases with increasing zone travel speed and with increasing temperature gradient (Cairns *et al.*, 1975). The grain aspect ratio increases with a decrease in the zone speed, as shown in Figure 2.8. Most mechanically alloyed products are therefore zone annealed at speeds less than 10 cm h^{-1} (Cairns *et al.*, 1975).

2.4 RECOVERY, RECRYSTALLISATION AND GRAIN GROWTH IN METALS

Some properties of a metal depend on it's microstructure. Deformation and annealing are two of the most important processing methods commonly used to control properties.

As is widely known, when a metal is plastically deformed, most of the mechanical energy expended in the deformation process is converted into heat. Only a small proportion is stored in the metal as point defects, dislocations, and stacking faults. Thus a deformed metal, being in a state of high energy, is thermodynamically unstable. The amount of stored energy depends on a number of variables. For a given deformation process, the stored energy varies from metal to metal, with purity, alloying elements, grain size, grain orientation, long range order and many other factors.

The annealing of a deformed metal involves a variety of changes through which the deformed state is taken continuously to states of lower energies. It has been customary to divide the whole annealing process into three main stages, namely recovery, recrystallisation and grain growth.

2.4.1 Recovery

This occurs without any perceptible change in the optical microstructure. It involves the annealing out of defects and their clusters, the annihilation and rearrangement of dislocations, subgrain formation and growth, and the formation of recrystallisation nuclei. In general, there is no essential change in the crystallographic texture of the deformed metal because there is no high-energy boundary migration.

The characteristic features of recovery are:

(1) there is no incubation period; and

(2) the rate of change is sharp initially, then becomes more gradual as time progresses, and finally asymptotically approaches zero.

The energy stored in a deformed metal represents the driving energy for the processes of recovery and recrystallisation. The stored energy is released as heat, which can be measured using a calorimeter. Electrical resistivity and hardness changes can also be recorded. In a series of experiments, Clarebrough *et al.* (1955), determined the stages of stored energy release for copper and nickel. As shown in Figure 2.9, some of their results correlate the energy release with the change of hardness. Since the major change in hardness occurs simultaneously with the recrystallisation of the matrix, the use of a hardness test is convenient to evaluate the extent of recovery in heat treated specimens. However, the use of the calorimetric method can provide quantitative data.

2.4.2 Recrystallisation

This annealing stage begins with the formation of stable nuclei for recrystallisation. These nuclei are essentially strain–free and capable of growing at the expense of the polygonized matrix by high-energy grain boundary migration. Recrystallisation is considered to be completed when the entire structure is replaced by new grains. There is consequently a large local reorientation or change in texture.

The driving energy for recrystallisation is the unreleased portion of the stored energy after recovery has taken place, which may correspond to approximately 90 percent of the total energy in the deformed specimen.

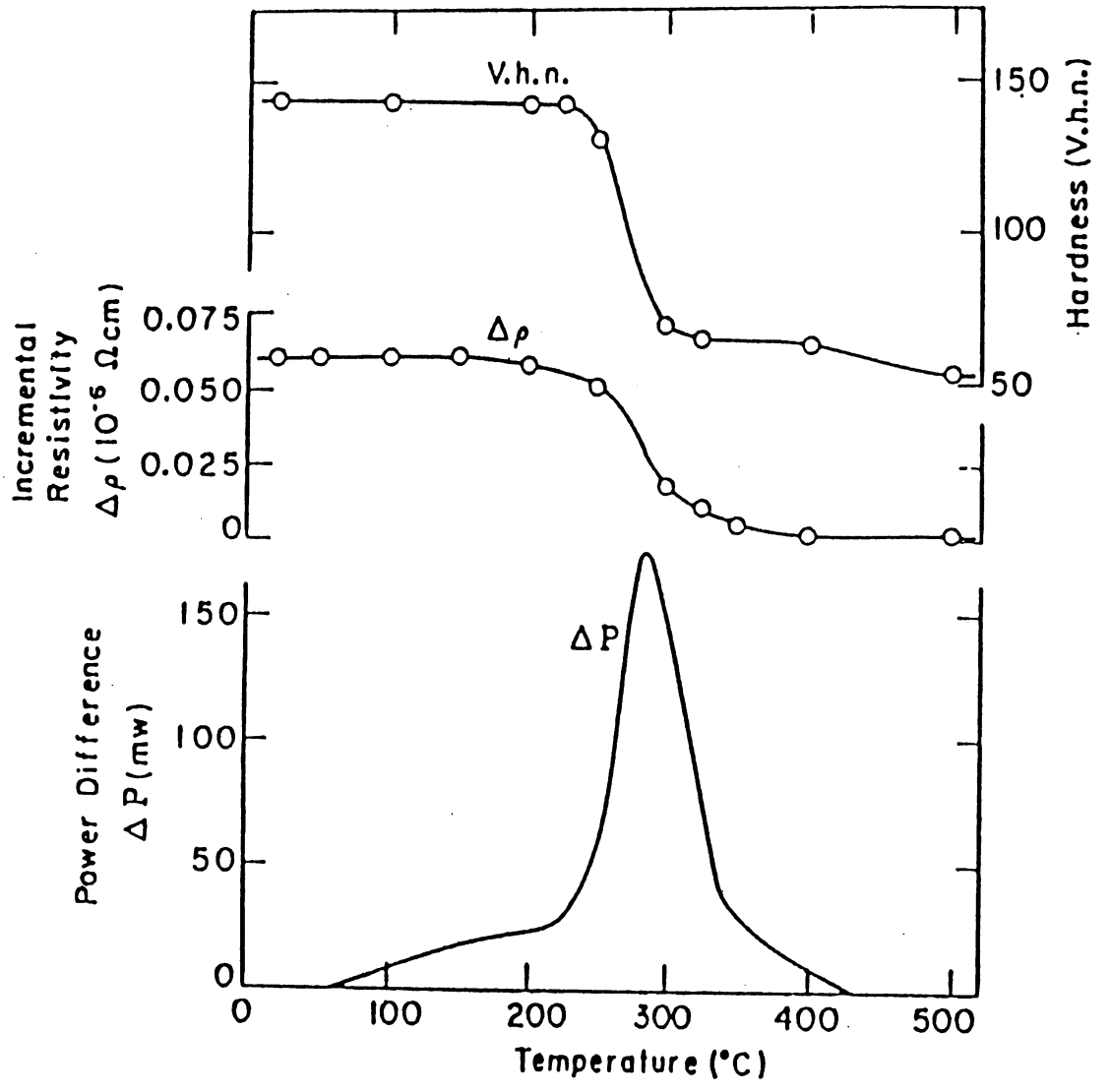

Figure 2.9: Power difference, representing released energy during the uniform heating of a plastically twisted copper rod. Changes in resistivity and hardness are shown (Clarebrough *et al.*, 1955).

The qualitative effects of a number of processing variables on recrystallisation have been established experimentally (Burke and Turnbull, 1952) :

(1) A certain minimum degree of deformation is necessary for recrystallisation to occur.

(2) The smaller the degree of deformation, the higher is the temperature required to cause recrystallisation.

(3) An increase in the annealing time decreases the temperature necessary for recrystallisation,

although recovery processes may then stifle recrystallisation altogether.

(4) The final grain size depends chiefly on the degree of deformation, and to a lesser extent on the annealing temperature, being smaller the greater the degree of deformation and the lower the annealing temperature.

(5) The larger the initial grain size, the greater is the amount of cold deformation required to give an equivalent recrystallisation temperature and time.

(6) The amount of cold work required to give equivalent deformation hardening increases with increasing deformation temperature.

(7) Continued heating after recrystallisation is complete, causes the grain size to gradually increase.

It seems obvious that the presence of large, hard and widely spaced particles of a second phase tends to enhance the nucleation for recrystallisation because more heterogeneous deformation occurs in the immediate vicinity of the particles. The critical size of a particle responsible for stimulating nucleation is a function of deformation (Humphreys, 1980). The critical size increases with decreasing strain. For a number of alloy systems, the minimum size of particle at which recrystallisation initiates is found to be around 1μm. The number of recrystallisation nuclei that can form at a particle depends on the size of the particle. On the other hand, it has been known that a finely dispersed second phase has a strong effect on inhibiting recrystallisation, in particular, nucleation (Doherty and Martin, 1963). The data for particle influence on recrystallisation are summarised in Figure 2.10. To retard recrystallisation the necessary particle spacing decreases as the particle size decreases. The effect of particles is not controlled solely by the average concentration of particles in the material studied; although many particles operate individually, a strong effect due to clusters of closely spaced particles is frequently found. How such a dispersion influences the deformation structure, hence, subsequent nucleation of recrystallisation is largely unclear. For mechanically alloyed metals, the mostly popular dispersoid phase used is Y_2O_3. The particle size of Y_2O_3 is around 0.05 μm as shown in Figure 2.11, and should retard recrystallisation. However, since the degree of deformation is involved in mechanical alloying is very large, this conclusion is not safe since the Y_2O_3 may still accelerate recrystallisation.

2.4.3 Grain Growth

This term is generally applied to the increase of grain size upon continued annealing after recrystallisation is complete. The consequence is to decrease the total grain boundary area in the specimen. Normal grain growth is relatively uniform, and during such grain growth the

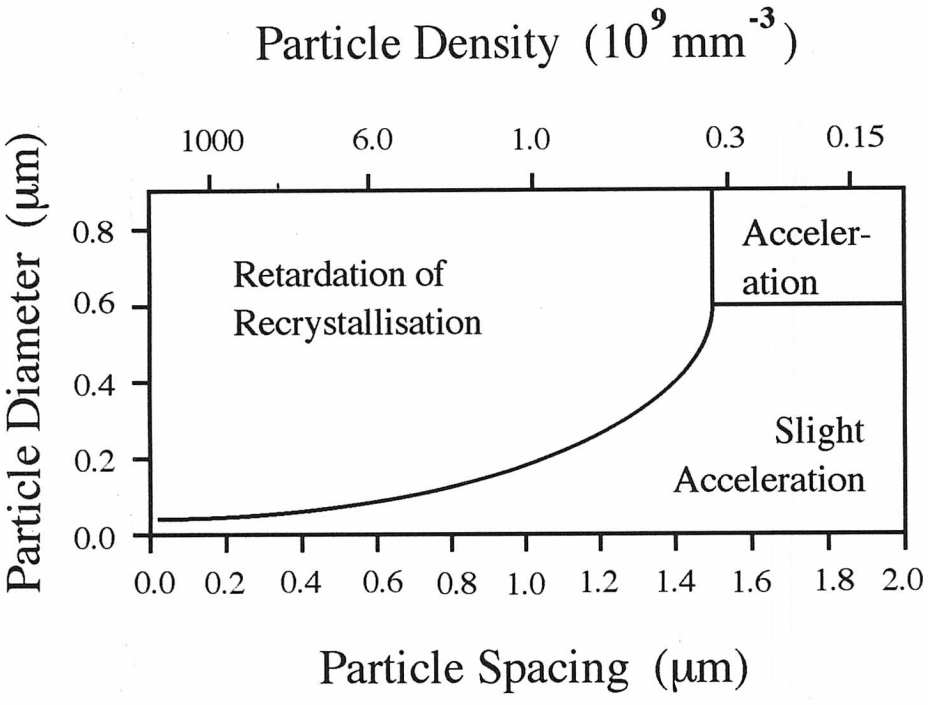

Figure 2.10: Summary of the effects of particles on the recrystallisation. Only the particles sufficiently closely spaced, to the left side of the line, are able to effect retardation (McQueen *et al.*, 1985).

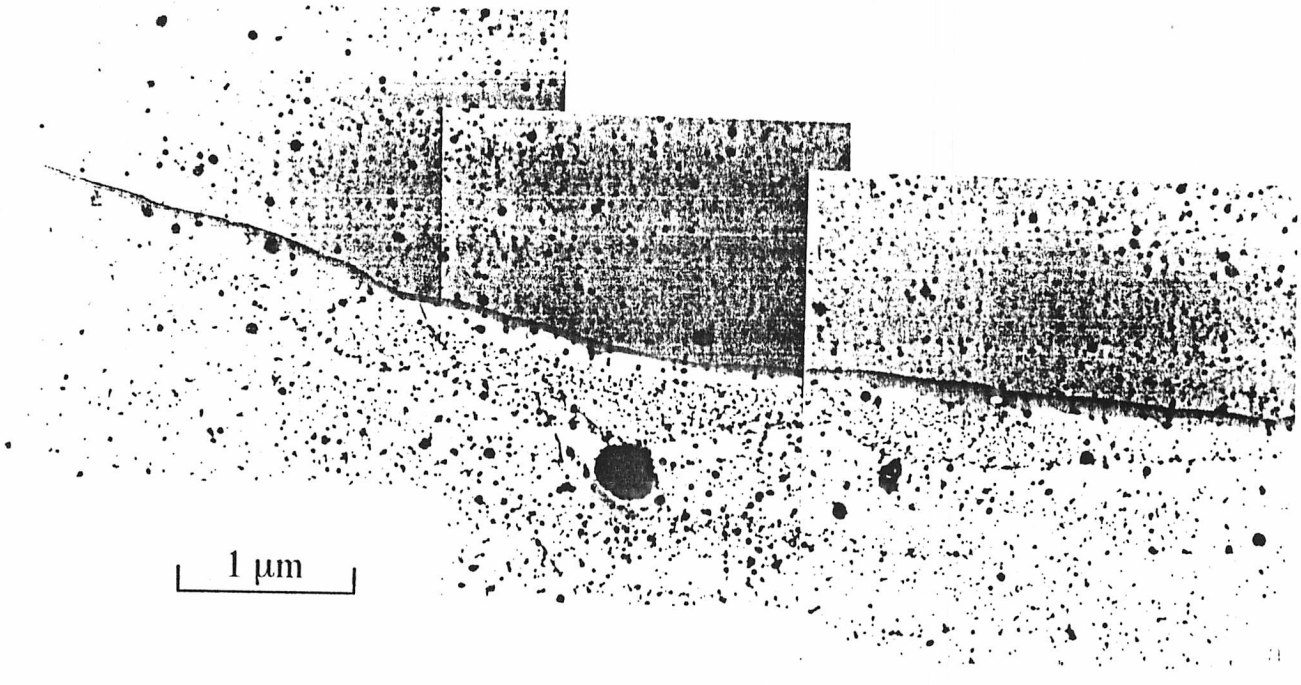

Figure 2.11: Transmission electron micrograph showing the distribution of Y_2O_3 in *MA956* steel (Baloch, 1989).

normalised-size and the shape distributions are nearly invariant. In abnormal grain growth, which is frequently called secondary recrystallisation, a few grains grow to disproportionately large sizes at the expense of the fine grains of the matrix. These latter matrix grains have been inhibited from growth by dispersed particles, or by a strong recrystallisation texture. Both normal grain growth and secondary recrystallisation result in large changes in the crystallographic textures.

2.5 RECRYSTALLISATION BEHAVIOUR OF MECHANICALLY ALLOYED METALS

Recrystallisation occurs when cold worked metals are heated to temperatures high enough to permit the movement of high-energy grain boundaries, which sweep through the metal and replace the cold worked grains by a new set of more nearly perfect crystals. In general, recrystallised metals have an equiaxed grain structure. However, there are now many cases reported in the literature in which unconventional alloying or processing leads to the development of a highly anisotropic grain structure as a consequence of recrystallisation. The directionally recrystallised structure closely resembles that obtained by directional solidification, with the elongated columnar grains aligned along a particular sample axis.

The majority of reported examples of directional recrystallisation are found in oxide dispersion strengthened (ODS) alloys, designed primarily for their exceptional creep resistance and high temperature stability.

The distinctive features of recrystallisation in mechanically alloyed oxide dispersion strengthened metals include the following: firstly, the high recrystallisation temperatures up to 0.9 of the melting temperature and secondly, the recrystallisation once initiated rapidly reaches completion.

2.5.1 Recrystallisation Mechanisms

Recrystallisation can occur by primary or secondary mechanisms. It is recognised that the columnar grain structure in nickel–base mechanically alloyed metals is generated by secondary recrystallisation, whilst the iron–base mechanically alloyed metals undergo primary recrystallisation from a cold-deformed microstructure. The driving force for secondary recrystallisation is the reduction of grain boundary energy. That for primary recrystallisation includes the reduction of dislocation–line energy and of grain boundary energy.

2.5.1.1 The Driving Force for Recrystallisation

The driving pressure for boundary migration can originate from dislocations and grain boundaries. The later is given by (Singer and Gessinger, 1982):

$$\Delta G_S \simeq \frac{2\sigma_o}{L} \tag{2.2}$$

where σ_o is the grain boundary energy per unit area and L is the mean grain intercept.

The stored energy due to dislocations is (Singer and Gessinger, 1982):

$$\Delta G_D \simeq \frac{1}{2} G b^2 \rho \tag{2.3}$$

where G is the shear modulus, b is the Burgers vector and ρ the dislocation density.

Assuming that $\rho = 10^{13}$ m^{-2} and $\sigma_o = 1$ J m^{-2}, for the mechanically alloyed steels, $\Delta G_S \simeq 5$ MPa and $\Delta G_D \simeq 3\times 10^{-2}$ MPa, so that ΔG_D is two orders of magnitude smaller than ΔG_S. It is clear that the reduction of grain boundary area is the major driving force for recrystallisation in the mechanically alloyed steels.

2.5.1.2 Particle Pinning

Grain boundary migration is inhibited by particles which exert a pinning force on the migrating boundary (Zener, 1948):

$$\Delta G_P \simeq \frac{3 f \sigma_o}{2 r_o} \tag{2.4}$$

where f and r_o are the volume fraction and mean particle radius, respectively. With the $r_o = 5.0$ *nm*, and $f = 0.03$ and 0.015 for *MA956* and *MA957* respectively (Gessinger, 1984), we get

$$\Delta G_P \simeq 0.90 \text{ MPa for } MA956 \text{ steel}$$

and

$$\Delta G_P \simeq 0.45 \text{ MPa for } MA957 \text{ steel}$$

The pinning forces are therefore smaller than the driving forces.

2.5.2 Nucleation Sites

There are four possible processes by which recrystallisation may be initiated:

(a) The classical fluctuation theory by Burke and Turnbull (1952).

(b) Polygonisation, (Cahn, 1950; Beck *et al.*, 1949).

(c) Subgrain coalescence, (Fujita, 1961; Hu, 1963).

(d) Strain induced boundary migration (Beck & Sperry, 1950; Bailey & Hirsch, 1962; Bailey, 1960, 1963).

In each case, once a recrystallisation nucleus is formed, it's ability to grow is dependent on the mobility of its grain boundaries. The classical model of nucleation is based on the assumption that nuclei are formed as a result of thermal fluctuations. However, the critical nucleus size and activation energy based on this theory turn out to be unrealistically large.

Models (b), (c), and (d) do not require the formation of a new orientation in the cold worked material. They are all variations on the same theme, distinct only in the mechanisms by which the recrystallisation nucleus is initiated.

It is now widely accepted that nucleation in recrystallisation is essentially the migration of an existing boundary. The concept of a nucleation rate still remains valid since there is as apparent incubation period, although this may be indicative of an initial period of growth rather than of time to form a nucleus (Christian, 1975a).

There is some dispute as to which of the two processes, strain–induced boundary migration or subgrain coalescence, will produce the recrystallisation nuclei.

2.5.2.1 Strain-Induced Boundary Migration

Recrystallisation can begin from existing subgrains or from high energy boundaries present in the material before deformation. The boundary bulges to give an area of low dislocation density, and this becomes the recrystallisation nucleus. The process requires an appreciable area of grain boundary to exist, separating an almost strain free region from the deformed matrix. Experiments have shown that there is no incubation period before bugling of the grain boundaries, and that the rate of boundary migration is highest initially and then decreases with annealing time.

The process of grain boundary migration can be considered to proceed as follows. Migration may start at an area of boundary across which there is a fairly large difference in dislocation density. As soon as the boundary moves, a relatively dislocation–free area is generated on one side of the boundary, and the driving force is then governed by the average value of stored energy. The activation energy can be expected to be approximately equal to that for grain boundary self-diffusion.

2.5.2.2 Subgrain Coalescence

Nielsen (1954) first proposed a mechanism of grain coalescence in secondary recrystallisation. He refers to this as 'geometrical coalescence' in which pair of neighbouring grains of close orientations are supposed to combine by boundary coalescence to form a recrystallisation

nucleus. Hu (1962) has observed using transmission electron microscopy that two neighbouring grains coalesce by the gradual disappearance of the boundary between them. Therefore, a change in the initial orientation of the subgrains is produced. The mechanism has been observed by a number of workers (Fujita, 1961; Hu, 1962; Lytton *et al.*, 1965).

The criterion for the disappearance of a subgrain boundary, as suggested by Hu (1962), is dependent on the nature of the connecting boundaries. Subgrains which are slightly misoriented with one another are unlikely to coalesce, and this is consistent with the observation that the tendency for recrystallisation to occur is stronger in areas of less sharp deformation textures (Hu, 1959). Hence recrystallisation takes place more readily between crystallites of sufficient misorientation. In areas of a wide range of orientations an incubation period during which coalescence occurs is required.

On the other hand, the concept of subgrain coalescence by subgrain rotation was proposed by Li (1962). He investigated the possibility of two subgrains being able to rotate during recrystallisation both from a thermodynamic and kinetic point of view, and suggested that subgrains might rotate by diffusional processes until adjacent subgrains were of similar orientation. The two subgrains involved would then have coalesced into one large grain with little grain boundary migration, the driving force arising from a reduction in boundary energies. The process is shown schematically in Figure 2.12.

Evidence supporting the subgrain coalescence theory has been found by Towner and Berger (1960) who observed an increase in subgrain boundary angle during subgrain growth of 2 to 6 minutes of an arc for an increase in subgrain size of $\times 2$. This is in accordance with the energetics described by Li, since under this mechanism subgrain boundaries of smallest angle must disappear first.

2.5.3 Grain Boundary Anisotropy and Mobility

It is becoming common to divide grain boundaries into two broad classes, "special" and "general", depending upon the properties associated with their energy, structure, and crystallographic parameters (Ralph *et al.*, 1992). *Special* boundaries include low angle grain boundaries and those that are at or near to a high density coincidence structure and accordingly have a short period repeat structure in the boundary plane. *General*, or *random*, boundaries make up the rest and there is no real agreement as to the limits (in periodicity or deviations in misorientation) as to how to classify a boundary as *special* or *general/random.*

One property that reflects the degree of "specialness" of a grain boundary is its migration rate. *Random* boundaries tend to be associated with a higher energy and higher migration

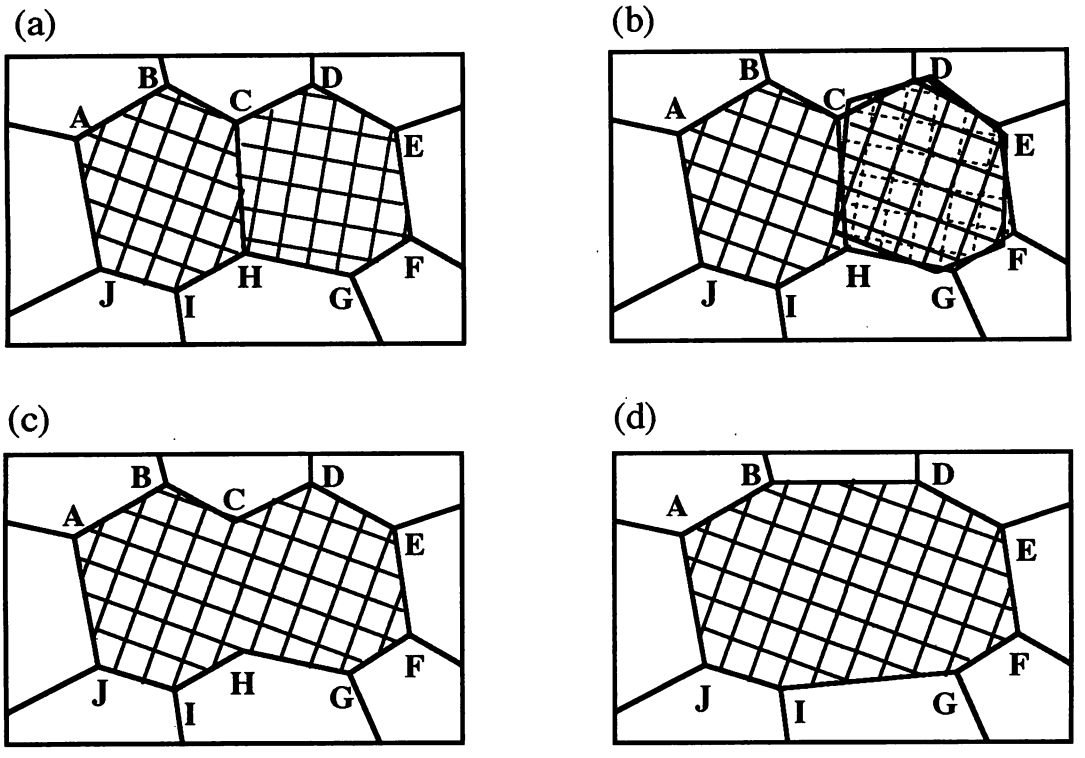

Figure 2.12: Coalescence of two subgrains by rotation of one. (a) The original subgrain structure before coalescence; (b) one subgrain undergoes a rotation; (c) the subgrain structure just after coalescence; (d) the final subgrain structure after some sub-boundary migration (Li, 1962).

rate than those which are *special.* In addition, the mobility of low angle grain boundaries is more sensitive to the presence of a dispersed phase.

The effect of nonuniform grain boundary energies and mobilities in textured materials can be explained by means of a simple example, namely by a texture composed of only two components A and B. Suppose that at the beginning of grain growth, the volume fraction of component B is much smaller than that of component A. Thus, due to their lower frequency, the B grains are surrounded by A grains forming A-B boundaries with high energy and high mobility, whilst the A grains, in contrast, due to their high frequency, are surrounded mainly by low angle A-A boundaries with low energy and mobility (Figure 2.13a).

At the beginning of grain growth, small B grains will have to shrink because of their convex curvature and will disappear, whereas, large B grains with concave grain boundaries will grow very fast. For both reasons the partial mean grain size of the B component increases rapidly from the beginning of grain growth, while the A grains, mainly surrounded by the low

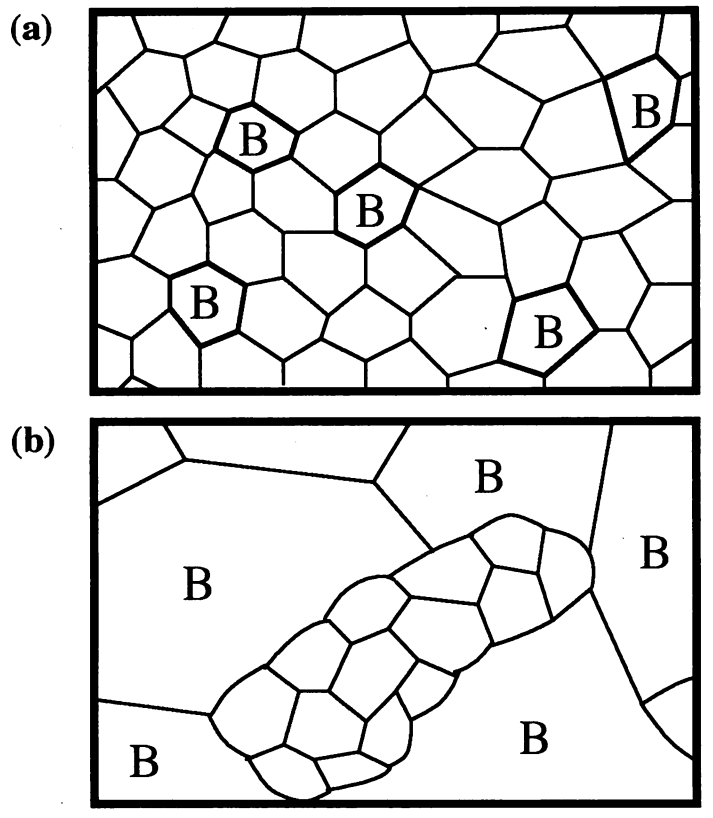

Figure 2.13: Microstructure with 2 texture components A, B (a) at the beginning of grain growth rate ($V^A > V^B$); (b) in an inbetween stage of grain growth rate ($V^B > V^A$). The $A - B$ grain boundaries are assumed to be high angle grain boundaries with high energies and high mobilities (after Heckelmann *et al.*, 1992).

mobility boundaries, show only minor growth. After some incubation time, relatively few large B grains are embedded in a fine grained A matrix (Figure 2.13b). It is obvious that the smaller the volume fraction of B at the beginning of grain growth, the larger is the incubation period until texture changes and the more marked is the abnormal grain growth (Heckelmann *et al.*, 1992).

2.6 THEORETICAL APPROACHES

The properties of mechanically alloyed oxide dispersion strengthening (ODS) superalloys are closely related to their grain structure and crystallographic texture (Benjamin and Volin, 1974; Gessinger, 1984), both of which are influenced by recrystallisation, which has some unusual characteristics for this class of materials. Consequently, there have been many studies of the recrystallisation behaviour of ODS alloys during the past two decades, many of them directed at explaining the exceptionally high recrystallisation temperature (around 0.9 of the

melting temperature) of these alloys. Hotzler and Glasgow (1982), using transmission electron microscopy, reported that directional recrystallisation in a nickel-base mechanically alloyed ODS superalloy *MA6000* is driven mainly by surface energy, and triggered by γ' phase dissolution which occurs at temperatures in excess of 1100 °C . However, Mino *et al.* (1987) found that this cannot be a satisfactory explanation because in some nickel-base superalloys, the recrystallisation temperature can be substantially in excess of that required for γ' dissolution. They suggested that the γ' dissolution might be a necessary but not sufficient condition for recrystallisation, and that the coarsening of dispersed oxide is the real trigger for the process.

Baloch and Bhadeshia (1990) used the empirical concept that a critical value of the kinetic strength is required to induce recrystallisation. The kinetic strength model has been further established by Mino *et al.* (1991), using differential scanning calorimetry and reaction rate theory. However, the cause of the exceptionally high recrystallisation temperature of mechanically alloyed ODS materials is still not clear. For example, the recrystallisation temperature exceeds 0.9 T_m (T_m is the melting temperature) for both steels and nickel-base alloys when they are produced by the mechanical alloying method. Conventional alloys recrystallise during heating at around 0.6 T_m.

More fundamental methods of analysing overall transformation kinetics are based on the Johnson-Mehl-Avrami method (Murakami *et al.*, 1993) to interpret the effect of yttria particles alignment. The "kinetic strength" concept and Johnson-Mehl-Avrami method are briefly outlined below.

2.6.1 Kinetic Strength Theory

The "kinetic strength" concept has been used for many decades, beginning with a form of the Hollomon–Jaffe tempering parameter (Hollomon and Jaffe, 1945) and has in recent years been re–emphasised in the modelling of the heat–affected zones of steel weld deposits by Alberry and coworkers (1977, 1979, 1983), and Ashby & Easterling (1982). In essence, the kinetic strength of a heat treatment is an integration of the time and temperature over the range of the heat treatment. The concept has been applied in the work of Baloch (1989), to the zone annealing of ODS superalloys. It was proposed that a minimum value of kinetic strength, D_E, is required to induce directional recrystallisation. If a given combination of specimen travel speed and peak temperature results in a value of kinetic strength which is less than D_E, then those conditions should not lead to complete recrystallisation. An excess of kinetic strength beyond D_E simply should lead to additional annealing after recrystallisation is completed. The kinetic strength may be expressed mathematically as:

$$D = \int_{t_0}^{t_f} \exp\left(-\frac{A}{RT}\right) dt \tag{2.5}$$

where A is an arbitrary activation energy, R is the Universal gas constant, and T is absolute temperature.

The transition from partially recrystallised to a fully recrystallised sample should then occur when D achieves a critical value $D = D_E$. A further useful concept is the effective temperature T_E associated with the heat treatment. It follows that the minimum effective temperature is given by

$$T_E = -\frac{A}{R} \ln\left(\frac{D_E}{\Delta t}\right) \tag{2.6}$$

where Δt is the annealing time.

The effective temperature T_E also permits an experimental evaluation of the value of the unknown activation energy A. The measured values of the activation energy A was found to be 402791 J mol^{-1} in *MA956* steel and 654257 J mol^{-1} in *MA957* steel respectively (Baloch, 1989). The critical values of kinetic strength, D_E, were 3×10^{-12} s and 5×10^{-20} s for *MA956* and *MA957* steels respectively, by empirical calculations (Baloch, 1989).

The kinetic strength idea is obviously empirical since the actual rate controlling functions are likely to be more complex. It is nevertheless useful in rationalising the affects of time and temperature within a specified set of data.

11.3.2 Johnson-Mehl-Avrami Method

The Johnson-Mehl-Avrami theory for overall transformation kinetics has been used by Murakami *et al.* (1993) to study the recrystallisation behaviour of mechanically alloyed ODS metals, as outlined below:

The grain boundary velocity during recrystallisation is given by Christian (1975a):

$$V = \delta\nu \exp\,(-Q/RT)[1 - \exp\,(-\Delta G/RT)] \tag{2.7}$$

where δ and ν are the distance and atomic jump frequency across the boundary respectively, R is the Universal gas constant, and Q is an activation energy for the transfer of atoms across the boundary. ΔG is the effective driving force for recrystallisation, which does not vary

with temperature, but is modified by the particle pinning force. For orientation independent pinning, the effective driving force is given as:

$$\Delta G \simeq \Delta G_S - (C_1 V_V V_M \sigma_o / r_o) \tag{2.8}$$

where ΔG_S is the stored energy in the material due to the grain boundaries, r_o is the particle radius, σ_o is the grain boundary energy per unit area, V_V is the molar volume of oxide particles and V_M is the molar volume of matrix metal. C_1 is a constant whose magnitude depends on the details of the pinning process.

However, considering about the significant alignment of particles in mechanically alloyed metals, the ΔG is modified to be an orientation dependent function as:

$$\Delta G_{X,Y,Z} \simeq \Delta G_S - (C_1 N_{X,Y,Z} V_M \sigma_o / r_o) \tag{2.9}$$

where $N_{X,Y,Z}$ is the number density of particles on the plane normal to the X, Y, and Z direction, respectively. The equation applies to the case where the particles are nonuniformly dispersed (Murakami *et al.*, 1993).

It is assumed that recrystallisation begins from a number of preexisting nuclei (grains), so that the fraction ξ of the sample that is isothermally-recrystallised can be obtained using the classic Johnson-Mehl-Avrami approach (Christian, 1975b) as:

$$\xi = 1 - \exp(-N_N V_X V_Y V_Z t^3) \tag{2.10}$$

where N_N is the fixed number of nuclei available per unit volume at the start of recrystallisation, $V_{X,Y,Z}$ is the grain boundary velocity along the X, Y, Z direction, and t is the isothermal heat-treatment time.

For continuous heating transformation, the heating curve is expressed as a series of isothermal steps whose effects are summed using the Schiel rule (Murakami *et al.*, 1993).

The use of this modified model can predict the effect of particle alignment, but the calculations do not fit well with the experimental data. These difficulties occur because when recrystallisation occurs at around 0.9 T_m, it happens very rapidly during isothermal heat treatment, or over a very narrow temperature range during continuous heating. Such data can only be represented by large activation energies in order to achieve high recrystallisation temperatures and rapid subsequent transformation.

Almost all of these difficulties are resolved when nucleation is considered in detail (Murakami, 1993). It turns out that the activation energy for nucleation in the mechanical alloys

should indeed very large. This is because the alloys have an unusually small grain size prior to recrystallisation. The nucleation of recrystallisation occurs by the bowing of grain boundaries, a process which for conventional alloys is straightforward since the distance between grain boundary junction is usually larger that between other pinning points. With the submicrometre grain size of mechanically alloyed metals, the junctions themselves act as severe pinning lines for grain boundary bowing, thus leads to an enormous activation energy for the nucleation and retards the onset of recrystallisation at very high temperature.

2.7 PROPERTIES AND APPLICATIONS OF MECHANICALLY ALLOYED ODS METALS

The production of a useful alloy product requires careful control of thermomechanical processing and grain structure (Benjamin, 1976). Early development of oxide dispersion strengthened materials was plagued by an apparent inability of a dispersion strengthened superalloy to match the properties even of a dispersion strengthened metal such as *TD Nickel* alloy. It was finally recongnized that good high temperature stress rupture properties were directly correlated with the development of a coarse elongated grain structure (Benjamin and Volin, 1974; Wilcox and Clauer, 1972). Grains with lengths of centimeters and diameters of around a millimeter each are typical (Frazier and Evans, 1968). In addition to the high temperature strength, the mechanically alloyed oxide dispersion strengthening alloys have an excellent resistance to oxidation, carburization and hot corrosion makes the alloy an ideal candidate for high temperature applications (McColvin and Smith, 1987). The distinct properties of two commercialised mechanically alloyed metals, nickel–base and iron–base, over the conventional metals are described below.

2.7.1 ODS Nickel–base Superalloys

Within a historical context, the MA process was developed as a means to combine dispersion strengthening with alloy strengthening – and this is presently the major use of the process. The major commercial dispersion strengthened nickel–base alloys produced are the INCONEL alloys *MA754* and *MA6000.*

MA754

The vane alloy *MA754*, without any γ' strengthening designed in, is capable of a service temperature of about 1000 °C . The stress rupture properties of *MA754* recrystallised bar tested at 1093 °C in the longitudinal direction are compared in Figure 2.14 with those of *TD–Ni*, *TD–NiCr*, *Nimonic 80A* and the cast cobalt alloy *MAR–M509.* Like other dispersion–strengthened materials, *MA754* has a very flat log stress versus log life curve and has notably

high strength for rupture at long times. Compared with a 100 h rupture stress of 102 MPa at 1093 °C in the longitudinal direction, the rupture stress in the transverse direction is only 42 MPa, reflecting the important effect of the elongated grain structure. The recrystallised bar is found to exhibit a strong {100} texture in the longitudinal direction which results in a low elastic modulus (151 GPa) and good thermal–fatigue resistance (Gessinger, 1984).

MA754 is currently used in the military aircraft engines *GE101*, *110* and *404*, and offers an effective alternative to single crystal castings and directionally solidified components (Fleetwood, 1986).

MA6000

MA6000 is γ' strengthened together with dispersion strengthening. Its specific strength is compared against conventional alloys in Figure 2.15. *MA6000* is stronger than the cast alloys at temperatures above 900 °C , as γ' strengthening declines. To maintain strength at high temperature in the face of enviormental attack, *MA6000* is less reliant on coatings than other alloys: it combines the cyclic oxidation resistance of alloy *713C* with the sulphidation resistance of *IN–738* (Kim and Merrick, 1979).

MA6000 seems particularly suited to small blades operated uncooled at high temperatures, blades machined from bar have been tested. Forging to near net shape is economically desirable, but with its high temperature strength the alloy cracks at chilled surfaces when conventionally forged. Alternatives being investigated are isothermal forging at low strain rates using heated dies, and conventional forging at high strain rates with thermal barriers to reduce surface chilling. Fully recrystallised blades with grains of high aspect ratio have been made using both routes and the effect of forging conditions on structure and properties is being studied.

Several additional nickel–base alloys are at an advanced stage of development. INCONEL alloy *MA758* has been developed for resistance to molten glass corrosion and is now commercially available. A new, but similar, ODS nickel–base superalloy *via* mechanical alloying, *TMO–2*, is being developed in Japan (Yamazaki *et al.*, 1990). The chemical compositions of typical alloys are given in Table 2.1.

2.7.2 ODS Iron–base Superalloys

The iron–base INCOLOY alloy *MA956* was originally developed for use in sheet form in gas–turbine combustors, but with its combination of high strength up to 1300 °C, corrosion resistance and formability, the alloy has found a number of other applications. Gas turbine applications under development include fabricated nozzles, inlet plenum and compressor nozzle parts of vehicle turbines, rings for aeroengine combustors, and a combustor baffle for industrial

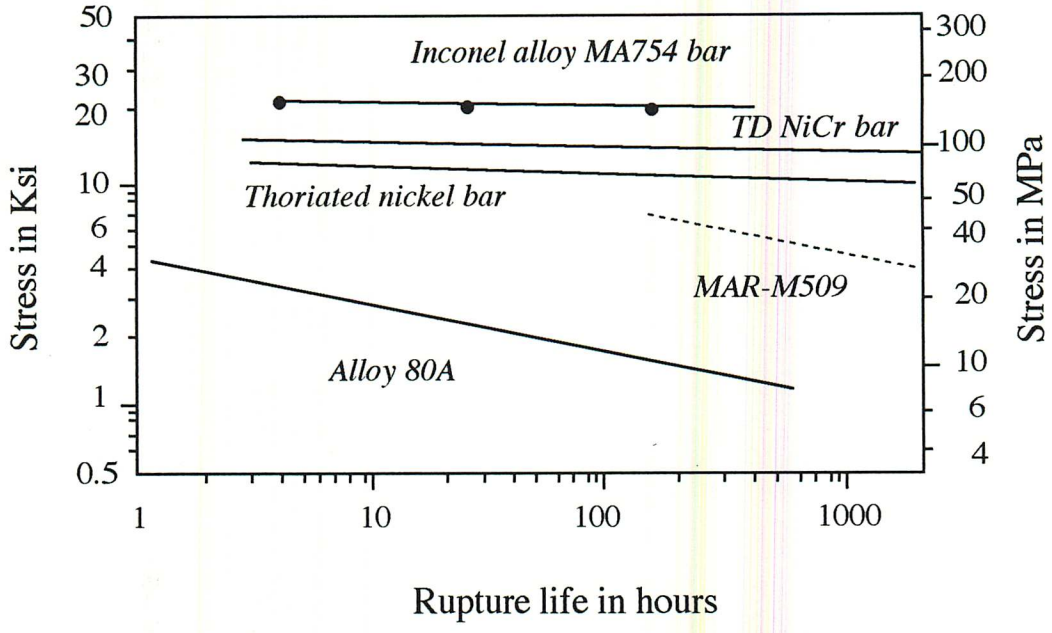

Figure 2.14: Stress rupture properties at 1093 °C of Inconel *MA754* compared with other bar materials (Fleetwood, 1986).

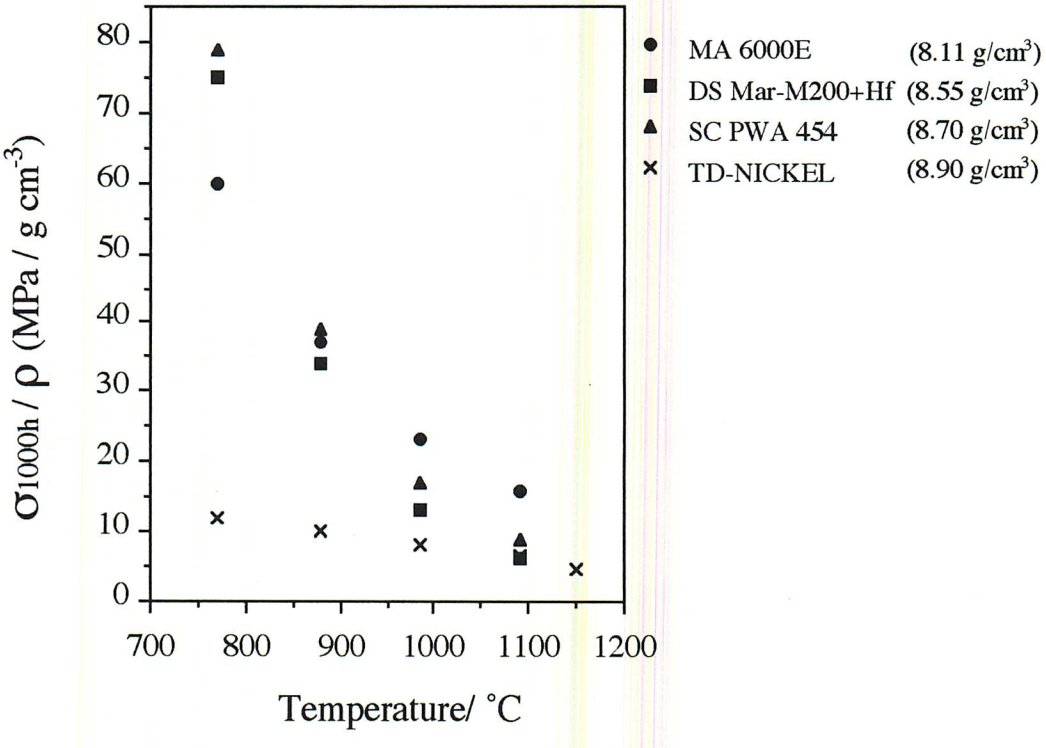

Figure 2.15: Specific stress rupture strength for 1000 h life of Inconel *MA6000* compared with other high-temperature high-strength alloys (Fleetwood, 1986).

Table 2.1: Chemical compositions of high temperature alloys (wt%, Ni balance.)

	Cr	Mo	W	Al	Ti	Ta	Zr	B	C	ThO_2	Y_2O_3
Nimonic 80A	19.5	–	–	1.4	2.4	–	0.06	0.003	0.005	–	–
TD Nickel	–	–	–	–	–	–	–	–	–	2.0	–
MA754	20.0	–	–	0.3	0.5	–	–	–	0.05	–	0.6
MA6000	15.0	2.0	4.0	4.5	2.5	–	0.15	0.01	0.05	–	0.6
TMO-2	5.9	2.0	12.4	4.2	0.8	4.7	0.05	0.01	0.05	–	1.1

turbines. Use in power stations include oil and coal burners and swirlers, and fabricated tube assemblies for fluid bed combustion. The other iron–base INCOLOY alloy *MA957* is developed as a nuclear fuel–cladding material in fast–breeder reactors (Koch, 1990).

The stress–rupture strength of *MA956* bar in the longitudinal direction at 1000 °C is more than twice those of alloys such as *Incoloy 800H*, *Inconel 617*, cast *HP alloy* modified with niobium and *HP-50WZ* (Kane *et al.*, 1984). In sheet form, *MA956* also exhibits high stress – rupture strength, ten times that of *Hastelloy X* at 1093 °C , which 0.2% yield strength is 201 MPa at 600 °C, 97 MPa at 1000 °C, and 76 MPa at 1200 °C.

The oxidation resistance of alumina forming *MA956* is generally regarded as superior to that of materials which develop chromia scales. The various alloy have been evaluated in a cycle oxidation test using air plus 5% water vapour. McColvin & Smith (1987) revealed the general superiority of alumina scale forming alloys over those forming chromia scales. The data show that *MA956* is superior (Figure 2.16). The chemical compositions of the alloys illustrated in Figure 2.16 are given in Table 2.2.

MA956 has been shown to possess superior oxidation and corrosion resistance over comparable alloys, combined with strength retention at very high temperatures. This excellent combination of high temperature properties makes *MA956* a prime contender for a wide range of high temperature aerospace, chemical petrochemical and metal processing applications.

However, due to the anisotropic grain characteristic, the mechanical properties in the transverse direction are weaker than in the longitudinal direction. Figure 2.17 illustrates the anisotropic properties changes of *MA956* bar. For some particular applications such as tubes, this anisotropy will cause serious problems. Thus, a refined understanding of grain structure and crystallographic texture control is worth investigation.

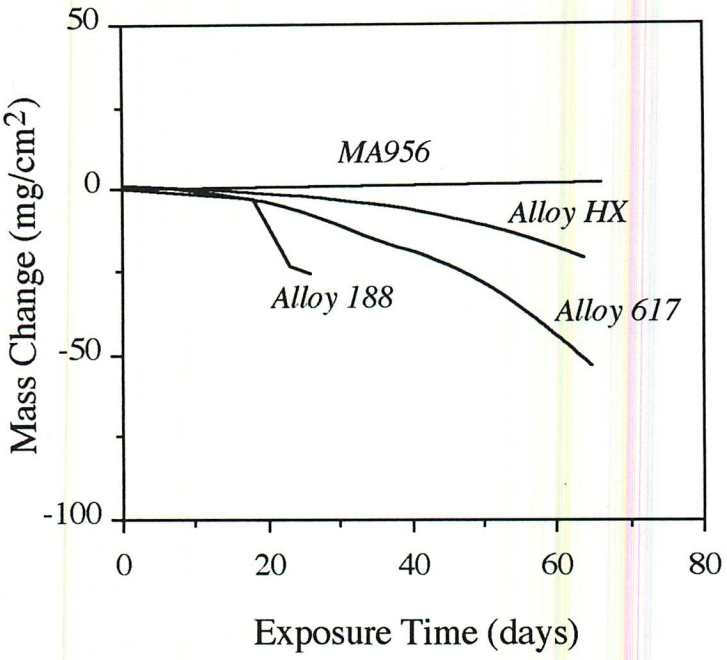

Figure 2.16: Cyclic oxidation data in Air + 5% water vapour at 1100 °C (McColvin and Smith, 1987).

Table 2.2: Chemical compositions of the alloys illustrated in Figure 2.16 (wt%).

	Fe	Ni	Cr	Al	Ti	Mn	Si	C	other
MA956	Bal	–	20.0	4.5	0.5	–	–	0.02	0.005 Y_2O_3
Alloy 617	0.1	Bal	22.5	1.1	1.1	0.1	0.1	0.05	13.0 Co, 9.0 Mo
Alloy 188	–	22.0	22.0	–	–	–	0.035	0.1	Co Bal, 0.9 La
Alloy HX	18.5	48	21.8	–	–	–	–	–	9.0 Mo

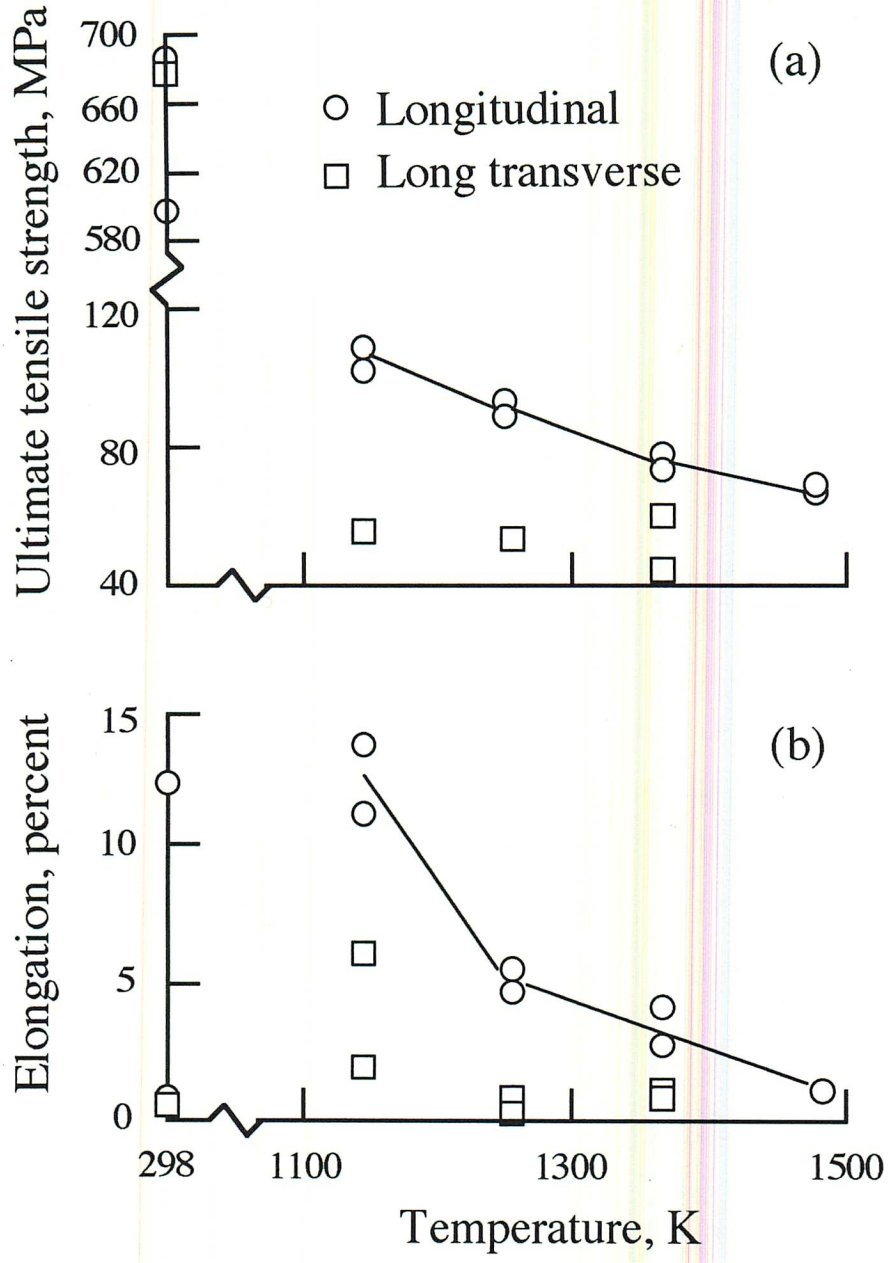

Figure 2.17: Tensile properties as a function of temperature for *MA956* tested in the longitudinal and long transverse bar directions (Whittenberger, 1981).

2.8 SUMMARY

Mechanical alloying as a practical technique for making ODS superalloys has evolved into a commercial scale production process. Alloys made by this method have the ability to retain creep strength at high temperatures. Optimization of the thermomechanical processing is necessary to achieve the most appropriate final grain size and morphology for each alloy and product form. At present, ODS superalloys are applied mainly to solve existing materials problems by direct replacement of conventional Ni and Co base alloys. However, new modified designs of high temperature plant are now being developed which will take full advantage of the opportunities for increased thermodynamic efficiency, better fuel utilisation, and greatly extended service lives.

To provide a much more flexible applications of mechanically alloyed ODS alloys requires a refined understanding of the recrystallisation grain structure.

CHAPTER THREE

EXPERIMENTAL TECHNIQUES

3.1 Materials and Fabrication

MA956 and *MA957* are oxide dispersion strengthened ferritic stainless steels. These alloys were supplied by INCO Alloys (Hereford) in an unrecrystallised state. They were fabricated by charging three primary powders (elemental iron, pre-alloyed metallic alloys, and yttria) into a water cooled vertical attritor for mechanical alloying. The consolidation of the resultant powder was achieved by extrusion at 1000 °C whilst packed in a mild steel can. This was followed by rolling at 1000 °C, with a reduction in diameter from 54 to 25 mm for *MA956* and from 54 to 9.5 mm for *MA957*. The chemical compositions of the specific materials used are given in Table 3.1.

Table 3.1: Chemical compositions of mechanically alloyed steels *MA956* and *MA957*, wt%.

	C	Cr	Al	Ti	Mo	Y_2O_3
MA956	0.01	20.0	4.5	0.5	–	0.5
MA957	0.01	14.0	–	1.0	0.3	0.27

Besides these two steels, some novel mechanically alloyed ODS steels were designed as discussed later in the thesis. The aim was to modify the conventional *MA957* steel with half a weight percent of nickel (*MA957-Ni*). A further composite alloy was also developed, consisting of a mixture of *MA957-Ni* steel with conventional *MA956*. The nominal compositions and details of the working procedures are shown in Chapter 8 and Chapter 9, respectively.

3.2 Heat Treatment

The specimens used in this study were in the form of 3 mm square rods 20 mm in length. They were cut from the as-extruded rod, which was 25 mm and 9.5 mm in diameter for *MA956* and *MA957* respectively. Isothermal annealing experiments were performed using

conventional resistance furnaces. To investigate the effect of preannealing heat treatments, the steels were recovery heat treated at a temperature at which recrystallisation did not occur. All of the specimens for heat treatment were put in quartz tubes with an argon gas protection atmosphere.

3.3 Hardness Tests

The hardness tests were carried out using a Vickers hardness testing machine. Measurements were made on polished specimens. The indentation load was 20 kg. The measurements were taken at 3 mm intervals along the extrusion direction; at least 5 readings were made and an average taken.

3.4 Optical Microscopy

Optical microscopy was used to observe the structures of as-received and heat treated samples. The specimens were hot mounted using an automatic mounting press, and then mechanically ground down to 1200 grade silicon carbide paper before further polishing using 1 μm diamond paste. The etchant used was 2g $CuCl_2$, 40ml HCl, and 40 to 80 ml methanol.

3.5 Transmission Electron Microscopy

A Philips EM 400T electron microscope was used for the examination of thin foils. The operating voltage was 120 kV. Thin discs were cut containing the extrusion direction and were subsequently ground down to 0.05 mm by abrasion on 1200 grit paper and then electropolished using a twin jet electropolisher in order to make thin foils for transmission electron microscopy. The polishing solution consisted of 5% perchloric acid, 25% glycerol and 70% ethanol mixture at – 10 °C . The voltage used was about 55 volts.

To analyse the grain misorientations, axis–angle pair measurements were made using selected area diffraction patterns (SADPs). The misorientations of adjacent grains were studied in order to establish whether they represented the high energy grain boundaries or whether they were simply subgrains. The orientation relationship between a pair of like crystals, the crystallographic bases of which are defined from a common origin, can be described using an axis-angle pair. From this, it can be inferred that if one of the crystals is rigidly rotated through the origin, through a right–handed angle of rotation θ, its orientation can be made to coincide with that of the other. Figure 3.1 illustrates schematically the superimposed diffraction patterns from adjacent crystals. The information there can be used to generate a coordinate transformation matrix (Bhadeshia, 1987), from which an axis-angle pair can be calculated.

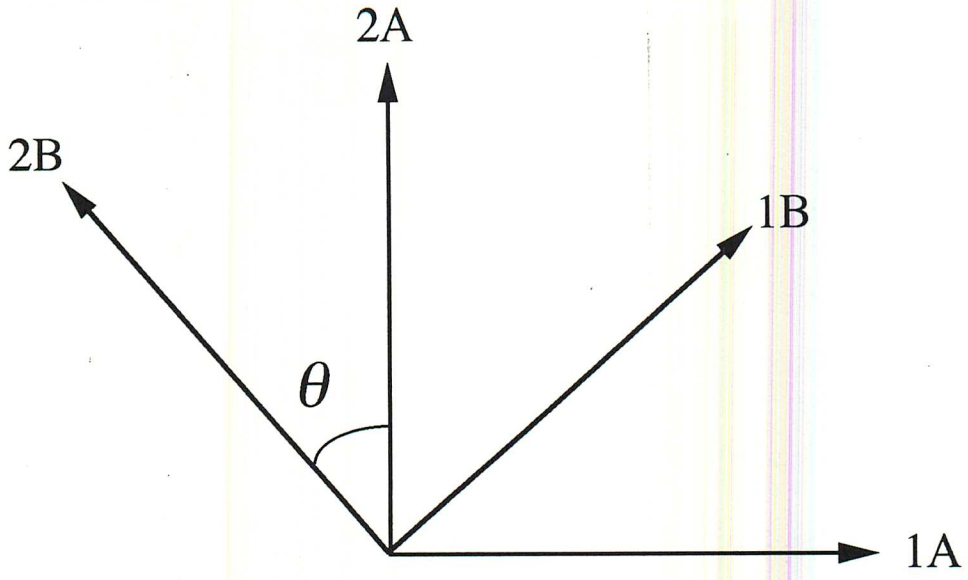

Figure 3.1: Vector positions of two superimposed diffraction patterns from grains 1 and 2.

Since the aim here was to differentiate between high energy and low energy boundaries, the measured misorientation was expressed in terms of an approximate Σ value. This represents the reciprocal density of coincidence sites between the two crystals. An orientation close to Σ=1 represents a sub-grain, whereas larger values correspond to increasingly larger misorientations and what is often known as high angle boundaries. The Σ value was in practice deduced by comparing the axis-angle pair with the largest θ (of all the symmetry related pairs) with a corresponding list for exact Σ misorientations as shown in Table 3.2 (Christian, 1965c; Bhadeshia, 1987).

3.6 Texture Analysis

To investigate the effects of compositions and working history on the development of texture in recrystallised specimens, a Siemens 200 X-ray diffractometer with a pole figure goniometer was employed to measure the textures by recording the (200) and (110) pole figures from longitudinal sections. The X-ray radiation used was β-filter MoK_{α}. A reflection method was used with the 2θ angles ranging from 0 to 80 measured relative to the normal to the longitudinal face of the sample. The samples were macroetched using 5 HCl : H_2O_2 prior to the X-ray experiments in order to remove any machining artifacts. The details of pole figure measurements and texture component representation are given in Appendix 1.

Although commonly used, such pole figure impose great difficulties on the quantitative

Table 3.2 Some CLS relations for Cubic Crystals (Christian, 1965; Bhadeshia, 1987).

Σ	Angle	Axis	Twin axes
3	60.0	< 111 >	< 111 >, < 112 >
5	36.9	< 100 >	< 012 >, < 013 >
7	38.2	< 111 >	< 123 >
9	38.9	< 110 >	< 122 >, < 114 >
11	50.5	< 110 >	< 113 >, < 233 >
13a	22.6	< 100 >	< 023 >, < 015 >
13b	27.8	< 111 >	< 134 >
15	48.2	< 210 >	< 125 >
17a	28.1	< 100 >	< 014 >, < 035 >
17b	61.9	< 221 >	< 223 >, < 334 >
19a	26.5	< 110 >	< 133 >, < 116 >
19b	46.8	< 111 >	< 235 >
21a	21.8	< 111 >	< 235 >, < 145 >
21b	44.4	< 211 >	< 124 >

interpretation of textures, since the superposition of the various types of poles leads to a high degree of ambiguity. To obtain a less ambiguous description, the orientation distribution function (ODF) must be calculated. The method of grain orientation distribution function nowadays provides a powerful tool to quantify and characterise such textures. However, as the ODF image in the Eulerian space is not very descriptive, for practical purposes a way of characterising these textures in a brief and concise manner without a loss of essential information is necessary. One possibility is to express the pole intensities along the selected fibres in the form of a diagram. This form of representation makes more sense since the textures identified in steels are frequently made up of more or less complete texture fibres. Figure 3.2 provides an overview of the key texture fibres found in the steels and their position in Eulerian space, whilst Figure 3.3 shows the fibres which can be described on the {110} pole figure. The pole intensity along the α-fibre is of importance for hot and cold-rolling textures as well as for recrystallisation textures. Especially in deep-drawing steels, the course of the pole intensity in the γ-fibre characterises the recrystallisation texture. For hot-rolled products the development of the surface texture can be monitored by the ζ-fibre. The η-fibre plays a role in the description of electrical sheet texture and the ϑ-fibre marks the undesired components of deep-drawing texture (Bleck *et al.*, 1991).

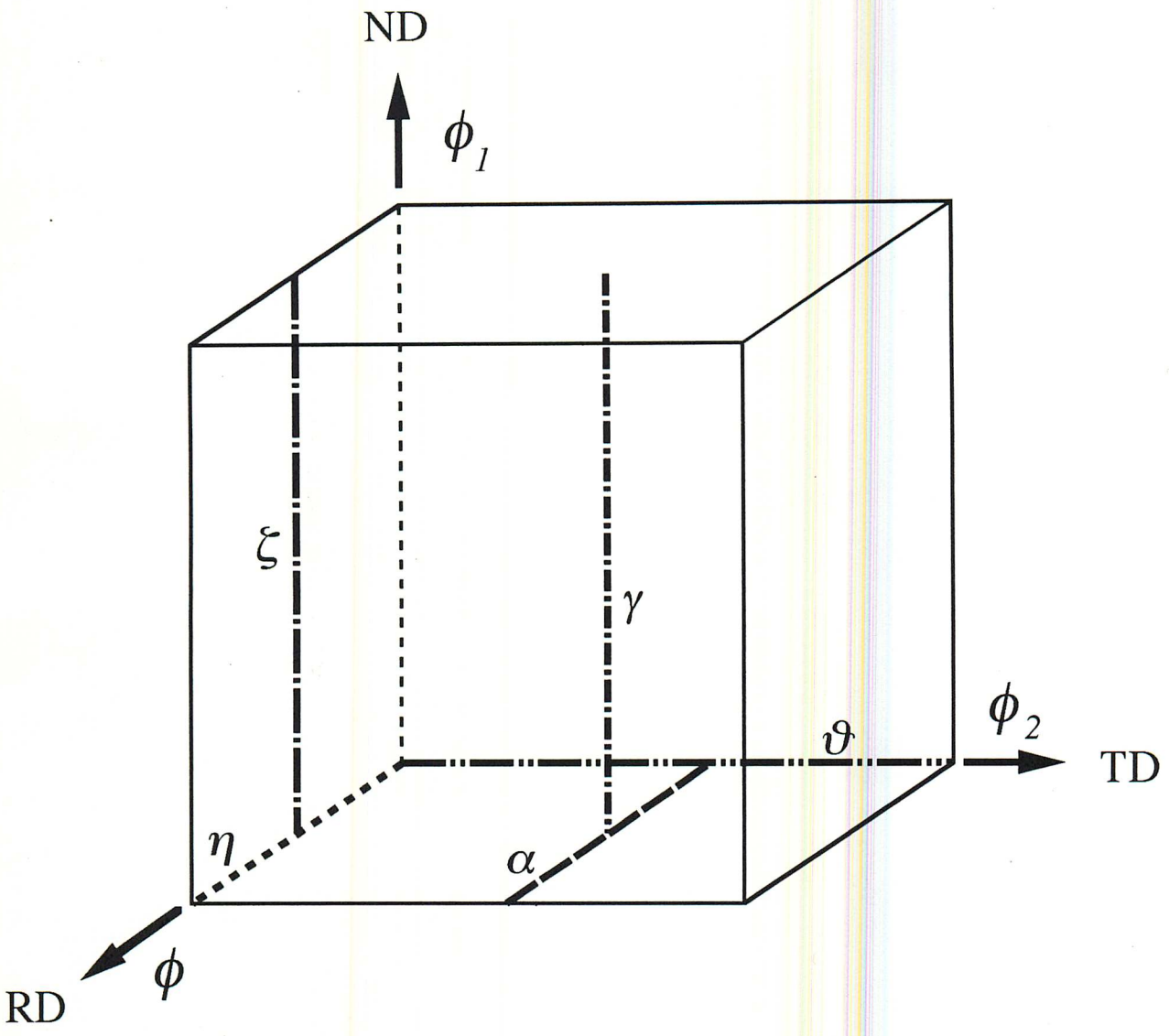

α-fibre : <110> // RD

γ -fibre : <111> // ND

ζ-fibre : <110> // ND

η-fibre : <001> // RD

ϑ-fibre : <001> // ND

Figure 3.2: Main texture fibres in steel sheets; presentation in the Eulerian space (Bleck *et al.*, 1991.)

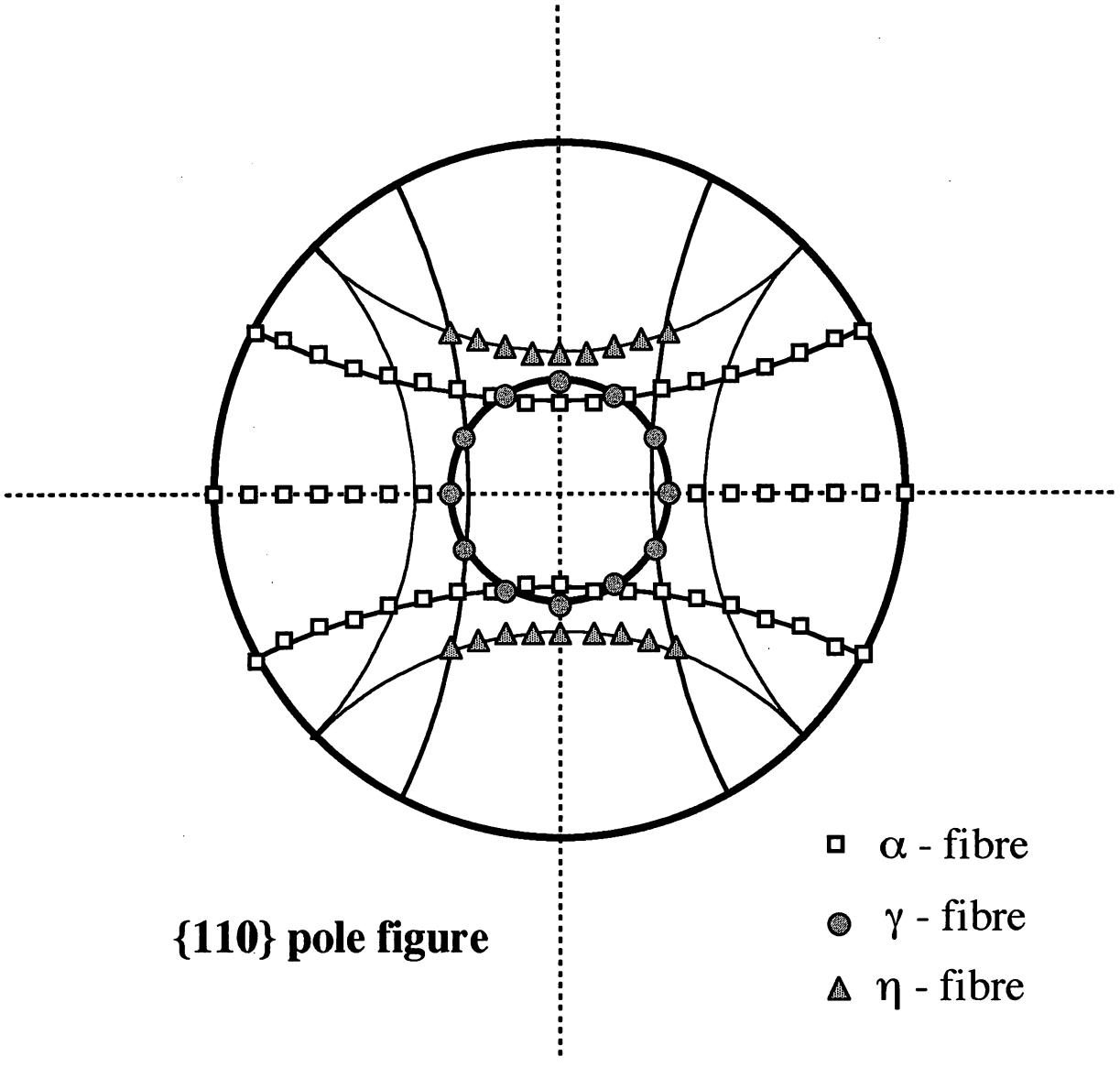

Figure 3.3: Fibres in a pole figure (Hölscher *et al.*, 1991).

3.7 Atom Probe Analysis

To evaluate the chemical composition profile and frequency distribution of atoms in mechanical alloys a VSW APFIM200 Atom Probe was employed. This is a combination of a field ion microscope (FIM) and a mass spectrometer of single–ion sensitivity. The instrument is operated via a PC–based control and data acquisition system with powerful statistical analysis packages built into the system.

The specimens used for atom probe were cut form the bulk unrecrystallised alloys as 0.35 mm squares 20 mm in length. The specimens were then subjected to a two-stage electropolishing process to make a needle-like form, with an end radius typically 50–100 nm. The solutions for electropolishing are as followed:

(1) First stage electropolishing:

25% $HClO_4$ in glacial acetic acid

(2) Second stage electropolishing:

3% $HClO_4$ in 2-butoxy-ethanol

The operation of electropolishing precess is carried out by controlling the voltage, which is 25 V, and 20 V in direct current for the first and second stage electropolishing process, respectively.

To make a needle-like form of specimen used for atom-probe observation required a skillful control on the profile of electropolishing specimen. The purpose of first stage electropolishing is to make a neck on the bulk specimen. This is achieved by putting some insulated material on the end of the sample, and then moving the specimen up and down to provide a smoothly necked sample. When the diameter of the necked region becomes about 10 μm, optical microscopy is used to monitor further changes, and the second-stage electropolishing is applied until the specimen divides into two parts. Figure 3.4 illustrates the relative features of the specimen during electropolishing process. Normally, the upper part is used for atom-probe observations. In general, the sharper the tip is, the easier to form the field-ion image.

In practice, the needle-like specimen prepared by electropolishing is mounted on a cryostat at a temperature of 26-100 K in a vacuum chamber (pressure $\leq 10^{-10}$ mbar), pointing towards a channel-plate/phosphor screen assembly. Subsequently, $10^{-5} \sim 10^{-4}$ mbar of inert gas, neon in this study, is introduced into the chamber and an increasing positive DC potential is applied to the specimen.

The formation of FIM image includes field adsorption, field ionisation, and field evaporation. Image gas atoms are polarised by the strong electric field and drawn towards the specimen surface. Field adsorption occurs on prominent surface atoms which are themselves polarised by the field. Field ionisation of the gas atoms occurs by tunnelling of electrons through the field adsorbed gas and into the metal. The positive image gas ions are then repelled away from the specimen towards the screen where the field-ion image is formed. In order to obtain stable, clear FIM images, it is necessary that the gas ionises before the specimen atoms field–evaporate. If this is the case, the removal (field evaporation) of atoms from the specimen can be monitored and carried out in a controlled manner as the DC voltage is increased and a smoothly-curved tip can be formed.

In APFIM (atom probe field ion microscopy) studies, the instrument is operated first as a field ion microscope in order to monitor the development of a stable, approximately smooth hemispherical tip for subsequent analysis. Ions are field evaporated from the specimen at a well-defined moment in time by the application of nanosecond rise-time high-voltage pulses (Figure 3.5). The time taken by the ion to reach a detector indicates the mass to charge ratio (m/n). This can then be interpreted to reveal the species concerned.

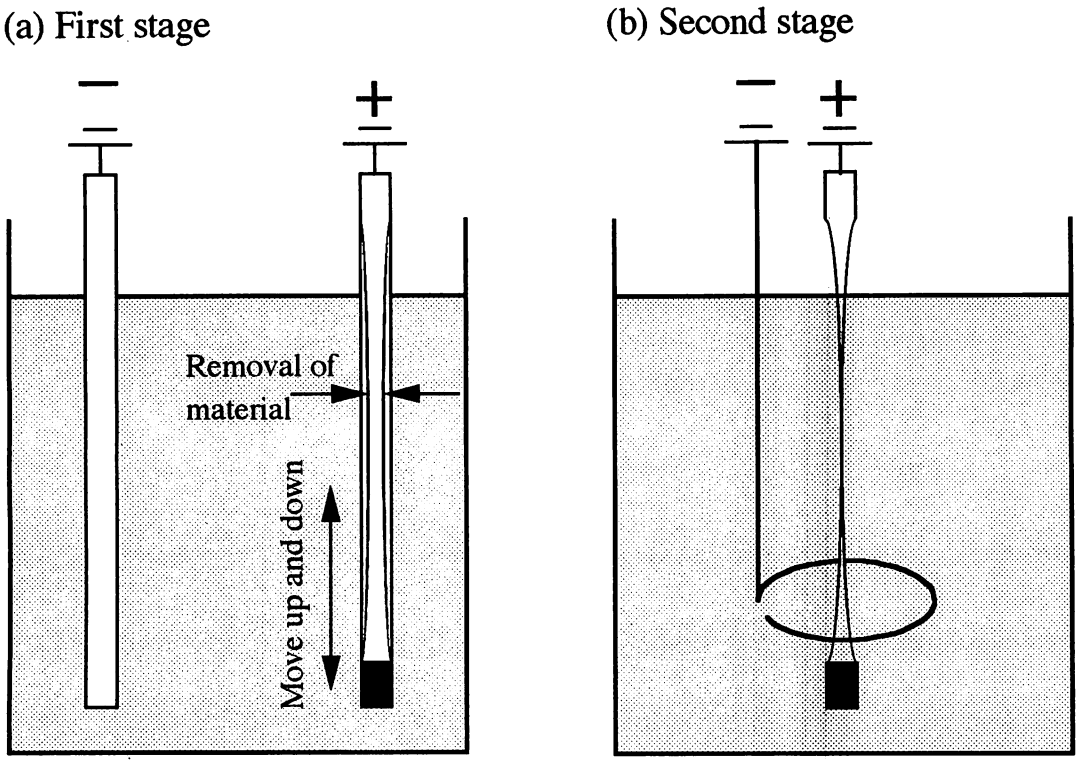

Figure 3.4: Electropolishing process used for Atom-probe sample preparation.

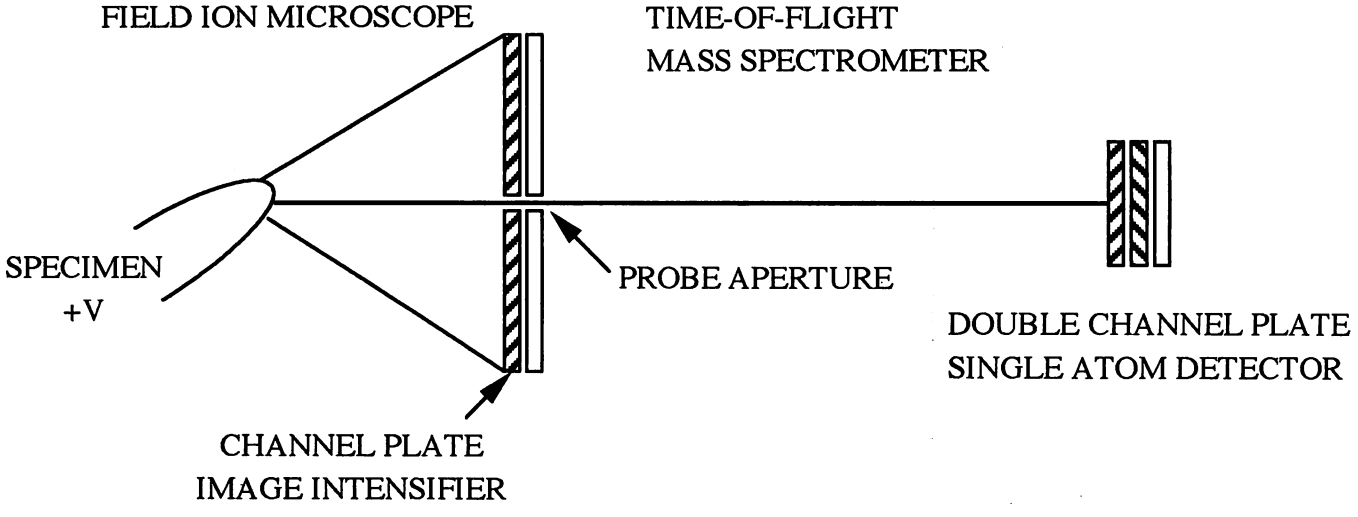

Figure 3.5: Principle of the conventional atom probe. The field-ion microscope is shown on the left and the time-of-flight mass spectrometer on the right. The mass spectrometer consists of a drift tube at the end of which is a detector which has single-atom sensitivity. A small probe aperture in the microchannel plate and phosphor screen assembly defines the area of the specimen surface from which atoms will be analysed in mass spectrometer (after Miller and Smith, 1989).

3.8 DSC Analysis

Differential scanning calorimetry was carried out using a Netzsch DSC 404/3/413/D machine which is a specially design high-temperature, heat flux DSC with computer control and data acquisition. It uses a Pt/Rh furnace which has very low temperature gradient characteristics. The sample and reference are placed in thermally balanced Pt crucibles. Any event leading to differences in heat evolution, or heat capacity between the sample and the reference cause a signal, which can be interpreted to reveal thermodynamic data associated with the event.

Calorimetric measurements were carried out during continuous heating (5–40 K min^{-1}), the sample mass typically at about 200 mg. A comparison is made between DSC runs in which the reference container was empty. In all cases, the samples were examined using optical microscopy, to confirm recrystallisation. All the experiments were carried out using an argon atmosphere in the DSC chamber.

3.9 Thermomechanical Tests

The hot-deformation behaviour was evaluated using compression tests. The samples were machined into 8 mm diameter by 12 mm length cylinders. The experiments were carried out in an adapted *Thermecmaster Z* thermomechanical simulator, which enables the simultaneous implementation and recording of time, temperature, load, diametral and longitudinal strains. The specimens were heated by induction, with a measured temperature variation along its length of only $\pm 5\,^{\circ}C$. The quench gas used was nitrogen. A uniaxial compressive load was applied via quartz discs. Test temperatures were selected at 950, 1000 and 1050 °C, with a 50% total reduction strain and 0.01 s^{-1} constant strain rate control. Dimensional changes during temperature changes were employed to measure the phase transformation temperatures of *MA957-Ni* steels as shown in Chapter 8.

CHAPTER FOUR

CRYSTALLOGRAPHIC TEXTURE IN MECHANICALLY ALLOYED OXIDE DISPERSION STRENGTHENED *MA956* & *MA957* STEELS

4.1 INTRODUCTION

Many mechanically alloyed metals are now commercially available, but steels produced using this method show particular promise in a variety of applications. For example, *MA956* is a chromium–rich ferritic stainless steel containing some eight atomic percent of aluminium forced into solution as an aid to oxidation resistance (Hack, 1984; Sundaresan and Frose, 1987), together with a dispersion of yttrium oxide particles for creep resistance. An alternative ferritic stainless steel variant (*MA957*) contains titanium rather than aluminium, and is designed for applications in the nuclear industry (Asano *et al.*, 1988). The steel powders, after mechanical alloying, and processing into bulk form have an ultrafine microstructure containing submicron grains of ferrite. The hardness in this condition is unacceptably high, so they are usually recrystallised into a coarse columnar grain structure akin to a directionally solidified microstructure.

A columnar (or *directionally recrystallised*) grain structure is ideal for elevated temperature applications where creep resistance is important. However, the crystallographic orientation of the columnar grains can be of importance in many applications. The factors controlling the recrystallisation texture are not understood for mechanically alloyed steels. The purpose of the work presented in this Chapter was to investigate the crystallographic textures of *MA956* and *MA957* both before and after the recrystallisation heat treatments. Both of the alloys are intended to be ferritic at all temperatures in the solid–state so that it should in principle be possible to relate textural changes during recrystallisation to the extensive data which already exist on the development of texture in rolled low–alloy steels (Hutchinson, 1974; Inagaki, 1981; Ray and Jonas, 1990).

4.2 EXPERIMENTAL PROCEDURE

The texture investigation required both as–received (cold deformed) and fully recrystallised samples. Recrystallisation anneals were carried out at 1350 °C for 1 hour, in order

to achieve complete recrystallisation. The typical microstructures of the recrystallised *MA956* and *MA957* steels are shown in Figure 4.1.

A *Siemens 200* X–ray diffractometer with a pole figure goniometer was employed to measure the textures by recording the {2 0 0} and {1 1 0} pole figures from longitudinal sections. The X–radiation used was β–filtered MoK_α. The reflection method was used with angles ranging from 0 to 80 ° measured relative to the normal to the longitudinal face of the sample. The samples were macroetched using 5 HCl : H_2O_2 prior to the X–ray experiments in order to remove any machining artifacts. It is well known that commercially produced hot rolled materials typically have a surface-to-centre texture gradient (Salsgiver *et al.*, 1988). However, this is difficult to study for rod and bar samples. Therefore, samples for texture measurement were cut as longitudinal sections.

Transmission electron microscopy was carried out using a *Philips EM400* microscope operated at 120 kV. Thin foils were prepared using a *Fischoine* twin–jet electropolisher with 5% perchloric acid, 25% glycerol and ethanol mixture. The polishing voltage used was about 55 volts.

4.3 RESULTS AND DISCUSSION

4.3.1 Crystallographic Texture: As–Received Samples

Figure 4.2 illustrates the {2 0 0} and {1 1 0} pole figures of the rolled *MA956* steel. The steel has the expected < 1 1 0 > fibre texture (Hatherley *et al.*, 1979). By contrast, the as-rolled *MA957* alloy exhibits a rather different < 1 1 0 > fibre texture (Figure 4.3) consisting of some weak components {0 0 1} < 1 1 0 >, {1 $\bar{1}$ 0} < 1 1 0 >, {1 $\bar{1}$ 1} < 1 1 0 > and {1 $\bar{1}$ 2} < 1 1 0 >. The texture is far less intense when compared with *MA956* and could be described as a very weak fibre texture.

The fact that both alloys exhibit a fibre texture is not surprising; they were both extruded and rolled into round bars with contoured rolls. It is well established that radially symmetrical deformation leads to a texture in which directions of the form < 1 1 0 > tend to lie parallel to the long axis of the sample (Hatherley and Hutchinson, 1979).

In general, the rolling and recrystallisation textures of body centered cubic steels are mostly composed of certain orientation fibres and their main features can thus be represented in a very condensed manner by plotting the orientation density along these fibres (Schlippenbach *et al.*, 1986). The most important of these fibres are listed below (RD refers to the rolling direction and ND to the normal to the sample plane):

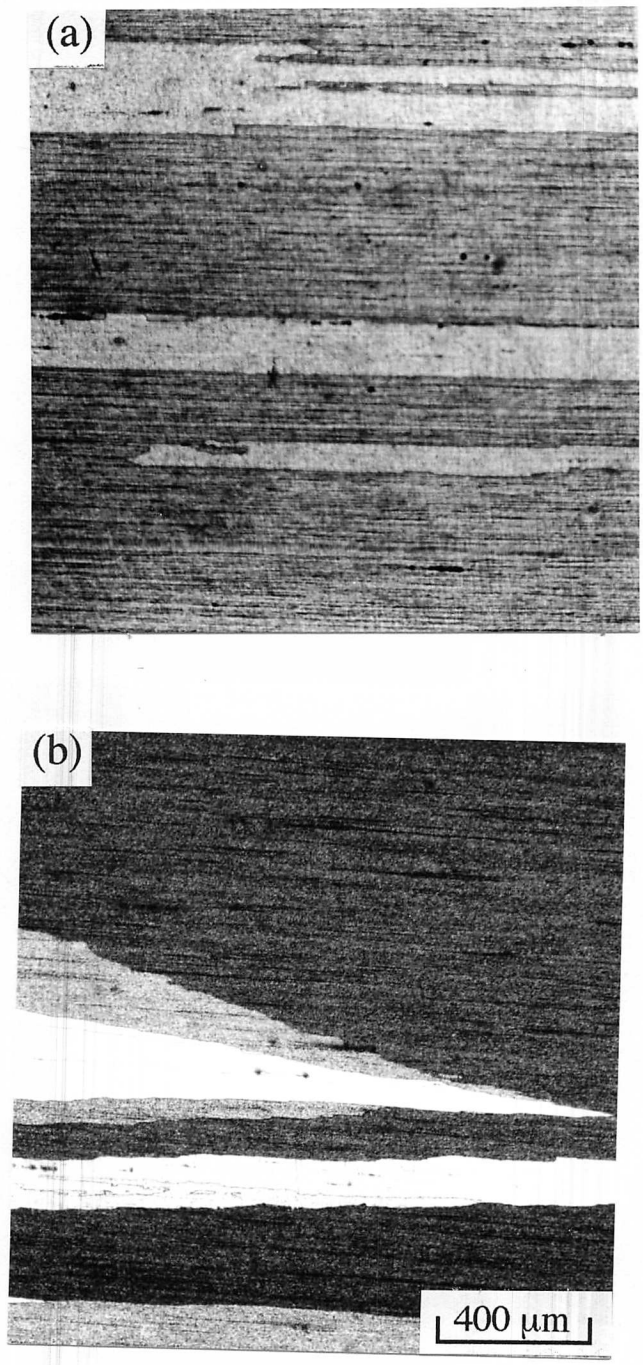

Figure 4.1: Typical microstructures of recrystallised (a) *MA956* and (b) *MA957* steels.

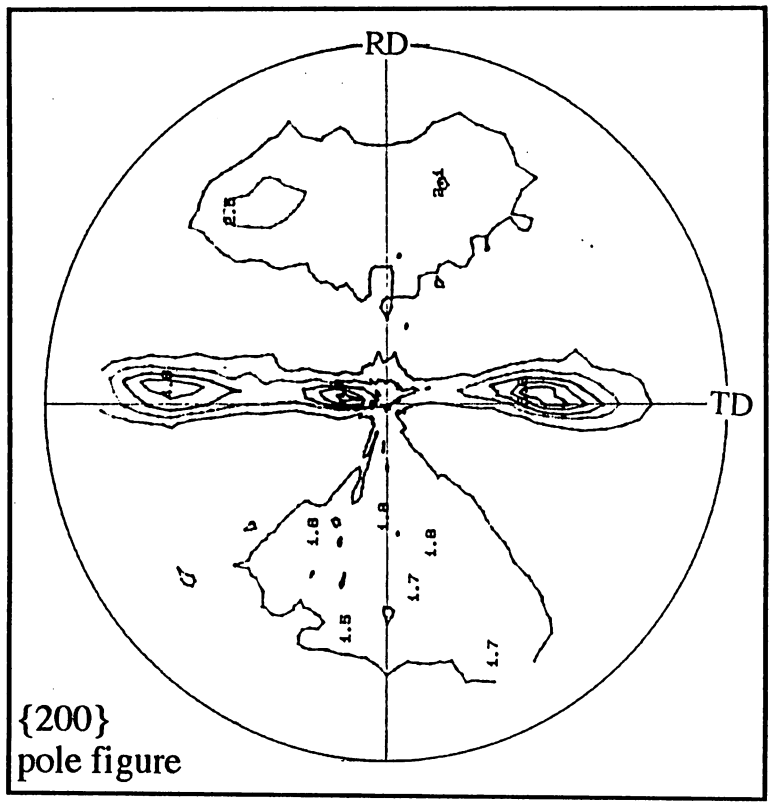

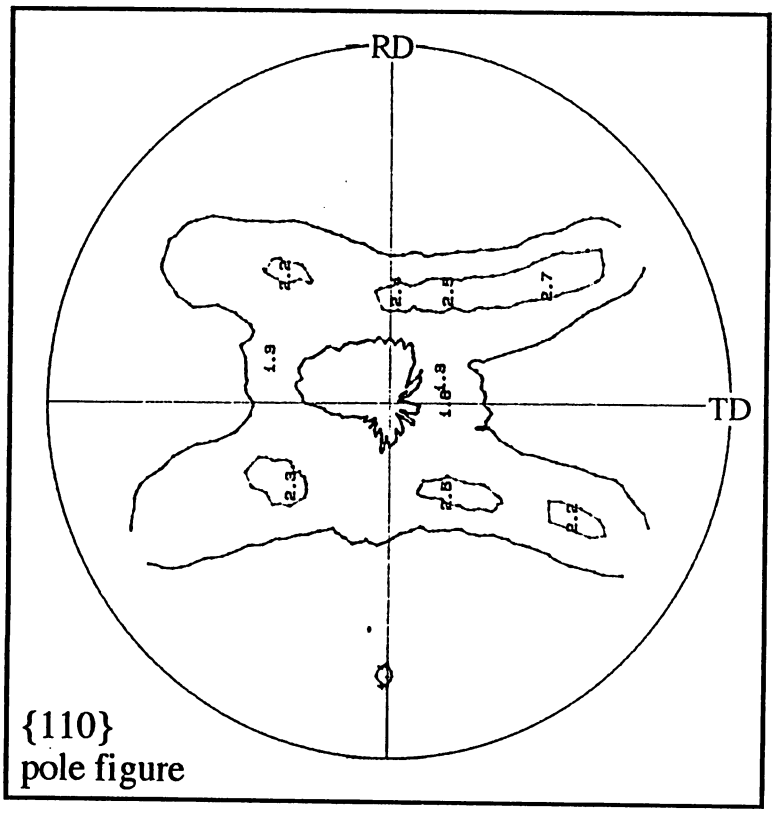

Figure 4.2: The {2 0 0} and {1 1 0} partial pole figures for as-received *MA956*. The numbers on each contour represent the intensity relative to that expected from a completely random sample.

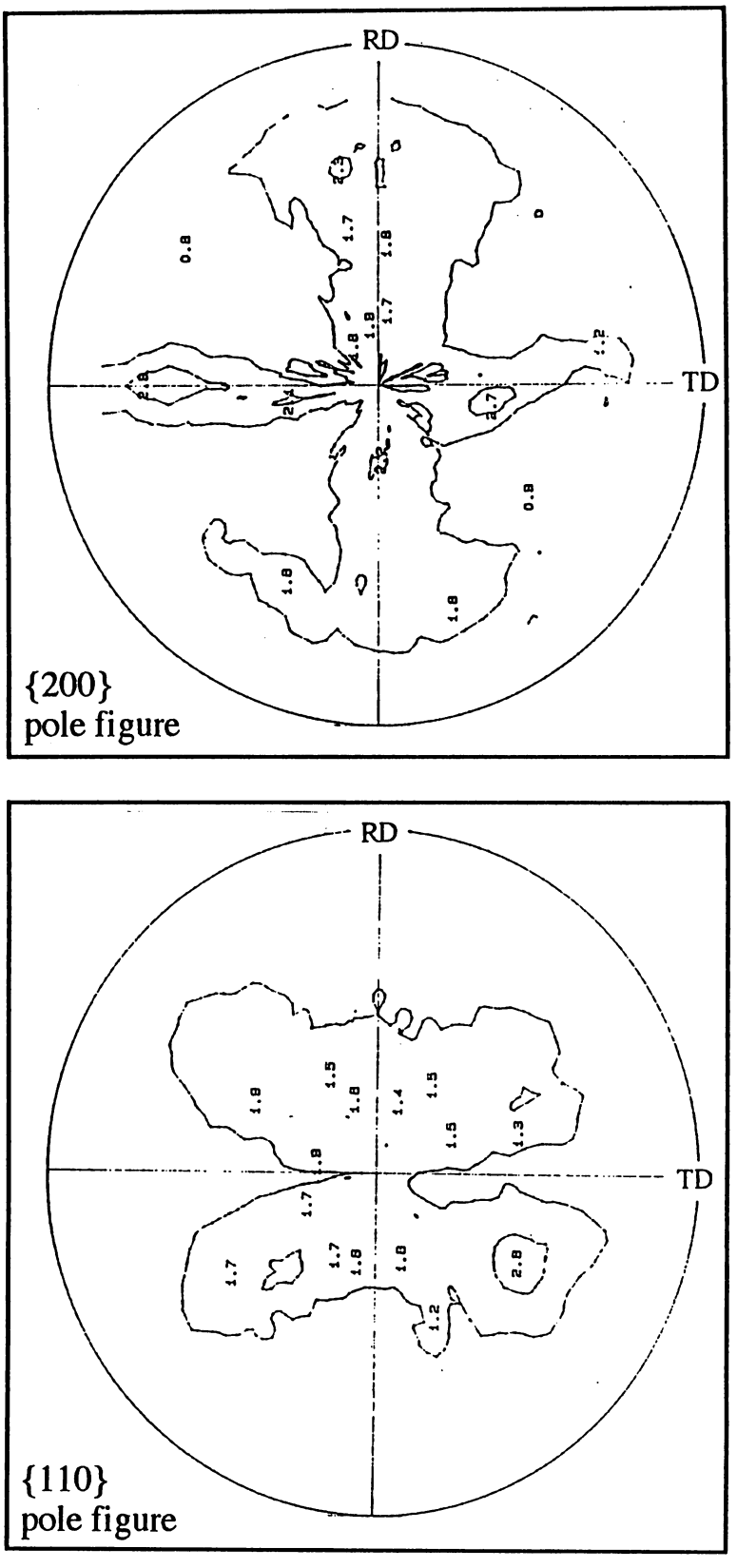

Figure 4.3: The {2 0 0} and {1 1 0} partial pole figures for as-received *MA957*.

α–fibre	$< 110 >\|\|$ RD	$\{001\} < 110 >$	to	$\{001\} < 110 >$
γ–fibre	$\{ 111 \} \|\|$ ND	$\{111\} < 1\bar{1}0 >$	to	$\{111\} < 11\bar{2} >$
η–fibre	$< 001 >\|\|$ RD	$\{100\} < 001 >$	to	$\{110\} < 001 >$

The results of the fibre texture analysis of the as–received material are shown in Figure 4.4. There is a prominent α–fibre texture in as–received *MA956* steel, whereas the deformed *MA957* steel is found to be much more random.

The experimental data were compared with published data on cast stainless steels Hölscher *et al.* (1991) found that in a Fe–16Cr wt.% alloy, the α– and γ–fibres dominated the hot rolling texture and were sharpened after cold rolling. Rickert *et al.* (1991), studied ferritic stainless steels and also reported the presence of strong α– and γ–fibres in the deformed state. The fibres in both studies displayed very strong intensities. This contrasts with the as–received mechanical alloys used here, which displayed relatively low intensities. The powder metallurgical route employed in the manufacture of the mechanical alloys clearly leads to a smaller degree of preferred orientation when compared with alloys which are cast.

In addition, it is also expected that the texture should sharpen as the extent of deformation increases. This contradicts the present results; *MA956* with an area reduction of 54% is found to have a sharper texture when compared with *MA957*, which had an area reduction of some 82%. Further discussion of this anomaly will follow later.

4.3.2 Crystallographic Texture: Recrystallised Samples

Figure 4.5 shows the pole figures of recrystallised *MA956*; the texture includes the $\{0\ 1\ 1\}$ $< 1\ 0\ 0 >$ component together with the sharpening of the $\{1\ 1\ 1\}$ retained deformation texture component. Once again, the recrystallised *MA957* sample shows a very different texture, as illustrated in Figure 4.6. The $\{0\ 0\ 1\} < 1\ 1\ 0 >$ cube component is strongly enhanced together with $\{0\ 1\ 1\} < 1\ 0\ 0 >$ "edge–cube" Goss texture component.

Texture analysis of the recrystallised steels is shown in Figure 4.7. When compared with the Figure 4.4, it is found that the α–fibre orientations (with the exception of the $\{111\} < 110 >$ component) is strongly decreased, whilst the $\{0\ 1\ 1\} < 1\ 0\ 0 >$ Goss orientation is developed in both the recrystallised *MA956* and *MA957* steels. The major difference of recrystallisation texture between *MA956* and *MA957* steels is that the sharpening of γ–fibre texture leads to the sharp $\{111\} < 1\bar{1}0 >$ and $\{111\} < 11\bar{2} >$ recrystallisation texture in *MA956* steel, whilst the $\{001\} < 110 >$ cube texture is highly developed in *MA957* steel.

To relate the recrystallisation textures to the original deformed state, it is necessary to consider the nucleation of recrystallisation. There are in general, three possibilities (Dillamore

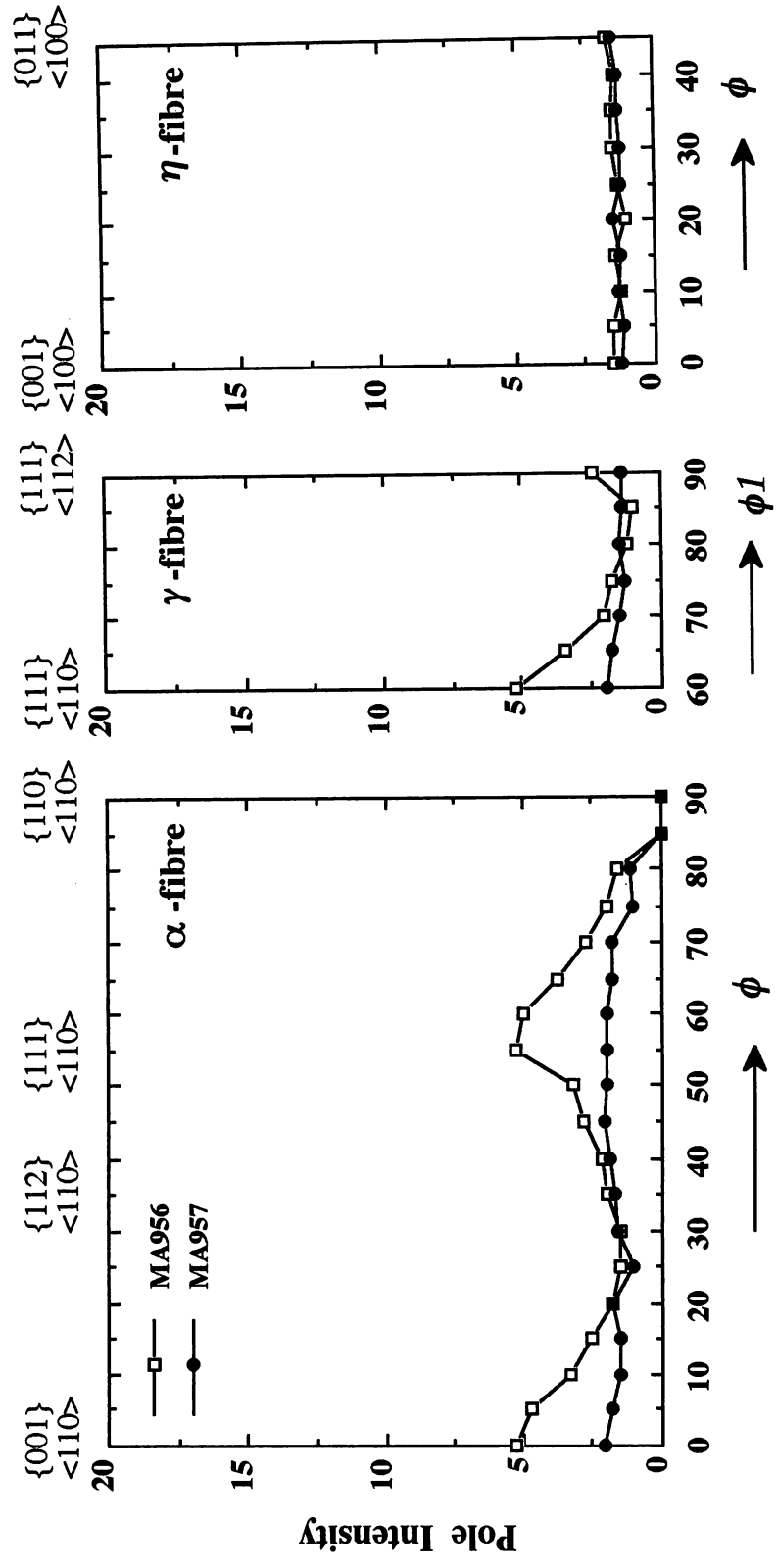

Figure 4.4: Fibres of deformation texture of as–received *MA956* and *MA957* steels.

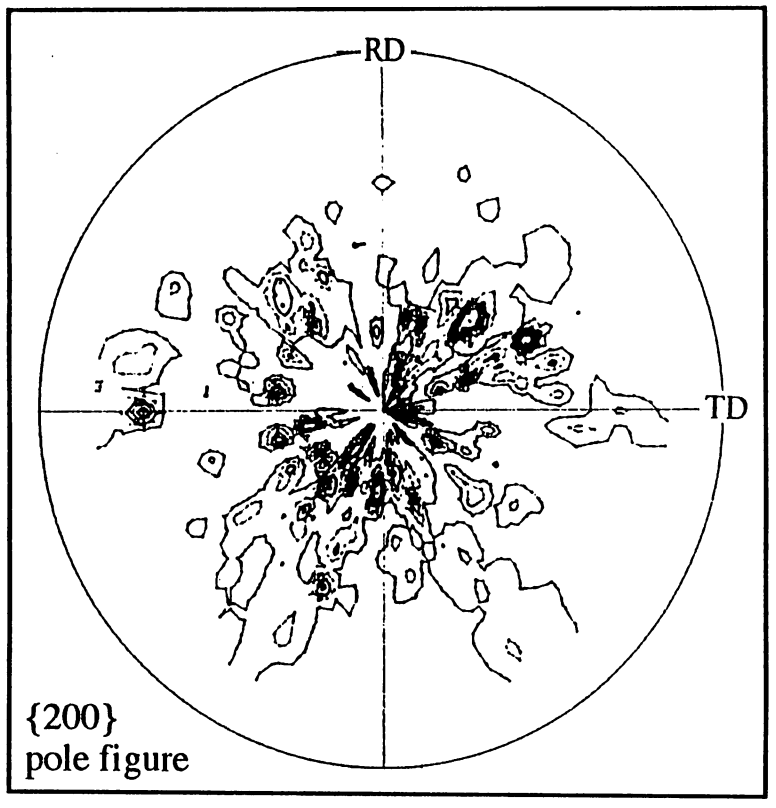

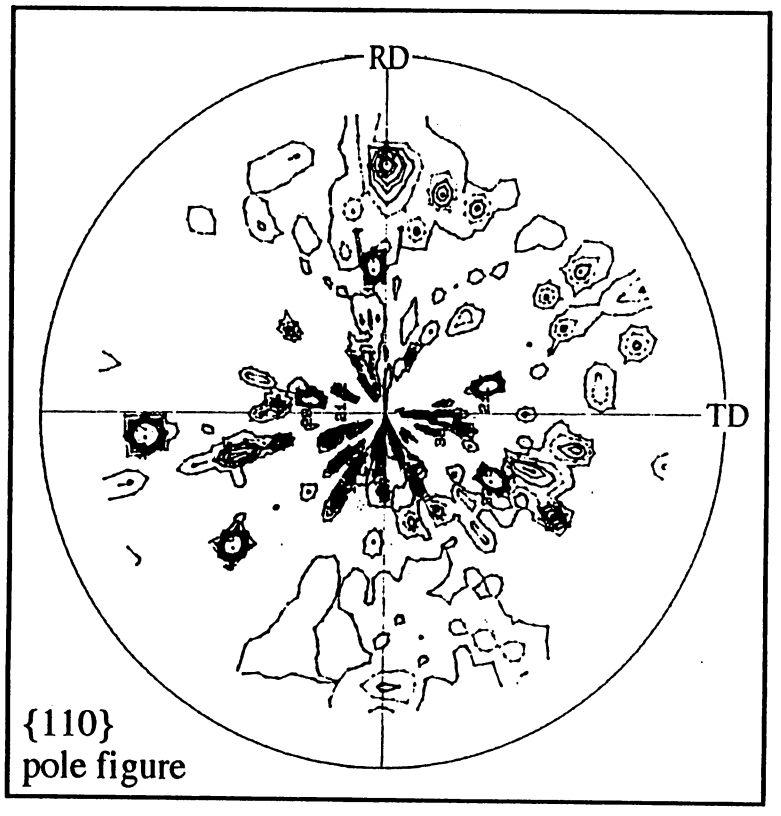

Figure 4.5: The {2 0 0} and {1 1 0} partial pole figures for recrystallised *MA956*.

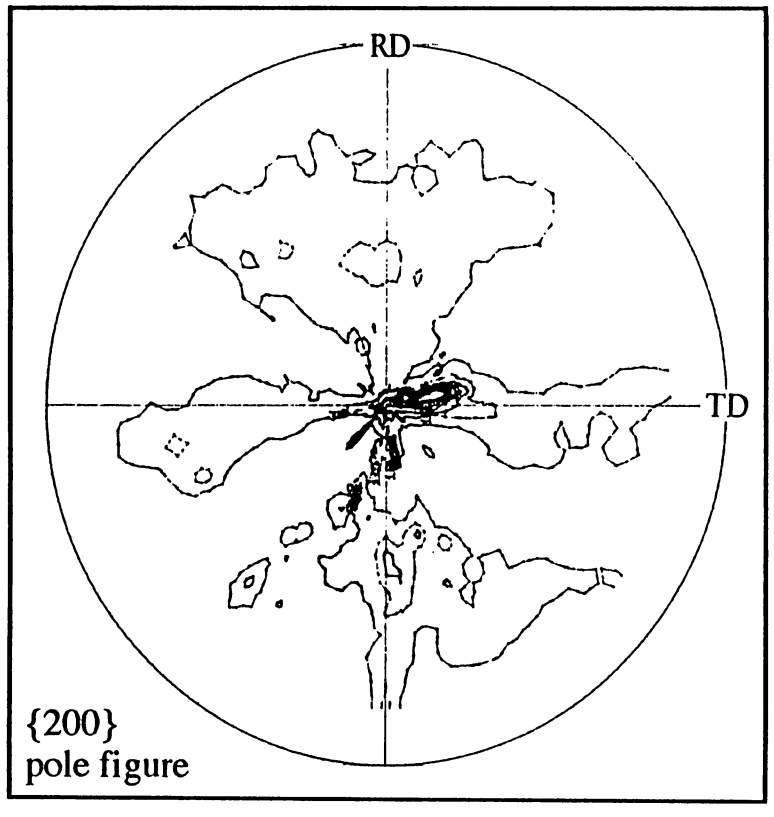

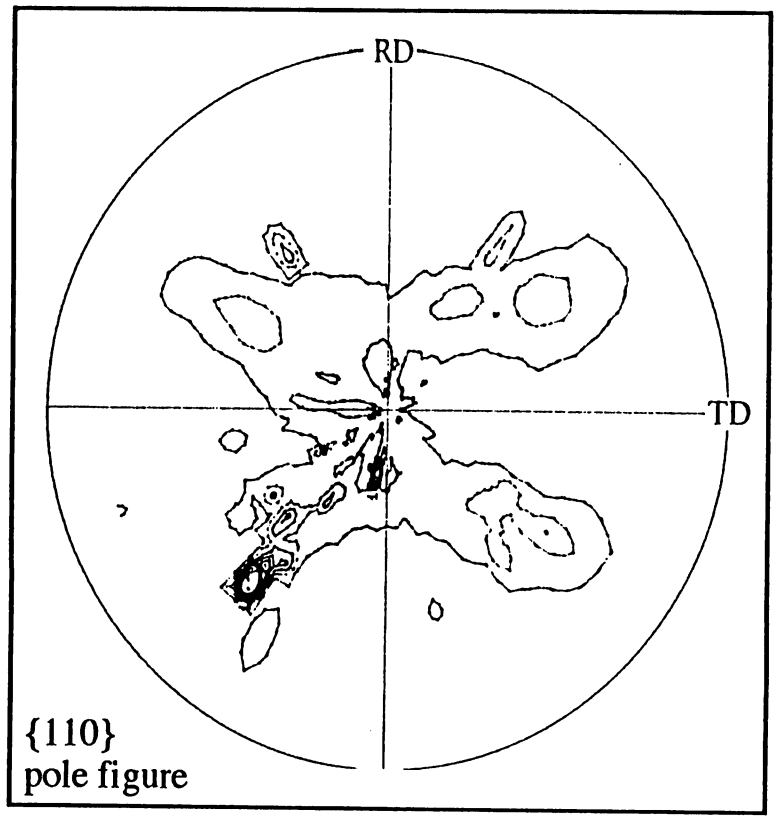

Figure 4.6: The {2 0 0} and {1 1 0} partial pole figures for recrystallised *MA957*.

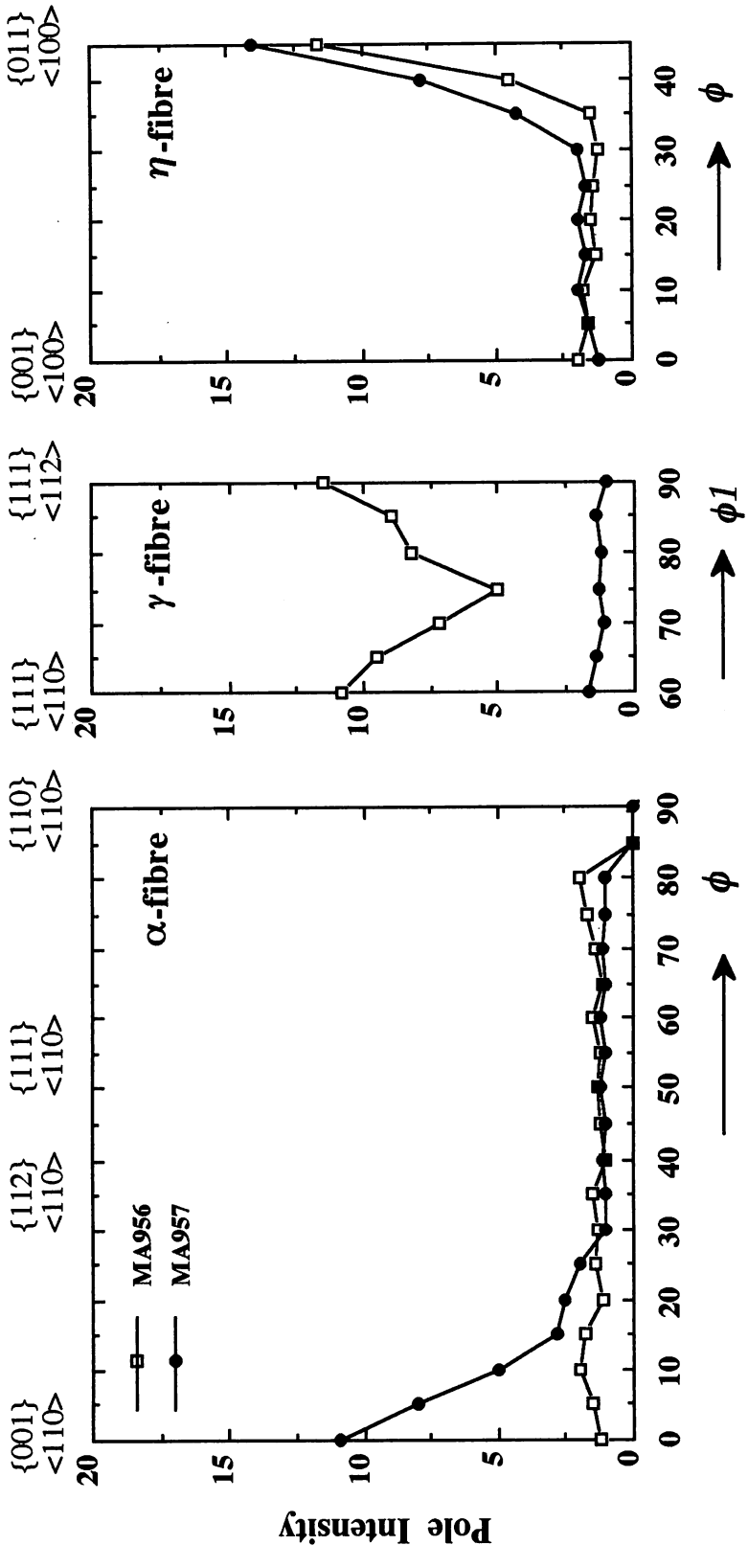

Figure 4.7: Recrystallisation texture of as-annealed *MA956* and *MA957* steels.

and Katoh, 1974; Hughes and Page, 1971). Recrystallisation may occur "continuously", involving basically the recovery of the microstructure via subgrain coalescence. It may nucleate at transition bands which are localised regions of sharp changes in lattice orientation, arising through inhomogeneous deformation. The third is strain induced grain boundary migration, which is alternatively called grain boundary nucleation.

The transition band mechanism can be ruled out for the alloys studied here – extensive metallography has failed to reveal such deformation bands (Baloch, 1989). Grain boundary nucleation is expected to lead to texture components close to the deformation texture. For *MA956*, such components are found in the deformed state. For example, a $\{1\ 1\ 1\} < 1\ 1\ \bar{2} >$ component of γ–fibre would be expected (Abe, 1966) as shown in Figure 4.3. Thus, the sharpening of γ–fibre in *MA956* steel is considered to be due to preferred nucleation at grain boundaries leading to the stablisation of the γ–fibre at the expense of α–fibre. This is consistent with the relatively large oxide content of *MA956*. In addition, subgrain coalescence may also play a role in the recrystallisation nucleation mechanism. This is consistent with the presence of the $\{0\ 1\ 1\} < 1\ 0\ 0 >$ component in the recrystallised steel.

It is said that within the major deformation texture components, the stored energy increases in the order $\{0\ 0\ 1\}$ — $\{1\ 1\ 2\}$ — $\{1\ 1\ 1\}$, while the very weak $\{0\ 1\ 1\}$ component has the highest stored energy of all (Hutchinson, 1974). Thus, the $\{0\ 1\ 1\}$ and $\{1\ 1\ 1\}$ texture component should nucleate first and therefore have the longest available time for growth. Since in mechanically alloyed steels recrystallisation occurs at very high temperatures, the most potent nuclei are expected to grow rapidly and become dominant in the final microstructure. This explains the strong Goss component $\{0\ 1\ 1\} < 1\ 0\ 0 >$ developed in recrystallised *MA956* steel.

In *MA957*, the annealed sample contained a strongly enhanced $\{0\ 1\ 1\} < 1\ 0\ 0 >$ edge–cube texture and the $\{0\ 0\ 1\} < 1\ 1\ 0 >$ texture. The former is the same as in *MA956*, indicating some recrystallisation by a subgrain coalescence mechanism. However, the cube component must be ascribed to grain boundary nucleation (Dillamore *et al.*, 1972). Moreover, the other much more important factor, phase transformation, is considered below.

4.3.3 Phase Transformation in MA957

As pointed out previously, the relatively weak texture of as–received *MA957* is inconsistent with the fact that it is associated with a much larger degree of deformation compared with *MA956*. There is also no rational basis for the detailed differences in the deformation textures of the two alloys. However, during the course of some experiments designed to enable a better

Table 4.1: Thermodynamic phase stability calculations for alloy *MA957*. The concentrations and phase fractions are stated in wt%. The body–centered cubic and face–centered cubic forms of iron are designated α and γ respectively.

Temperature °C	α wt.%	γ wt.%	Cr_α wt.%	Cr_γ wt.%	Mo_α wt.%	Mo_γ wt.%	C_α wt. %	C_γ wt.%
950	100	–	14.00	–	0.300	–	0.010	–
970	97.9	2.1	14.04	11.98	0.301	0.244	0.009	0.035
990	97.7	2.3	14.05	11.96	0.301	0.244	0.009	0.034
1010	98.6	1.4	14.01	11.92	0.301	0.244	0.010	0.035
1030	100	–	14.00	–	0.300	–	0.01	–

control of the grain microstructure (Chapter 5), it was discovered that *MA957*, which has a relatively small chromium concentration and no aluminium, can undergo partial transformation to austenite. Prior to this result, it has always been assumed that both of the steels studied here are ferritic at all temperatures below the liquidus temperature.

The optical micrograph presented in Figure 4.8a shows the austenite obtained during air cooling a sample from 1350 °C (where it recrystallises). The austenite grows in the form of allotriomorphs at the recrsytallised–grain boundaries and as Widmanstätten austenite plates emanating from the allotriomorphs. On further cooling, the austenite transforms into martensite, as illustrated in Figure 4.8b.

To verify further that the alloy should in fact be able to transform to austenite, thermodynamic phase stability calculations were carried out using the *MTDATA* package of the National Physical Laboratory (1992). This allows the prediction of phase diagrams; the calculations for *MA957* took account of the elements iron, carbon, chromium and molybdenum, the permitted phases being ferrite and austenite. It is clear from Table 4.1 that the formation of a small amount of austenite can be expected in the temperature range 970–1010 °C. These calculations assume a homogeneous alloy – any variations in chemistry may lead to corresponding variations in phase stabilities.

Further confirmatory metallography of a recrystallised sample heat–treated at 1000 °C for 24 hr is illustrated in Figure 4.9, which shows allotriomorphs of austenite at the recrystallised ferrite grain boundaries. Similar isothermal heat–treatments at 950 and 1050 °C failed to reveal any austenite, confirming the thermodynamic calculations.

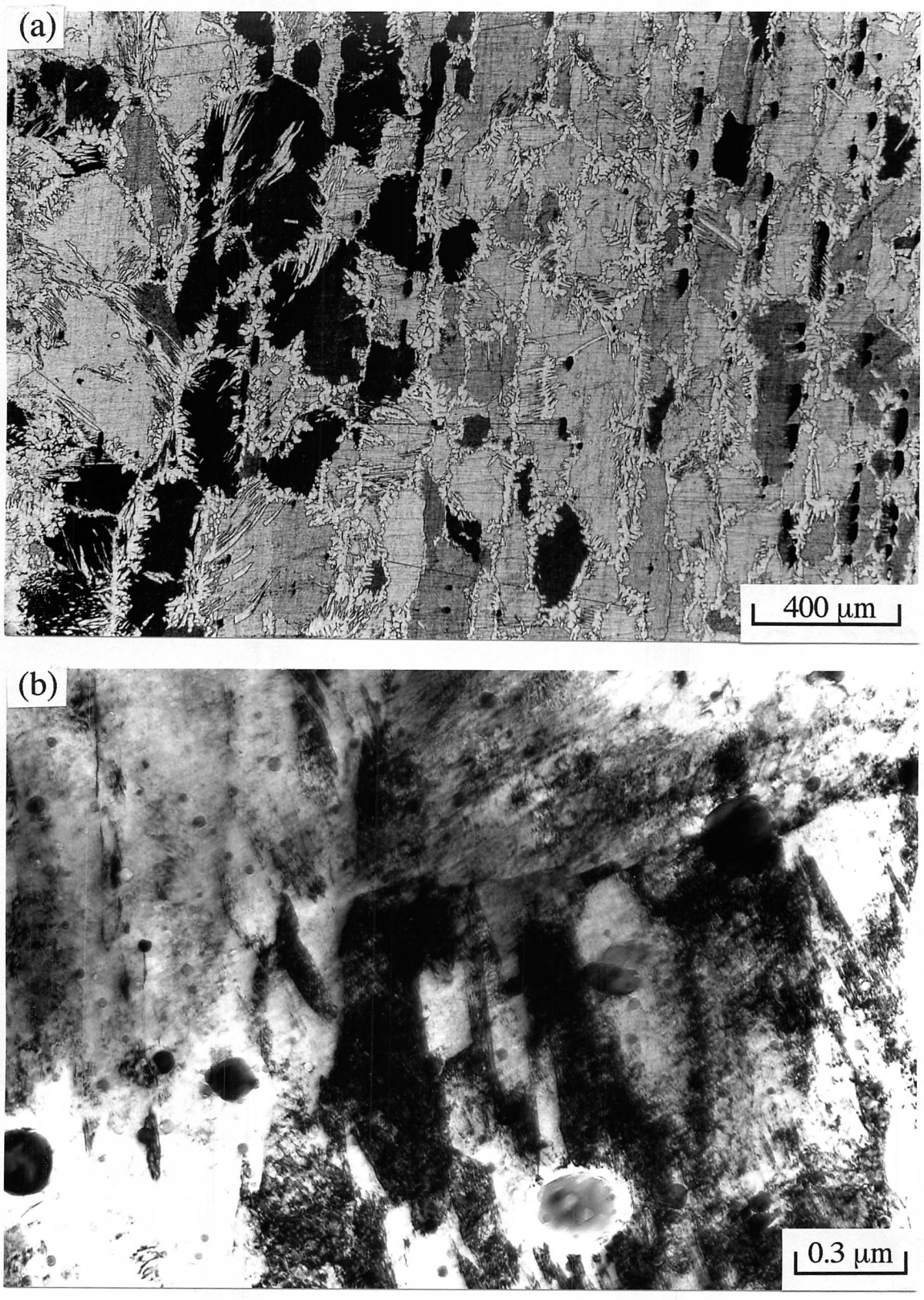

Figure 4.8: A sample of *MA957* recrystallised at 1350 °C for 10 min, followed by air cooling through a temperature range where austenite forms. (a) Optical micrograph illustrating allotriomorphic and Widmanstätten austenite. (b) Transmission electron micrograph to illustrate the martensite that forms as the austenite decomposes martensitically on cooling to ambient temperature.

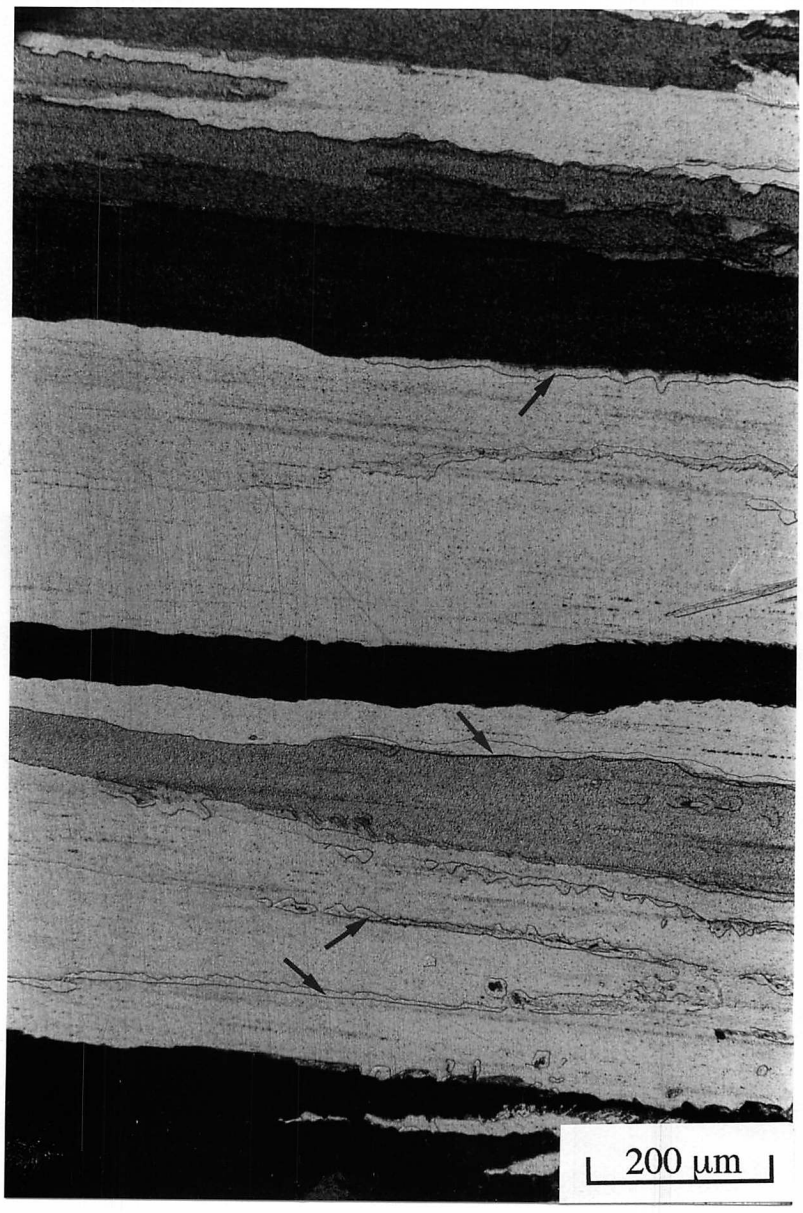

Figure 4.9: A sample of recrystallised *MA957* after isothermal heat treatment at 1000 °C for 24 hr, followed by air cooling to ambient temperature. Allotriomorphs of austenite can be seen at the recrystallised ferrite grain boundaries (arrows).

In the light of the previous discussion, the main differences of texture, both in the as–received and recrystallised states between *MA956* and *MA957* steels, can be related to the occurrence of austenite in *MA957* steel at the temperature within the hot–working temperature range. The austenite leads to a weakening of the recrystallisation texture. The expected cube texture in the austenite would transform into the $\{0\ 0\ 1\} < 1\ 1\ 0 >$ ferrite texture, consistent with the observation that the latter component is enhanced in *MA957* relative to *MA956*.

Finally, it is appropriate to compare the present work with some results published by Alamo *et al.* (1992). They also studied the crystallographic textures of *MA957* and *MA956*. Although their experiments cannot be directly compared with the present work, it is interesting that when the $\{1\ 1\ 0\}$ pole figures of cold deformed *MA956* and *MA957* are compared, the texture is found to be weaker in the latter. This is consistent with the observation reported here that the texture is weaker in *MA957* in the as–received condition.

4.4 CONCLUSIONS

The deformation and recrystallisation textures of two mechanically alloyed stainless steels have been examined.

Alloy *MA956*, which has a large chromium, aluminium and yttria concentration, is ferritic in the solid state and on deformation gives the expected fibre texture. Because of the large yttria concentration, recrystallisation seems to cause the sharpening of γ–fibre. Also, the development of Goss component can be attributed to the nucleate by a subgrain coalescence mechanism.

By contrast, alloy *MA957* was found to exhibit a very weak deformation texture in spite of the fact that it had been deformed to a larger extent. This result can be explained by the discovery that the alloy is not fully ferritic at all temperatures in the solid state. Because of its relatively low chromium concentration, and the absence of aluminium, it becomes partially austenitic within the temperature range 970–1010 °C. The austenite then transforms to martensite on cooling, giving a new set of orientations, and consequently, a more random crystallographic texture. During annealing, recrystallisation nucleates both *via* a subgrain coalescence mechanism and *via* grain boundary migration. The existence of the austenite phase tends to enhance the development of cube texture.

CHAPTER FIVE

GRAIN CONTROL IN MECHANICALLY ALLOYED OXIDE DISPERSION STRENGTHENED *MA957* STEEL

5.1 INTRODUCTION

Oxide dispersion strengthened (ODS) alloys produced using a mechanical alloying technique have the potential for better creep resistance and stability at high temperatures, when compared with conventional alloys (Cairns *et al.*, 1975; Vandermeulen and Coheur, 1981; Fleetwood 1986). In the mechanical alloying process, metallic powders or intermetallic compounds are induced to form a solid solution by means of intense deformation. There are two major commercial variants of mechanical alloys, the nickel base alloys destined for aerospace applications (Fleetwood 1986; Sundaresan *et al.*, 1987), and others which are based on ferritic iron with potential applications at somewhat lower temperatures. The density of the ferritic alloys is about 10% lower than the nickel base alloys, providing a significant strength to weight advantage, and a lower thermal expansion coefficient of benefit in circumstances where thermal fatigue is an important design criterion (Fischer *et al.*, 1977). In nuclear reactor applications, the ferritic structure is more resistant to neutron damage (Huet and Leroy, 1974). As described in Chapter 2, the mechanically alloyed ferritic stainless steel *Incoloy MA957* has been developed as a nuclear fuel cladding material for fast-breeder reactors (Asano *et al.*, 1988).

After mechanical alloying and processing into bulk form, *MA957* has an ultrafine microstructure containing submicron grains of ferrite. The hardness in this condition is unacceptably high, so that the alloy is used in the recrystallised condition. The recrystallisation can be carried out isothermally, in a temperature gradient, or using zone annealing. All of these heat treatments result in a coarse columnar grain structure akin to a directionally solidified microstructure. The reason for the persistent recrystallisation into a columnar rather than an equiaxed grain structure is that the alloy contains a dispersion of oxide particles which are aligned along the extrusion direction (Baloch, 1989), so that the easiest grain growth path is along the extrusion direction.

A columnar (or *directionally recrystallised*) grain structure is ideal for elevated temperature applications where creep resistance is important. However, when the alloy is made in tubular

form, its resistance to hoop stresses is found to be less than desirable. Different metal working conditions can influence the degree of anisotropy (Grundy and Patton, 1985), but it has not yet been possible to produce an equiaxed microstructure on the scale 20–40 μm. The major aim of this work was to develop heat–treatments capable of causing recrystallisation into equiaxed grains, even though the starting microstructure contains a highly anisotropic dispersion of oxide particles. The method used involves the control of stored energy prior to recrystallisation, and the exploitation of the recently discovered phase transformation in alloy *MA957* (Chapter 4).

5.2 EXPERIMENTAL PROCEDURE

The stored energy prior to recrystallisation was controlled by "preannealing" at a temperature high enough to permit recovery but not recrystallisation. Thus, preannealing was carried out at 1150 °C before heating to 1350 °C to induce recrystallisation.

Square sectioned specimens of dimensions $3 \times 3 \times 20$ mm were cut from the as–extruded rod. The heat treatments were carried out in a conventional resistance furnace, the samples being protected by sealing in quartz tubes filled with a partial pressure of pure argon.

For metallographic observations, optical microscopy and transmission electron microscopy were carried out to observe the as-received and recrystallised structures. Whilst, differential scanning calorimetry was employed to measure the recrystallisation temperature and the changes of stored energy by preannealing heat treatment.

Thermodynamic phase stability calculations were carried out using the *MTDATA* package of the National Physical Laboratory (1992) to calculate the equilibrium phases expected in *MA957* steel as a function of temperature, and to study the metastable equilibrium between ferrite and austenite. The calculations allowed for the elements Fe, Cr, Mn, Mo, C, Ni, V, Si, Sn, Cu, P, and S and the phases of carbides, austenite, and ferrite. The calculations covered the temperature range from 1400 °C to 900 °C with a step by 20 °C .

5.3 PREANNEALING EXPERIMENTS

It was emphasised earlier that alloy *MA957* tends to recrystallise into coarse columnar grains parallel to the extrusion/rolling direction. The alloy therefore recrystallises directionally. This is irrespective of whether the heat–treatment is carried out with the sample in a temperature gradient, whether the sample is zone–annealed (*i.e.* a moving hot–zone traverses the length of the sample) or whether it is isothermally annealed. Indeed, the grains always tend to grow along the extrusion direction, even when the temperature gradient is orientated normal to the extrusion direction (Baloch, 1989). For all heat–treatments, a jagged recrystalli-

sation front develops and propagates along the length of the sample, presumably because the "nucleation" occurs at the sample surfaces.

It follows that unlike some other alloys, the reason why recrystallisation is directional has little to do with the existence of any temperature gradients during annealing. Transmission electron microscopy has revealed that the distribution of yttria particles is not uniform (Baloch, 1989); the particles tend to align parallel to the extrusion direction. Consequently, the grain boundary velocity is anisotropic, being largest along the extrusion direction. This is responsible for the development of the directional microstructure.

The particle dispersions are therefore not strong enough to pin grain boundaries, they simply hinder grain boundary motion, to varying degrees along different directions. In fact, the mechanical alloying and extrusion process results in a cold–worked microstructure with an ultrafine, submicron sized grain structure which is very hard. Most of the stored energy of the alloy is thus in the form of grain boundaries. This stored energy is so large that moving grain boundaries can easily overcome the drag from the particle dispersion.

To summarise, the anisotropy of the directionally recrystallised microstructure is because the growth velocity is much higher along the extrusion direction. Once initiated at the sample surfaces, the recrystallisation front propagates so rapidly that there is no opportunity for recrystallisation to develop from other locations in the sample (Fig 5.1a). The grain intercept along the transverse direction tends to be insensitive to the heat–treatment, probably being controlled by the number of initial sites at which recrystallisation can commence. Thus, a more isotropic grain structure could in principle be produced by reducing the grain velocity along the longitudinal direction (Fig. 5.1b). This can be achieved by reducing the stored energy, by some recovery process prior to recrystallisation proper.

Recrystallisation in *MA957* tends to happen at temperatures in excess of 1300°C, so a systematic set of *preannealing* experiments was designed to dissipate some of the stored energy. This involved prolonged annealing at 1150 °C before heating to 1350 °C to induce recrystallisation.

Fig. 5.2 shows that the preannealing heat–treatment at 1150 °C for 10 min–80 hr has no obvious effect on the optical microstructure, although the hardness drops slightly (Fig. 5.3). This is consistent with recovery effects occurring during the preannealing process. Subsequent recrystallisation at 1350 °C in some cases produced equiaxed grain microstructures (Fig. 5.4), but the results were erratic. Such behaviour is a reflection of the fact that mechanical alloying is a difficult process, the alloys being somewhat inhomogeneous. In fact, an attempt to reproduce the equiaxed microstructure illustrated in Fig. 5.4 failed, as illustrated in Fig. 5.5. However,

(a) High stored energy, high anisotropic growth velocity

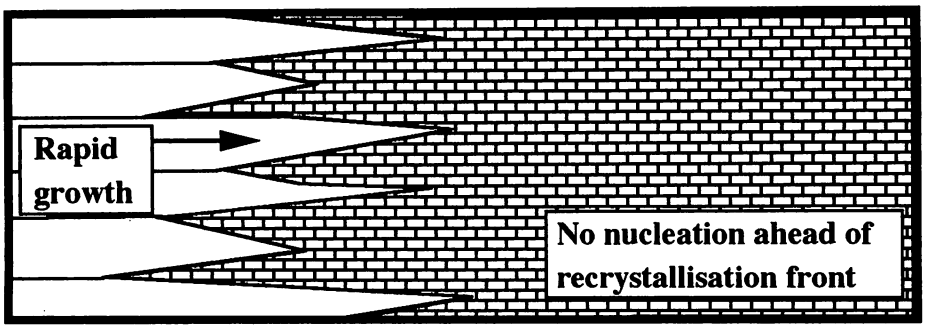

(b) Low stored energy, low anisotropic growth velocity

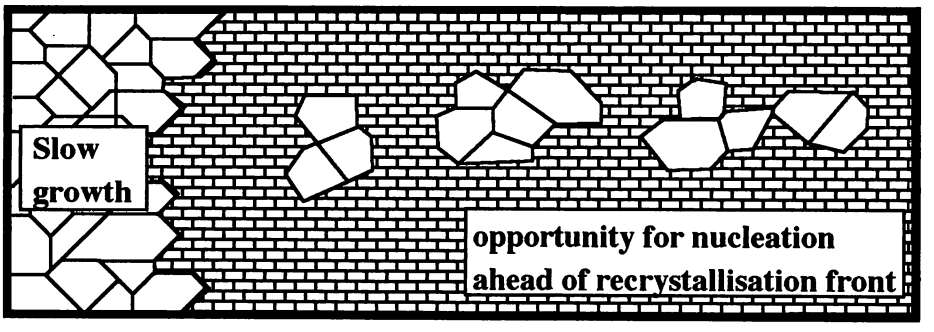

Figure 5.1: Schematic development of the recrystallisation process for varying quantities of stored energy.

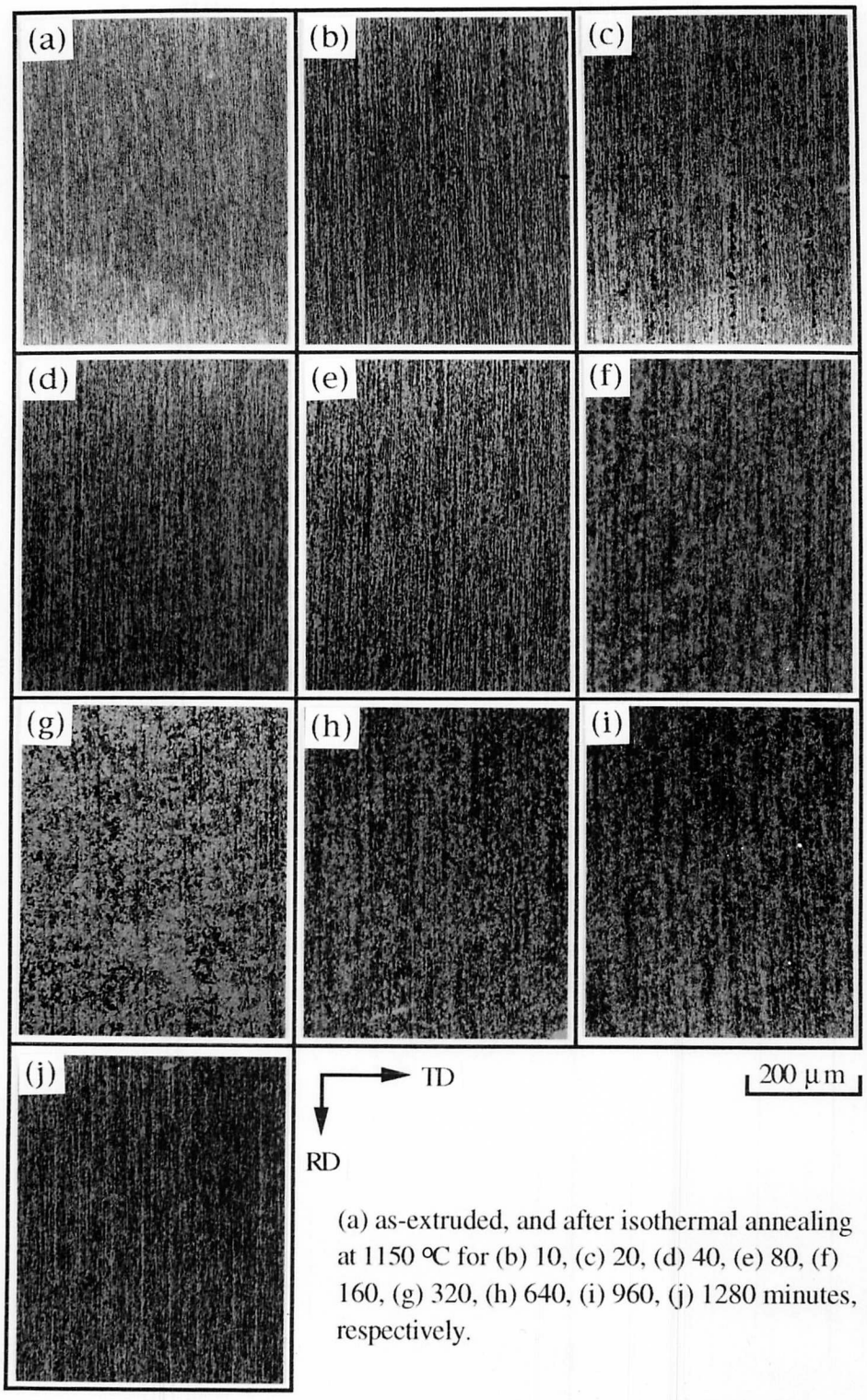

(a) as-extruded, and after isothermal annealing at 1150 °C for (b) 10, (c) 20, (d) 40, (e) 80, (f) 160, (g) 320, (h) 640, (i) 960, (j) 1280 minutes, respectively.

Figure 5.2: Set of micrographs illustrating no obvious change in the optical microstructure during the preannealing heat treatment at 1150 °C.

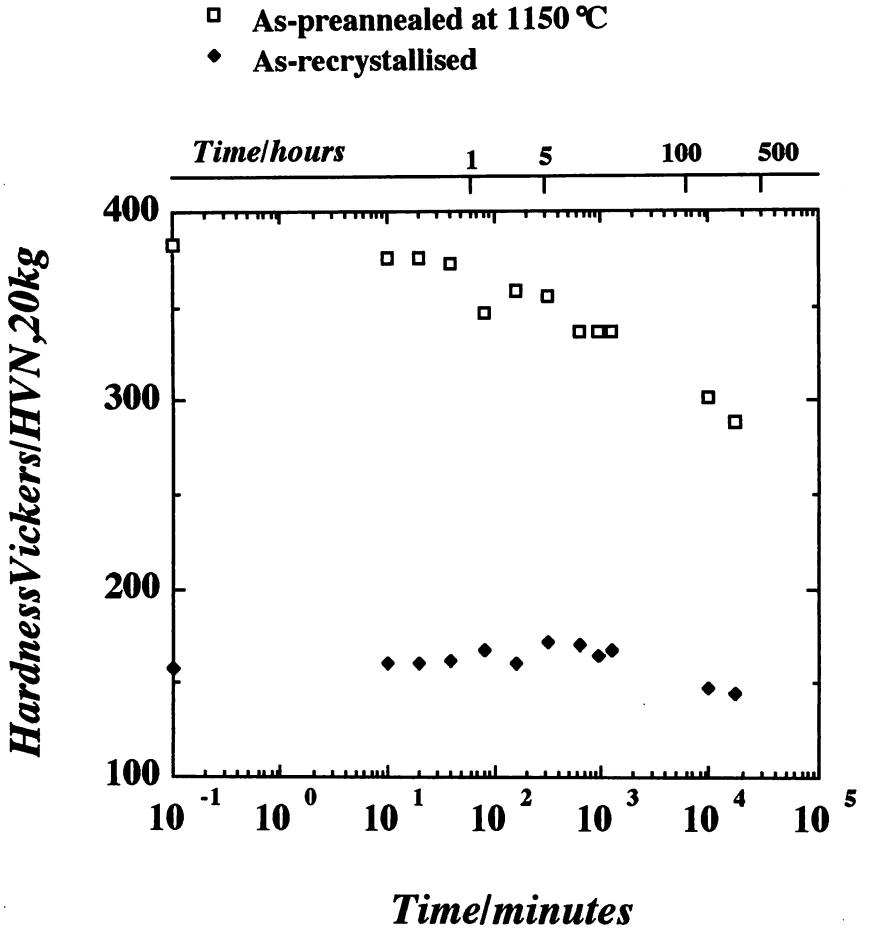

Figure 5.3: Vicker's hardness data for preannealed samples, and for samples which were subsequently recrystallised by heating to 1350 °C.

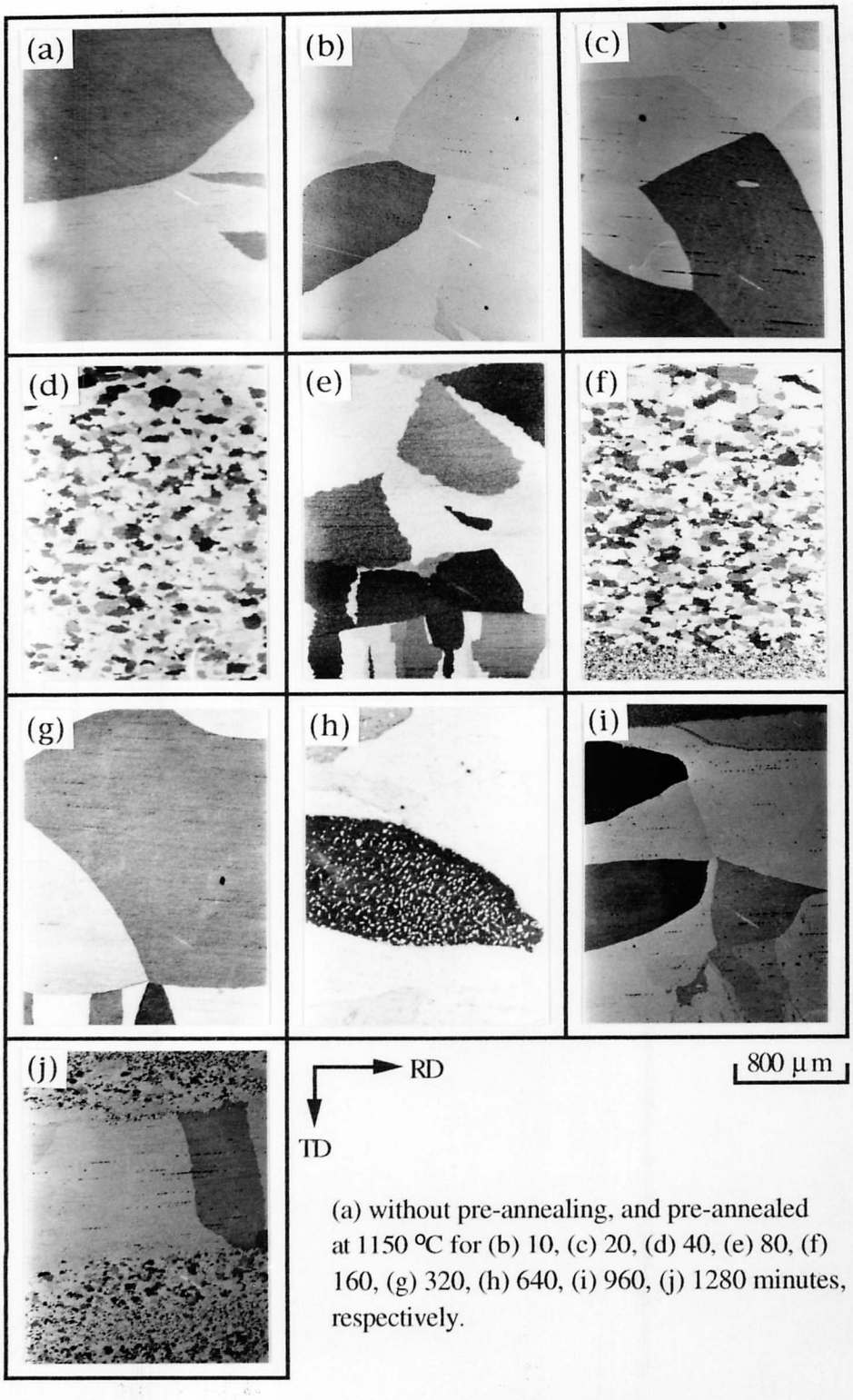

(a) without pre-annealing, and pre-annealed at 1150 °C for (b) 10, (c) 20, (d) 40, (e) 80, (f) 160, (g) 320, (h) 640, (i) 960, (j) 1280 minutes, respectively.

Figure 5.4: Optical micrographs illustrating the recrystallised microstructures of the preannealed samples shown in Fig. 5.2.

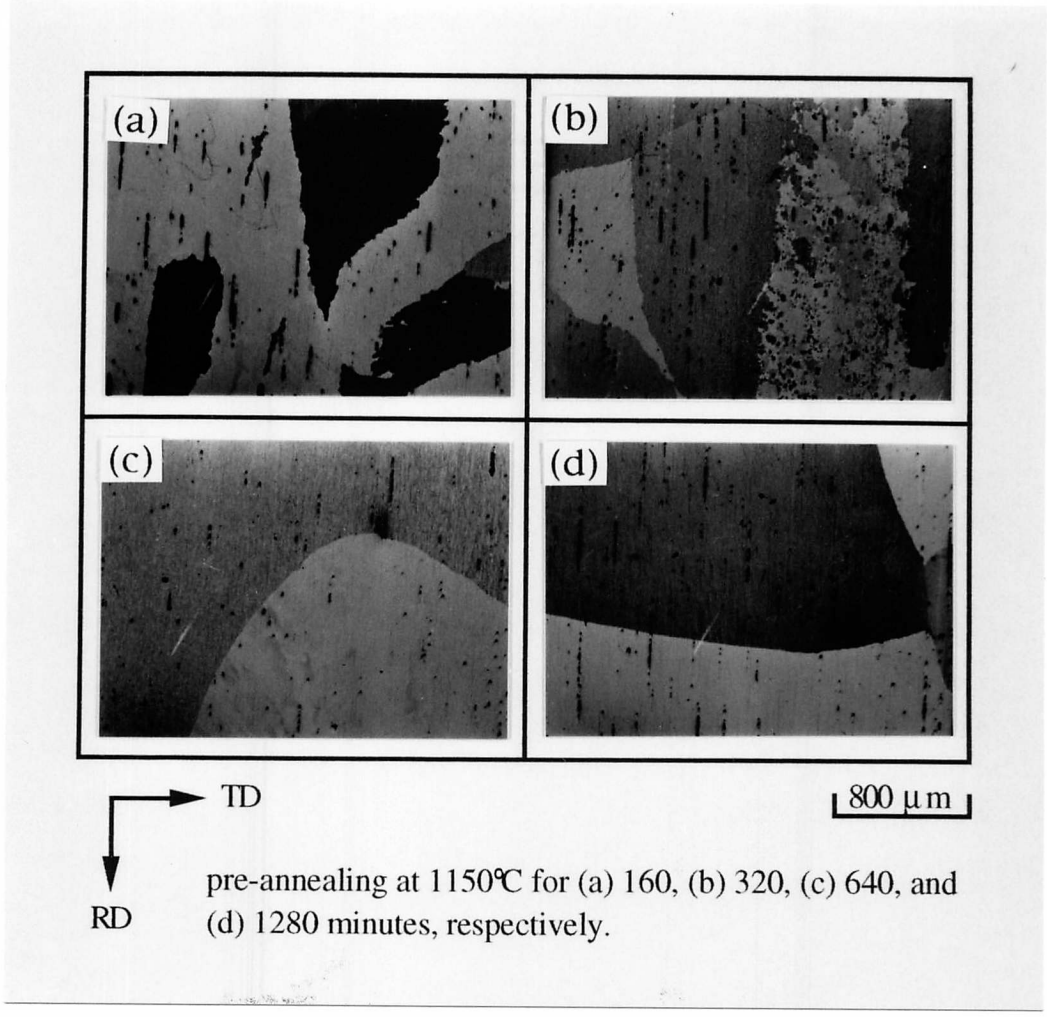

Figure 5.5: The microstructure obtained by repeating the heat–treatment shown in Fig. 5.4.

preannealing for 160 hr at 1150 °C gave a reproducible equiaxed, fine–grained microstructure, irrespective of the position of the sample within the extruded bar, as illustrated in Fig. 5.6. It is concluded that this is because the stored energy (and hence the growth velocity) has in all positions been reduced sufficiently to give the transition from a directionally recrystallised to an equiaxed microstructure.

Consistent with this, further preannealing (280 hr at 1150 °C) resulted in a deterioration of the microstructure, as illustrated in Fig. 5.7. Although equiaxed grains were obtained, their size was finer and varied as a function of position. Clearly, the stored energy had fallen to a level where the grain size begins to be limited by Zener pinning, as the pinning force becomes comparable to the driving force for grain boundary migration. The microstructure thus becomes sensitive to any inhomogeneous distribution of particles.

These ideas are summarised in Fig. 5.8. When the driving force for recrystallisation is very large, a directional grain structure is obtained because the growth rate along the length direction is large (relative to the pinning force), so that there is no opportunity for recrystallisation to develop at places other than the initial nucleation site. This is not the case at intermediate stored energies and almost uniform equiaxed grain structures are obtained. When the driving force for recrystallisation becomes comparable to the pinning force, there is not only a refinement in the microstructure, but a heterogeneous grain size reflecting variations in the oxide dispersions within the alloy.

The effect of preannealing on the stored energy and microstructure was confirmed further using transmission electron microscopy and differential scanning calorimetry. Fig. 5.9 illustrates the effect of preannealing on the annihilation of dislocations in the deformed material. These qualitative observations show that there is a clear reduction in the dislocation density during the preannealing heat treatment (1050 °C for 160 hr). The corresponding decrease in the stored energy is apparent from the data presented in Table 5.1 (the DSC curves are presented in Fig. 5.10).

	As-received	As-preannealed at 1150 °C for 160 hr	As-preannealed at 1150 °C for 280 hr
J/g	1.0	0.7	0.5

Table 5.1 Effect of preannealing on the stored energy on *MA957* steel

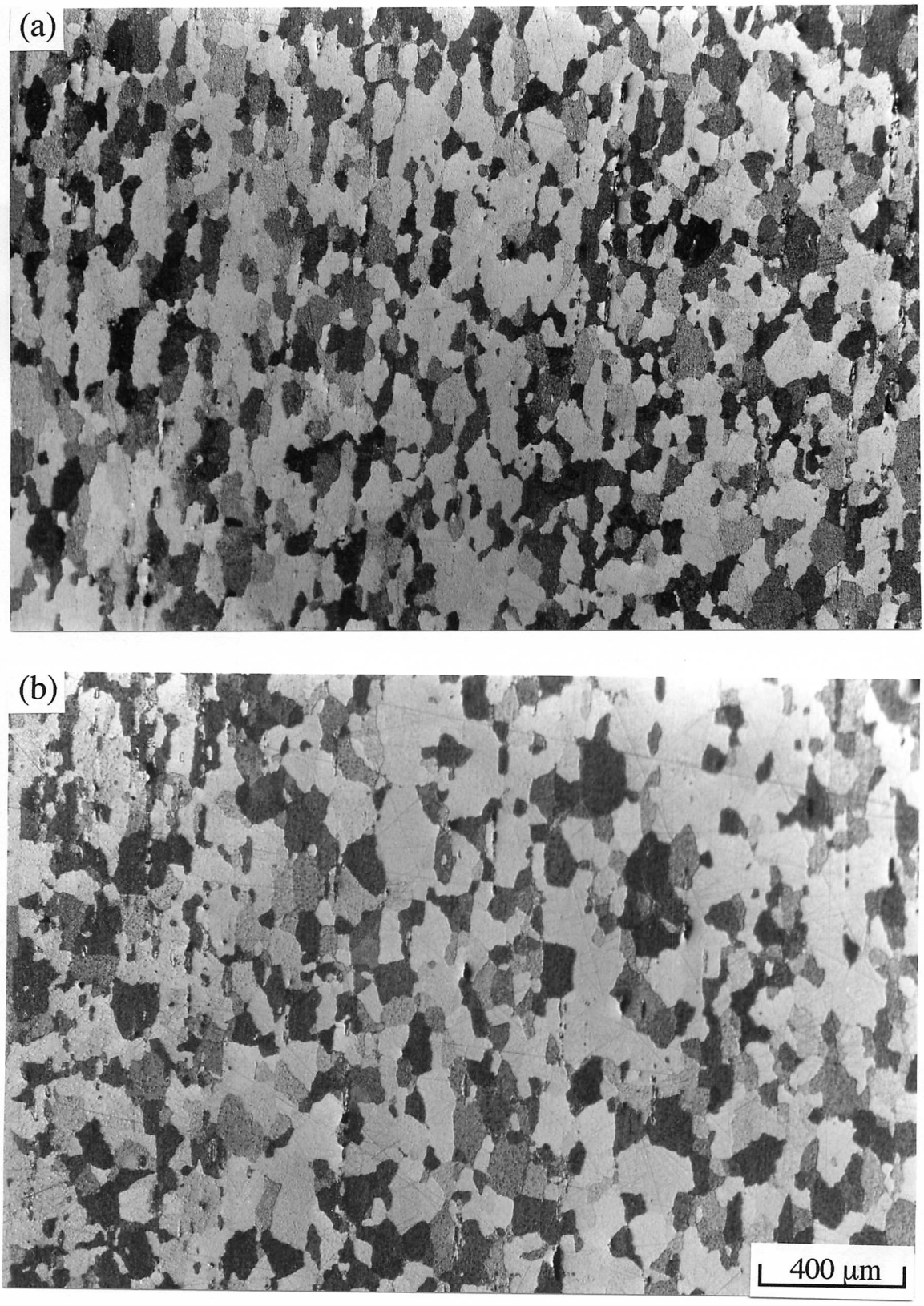

Figure 5.6: Optical micrographs illustrating the recrystallised microstructures of *MA957* steel as preannealed at 1150 °C for 160 hours, then recrystallised at 1350 °C for (a) 20 minutes, and (b) 40 minutes, respectively.

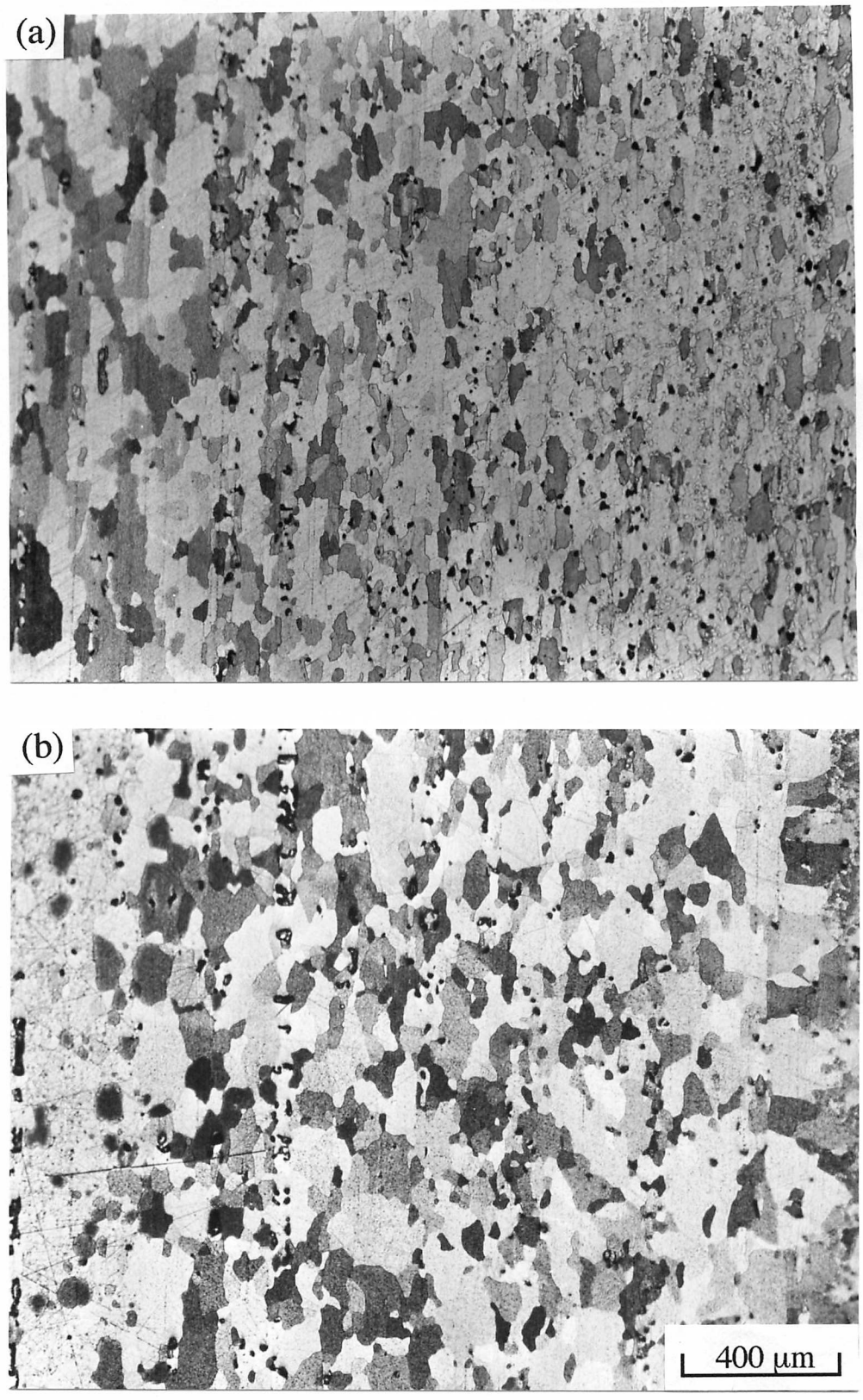

Figure 5.7: Optical micrographs illustrating the recrystallised microstructures of *MA957* steel as preannealed at 1150 °C for 280 hours, then recrystallised at 1350 °C for (a) 20 minutes, and (b) 40 minutes, respectively.

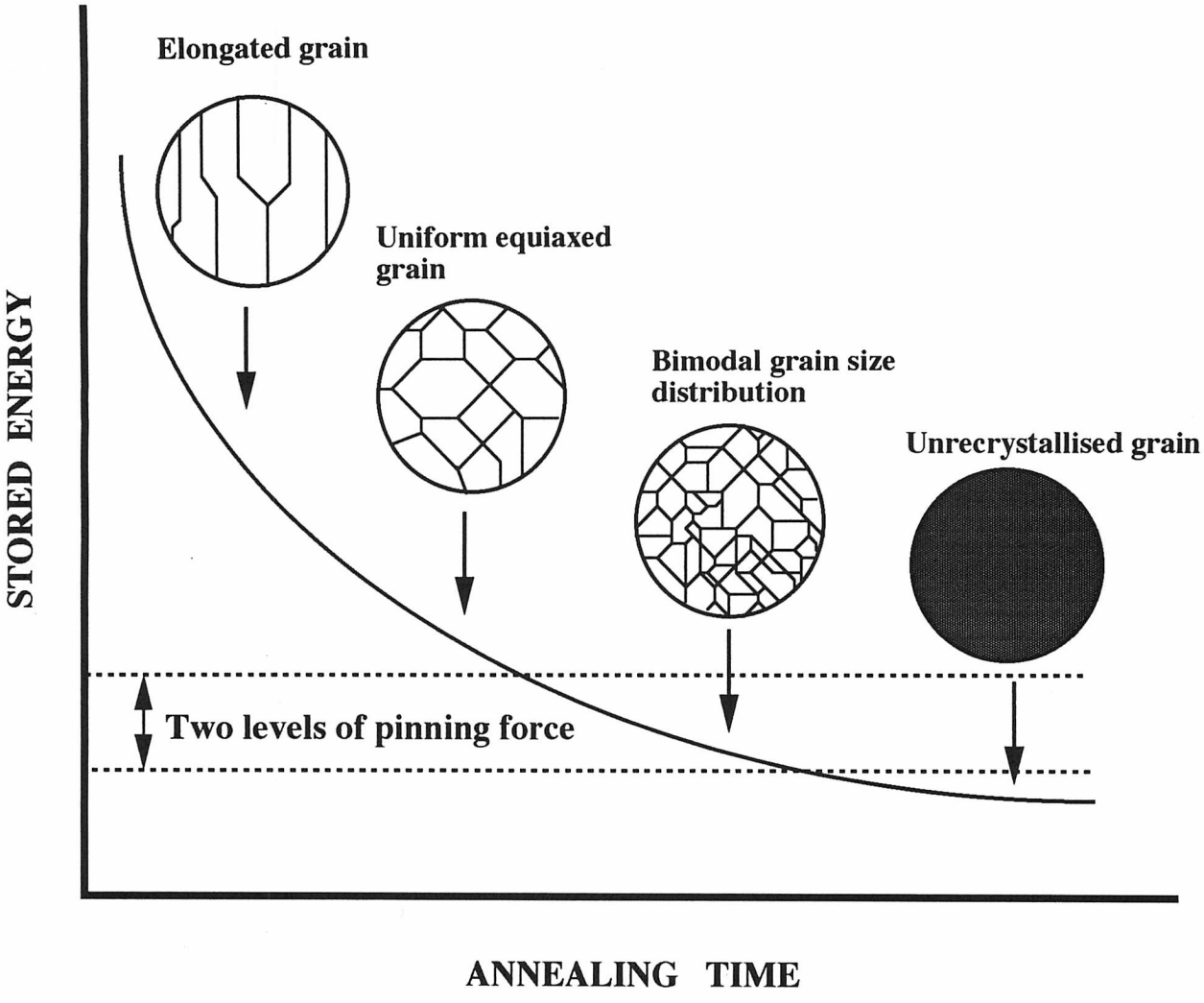

Figure 5.8: Schematic illustration of the role of stored energy in determining the final microstructure, in an alloy which is preannealed and then recrystallised. Two levels of pinning force are illustrated in order to emphasis that the mechanically alloyed steel contains an inhomogeneous distribution of particles.

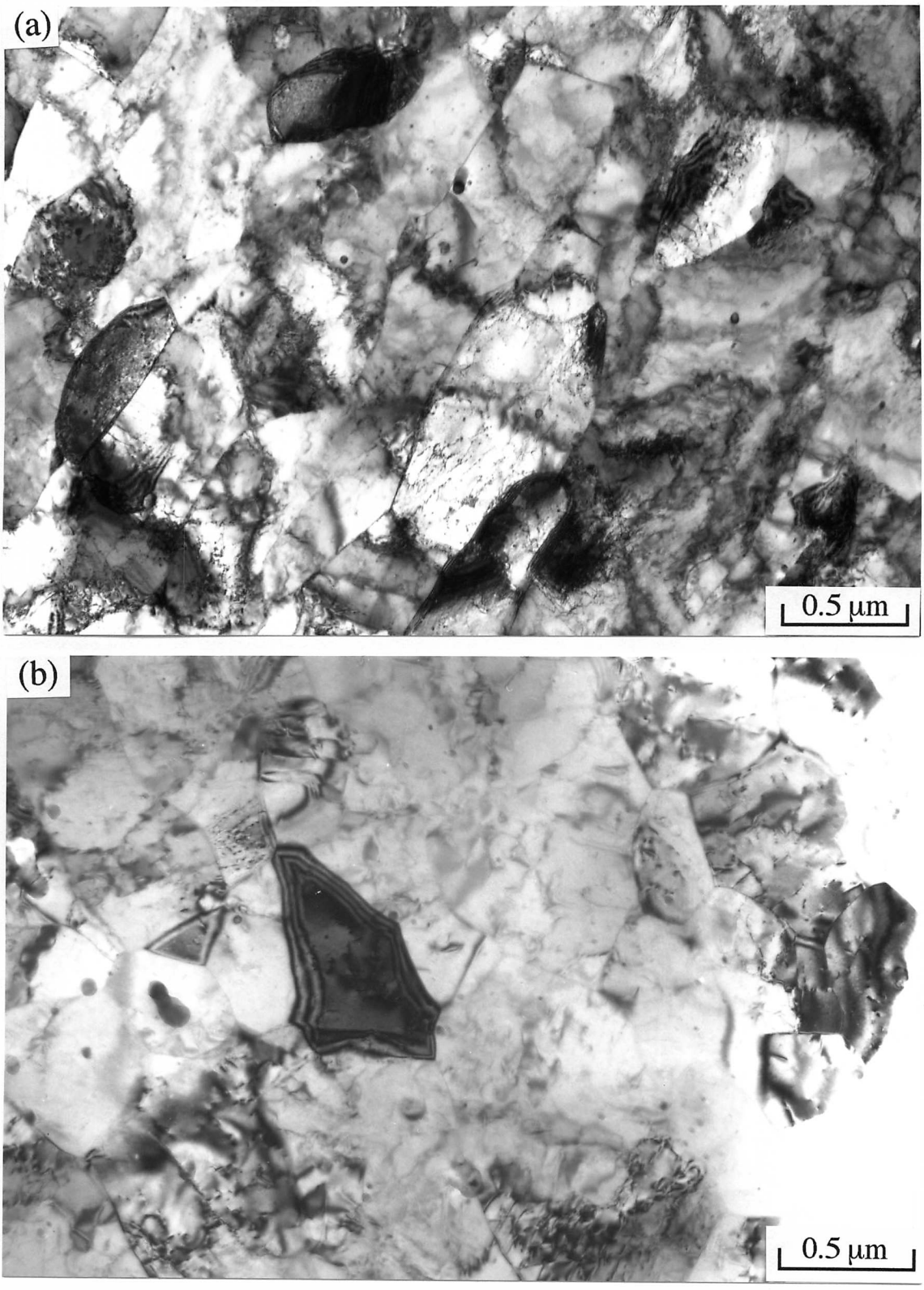

Figure 5.9: Transmission electron micrograph shows the microstructure of *MA957* steel in (a) as–received condition, and (b) as–preannealed at 1150 °C for 160 hours. The low dislocation density in as–preannealed steel indicated the release of stored energy after recovery annealing.

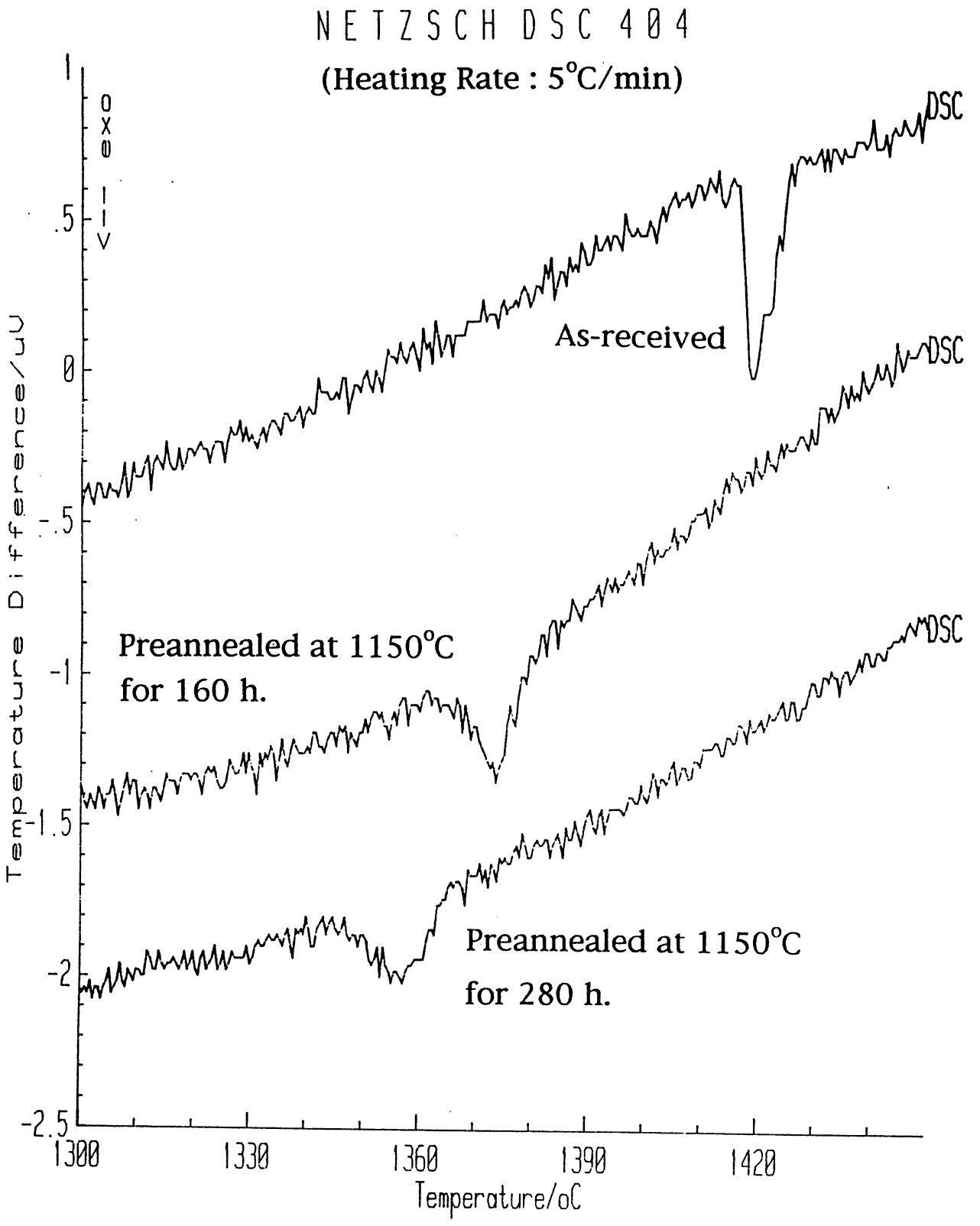

Figure 5.10: DSC Curves of MA957 steel in as-received, and as-preannealed at 1150 °C for 160 and 280 hours, respectively.

5.4 CRYSTALLOGRAPHIC TEXTURE OF FINE RECRYSTALLISED STRUCTURE

As discussed in Chapter 4 the recrystallised ODS steels have a stronger cube texture component due to the effect of the high recrystallisation temperature and high stored energy on the nucleation sequence. Since the preanneal can significantly reduce the stored energy, it may also influence the recrystallisation texture. Therefore, appropriate X-ray pole figures were measured. Fig. 5.11 and Fig. 5.12 show the recrystallisation textures of the fine grained steels which were preannealed at 1150 °C for 160 hours followed by a recrystallisation treatment at 1350 °C for 10 and 20 minutes respectively, in order to produce a fine grain structure. Instead of the sharpened cube texture component, $\{0\ 0\ 1\} < 1\ 1\ 0 >$, associated with the coarse recrystallised grains (Chapter Four), a more random texture was observed on the steel preannealed plus recrystallised. Prolonged annealing at the recrystallisation temperature simply caused a sharpening of cube-on-edge texture towards the $\{0\ 1\ 1\} < 1\ 0\ 0 >$ component.

It was considered in Chapter 4 that the recrystallisation of the as-received steel at very high temperatures causes the recrystallisation texture to be dominated by the component $\{1\ 1\ 0\}$. However, the recovery preanneal tends to preferentially release the stored energy on this component due to the higher stored energy provides the easy rearrangement, or annihilation, of dislocations during recovery (Cotterill and Mould, 1976), thus enhancing the probability of the other components during the early stages of recrystallisation. Therefore, a recrystallisation texture with less strong Goss component, $\{0\ 1\ 1\} < 1\ \bar{1}\ 0 >$, was produced (Fig. 5.11). Further increases in the annealing time at recrystallisation temperature led to the sharpening of this Goss component (Fig. 5.12) due to the preferred grain growth mechanism.

5.5 REFINEMENT BY TRANSFORMATION

MA957 is essentially an iron–chromium alloy which is designed to be a ferritic stainless steel. Alloys like these rely on the "γ–loop" on the phase diagram; this means that beyond a certain limiting concentration of chromium, the alloy becomes ferritic up to the melting temperature, whereas below that concentration, there is a range of temperatures over which austenite can also form. As pointed out in Chapter 4, *MA957* lies just within the γ–loop, so that a small amount of austenite can be generated by heat–treatment in the range 970–1010 °C . The occurrence of the austenite phase in this steel was established using thermodynamic phase stability calculations and further confirmed using metallography. The details of the metallography have been shown in Chapter 4, but Fig. 5.13a illustrates the austenite layers formed at the columnar ferrite grain boundaries during isothermal heat–treatment at 1000 °C

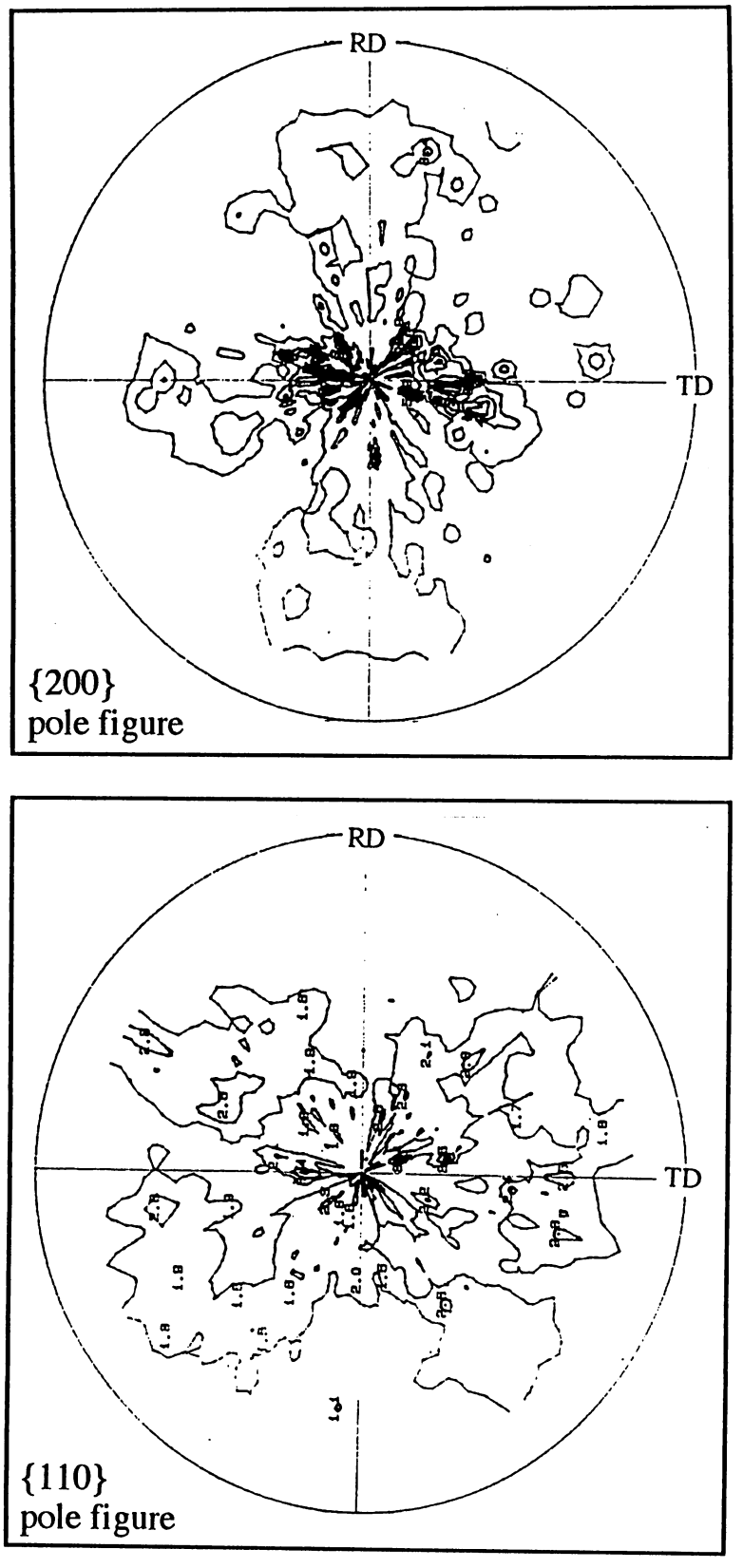

Figure 5.11: The partial pole figures for recrystallised *MA957* steel (preannealed at 1150 °C for 160 hours then recrystallised at 1350 °C for 20 min; fine grained microstructure).

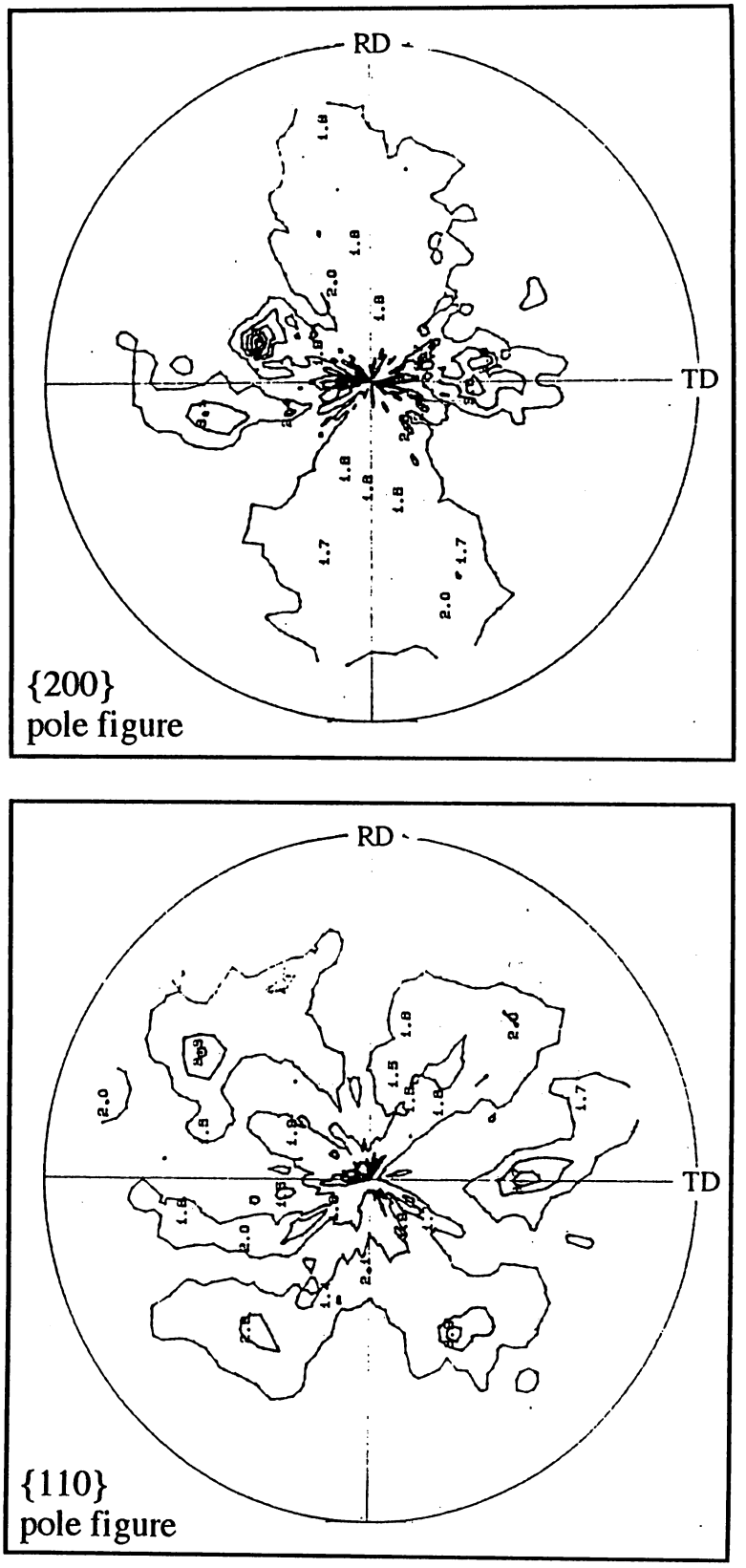

Figure 5.12: The partial pole figures for recrystallised *MA957* steel preannealed at 1150 °C for 160 hours then recrystallised at 1350 °C for 40 min; fine grained microstructure).

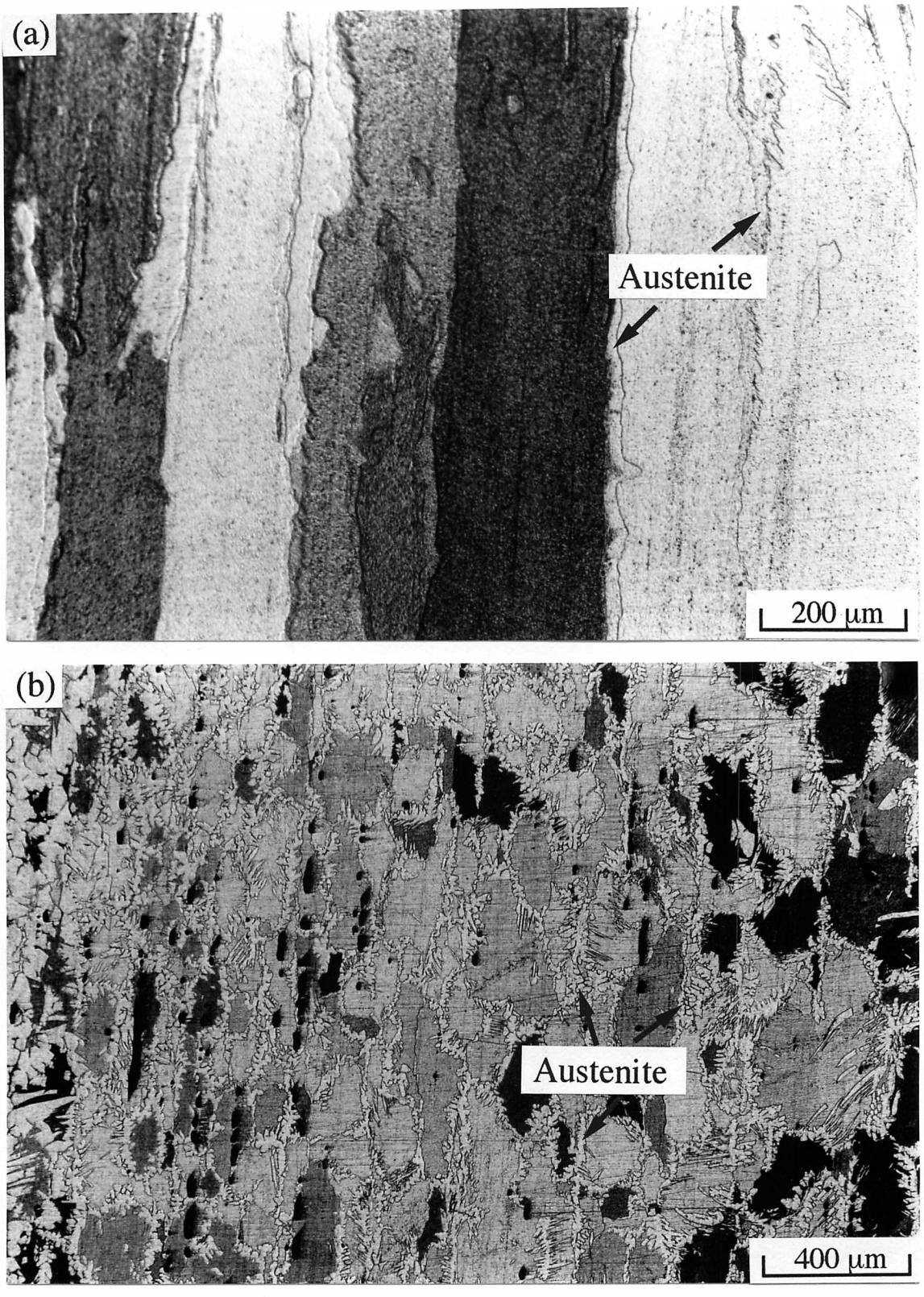

Figure 5.13: Allotriomorphic and Widmanstätten austenite obtained at the ferrite grain boundaries during air cooling the sample from the recrystallisation temperature.

Temperature	α	γ	Cr_α	Cr_γ	Ni_α	Ni_γ	Mo_α	Mo_γ	C_α	C_γ
°C	wt.%	wt.%	wt.%	wt.%	wt.%	wt.%	wt. %	wt.%	wt.%	wt.%
830	100	–	14.00	–	0.500	–	0.300	–	0.010	–
870	80.8	19.2	14.39	12.36	0.426	0.813	0.309	0.261	0.007	0.024
910	61.8	38.2	14.88	12.57	0.379	0.695	0.321	0.266	0.005	0.018
950	54.3	45.7	15.13	12.66	0.371	0.653	0.326	0.269	0.005	0.016
990	55.5	44.5	15.11	12.62	0.382	0.647	0.326	0.268	0.005	0.016
1030	63.5	36.5	14.89	12.45	0.407	0.663	0.321	0.264	0.006	0.022
1070	77.0	23.0	14.53	12.21	0.442	0.694	0.312	0.258	0.006	0.022
1110	94.3	5.7	14.12	11.94	0.486	0.735	0.303	0.252	0.009	0.030
1150	100	–	14.00	–	0.500	–	0.300	–	0.010	–

Table 5.1 Thermodynamic phase stability calculations (MTDATA, 1992) for modified *MA957* alloy with 0.5 wt.% nickel addition. The concentrations and phase fractions are stated in wt%. The body–centered cubic and face–centered cubic forms of iron are designated α and γ respectively.

for 24 hr. Both allotriomorphic and Widmanstätten austenite can be generated during air cooling from 1350 °C as the alloy clips the γ–loop (Fig. 5.13b).

The generation of the austenite phase thus can provide an alternative method of refining the microstructure *after* the extruded sample is recrystallised into a coarse–grained directional microstructure at 1350 °C. If the sample is cooled slowly from the recrystallisation heat–treatment temperature, then allotriomorphic or Widmanstätten austenite is generated at the ferrite grain boundaries (Fig. 5.13). This austenite decomposes to martensite as the sample cools to ambient temperature.

In order to enhance the occurrence of the austenite phase, a small modification of the basic composition of alloy *MA957* which maintains the large chromium concentration necessary for oxidation and corrosion resistance is proposed (Chapter 4). Thermodynamic phase stability calculations suggest that an addition of only 0.5 wt.% of nickel increases the temperature range over which the austenite is stable and considerably increases the maximum amount of austenite that can exist (Table 5.2). This should make the alloy more amenable to austenite formation when heat treated in the two–phase field. Therefore, the grain refinement of the modified *MA957* steel can in principle be achieved by annealing in the two–phase field, shown in Fig. 5.14. The modified alloys for confirmatory experiments are reported in Chapter 8.

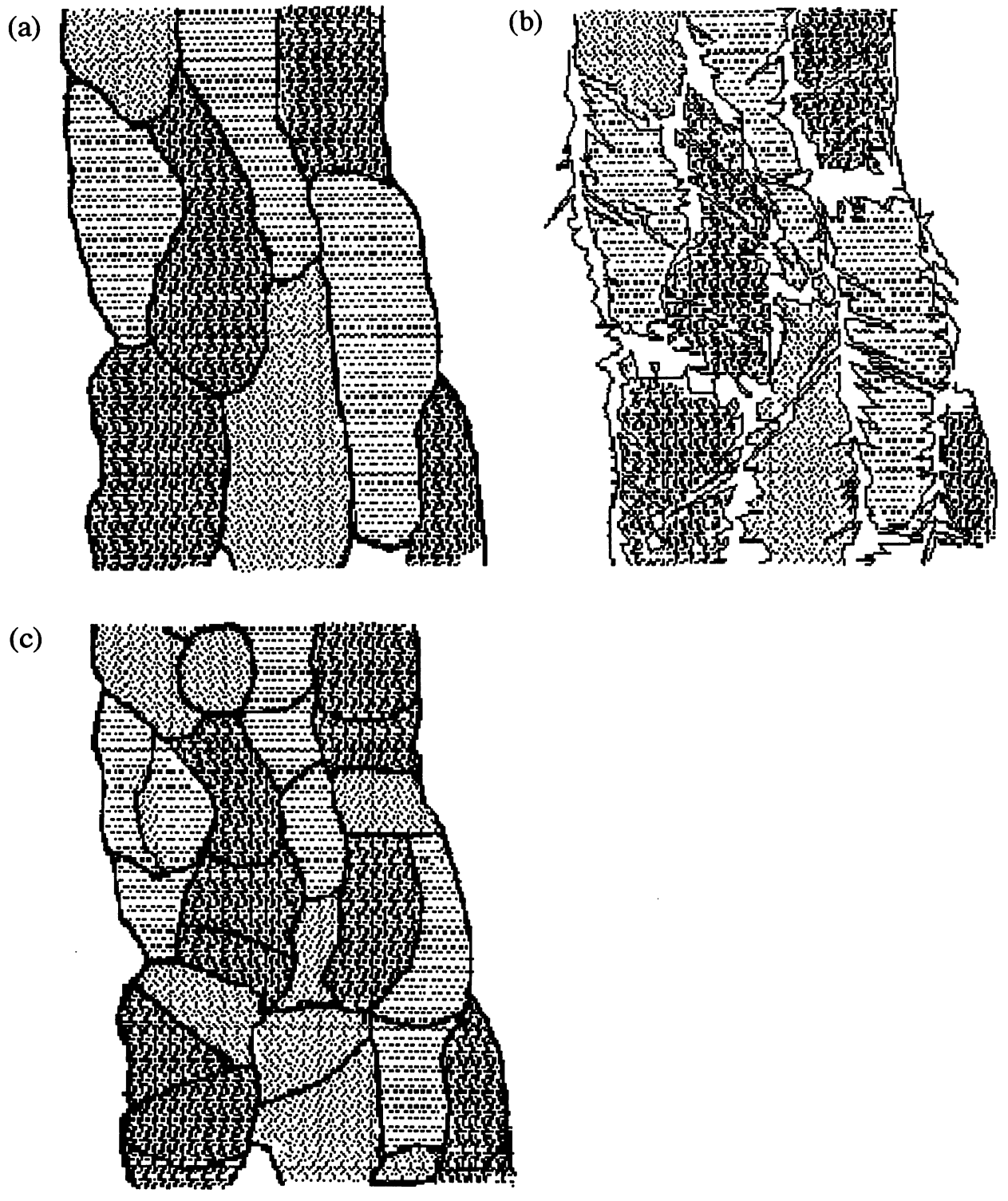

Figure 5.14: Schematic diagram showing the sequences of grain refining by means of austenitic phase transformation in *MA957* steel, (a) recrystallised, (b) as (a) plus ferrite & austenite two–phase region isothermal annealing, (c) as (b) followed by air cooling.

5.6 CONCLUSIONS

A reduction in the stored energy of *MA957* to an optimum value permits the recrystallisation process to generate a uniform, equiaxed grain structure with a grain size in the range consistent with the achievement of more isotropic mechanical properties. This is in spite of the fact that the alloy is not homogeneous with respect to the dispersion of oxide particles. The grain refinement achieved by preanneal is attributed to the controlling of stored energy to reduce the grain boundary velocity to a level which allows nucleation to develop at many sites. Due to the change on nucleation mechanism associated with the preanneal extent, there shows a different recrystallisation texture. Instead of the sharpened cube texture component, $\{0\ 0\ 1\} < 1\ 1\ 0 >$, associated with the coarse recryatallised grains, the finer recrystallisation grains generate a randomised recrystallisation texture. Further prolonged annealing simply cause the sharpening of the cube-on-edge texture towards the $\{0\ 1\ 1\} < 1\ 0\ 0 >$ component, which is coming from the preferred grain growth after preannealing heat treatment.

Alternatively, grain refinement may also be achieved by inducing the formation of austenite at an intermediate temperature range, the austenite decomposing to martensite on cooling to ambient temperature. A thermodynamic analysis has indicated that a small change in the chemical composition (the addition of 0.5 wt.% Ni) could make the formation of austenite more easy. In comparison with the prolonged preanneal treatment, the austenite phase transformation should be able to provide a much easier and economic way for grain refinement.

CHAPTER SIX

ATOMIC STRUCTURE OF MECHANICALLY ALLOYED STEELS

6.1 INTRODUCTION

The synthesis of materials by high energy ball milling of powders, termed mechanical alloying, was first developed by Benjamin (1970) to provide complex oxide dispersion strengthened alloys for high temperature applications. There have been many studies on the recrystallisation behaviour of mechanically alloying metals during the past two decades. However, the atomic structure of the mechanically alloyed solid solutions does not appear to have been examined in detail. Given the nature of the mechanical alloying process, it is possible that the distribution of atoms is likely to be in a nonequilibrium state.

The intense deformation associated with mechanical alloying can force atoms into positions where they would prefer not to be when at equilibrium. The purpose of the work presented in this Chapter was to investigate the atomic structure of a solid solution formed by the mechanical alloying process.

6.2 EXPERIMENTAL PROCEDURE

Samples with dimensions $0.35 \times 0.35 \times 20$ mm were cut from the mechanically alloyed steels *MA956* and *MA957* rods, whose chemical compositions presented in weight percent and atomic percent are given in Table 6.1. The alloys were prepared at INCO (Hereford) using mechanically alloyed powder which was consolidated by hot extrusion followed by hot rolling. This gives the cold–worked microstructure illustrated in Fig. 6.1, with an ultrafine submicron grain size. The samples were studied in this as–received condition, without the usual heat treatment which leads to recrystallisation into a coarse and highly anisotropic columnar grain structure.

A two–stage electropolishing technique was used to prepare fine tips for field ion microscopy. The electropolishing solutions were 25% perchloric acid, 25% glycerol, and 70% ethanol for the first stage, and 3% perchloric acid in 2–butoxy–ethanol for the second–stage.

Atom probe techniques and their applications have been described elsewhere (Miller, 1987; Miller and Smith, 1989). The particular apparatus used here consists of the APFIM200 field

Alloy	C	Cr	Al	Ti	Mo	Y_2O_3
MA956 wt.%	0.01	20.0	4.5	0.5	–	0.50
MA956 at.%	0.044	20.2	8.8	0.55	–	
MA957 wt.%	0.01	14.0	–	1.0	0.3	0.27
MA957 at.%	0.046	14.9	–	1.15	0.17	

Table 6.1 Chemical compositions. The atom percent data exclude the yttrium oxide

ion microscope combined with a reflection time–of–flight mass spectrometer, an instrument capable of both spatial and chemical resolution on an atomic scale (Miller and Smith, 1989). The chemical analysis can be carried out on atoms which are induced to evaporate from the sample using voltage pulses, the pulse fraction being 20% of the sample tip voltage. The sample temperature was maintained at 60 K throughout the experiments.

6.3 RESULTS AND DISCUSSION

6.3.1 Chemical Analysis

The mass spectrometer on the APFIM200 gives the time–of–flight of each ionised atom as it is evaporated from the sample tip and eventually detected. These data then have to be converted into mass/charge ratios for the identification of the species concerned (Miller and Smith, 1989). Fig. 6.2 shows the relationship of isotopic abundances as a function of the mass/charge ratios of the elements that occur in mechanically alloyed steels. It is evident that there is considerable overlap between elements, but the problem is not as severe as might appear at first sight. Much of the overlap is due to isotopes with low abundance, which may be neglected without a great sacrifice to accuracy. This is illustrated in Fig. 6.3. The reasonable accuracy of this procedure is seen from Fig. 6.4, where the results from the atom probe data seem to compare well against the bulk chemistry of the alloy.

6.3.2 Chemical Structure of the Solid Solution

Any solid solution which is in thermodynamic equilibrium (for example, a homogenised phase) will nevertheless exhibit concentration fluctuations of increasing magnitude as the size of the region which is chemically analysed decreases (Landau and Lifshitz, 1958; Russell, 1971). These are random fluctuations which obey the laws of stochastic processes, and represent the real distribution of atoms in the solution. The essential purpose of the present experiments was to establish whether there exist any concentration fluctuations which are in excess of those

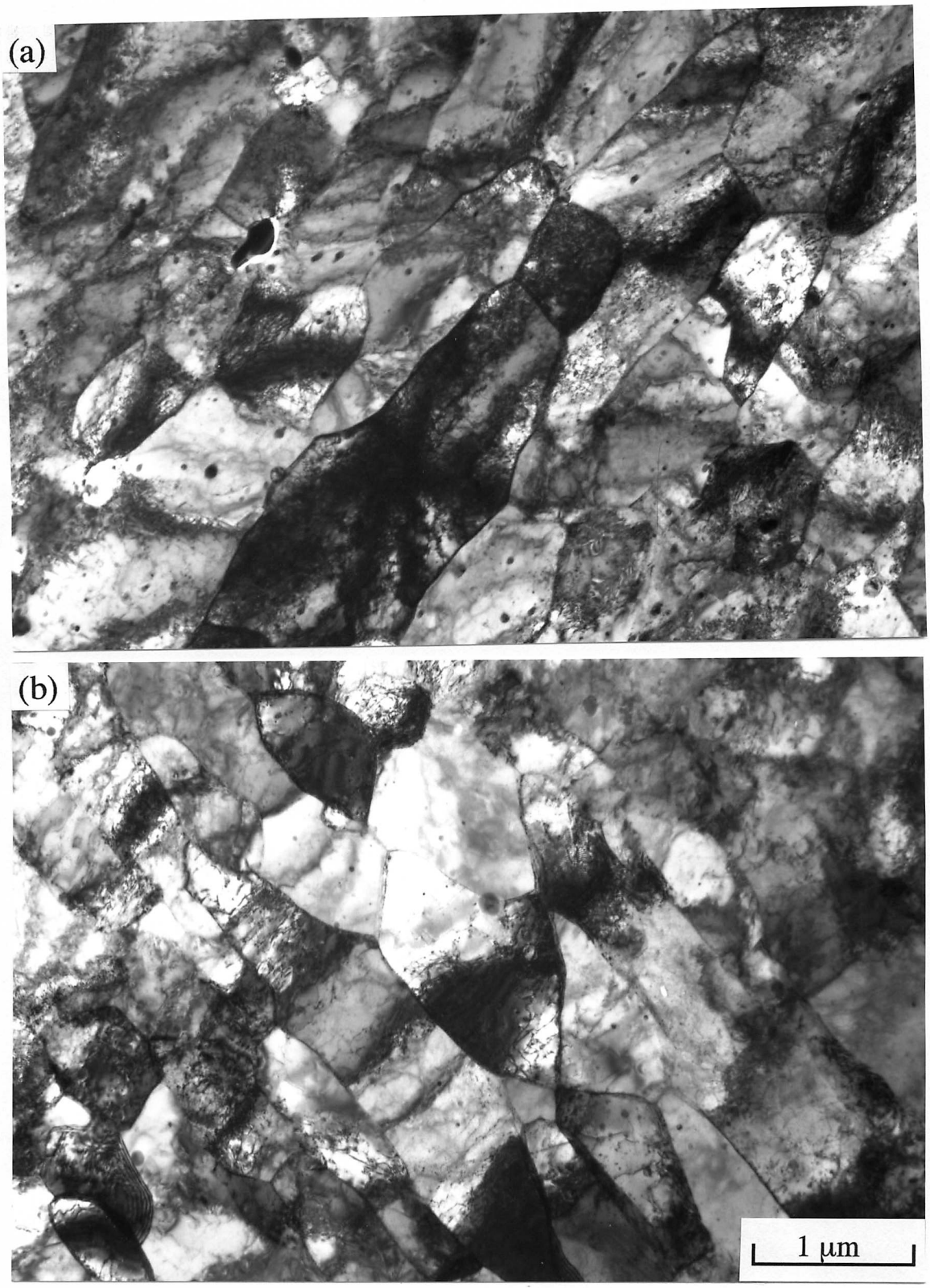

Figure 6.1 Transmission electron micrographs taken from longitudinal sections of alloys (a) *MA956* and (b) *MA957*. The samples are in the as–received condition, identical to those used for field ion microscopy.

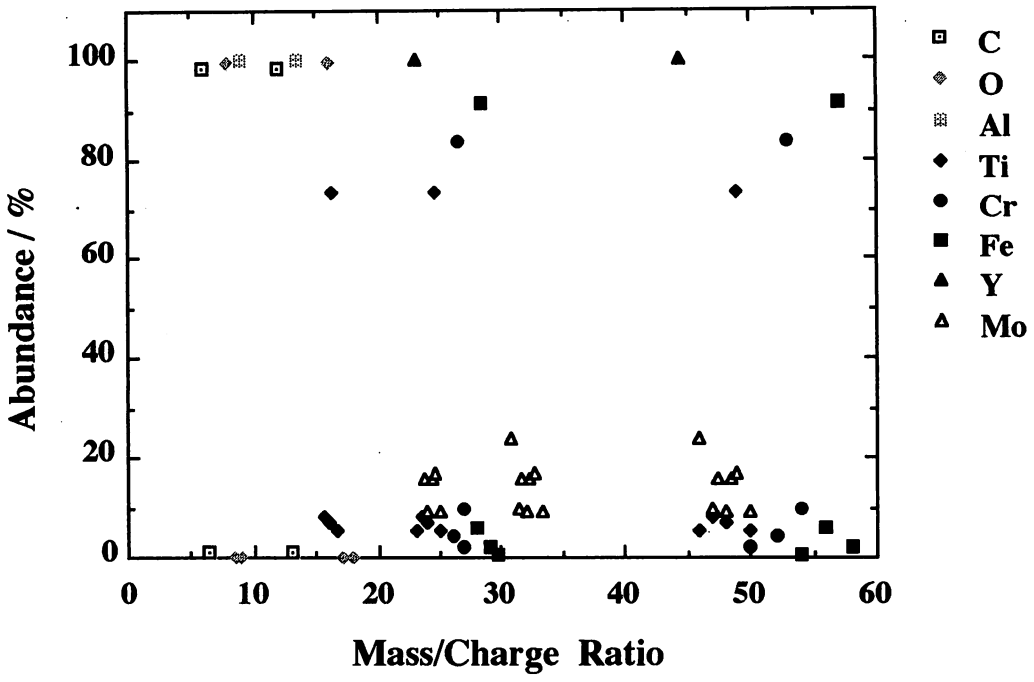

Figure 6.2: The natural abundance of various ionised species of relevance to the present work.

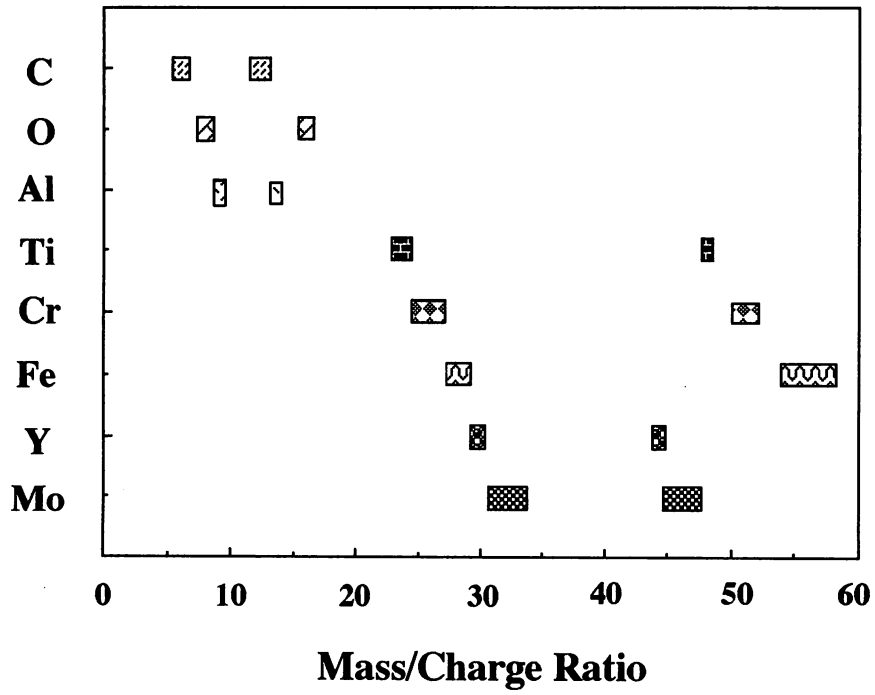

Figure 6.3: The range file used in the analysis of the atom probe data, after neglecting those species which have a relatively low abundance.

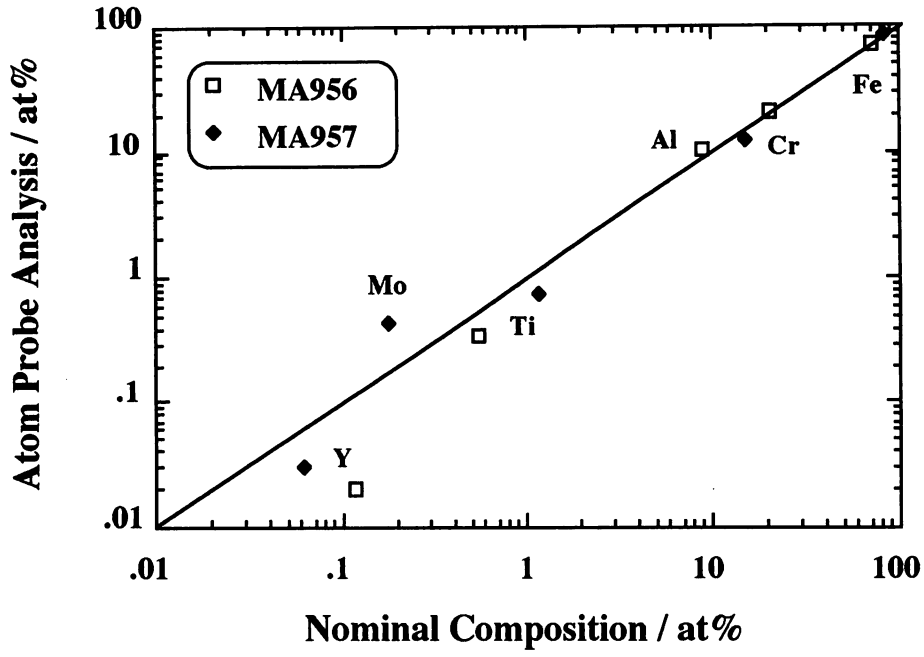

Figure 6.4: The agreement between the measured and actual bulk compositions of the alloys studied.

expected in a chemically homogeneous solid solution, and hence to comment on the true atomic state of the solution produced by the mechanical alloying of commercial steels.

The equilibrium fluctuations discussed above cannot usually be observed directly because of the lack of spatial resolution and noise in the usual microanalysis techniques. The fluctuations only become prominent when the resolution of chemical analysis falls to less than about a thousand atoms block. The atom probe technique used here collects the experimental data on an atom by atom basis (*i.e.* the highest conceivable spatial resolution). The analysis also contains no error of the type associated with X–ray emissions where the same area when analysed twice will in general give different results because of the stochastic nature of X–ray emissions.

Composition profiles are an important method of analysis in Atom–Probe technique. However, several factors have to be taken into consideration to prevent a misleading interpretation of the data. An important consideration is to select a suitable block size. If the block size is too large then not only will the amplitude of the composition fluctuation be attenuated but also spurious periodicities may be introduced. To avoid this phenomenon, it is usually advisable to run the data through a series of different block sizes to ensure the validity of the information.

The optimum number of atoms in each data point for displaying composition profiles usually ranges from 50 to 200 atoms (Miller and Smith, 1989). It was found that a block size with 50 atoms cluster gave reliable results.

Fig. 6.5 illustrates the variation in the chromium concentration (fifty atom blocks) of the ferrite in *MA956* and *MA957*. Similar data for aluminium in *MA956* are presented in Fig. 6.6. There are real fluctuations, therefore further analysis is carried out to show whether they are beyond what is expected in a homogeneous solution.

The statistical fluctuations mentioned above are given by the standard deviation (Blavette *et al.*, 1986):

$$\sigma_d = \sqrt{C_o(1 - C_o)/N} \tag{6.1}$$

where C_o is the concentration and N the number of collected ions per sampling block. Fluctuations in excess of $2\sigma_d$ indicate clustering, with 95% confidence (Blavette *et al.*, 1986). Figs. 6.5 and 6.6 show that the fluctuations in concentration are always below the $2\sigma_d$ value.

6.3.3 Frequency–Distributions

The frequency distribution is obtained by plotting the total number of composition blocks with a given number of atoms of a specified element B against the concentration. Each atom in a block is assumed to be drawn from a population such that the probability of a B atom is p. For a random solution, the distribution of concentrations should be binomial.

Furthermore, the distribution of χ^2 value is needed to make a more precise judgment of the significance of any differences between the observed frequency and binomial distribution. The chi-squared variable (χ^2) is given by (Miller *et al.*, 1981):

$$\sum \frac{(o_i - e_i)^2}{e_i} \tag{6.2}$$

where o_i is the observed frequency of blocks of a specified element and e_i is the expected number estimated from the binomial distribution.

Any significant deviations from the binomial distribution would indicate either the clustering of like atoms or the ordering of unlike pairs. For a true deviation from the binomial distribution, the statistic χ^2 will be large.

Figs. 6.7–6.9 show that the experimental distributions are essentially identical to the calculated binomial distributions, indicating that the solution is random. Table 6.2 shows the χ^2 values, which also indicate the absence of clustering.

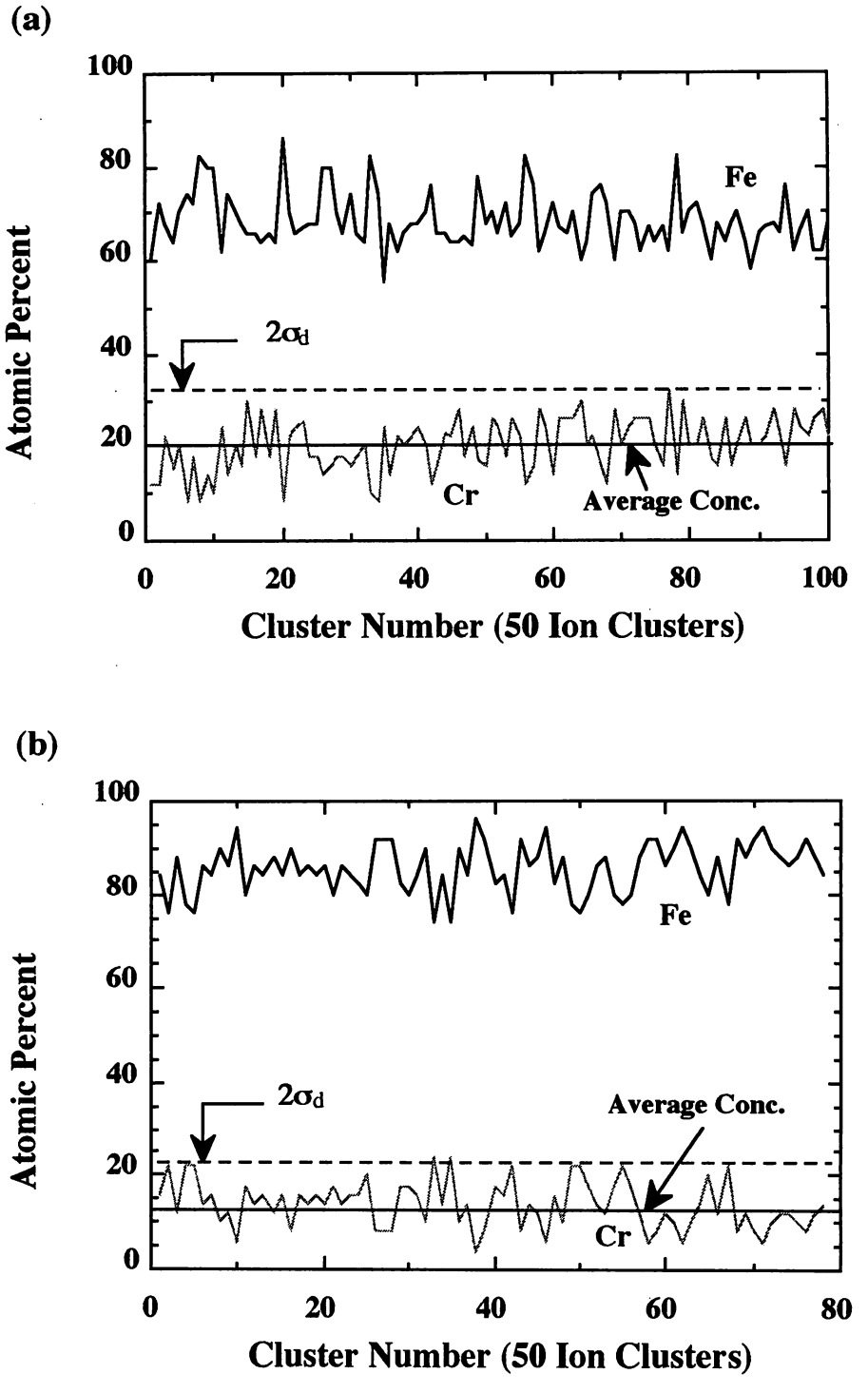

Figure 6.5 The composition profiles of chromium as a function of depth, in as-received *MA956* and *MA957* steels.

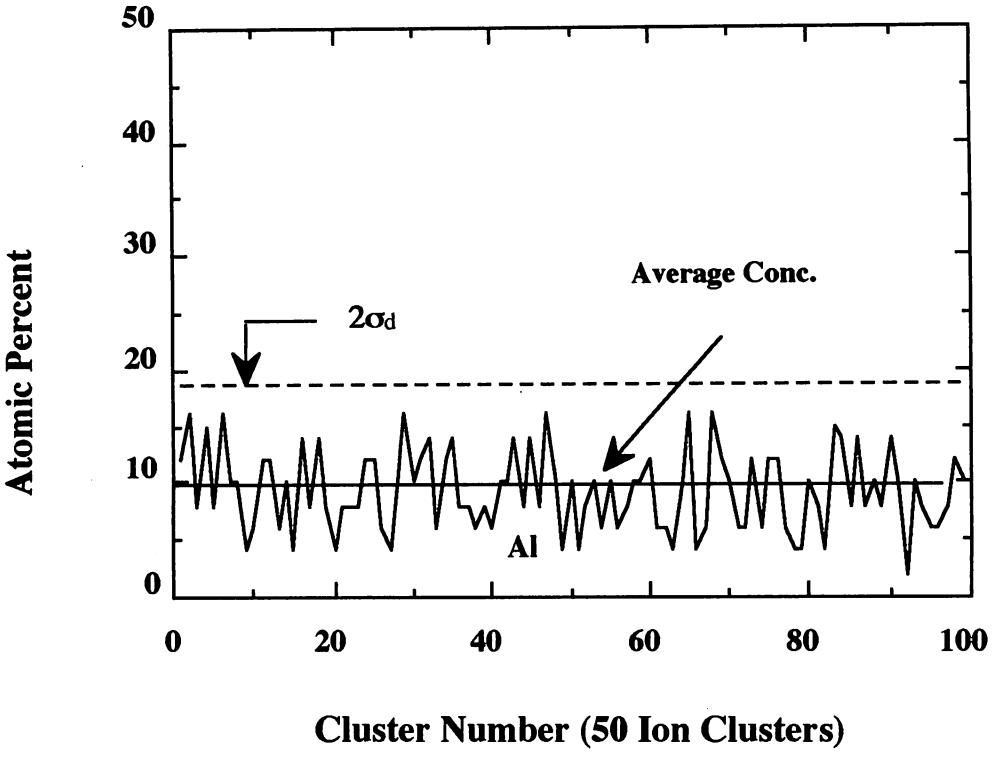

Figure 6.6 The composition profiles of aluminium as a function of depth, in as-received *MA956* steel.

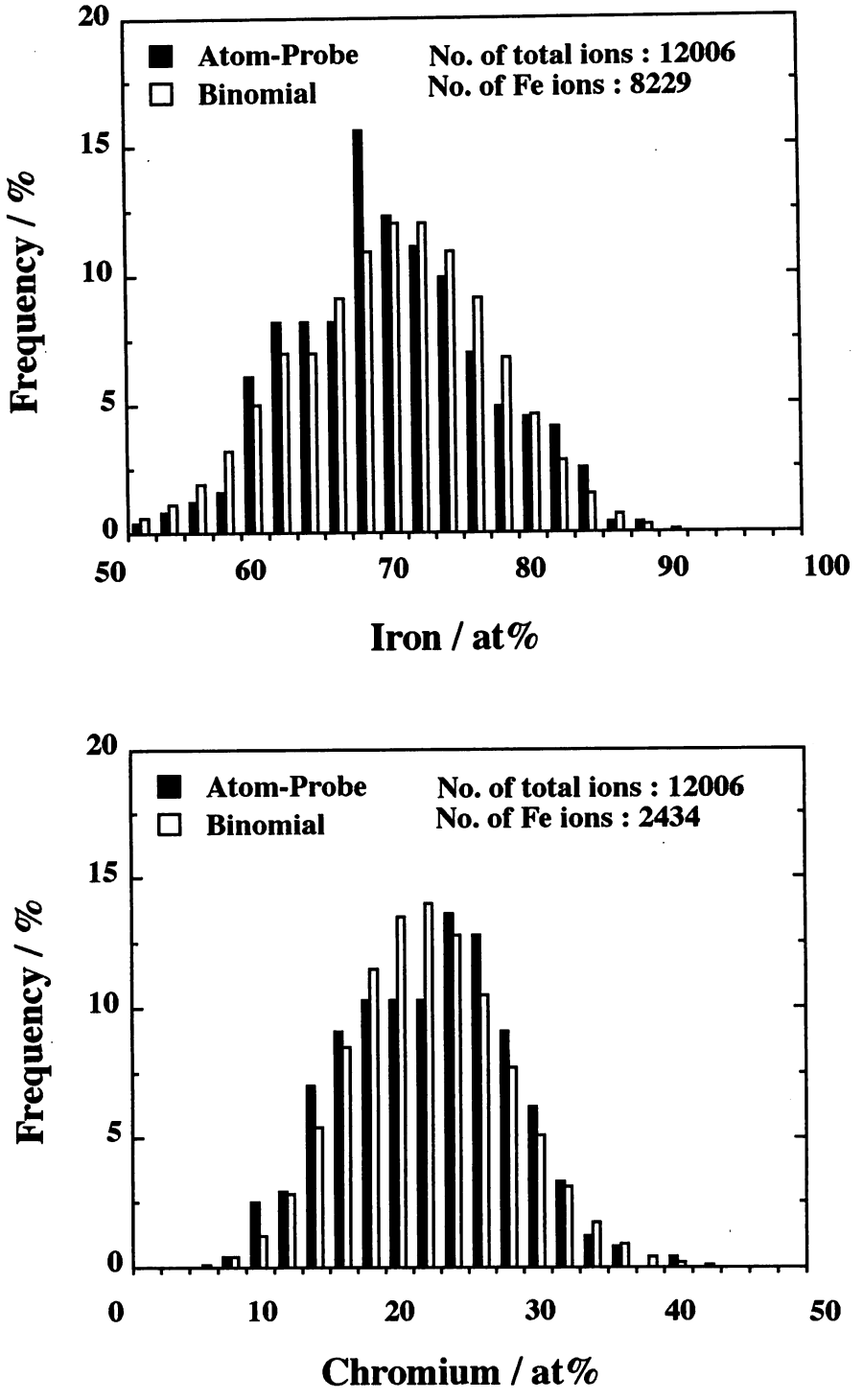

Figure 6.7 Frequency–distribution curves for Fe and Cr in as–received MA956 steel.

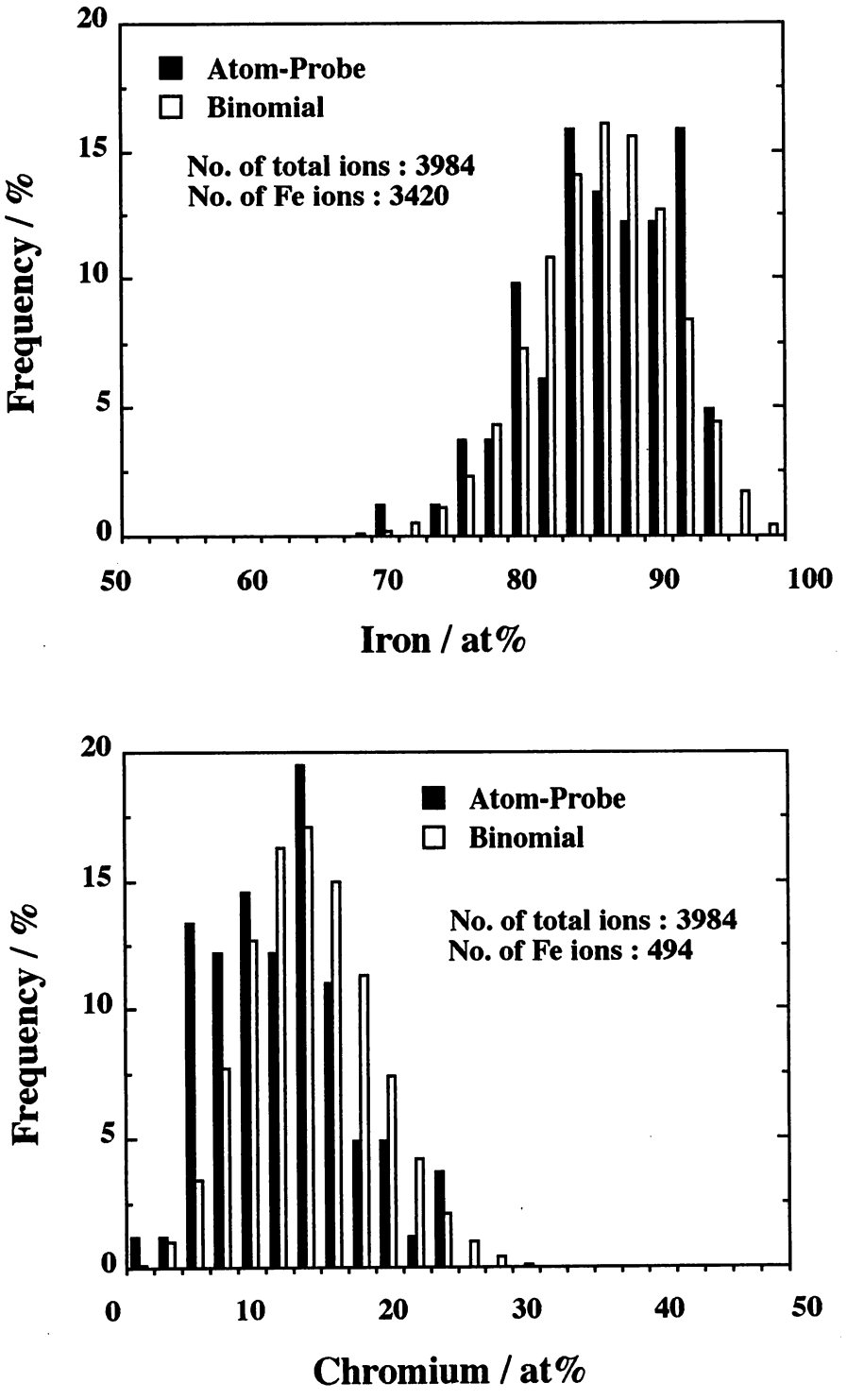

Figure 6.8 Frequency–distribution curves for Fe and Cr in as–received *MA957* steel.

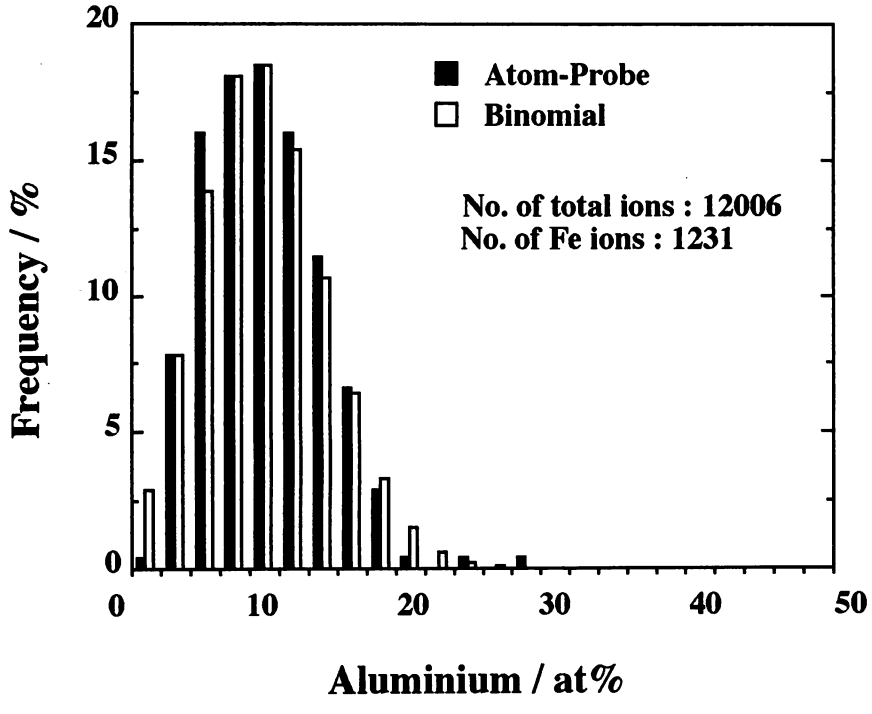

Figure 6.9 Frequency–distribution curves for aluminium in as–received *MA956* steel.

Alloy	Element	χ^2	Significance
MA956	Cr	10.64	no significance
MA956	Al	1.166	no significance
MA957	Cr	13.25	no significance

Table 6.2 Analysis on the distribution of solute species in as-received MA steels compared with the binominal distribution.

6.3.4 Pair Probabilities

The atom probe data can be analysed further if it is assumed that successive atoms picked up by the mass spectrometer were near neighbour atoms in the sample. Successive atoms which are identical then represent bonds between like atoms *etc.*, so that pair probabilities used in solid solution theory can be measured experimentally. These data can be compared against calculated pair probabilities. Thus, in a *random* $A-B$ solution, the probability p_{AB} of finding $A-B$ or $B-A$ bonds (near neighbours) is given by $p_{AB} = 2x_A x_B$ where x_i is the atom fraction of element i. Similarly, $p_{AA} = x_A^2$ and $p_{BB} = x_B^2$. B is the solute element (such as Cr or Al) whereas A represents the remainder of atoms. N represents the total number of atoms

included in the analysis. The calculations assume a random solution. Table 6.3 shows clearly that the experimentally measured pair probabilities agree remarkably with those calculated assuming a random solution.

Alloy	Element	p_{AA}	p_{AB}	p_{BB}	N
MA956	Cr (Measured)	0.636	0.323	0.041	12006
MA956	Cr (Calculated)	0.637	0.322	0.041	
MA956	Al (Measured)	0.806	0.184	0.010	12006
MA956	Al (Calculated)	0.832	0.161	0.008	
MA957	Cr (Measured)	0.767	0.217	0.015	3984
MA957	Cr (Calculated)	0.724	0.254	0.022	

Table 6.3 Pair probability analysis. B is the solute element (such as Cr or Al) whereas A represents the remainder of atoms. N represents the total number of atoms included in the analysis. The calculations assume a random solution.

6.3.5 Field Ion Microscopy

It is generally accepted that the directional recrystallisation that occurs on annealing a mechanically alloyed nickel–base alloy is a secondary recrystallisation process. The ultrafine-grained equiaxed microstructure produced by primary recrystallisation during fabrication is replaced by a much coarser columnar grain structure (Evans and Martin, 1992). It is often assumed that this scenario also represents iron–base mechanical alloys, but recent evidence suggests otherwise (Chapter 5). It appears that fabrication leaves these alloys in a cold deformed state, so that subsequent annealing leads to primary recrystallisation to a coarse columnar grain structure (Baloch, 1989). Consistent with this, transmission electron microscopy has revealed a large dislocation density within the flattened fine grains of the fabricated alloy.

The present work confirms that the prior to the formation of the coarse recrystallised grain structure the alloy is in fact in the cold deformed state. Field ion microscopy has revealed a fine dislocation cell structure (Fig. 6.10) on the scale of some 30 nm cell size. The small crystallographic misorientation across the cell boundaries are revealed by the approximate continuity of the rings of imaged atoms across the cell walls.

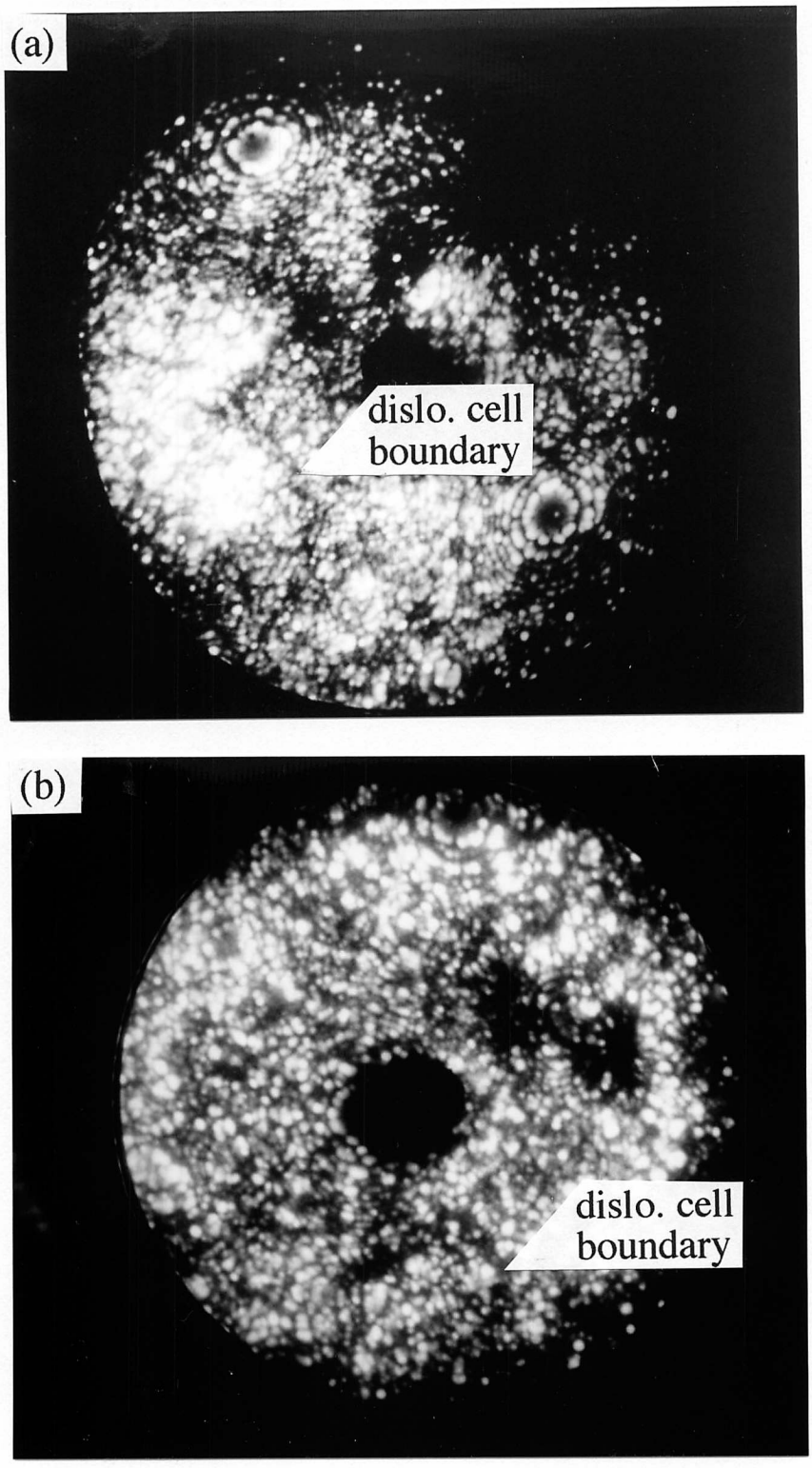

Figure 6.10 Field ion micrograph of as–received *MA956* and *MA957* steels. The sample temperature is 26 K and the tip voltage about 10 kV.

6.4 SUMMARY & CONCLUSIONS

The process of mechanical alloying involves the formation of solid solutions by the intense deformation of mixtures of different powders. It can therefore force atoms into positions where they may not prefer to be under equilibrium conditions. In this work the atomic structure of two mechanically alloyed steels with the commercial designation *MA956* and *MA957* was investigated in the unrecrystallised state using the technique of field-ion microscopy and atom probe analysis, which permits the determination of both microstructure and chemistry with an atomic resolution.

It is found that there is a very fine dislocation cell structure(on the scale of about 30 nm) in the alloys prior to recrystallisation heat treatments. This is consistent with our earlier microstructural and thermodynamic data that the alloys are in a cold-deformed state after mechanical alloying, extrusion and/or hot-rolling. This is in contrast to the mechanically alloyed nickel-base superalloys which have consistently been found to be in a primary recrystallised state following extrusion.

Analysis of atom-by-atom data suggests that the solid solutions of *MA956* and *MA957* are random in that the frequency distributions, and pair probabilities can be calculated simply from the alloy chemistry. This is unexpected, since thermodynamic data suggested that, for example, that the iron and chromium atoms prefer to be in the vicinity of like atoms (Miller, 1988; Uemori *et al.*, 1988)). Thus, it can be concluded that the alloy is in a mechanically homogenised nonequilibrium state, and that prolonged annealing at low temperatures should lead to, for example, the clustering of chromium atoms. This should be the subject of a future study.

CHAPTER SEVEN

DYNAMIC RECRYSTALLISATION IN HOT-DEFORMED OXIDE DISPERSION STRENGTHENED *MA956* & *MA957* STEELS

7.1 INTRODUCTION

The mechanically alloyed steels which are the subject of this thesis have an unusually fine scale microstructure in the as–received condition. It was therefore considered worthwhile to investigate their high temperature deformation behaviour, with the hope of revealing any anisotropy with respect to the extrusion direction. The experiments were conducted well below the ordinary recrystallisation temperature, but unexpectedly revealed a dynamic recrystallisation behaviour with several interesting additional features.

7.2 EXPERIMENTAL PROCEDURE

Compression tests were employed to evaluate the hot-deformation behaviour of as-received *MA956* and *MA957* steels, both of which were obtained as 25 mm diameter bars. The samples for the compression experiments were cut from the longitudinal and transverse directions and were machined into 8 mm diameter by 12 mm length cylinders. The experiments were carried out in an adapted *Thermecmaster Z* thermomechanical simulator. The specimens were heated by induction, with a measured temperature variation along the length direction of only ± 5 °C. The uniaxial compressive load was applied *via* quartz discs. Test temperatures were selected at 950, 1000 and 1050 °C, with a 50% total reduction strain and 0.01 s^{-1} constant strain rate control.

Both optical microscopy and transmission electron microscopy were used to observe the deformed microstructures. Hardness was measured after hot deformation.

7.3 RESULTS AND DISCUSSION

7.3.1 Hot-Deformed Microstructures

Figures 7.1 – 7.3 show the optical micrographs of hot-deformed *MA956* steel, with the compression axis parallel or normal to the rolling direction for temperatures ranging from 950 to 1050 °C. In spite of these relatively low temperatures, elongated grain structures can

be seen in all the samples. Furthermore, the elongated grains always occur with their long axes along the rolling direction, irrespective of the orientation of the compression direction. It also appears that the fraction of recrystallised microstructure increases with increasing hot deformation temperature. The samples deformed along the rolling direction recrystallise more readily.

Figures 7.4 – 7.6 illustrate similar observations for hot-deformed *MA957* steel. The recrystallised grains tend to be coarser in *MA957* compared with *MA956*, consistent with the usual recrystallisation microstructures of these alloys. *MA956* was found to recrystallise more easily than *MA957* during hot deformation; this might be expected since *MA956* steel has a lower recrystallisation temperature in normal circumstances.

7.3.2 Hot-Deformation Behaviour

Figures 7.7 – 7.9 illustrate the stress–strain curves from *MA956* samples compressed along the rolling direction and normal to the rolling direction for a variety of temperatures. The stress does not increase monotonically with strain, in spite of the increase in cross-sectional area during the compression test, so that the work hardening characteristics usually observed are not found for the as–received alloys. Instead, softening occurs during hot deformation. This is due to dynamic recrystallisation during deformation, as is evident from the metallographic observations (Figures 7.1 – 7.6). It is noteworthy that the sort of stress–strain curves reported here are similar to those found during the hot–rolling of steel sheet where dynamic recrystallisation is common (McQueen and Jonas, 1975).

To further analyse the data, the critical strain ϵ_c for the start of recrystallisation, and the strain ϵ_x equivalent to that required to recrystallise a significant fraction of the material for each test temperature (compressed along the rolling direction) are given in Table 7.1.

According to Rossard (1973), ϵ_c should be slightly less than the peak strain ϵ_p because, while the first nuclei are softening the material locally, the remaining material continues to get stronger by work hardening. ϵ_c is given by the approximate relation (McQueen *et al.*, 1975) :

$$\epsilon_c \simeq 5\epsilon_p/6 \simeq 0.83\epsilon_p \tag{7.1}$$

However, the critical strain for dynamic recrystallisation may not in fact be attained for a variety of reasons. For example, the material could continue to strain harden, developing higher and higher flow stress, until failure occurs. The definition of ϵ_x is therefore useful, as the strain from the peak position to that at which the stress reaches a minimum in case of cyclically dynamic recrystallisation, and from the peak position to that the stress reaches a

Compressed along the rolling direction

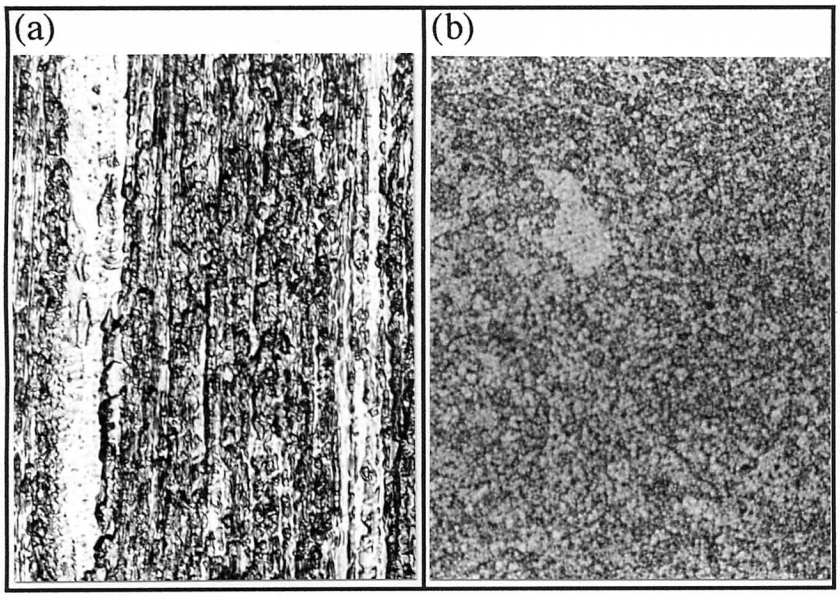

Sampling configurations

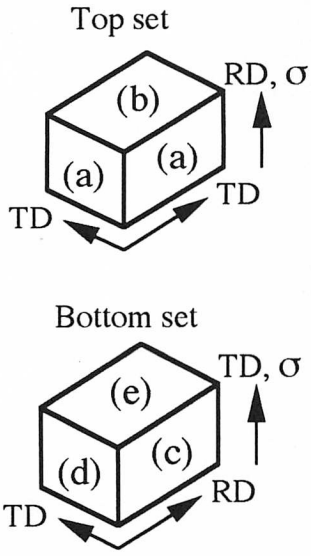

Compressed normal to the rolling direction

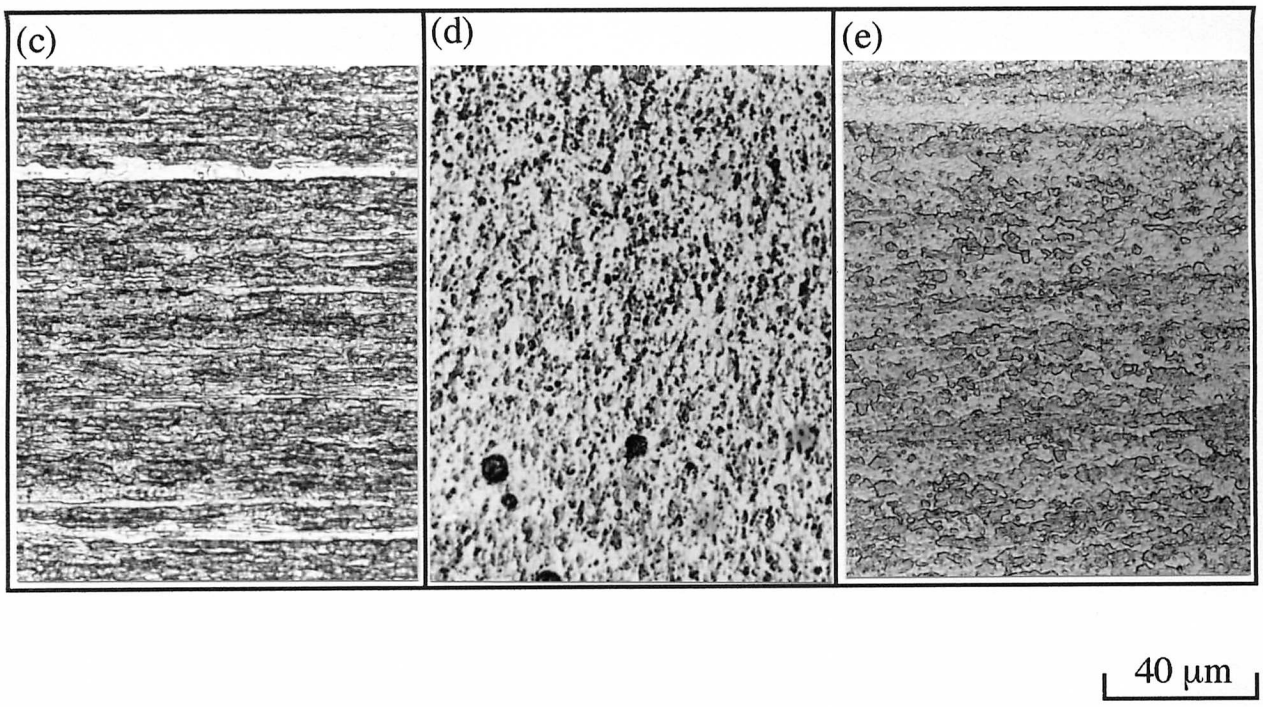

Figure 7.1: Set of micrographs illustrating the hot-deformed microstructures of *MA956* steel compressed at 950 °C.

Compressed along the rolling direction

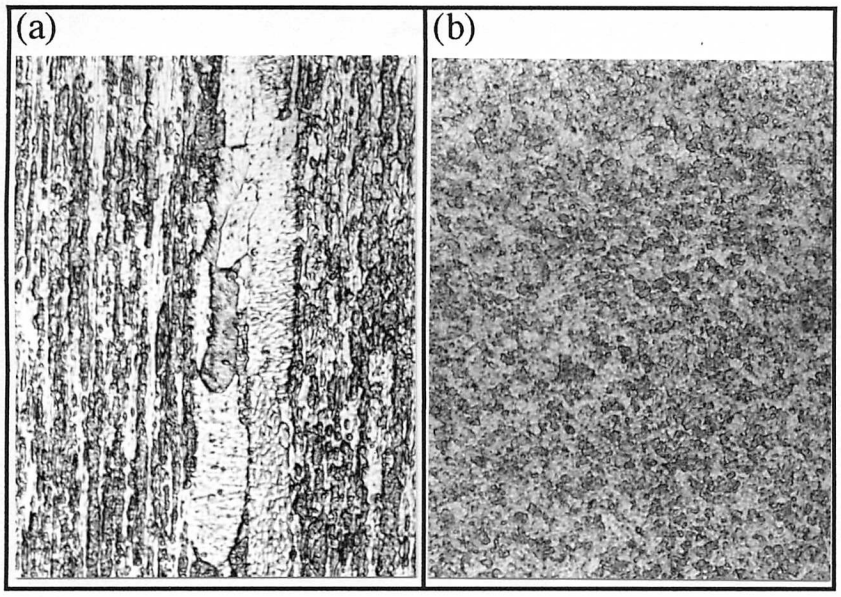

Sampling configurations

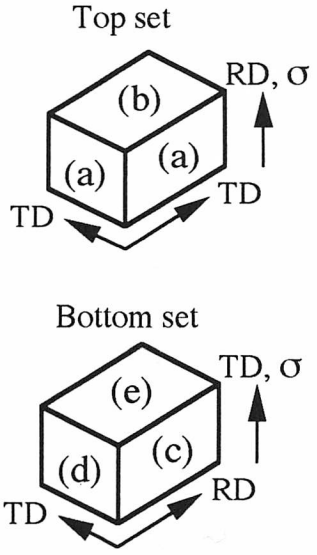

Compressed normal to the rolling direction

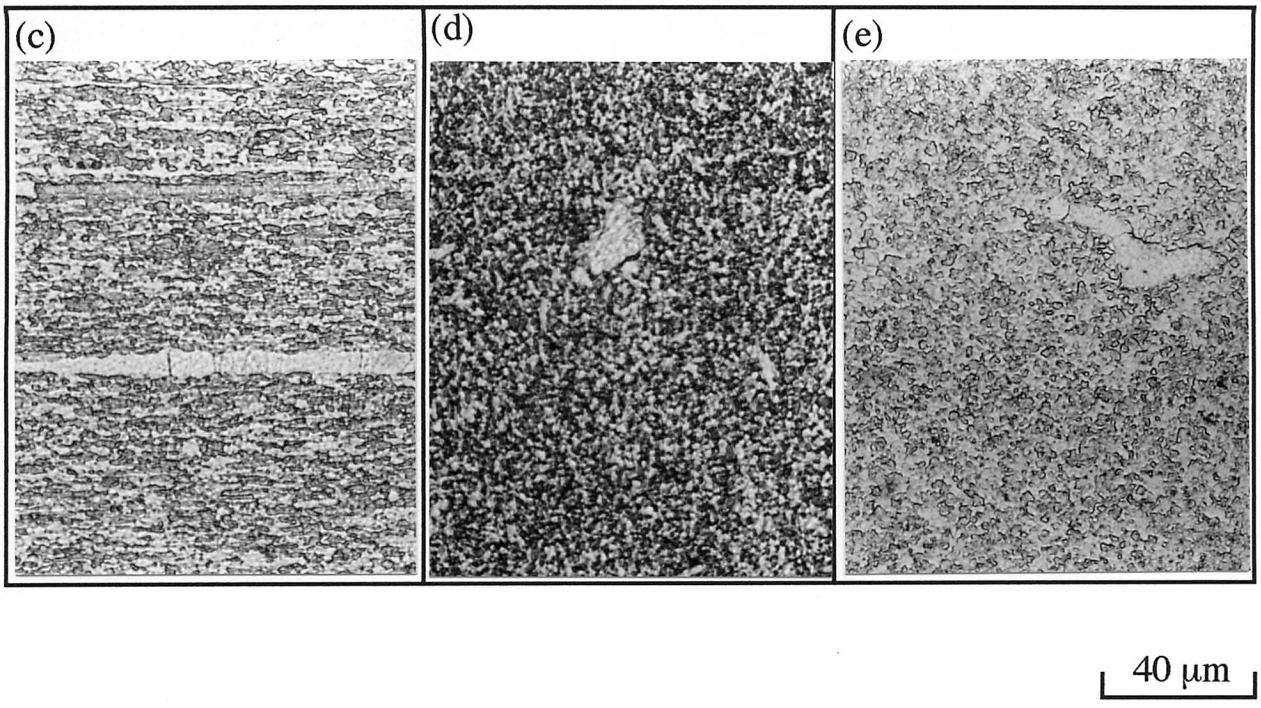

Figure 7.2: Set of micrographs illustrating the hot-deformed microstructures of *MA956* steel compressed at 1000 °C.

Compressed along the rolling direction

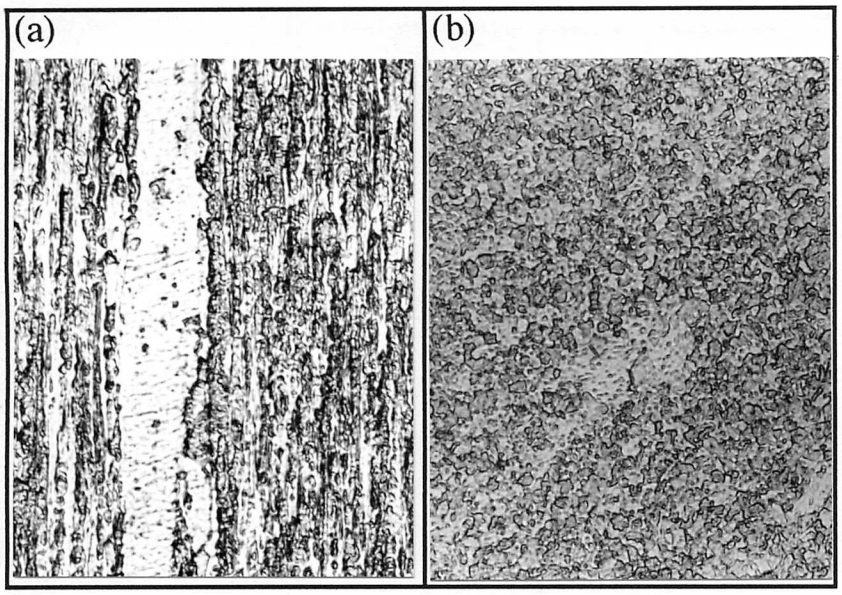

Sampling configurations

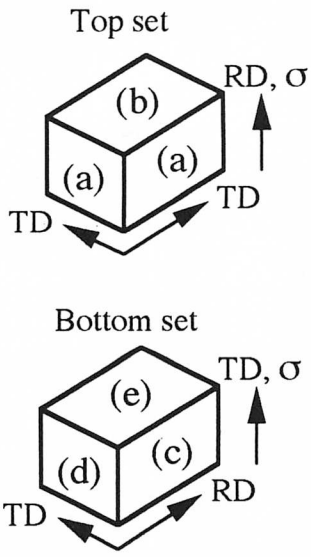

Compressed normal to the rolling direction

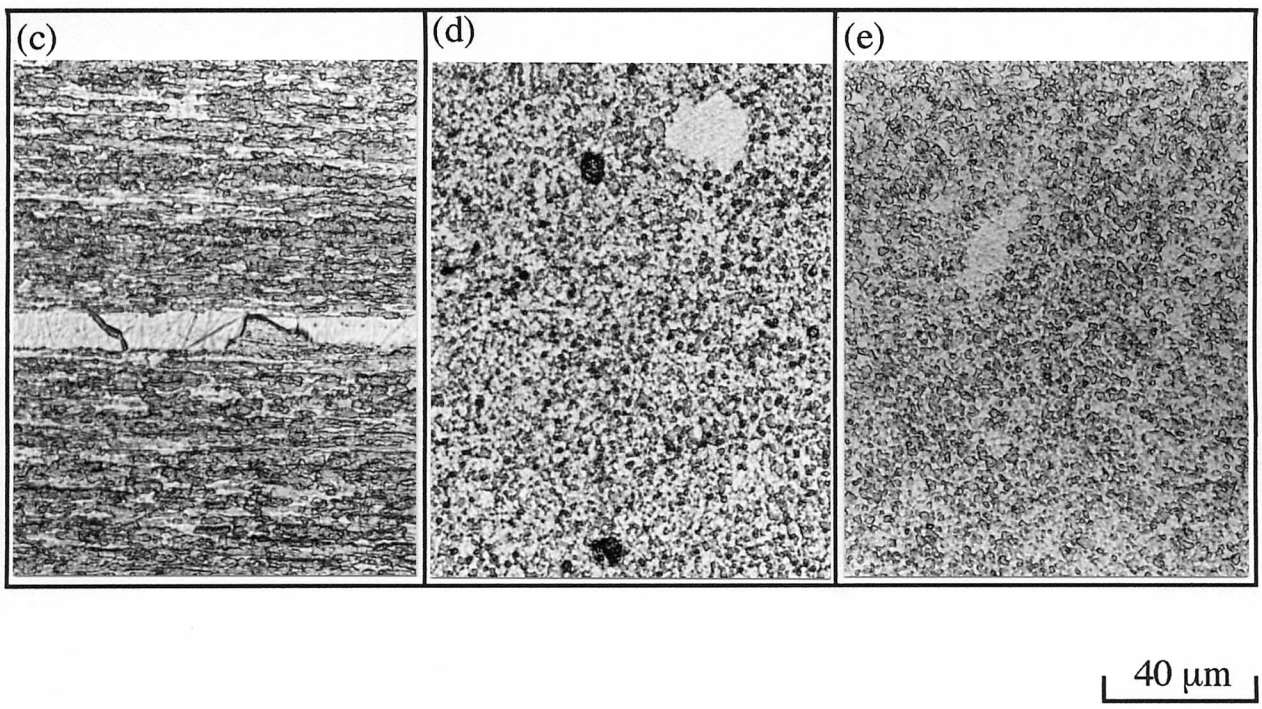

Figure 7.3: Set of micrographs illustrating the hot-deformed microstructures of *MA956* steel compressed at 1050 °C.

Compressed along the rolling direction

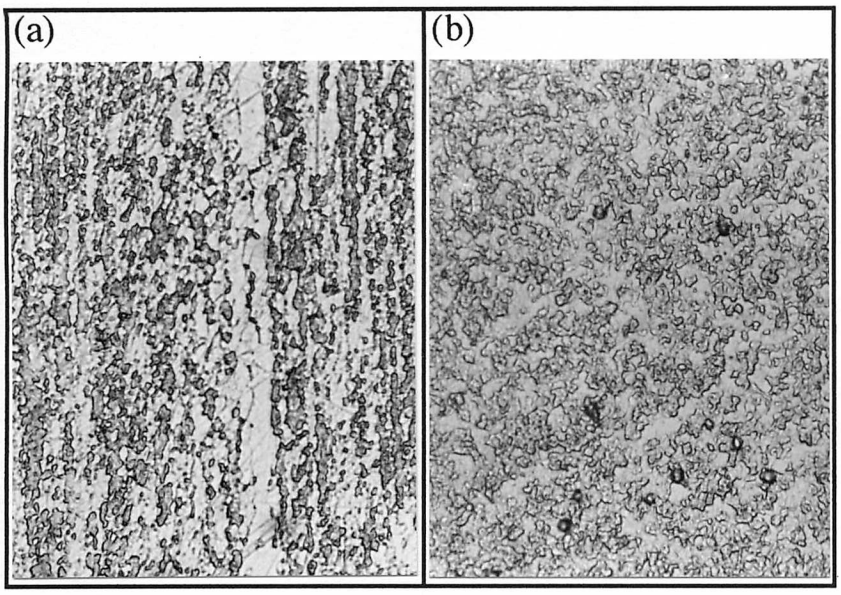

Sampling configurations

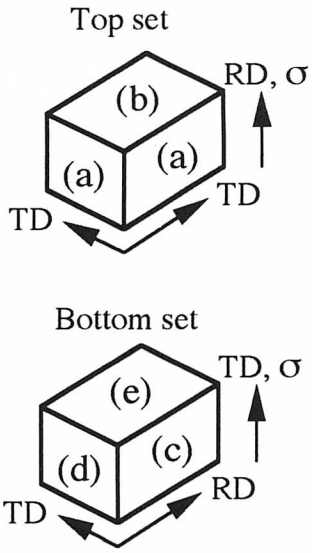

Compressed normal to the rolling direction

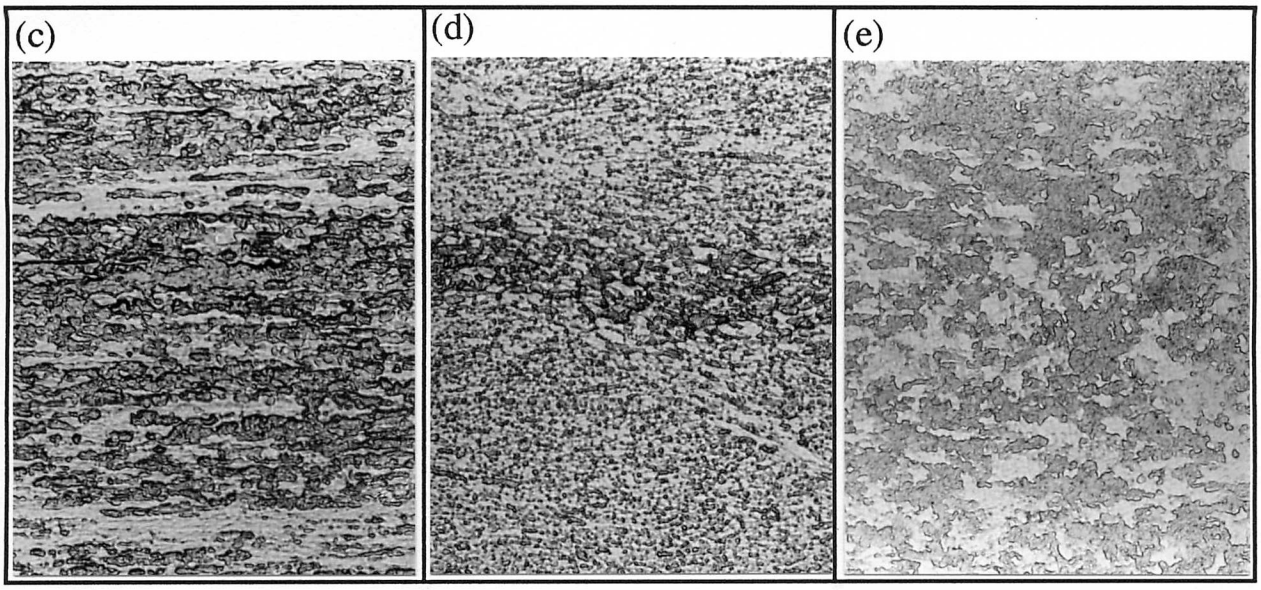

40 μm

Figure 7.4: Set of micrographs illustrating the hot-deformed microstructures of *MA957* steel compressed at 950 °C.

Compressed along the rolling direction

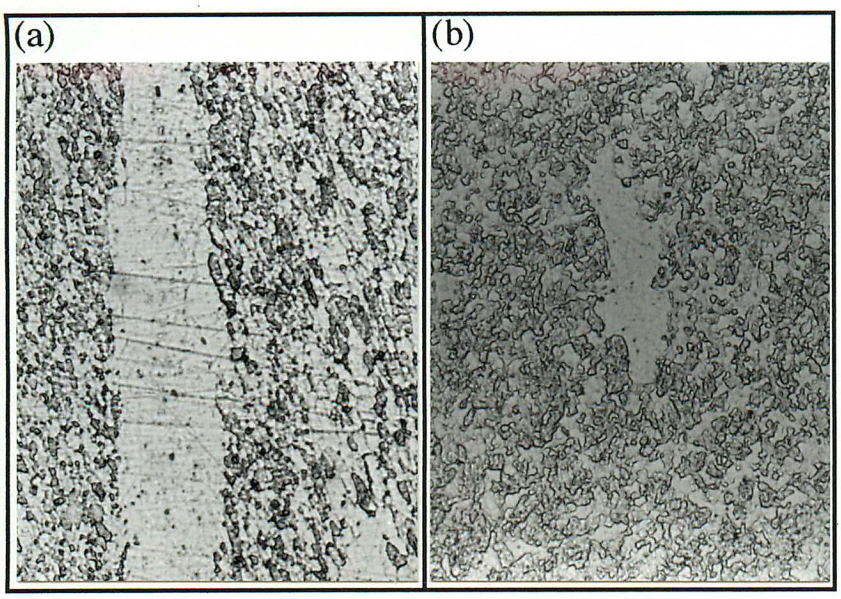

Sampling configurations

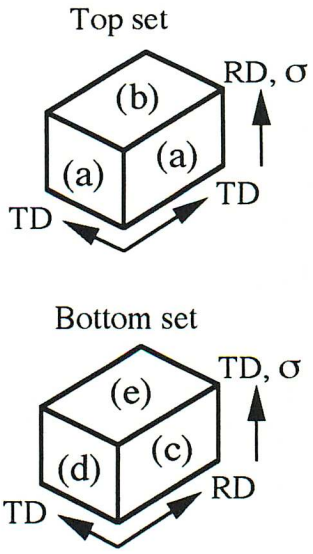

Compressed normal to the rolling direction

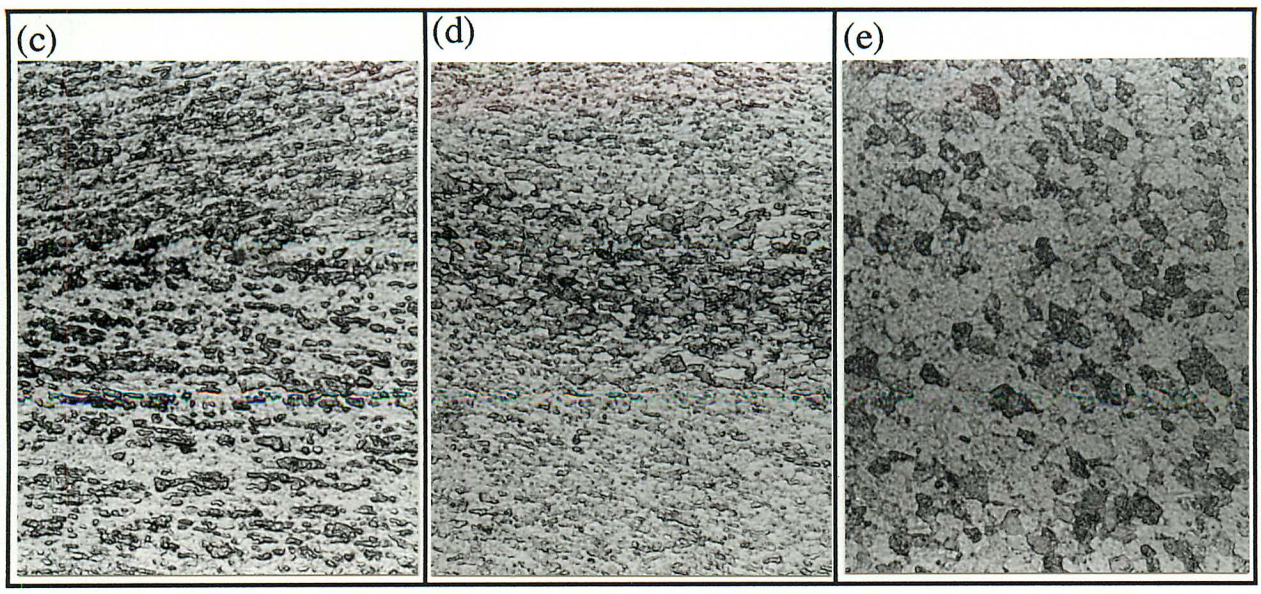

40 μm

Figure 7.5: Set of micrographs illustrating the hot-deformed microstructures of *MA957* steel compressed at 1000 °C.

Compressed along the rolling direction

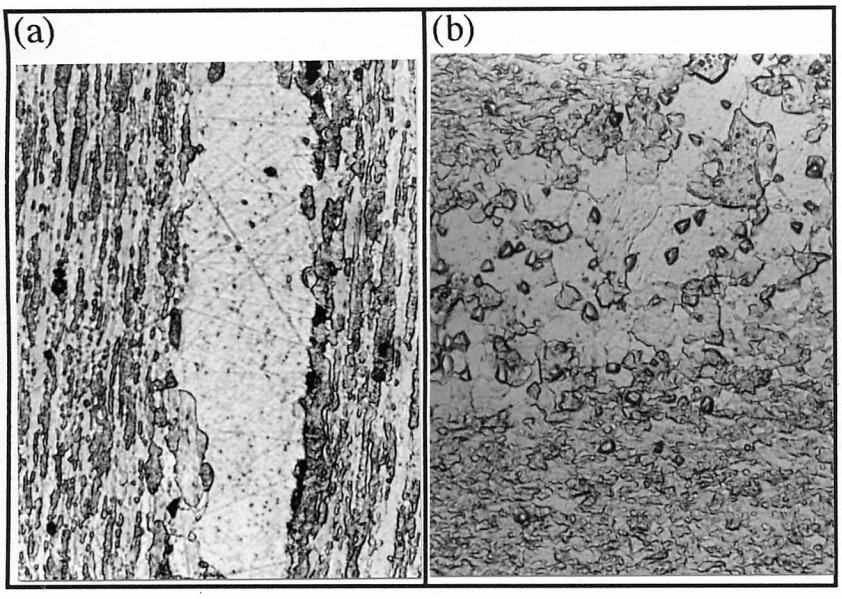

Sampling configurations

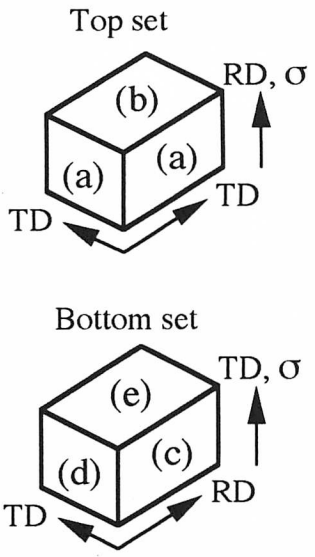

Compressed normal to the rolling direction

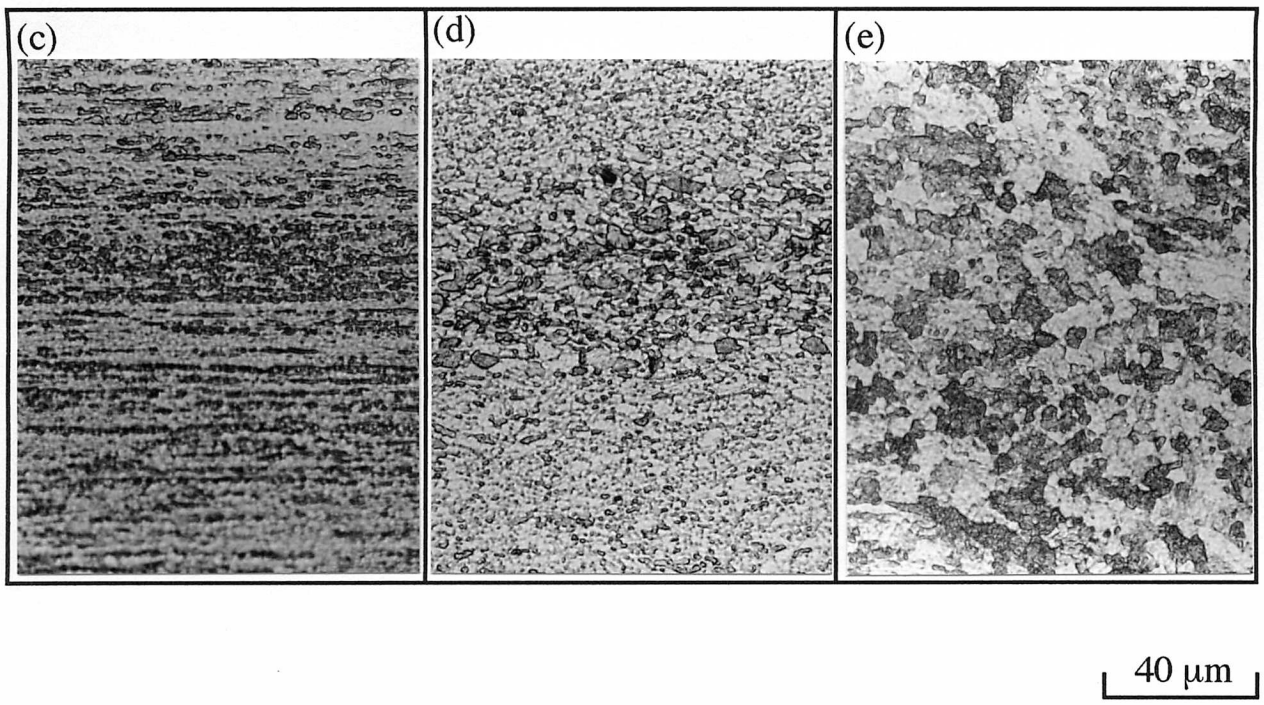

Figure 7.6: Set of micrographs illustrating the hot-deformed microstructures of *MA957* steel compressed at 1050 °C.

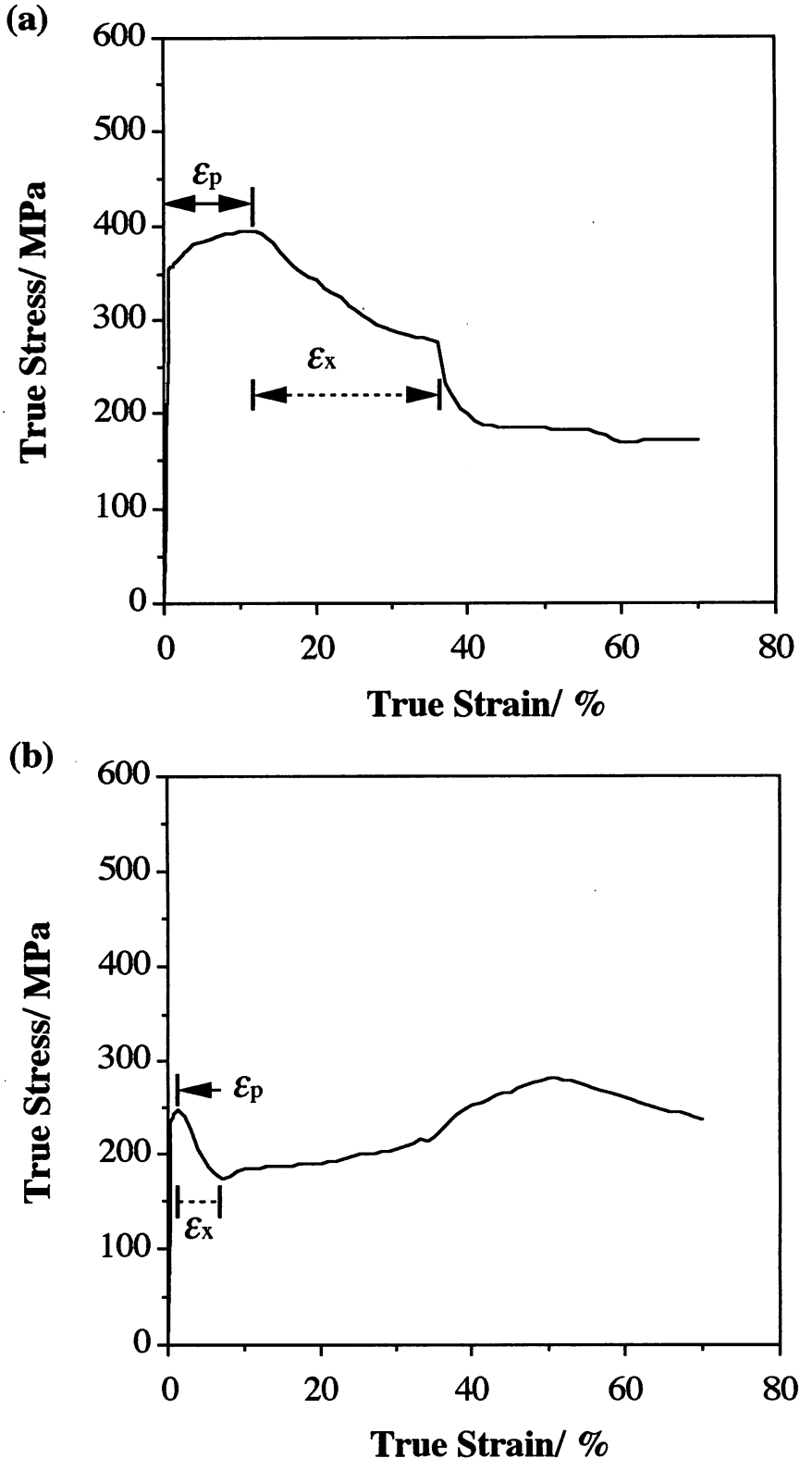

Figure 7.7: Stress–strain curves for *MA956* as deformed at 950 °C, (a) compressed along the rolling direction, (b) compressed normal to the rolling direction.

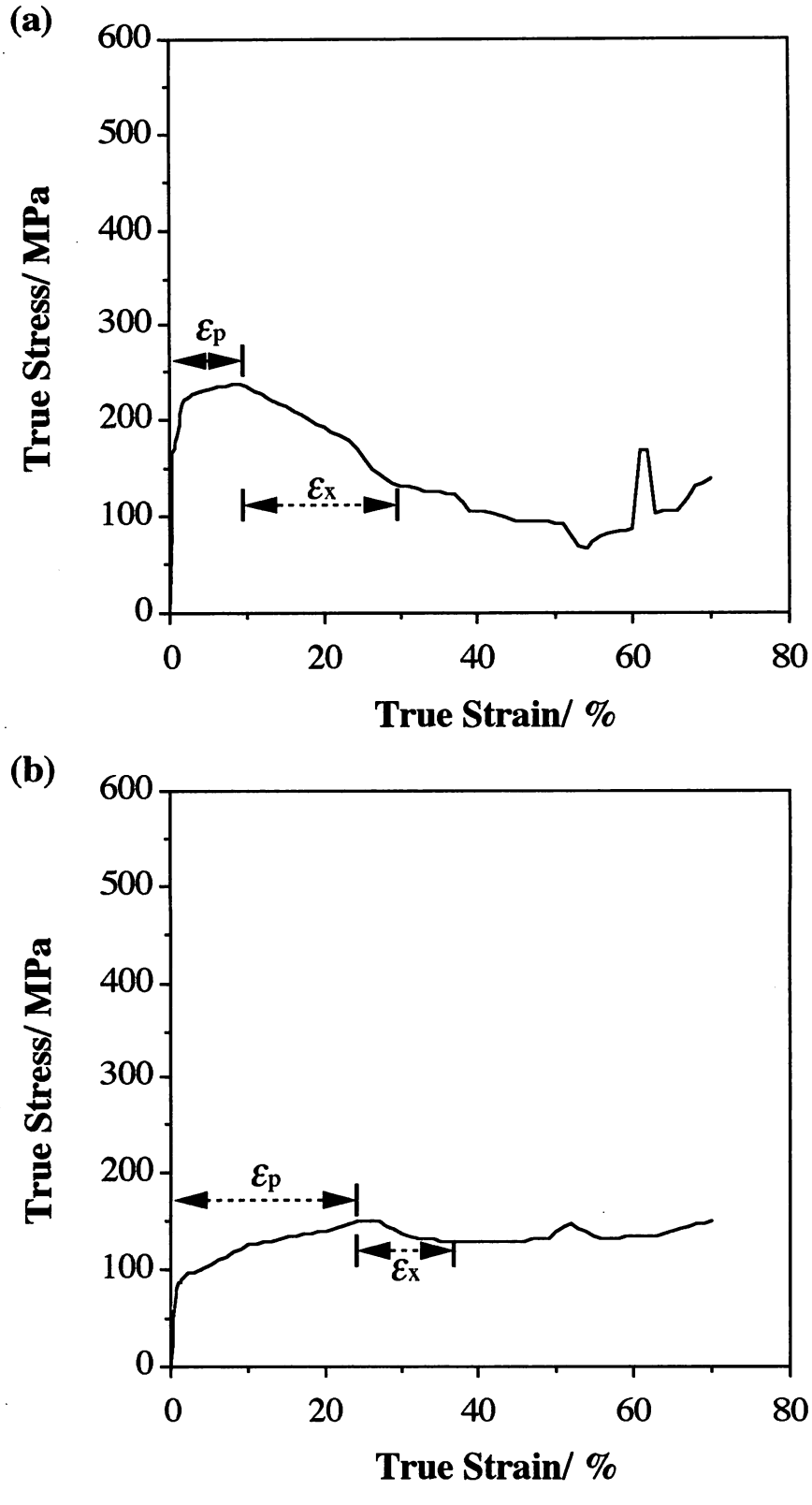

Figure 7.8: Stress–strain curves for *MA956* as deformed at 1000 °C, (a) compressed along the rolling direction, (b) compressed normal to the rolling direction.

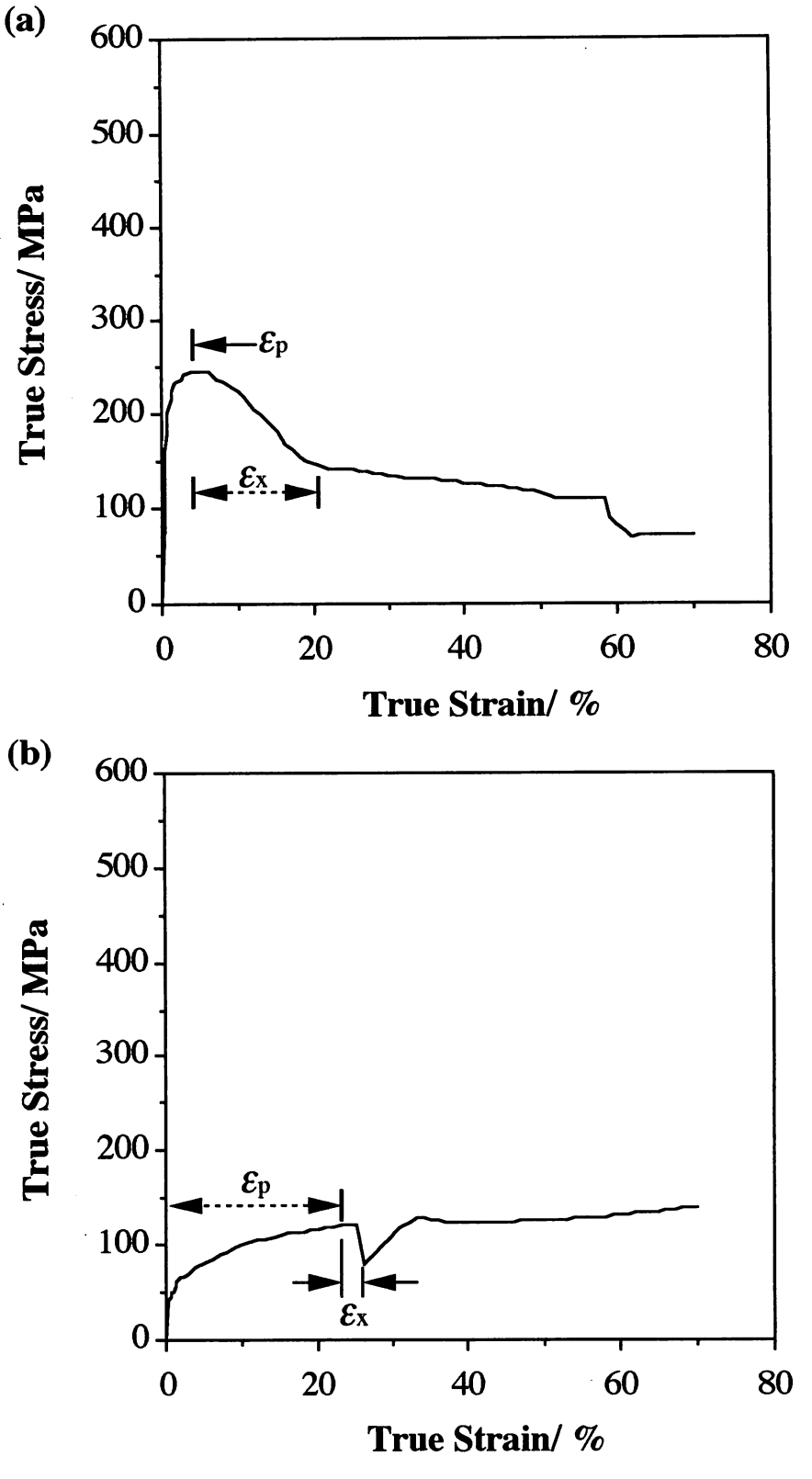

Figure 7.9: Stress–strain curves for *MA956* as deformed at 1050 °C, (a) compressed along the rolling direction, (b) compressed normal to the rolling direction.

Deformation Temperature, °C	ϵ_p	ϵ_c	ϵ_x
950	0.12	0.10	0.28
1000	0.10	0.08	0.20
1050	0.04	0.03	0.16

Table 7.1 The critical strain ϵ_c, peak strain ϵ_p and ϵ_x required to recrystallise a significant fraction of the material for dynamic recrystallisation. *MA956* hot compressed along rolling direction.

minimum or approximately a steady state in case of continuous softening (Glover and Sellars, 1973; Courtney, 1990).

In general, the critical strain ϵ_c for recrystallisation increases with the strain rate and with decreasing deformation temperature (Luton and Sellars, 1969). Consistent with this, the results in Table 7.1 show that ϵ_c and ϵ_x both decrease with increasing hot-deformation temperature. Recrystallisation at lower temperatures requires a longer time to complete, so that the observed trend in ϵ_x is also reasonable.

Similar changes in ϵ_c and ϵ_x with the deformation temperature were found for deformation normal to the rolling direction, except the sample deformed at 950 °C (Table 7.2). The reason for this discrepancy is unclear but Figure 7.7b shows an unusual deformation curve with a large "yield drop".

Deformation Temperature, °C	ϵ_p	ϵ_c	ϵ_x
950	0.024	0.020	0.046
1000	0.240	0.200	0.130
1050	0.220	0.183	0.045

Table 7.2 The critical strain ϵ_c, peak strain ϵ_p and ϵ_x required to recrystallise a significant fraction of the material for dynamic recrystallisation. *MA956* hot compressed normal to rolling direction.

From Figures 7.7 – 7.9, it seems that there shows two-stages of dynamic recrystallisation for *MA956* hot compressed both along the rolling direction and normal to the rolling direction. It is suspected that this nonuniformity of the recrystallisation behaviour is related to corresponding

heterogeneities in the dispersoid distributions.

The investigation of hot-deformed *MA957* steel was carried out under the same conditions as *MA956*. However, due to the poor workability of this steel, serious cracking was generated during hot-deformation. Hence, complete stress–strain curves could not be obtained. Instead, partial stress–strain curves recorded for *MA957* are shown in Figures 7.10 – 7.12 from the samples compressed along the rolling direction, and normal to the rolling direction, for a variety of temperatures. There is an obvious decrease of stress with increasing compression strain due to the dynamic recrystallisation, as shown in Figure 7.11a and 7.12a. In addition, the strength decreases with increasing temperature. The monotonous decrease in stress as a function of strain is due to the cracking generated during hot-deformation.

Whittenberger (1981) investigated the hot working behaviour of *MA956* and reported that it has a poor ductility in the temperature rage 1144 to 1477 K. It is said that *MA956* deforms *via* a crack nucleation and growth mechanism within this temperature range, eventually leading to sudden fracture. It is demonstrated here that *MA957* has a poor hot workability compared with *MA956*. Consistent with the present work, Alamo *et al.* (1990) reported a higher ductility in *MA956* than *MA957*. The peak value of elongation was in their work found to be at a test temperature of around 650 °C (Alamo *et al.*, 1990).

The yield strength of *MA957* is always found to be higher than that of *MA956* (Table 7.3 and Figure 7.13). Consistent with this, Alamo *et al.* (1990) also reported that *MA957* always has a higher hardness and strength than *MA956*. The results may look strange at first glance. Strengthening factors include grain size effects, second phase particles, dislocations, and solid solution composition (Pickering, 1992). Both *MA956* and *MA957* have the sub-micrometre grains (around 0.3 μm) and high dislocations densities in the as-received state (Chapter 6). However, *MA956* contains a larger yttria and solute concentration. It should therefore be stronger than *MA957*. Nevertheless, the hardness and yield strength of *MA957* are larger, indicating a higher degree of deformation in the microstructure of the as-received state. This is consistent with its larger stored energy. Thus, *MA957* probably lacks ductility relative to *MA956* because of its higher starting strength.

7.3.3 Mechanism for Dynamic Recrystallisation

Static recovery and recrystallisation occur in the absence of applied stress. The adjective "dynamic" on the other hand implies that recovery and recrystallisation processes occur during deformation.

Whether only dynamic recovery, or dynamic recovery and recrystallisation, are observed

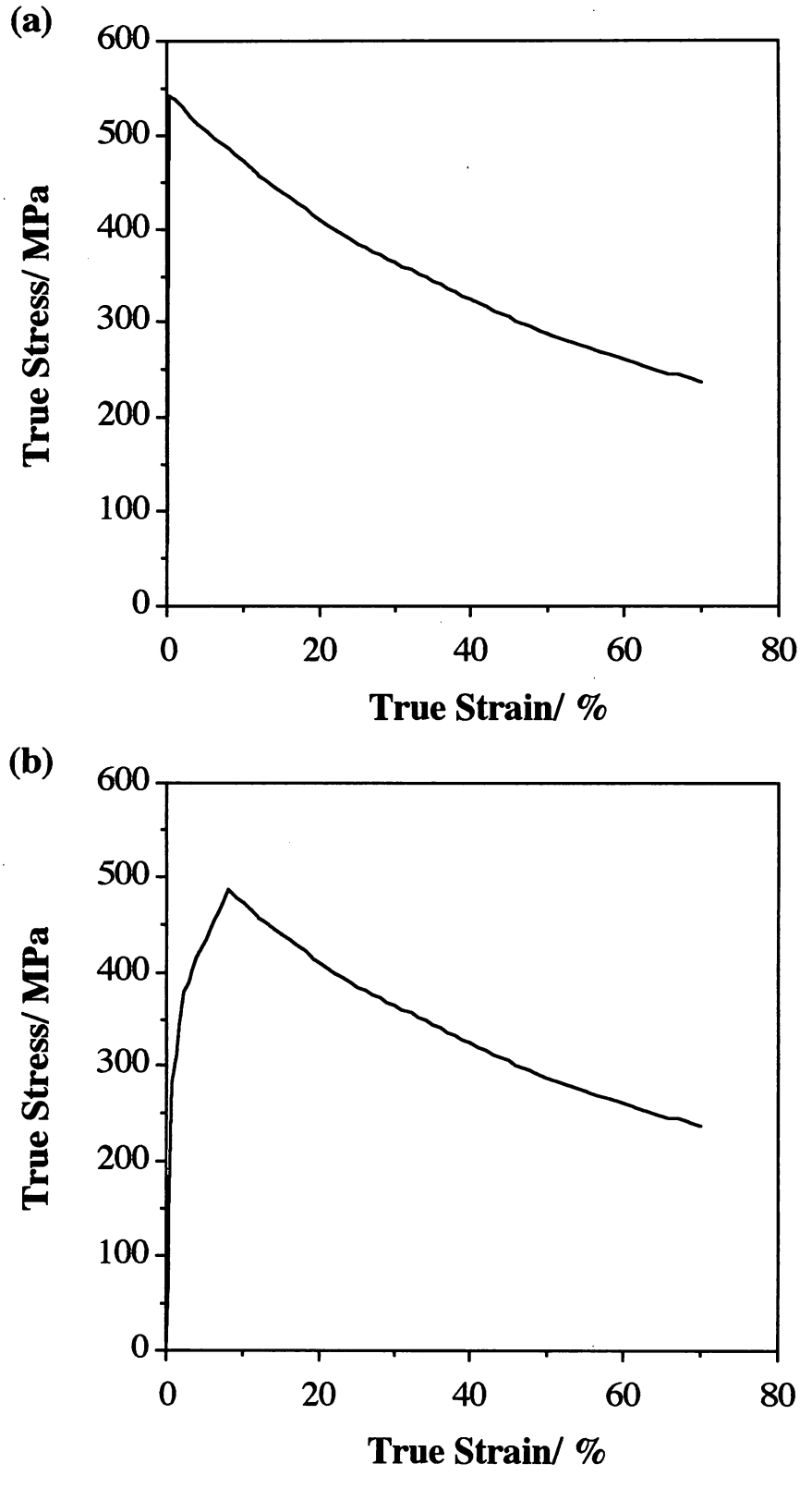

Figure 7.10: Stress–strain curves for *MA957* as deformed at 950 °C, (a) compressed along the rolling direction, (b) compressed normal to the rolling direction.

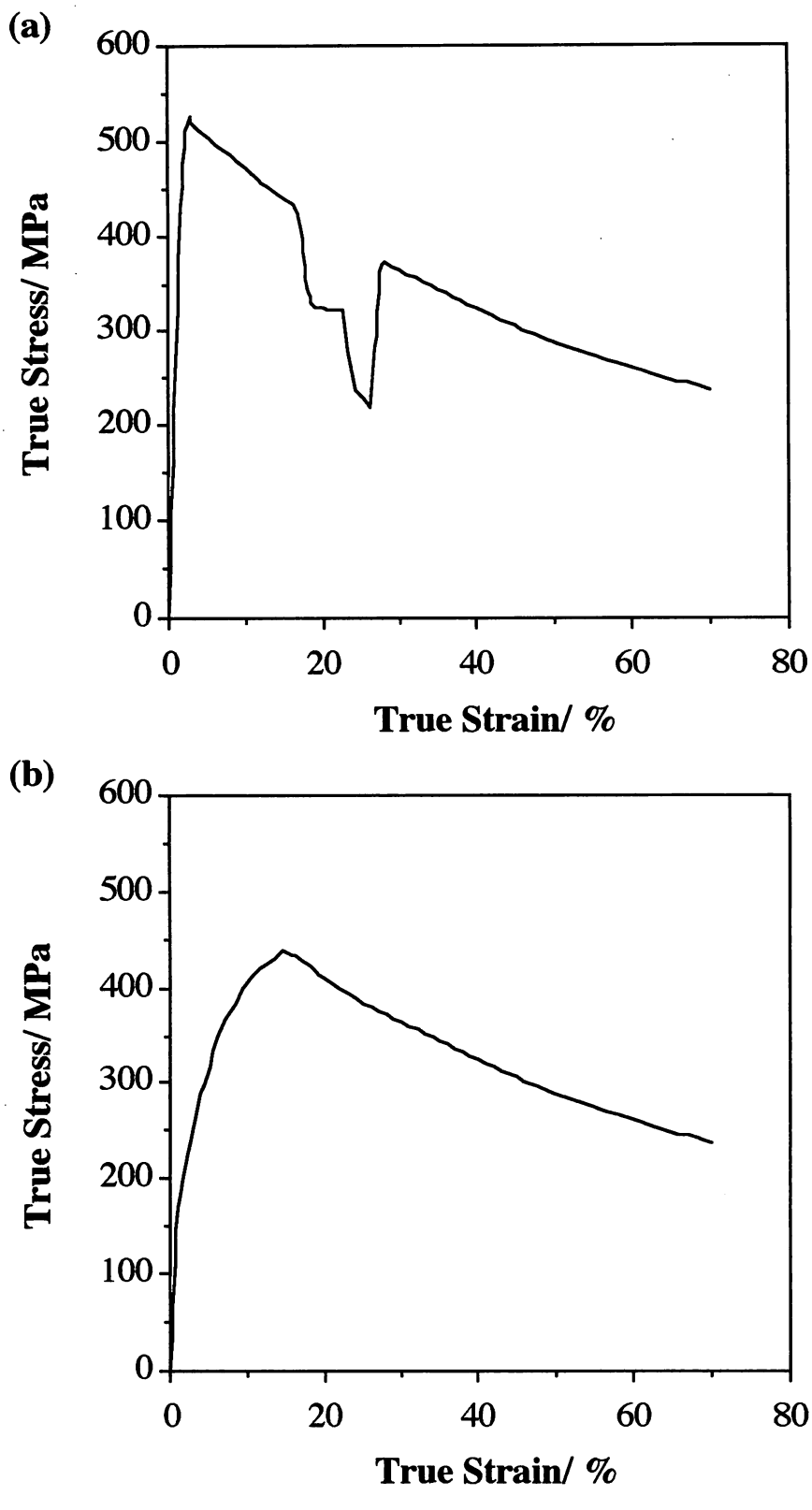

Figure 7.11: Stress–strain curves for *MA957* as deformed at 1000 °C, (a) compressed along the rolling direction, (b) compressed normal to the rolling direction.

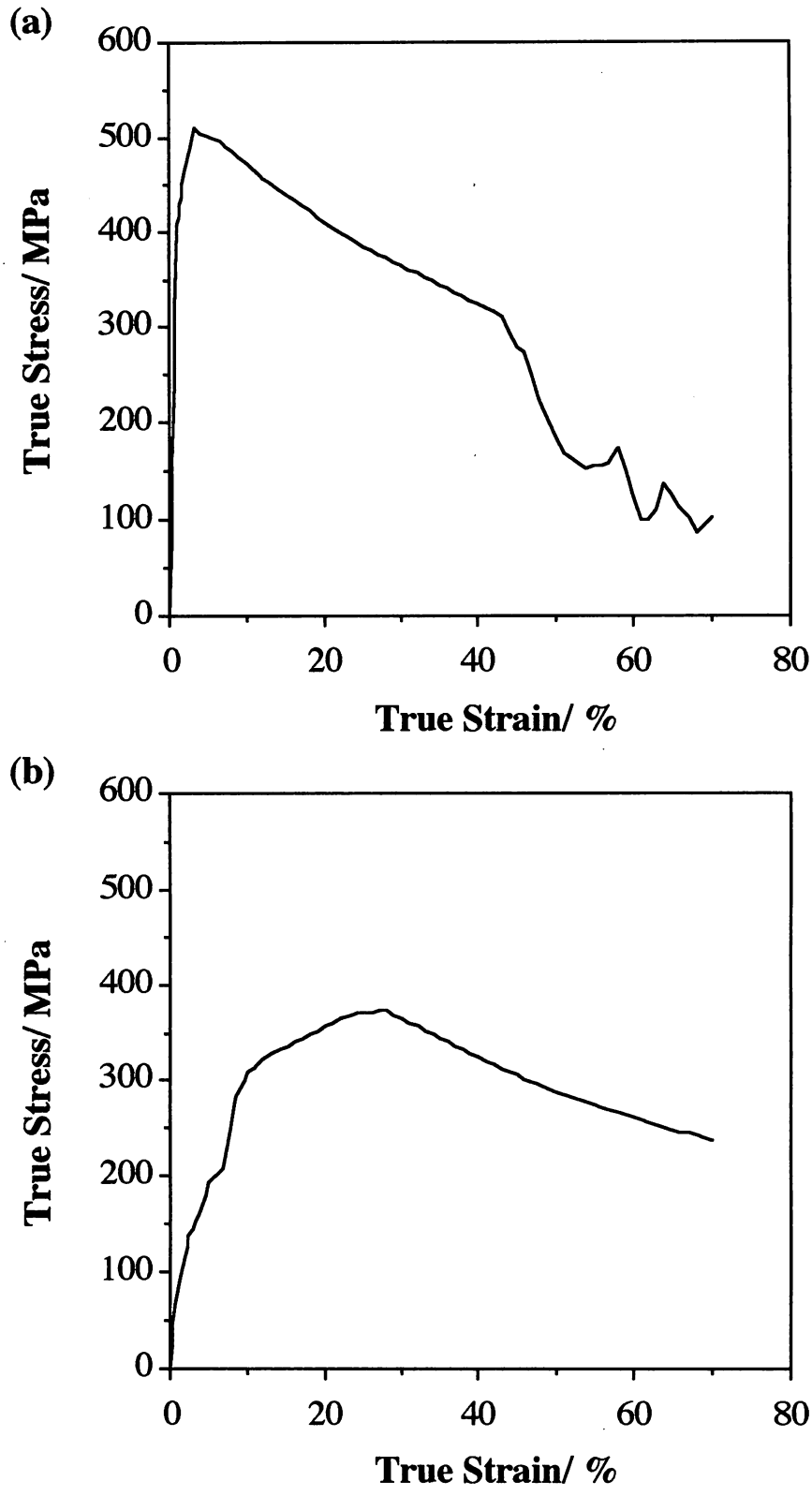

Figure 7.12: Stress–strain curves for *MA957* as deformed at 1050 °C, (a) compressed along the rolling direction, (b) compressed normal to the rolling direction.

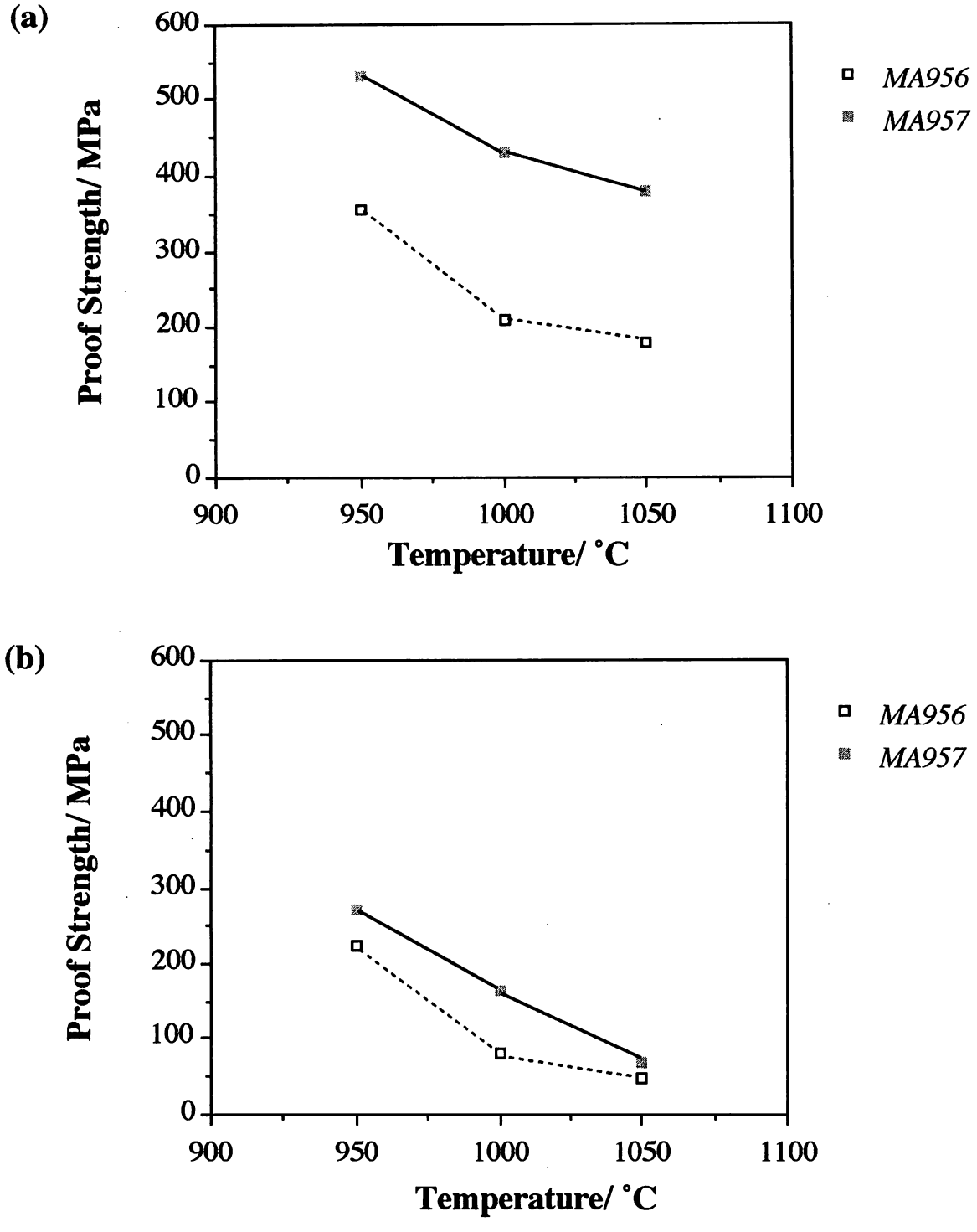

Figure 7.13: Comparison of proof strength (0.2 %) of *MA956* and *MA957* both at ambient temperature and high temperatures, (a) compressed along the rolling direction, (b) compressed normal to the rolling direction.

Alloy	Deformation Temperature, °C		
	950	1000	1050
MA956 RD	355 MPa	208	178
MA956 TD	225	80	48
MA957 RD	>530	430	380
MA957 TD	273	165	70

Table 7.3 The proof strength (0.2 % of offset) of hot compressed *MA956* and *MA957* steels. RD: compressed along rolling direction, TD: compression axis normal to rolling direction.

during hot working depends on the stresses and the strain rates involved. Larger strains give a greater tendency for recrystallisation. Materials that do not dynamically recrystallise exhibit rapid recovery rates, and thus a dislocation density and configuration sufficient to nucleate and drive the recrystallisation process is not developed. This includes materials with a high stacking fault energy (SFE) such as Al, ferritic-Fe, and Zr. By contrast, those materials with low SFE tend to dynamically recrystallise more readily. Thus, nickel and its alloys, austenitic iron, copper and brass recrystallise dynamically (Courtney, 1990).

The present results indicate that the ferritic steels undergo dynamic recrystallisation, and this might be considered inconsistent with the general trends discussed above. However, mechanically alloyed steels contain an incredible amount of stored energy, the key parameter which determines whether or not dynamic recrystallisation should occur. The softening evident in the as-deformed hardness data is also consistent with dynamic recrystallisation (Figures 7.14 – 7.15). It is noted that *MA957* has always a higher hardness than *MA956* both in as-received and deformed state. However, there is no significant difference in the hardness data for the two test orientations (c.f. Figure 7.15 and 7.16), because a hardness indent involves a three-dimensional state of stress. Moreover, transmission electron metallographic observations revealed the partial recrystallised microstructure (Figure 7.16) confirmed the optical observations.

There are two features which need explanation – (i) the fact that recrystallisation occurs more readily during deformation when compared with static heat treatment, and (ii) the differences in recrystallisation behaviour as a function of the orientation of the deformation axes with respect to the rolling direction.

The first observation probably cannot be attributed to any increase in stored energy as a consequence of deformation because the materials already contain an unusually large amount of

excess energy. It is likely instead that the stress assists the migration of the glissile components of sub-grain or grain boundaries, thereby permitting easier recrystallisation. This would be true irrespective of the orientation of the strain axis since it is shear stresses which are important in the movement of dislocations.

From Table 7.3, the "yield stress" is smaller when the compression axis is normal to the rolling direction. This is a very useful result because in compression, one might expect a net transport of material in a direction normal to the compression axis. When this latter direction is also parallel to the rolling direction, the net flow should be easier since the particles are aligned parallel to the flow direction (Figure 7.17).

For the same reason, the stress needed to overcome the barriers should be less sensitive to temperature when the compression axis is normal to the rolling direction since the boundaries are essentially migrating in particle free regions. Notice also that work hardening is more rapid for this deformation configuration. This is also expected since for the case where the particles are aligned to the compression axis, it is predominantly the need to overcome the particles that determines yield.

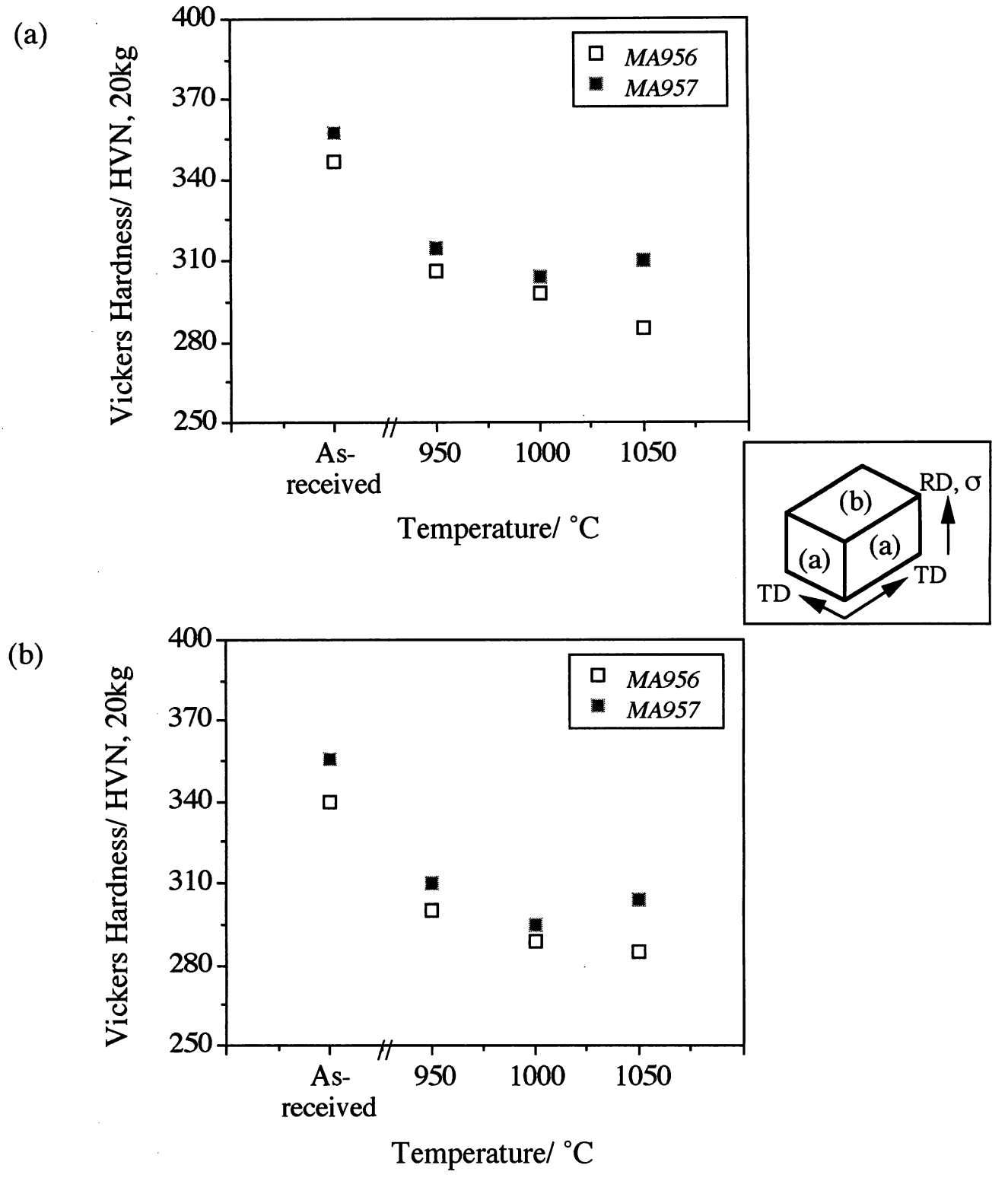

Figure 7.14: Recorded hardness changes in hot-deformed *MA956* and *MA957* steels as compressed along rolling direction for a variety of deformation temperatures, (a) section containing the stress axis and rolling direction, (b) section normal to stress axis and rolling direction.

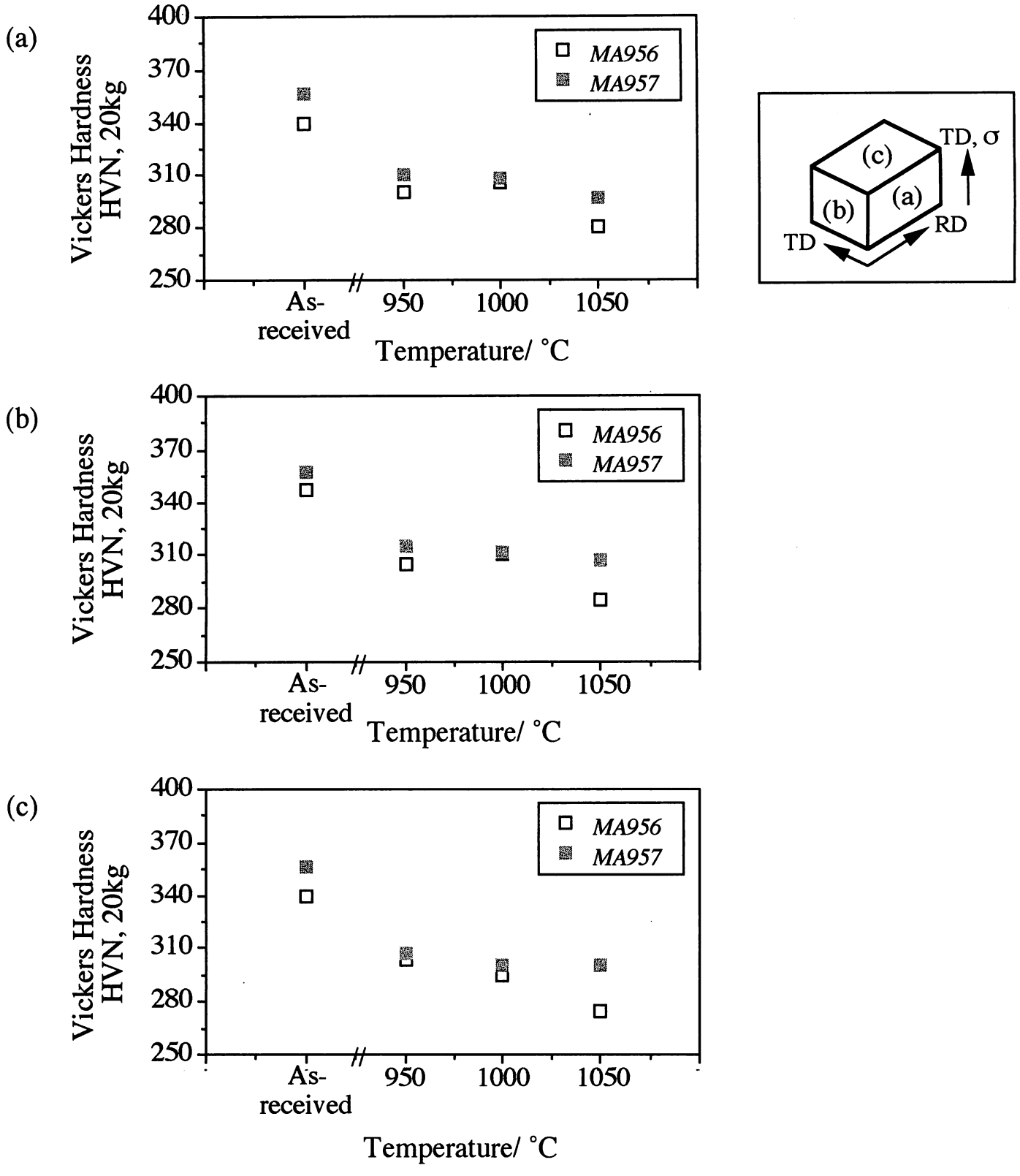

Figure 7.15: Recorded hardness changes in hot-deformed *MA956* and *MA957* steels as compressed along rolling direction for a variety of deformation temperatures, (a) section containing the stress axis and rolling direction, (b) section containing the stress axis but normal to the rolling direction, (c) section containing the rolling direction but normal to stress axis.

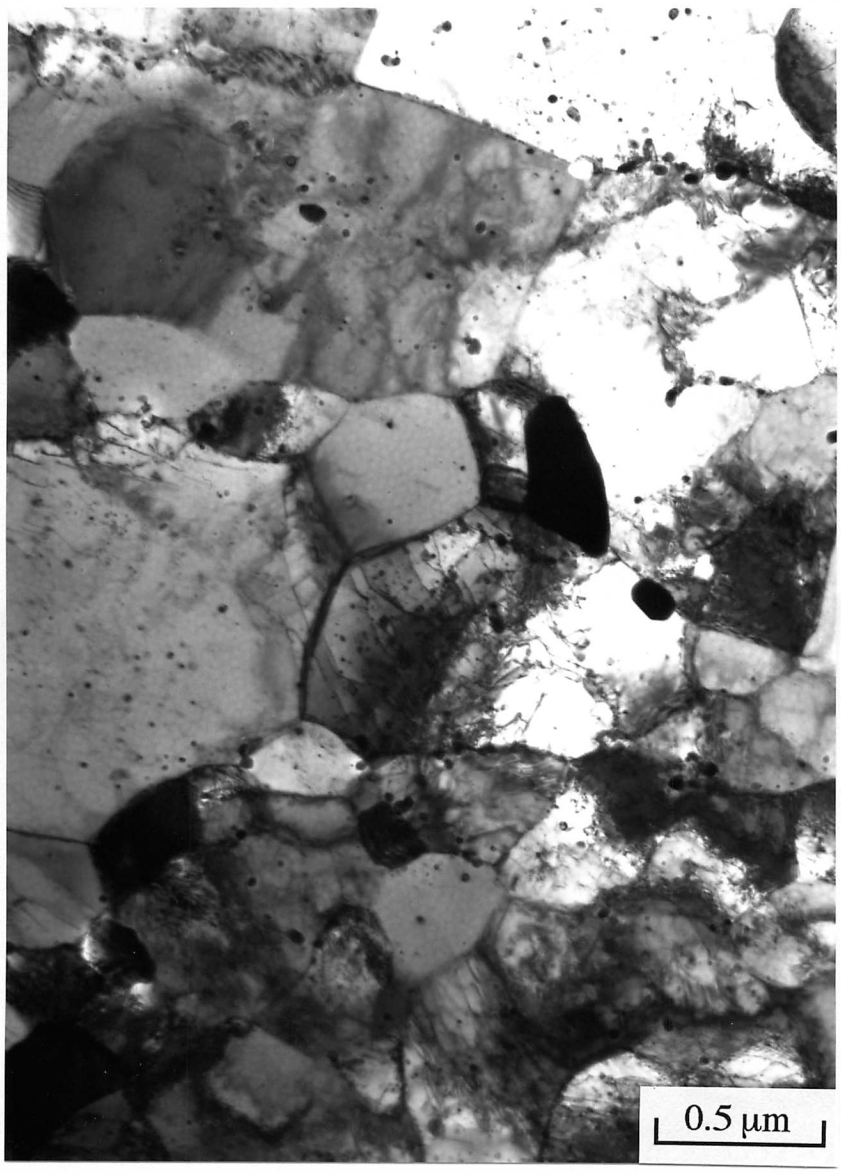

Figure 7.16: TEM of the partially recrystallised microstructure in *MA956* steel as hot-deformed at 1000 °C (sample compressed along the rolling direction).

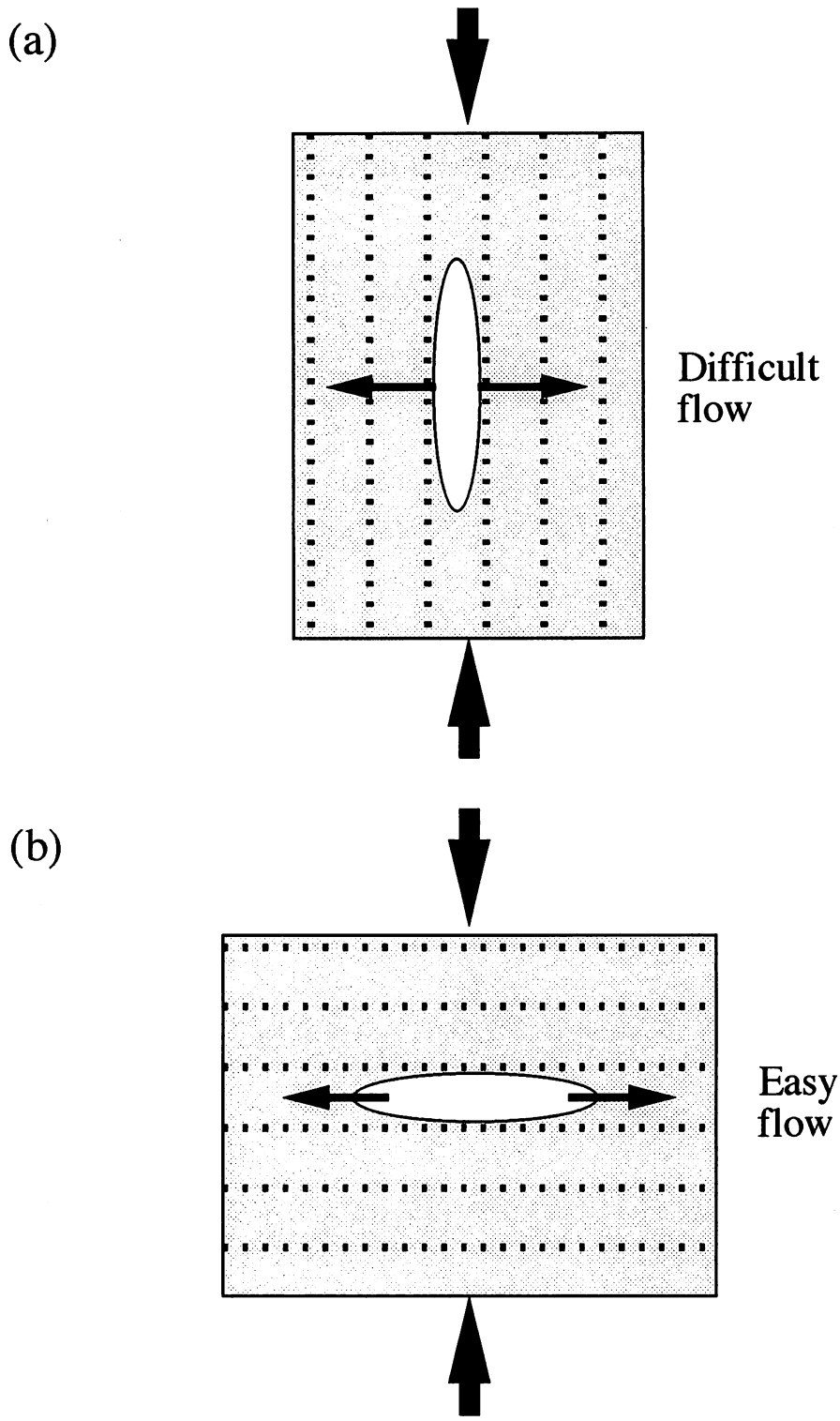

Figure 7.17: Schematic diagrams illustrating the effect of dispersoid alignment on the material flow with the change of deformation configurations, (a) compressed along the rolling direction, (b) compressed normal to the rolling direction.

7.4 CONCLUSIONS

The hot-deformation behaviour and it's related effect on deformed microstructures in *MA956* and *MA957* steels has been investigated. It is found that dynamic recrystallisation occurs during hot-deformation, causing the softening. The occurrence of dynamic recrystallisation in mechanically alloyed steels is attributed to the high stored energy in the as-received state. Stress appears to assist the migration of the glissile components of sub-grain or grain boundaries, thereby permitting easier recrystallisation. In addition, the dynamically recrystallised microstructure shows an anisotropic character.

CHAPTER EIGHT

TRANSFORMABLE MECHANICALLY ALLOYED OXIDE DISPERSION STRENGTHENED STEEL

8.1 INTRODUCTION

Mechanically alloyed metals are made by a powder metallurgical technique in which elemental powders or master alloy powders are deformed together to such an extent that they eventually form solid solutions. At the same time, immiscible dispersoids may be incorporated in order to increase the creep strength. As discussed in previous Chapters, for steels there are two major commercial variants produced by this route: *MA956* and *MA957*. The alloys are consolidated by extrusion and hot rolling into the required shape, giving an incredibly fine (sub-micrometre) grain size and a hardness/toughness combination which is not terribly useful. Consequently they are given a recrystallisation heat treatment which leads to the formation of very coarse columnar grains. These columnar grains always grow along the extrusion direction because the consolidation process leads to an alignment of dispersoids along the main deformation direction (Baloch, 1989). The microstructure is much like that obtained during directional solidification, and is said to have been generated by a process of "directional recrystallisation".

The directionally recrystallised microstructure is obviously benefit from the point of view of creep properties when the columnar grains are aligned parallel to the stress axis. However, the transverse properties tend to be much weaker. For many potential applications, an equiaxed grain microstructure could be more appropriate compared with a columnar grain structure. A method for achieving this equiaxed grain structure has already been suggested (Chapter 5), but it requires prolonged heat treatment at elevated temperature (in excess of 1000 °C).

Both *MA956* and *MA957* are supposed to be ferritic at all temperatures below the solidus. This is because they contain large chromium concentrations, and in the case of *MA956*, a substantial amount of aluminum is present in solid solution. The phase diagram therefore contains a "γ-loop" so that austenite does not occur once the chromium concentration exceeds a critical value. On the other hand, because of its relatively low chromium concentration and no aluminum, *MA957* in fact just clips the γ-loop so that a few percent of austenite can indeed be generated using appropriate heat treatment (Chapter 5). This austenite has a low

Alloy	C	Cr	Ti	Mo	Ni	Y_2O_3
MA957	0.010	14.00	1.00	0.30	–	0.27
MA957-Ni-A	0.016	9.96	0.76	0.20	0.46	0.18
MA957-Ni-B	0.015	12.54	0.99	0.26	0.57	0.22
MA957-Ni-C	0.016	13.87	1.12	0.29	0.62	0.24
MA957-Ni-D	0.015	14.53	1.17	0.30	0.61	0.25

Table 8.1 Chemical compositions, wt.%

hardenability so that it decomposes into martensite on cooling to ambient temperature. This suggests a method of grain refinement by exploiting the phase transformation to and from austenite. Furthermore, because the alloy is so close to the γ-loop, a minor modification of the chemistry can be demonstrated (Chapter 5) to lead to quite substantial increases in the austenite content. The purpose of the present work was to carry this idea forward and make transformable mechanically alloyed ODS stainless steels.

8.2 EXPERIMENTAL PROCEDURE

The modification of standard *MA957* (Table 8.1) was formulated using phase diagram modelling. These calculations will be discussed later, but to summarise, they suggested that an addition of just 0.5 wt.% of nickel could increase the maximum austenite fraction attainable in *MA957* to 0.5 (Figure 8.1). The modified alloys were therefore designated "*MA957-Ni*".

Conventional *MA957* steel is fabricated by charging three primary powders (elemental iron, pre–alloyed metallic powders, and yttria powder) into a water cooled vertical attritor for mechanical alloying. The powder is consolidated by extrusion at 1000 °C whilst packed in a mild steel can. This is followed by rolling at 1000 °C, with a reduction in diameter from 54 to 9.5 mm. The modified *MA957-Ni* steels were prepared differently, using standard low carbon ferrochrome, ferrotitanium, iron, nickel, molybdenum and yttrium oxide powders, rather than from standard master alloys. A number of variants were prepared because of potential uncertainties in the manufacturing process. Powders from each run of modified *MA957-Ni* were canned into 2" diameter × 4" high mild steel cans for consolidation, then hot-extruded to 12.5 mm diameter bar using a furnace preheating temperature of 1070 °C. The alloys were not hot-rolled after extrusion. Their compositions are listed in Table 8.1, which shows variations in the chromium as well as nickel concentrations.

Phase changes were monitored using a thermomechanical simulator (*Thermecmaster Z*) as a dilatometer. The samples for this were in the form of 8 mm diameter by 12 mm length

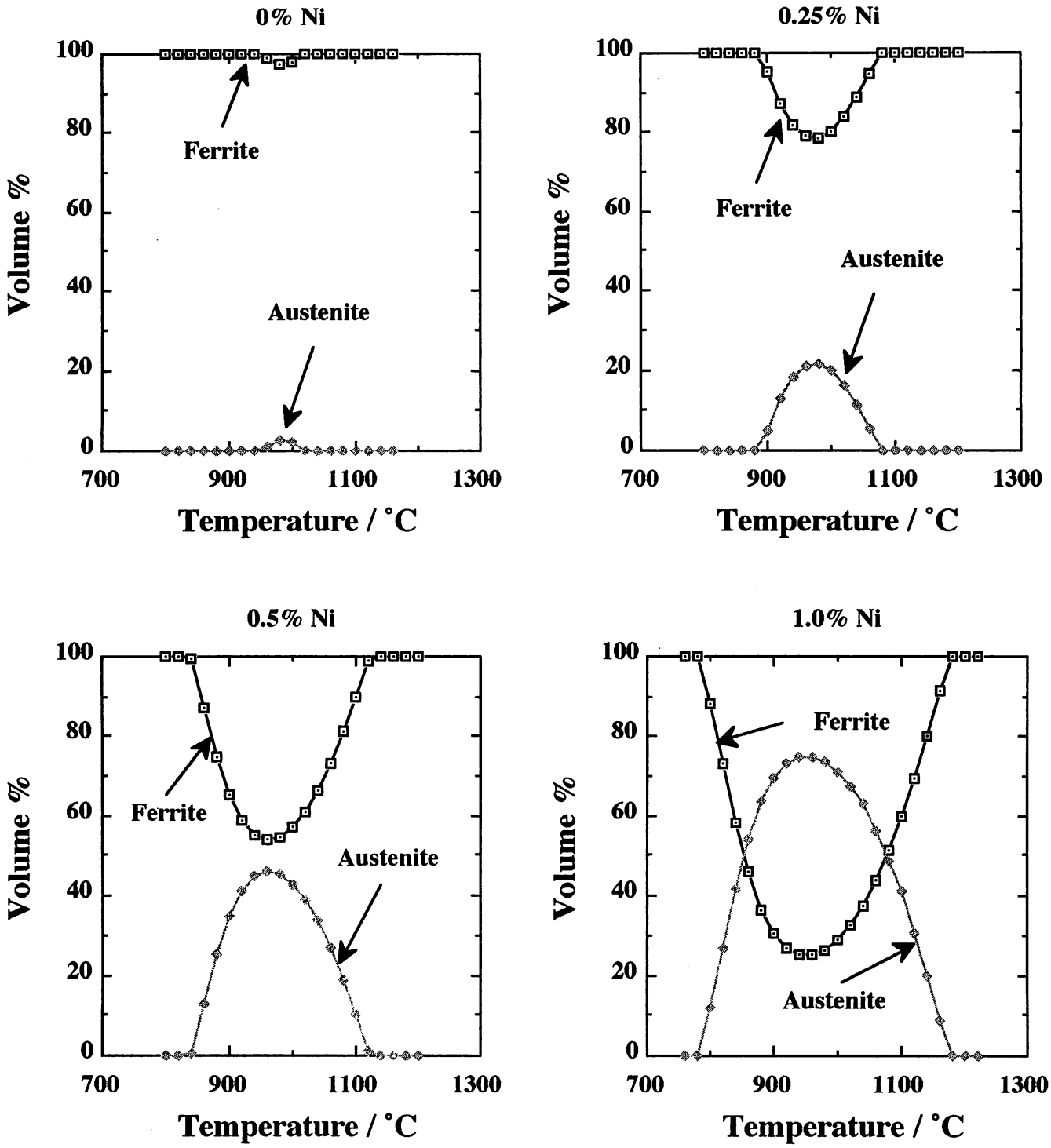

Figure 8.1: Calculated effect of nickel on the volume fraction of austenite and ferrite calculated as a function of temperature in *MA957*.

cylinders. In addition, differential scanning calorimetry (DSC) was used to characterise the transformation behaviour, and monitor the stored energy. The calorimetric measurements were carried out during continuous heating and cooling, the sample mass typically being about 200 mg. The reference consisted of a similar size and shaped sample of recrystallised *MA957*. In all cases, the DSC samples were examined using optical microscopy. All the experiments were carried out using an argon atmosphere in the DSC chamber.

Optical microscopy was used to observe the microstructures both of the as-received and heat treated specimens. The etchant used was 2g $CuCl_2$, 40 ml HCl, and 40 to 80 ml ethanol. Transmission electron microscopy was carried out using a *Philips EM400* microscope operated at 120 KV. Thin foils were prepared using a *Fischione* twin–jet electropolisher with an electrolyte consisting of 5% perchloric acid, 25% glycerol and ethanol. The polishing voltage was about 55 volts.

A *Siemens 200* X–ray diffractometer with a pole figure goniometer was employed to measure the textures by recording the {2 0 0} and {1 1 0} pole figures from longitudinal sections. The X–radiation used was β–filtered MoK_α. The reflection method was used with angles ranging from 0 to 80 ° measured relative to the normal to the longitudinal face of the sample. The samples were macroetched using 5 HCl : H_2O_2 prior to the X–ray experiments in order to remove any machining artifacts.

8.3 RESULTS AND DISCUSSION

8.3.1 Thermodynamic Calculations

Equilibrium phase diagrams for the specific alloys listed in Table 8.1 were calculated using the MTDATA program and SGTE thermodynamic data set (1993). Once the components and phases have been specified, the program retrieves the appropriate data and derives the equilibrium state by minimising the free energy of the system as a whole. The output therefore consists of the fractions of the phases and their detailed chemistries. The calculations were carried out permitting the existence of austenite and ferrite as the phases, and the elements iron, carbon, nickel, chromium and molybdenum.

The calculated phase composition results are presented in Tables 8.2 – 8.5, and the volume fractions of phases as a function of temperature are illustrated in Figure 8.2. By fortunate circumstance, a whole series of alloys with significantly different potentials for producing austenite, had been achieved experimentally. The differences between the alloys are due to variations in their chromium and nickel concentrations. The alloy partitioning behaviour indicated by the calculations in Tables 8.2 – 8.5 is as expected; austenite stablising elements such as carbon

Temperature	α	γ	Cr_α	Cr_γ	Ni_α	Ni_γ	Mo_α	Mo_γ	C_α	C_γ
°C	wt.%	wt.%	wt.%	wt.%	wt.%	wt.%	wt. %	wt.%	wt.%	wt.%
780	100	–	9.96	–	0.460	–	0.200	–	0.016	–
800	90.0	10.0	9.96	9.82	0.416	0.852	0.202	0.183	0.010	0.072
820	68.2	31.8	10.08	9.70	0.349	0.698	0.208	0.182	0.006	0.038
840	28.2	71.8	10.38	9.79	0.273	0.533	0.224	0.191	0.003	0.021
860	–	100	–	9.96	–	0.460	–	0.200	–	0.016
1160	–	100	–	9.96	–	0.460	–	0.200	–	0.016
1180	5.3	94.7	11.33	9.88	0.331	0.467	0.240	0.198	0.005	0.017
1200	24.9	75.1	10.98	9.62	0.356	0.495	0.230	0.190	0.005	0.020
1220	46.5	53.5	10.64	9.37	0.385	0.526	0.220	0.183	0.007	0.024
1240	68.5	31.5	10.34	9.14	0.415	0.558	0.211	0.176	0.009	0.031
1260	88.3	11.7	10.09	8.97	0.443	0.587	0.204	0.171	0.012	0.043
1280	100	–	9.96	–	0.460	–	0.200	–	0.016	–

Table 8.2 Thermodynamic phase stability calculations for alloy *MA957-Ni-A*. The concentrations and phase fractions are stated in wt%. The body–centered cubic and face–centered cubic forms of iron are designated α and γ respectively.

and nickel preferentially partition into the austenite, and vice versa. It should be emphasised that the calculations are for the equilibrium state, which may not in practice be completely achieved during rapid heat treatment. One interesting point is that the hardenability of the austenite to martensite transformation is expected to be low, except for *MA957-Ni-C*, in which the γ has a large nickel and carbon concentration.

Temperature	α	γ	Cr_α	Cr_γ	Ni_α	Ni_γ	Mo_α	Mo_γ	C_α	C_γ
°C	wt.%	wt.%	wt.%	wt.%	wt.%	wt.%	wt. %	wt.%	wt.%	wt.%
800	100	–	12.54	–	0.570	–	0.260	–	0.015	–
820	89.0	11.0	12.66	11.54	0.512	1.038	0.263	0.232	0.011	0.051
840	73.1	26.9	12.90	11.57	0.451	0.892	0.270	0.232	0.008	0.035
860	55.7	44.3	13.22	11.68	0.403	0.779	0.279	0.236	0.006	0.026
880	40.5	59.5	13.57	11.84	0.373	0.704	0.288	0.241	0.005	0.022
900	29.2	70.8	13.89	11.99	0.356	0.658	0.296	0.245	0.005	0.019
920	21.8	78.2	14.13	12.10	0.349	0.632	0.301	0.249	0.005	0.018
940	17.6	82.4	14.30	12.17	0.348	0.617	0.305	0.250	0.005	0.017
960	15.9	84.1	14.38	12.19	0.351	0.611	0.306	0.251	0.005	0.017
980	16.3	83.7	14.40	12.18	0.358	0.611	0.306	0.251	0.005	0.017
1000	18.3	81.7	14.36	12.13	0.368	0.615	0.305	0.250	0.005	0.017
1020	21.9	78.1	14.27	12.06	0.380	0.623	0.302	0.248	0.005	0.018
1040	27.0	73.0	14.13	11.95	0.394	0.635	0.299	0.246	0.005	0.019
1060	33.5	66.5	13.96	11.83	0.411	0.650	0.295	0.242	0.006	0.020
1080	41.3	58.7	13.76	11.68	0.430	0.668	0.290	0.239	0.006	0.021
1100	50.5	49.5	13.53	11.53	0.452	0.690	0.284	0.235	0.007	0.024
1120	60.8	39.2	13.30	11.36	0.477	0.715	0.279	0.231	0.008	0.027
1140	72.1	27.9	13.06	11.20	0.504	0.741	0.273	0.227	0.009	0.031
1160	83.7	16.3	12.83	11.04	0.531	0.769	0.267	0.223	0.011	0.037
1180	100	–	12.63	–	0.558	–	0.262	–	0.013	–

Table 8.3 Thermodynamic phase stability calculations for alloy *MA957-Ni-B*. The concentrations and phase fractions are stated in wt%. The body–centered cubic and face–centered cubic forms of iron are designated α and γ respectively.

Temperature	α	γ	Cr_α	Cr_γ	Ni_α	Ni_γ	Mo_α	Mo_γ	C_α	C_γ
°C	wt.%	wt.%	wt.%	wt.%	wt.%	wt.%	wt. %	wt.%	wt.%	wt.%
800	100	–	13.87	–	0.620	–	0.290	–	0.016	–
820	97.0	3.0	13.92	12.36	0.601	1.228	0.291	0.257	0.015	0.060
840	86.5	13.5	14.11	12.36	0.547	1.089	0.295	0.256	0.011	0.145
860	75.6	24.4	14.34	12.42	0.504	0.980	0.301	0.256	0.010	0.036
880	65.9	34.1	14.58	12.50	0.474	0.902	0.307	0.258	0.008	0.031
900	58.5	41.5	14.79	12.57	0.456	0.850	0.311	0.260	0.008	0.028
920	53.4	46.6	14.95	12.63	0.448	0.817	0.315	0.262	0.007	0.026
940	50.6	49.4	15.05	12.66	0.477	0.798	0.317	0.262	0.007	0.025
960	49.8	50.2	15.09	12.66	0.450	0.788	0.318	0.263	0.007	0.025
980	50.6	49.4	15.08	12.63	0.458	0.786	0.317	0.262	0.007	0.025
1000	53.0	47.0	15.01	12.58	0.469	0.790	0.316	0.261	0.008	0.026
1020	56.8	43.2	14.91	12.50	0.484	0.799	0.313	0.259	0.008	0.027
1040	61.8	38.2	14.78	12.40	0.501	0.812	0.310	0.257	0.008	0.028
1060	67.9	32.1	14.62	12.30	0.521	0.828	0.307	0.255	0.009	0.031
1080	74.9	25.1	14.44	12.18	0.544	0.848	0.303	0.252	0.010	0.034
1100	82.7	17.3	14.25	12.06	0.568	0.870	0.298	0.249	0.011	0.039
1120	91.0	9.0	14.06	11.94	0.593	0.892	0.294	0.247	0.013	0.045
1140	99.1	0.9	13.89	11.84	0.617	0.913	0.290	0.245	0.016	0.053
1160	100	–	13.87	–	0.620	–	0.290	–	0.0160	–

Table 8.4 Thermodynamic phase stability calculations for alloy *MA957-Ni-C*. The concentrations and phase fractions are stated in wt%. The body–centered cubic and face–centered cubic forms of iron are designated α and γ respectively.

Temperature	α	γ	Cr_α	Cr_γ	Ni_α	Ni_γ	Mo_α	Mo_γ	C_α	C_γ
°C	wt.%	wt.%	wt.%	wt.%	wt.%	wt.%	wt. %	wt.%	wt.%	wt.%
820	100	–	14.53	–	0.610	–	0.300	–	0.015	–
840	96.8	3.2	14.59	12.68	0.591	1.182	0.301	0.262	0.014	0.052
860	88.4	11.6	14.77	12.70	0.549	1.073	0.305	0.261	0.012	0.042
880	80.9	19.1	14.95	12.74	0.520	0.992	0.309	0.261	0.010	0.036
900	74.9	25.1	15.12	12.79	0.501	0.935	0.313	0.262	0.009	0.032
920	70.8	29.2	15.24	12.82	0.491	0.898	0.315	0.263	0.009	0.030
940	68.6	31.4	15.31	12.83	0.489	0.875	0.317	0.263	0.009	0.029
960	68.1	31.9	15.33	12.82	0.492	0.862	0.317	0.263	0.009	0.029
980	69.2	30.8	15.31	12.79	0.499	0.858	0.317	0.262	0.009	0.029
1000	71.6	28.4	15.24	12.74	0.511	0.861	0.315	0.261	0.009	0.030
1020	75.4	24.6	15.14	12.67	0.525	0.869	0.313	0.260	0.010	0.032
1040	80.1	19.9	15.01	12.58	0.543	0.881	0.310	0.258	0.010	0.034
1060	85.8	14.2	14.87	12.49	0.563	0.896	0.307	0.256	0.011	0.038
1080	92.2	7.8	14.71	12.39	0.584	0.913	0.304	0.254	0.013	0.043
1100	98.9	1.1	14.56	12.30	0.606	0.930	0.301	0.252	0.015	0.049
1120	100	–	14.53	–	0.610	–	0.300	–	0.015	–

Table 8.5 Thermodynamic phase stability calculations for alloy *MA957-Ni-D*. The concentrations and phase fractions are stated in wt%. The body–centered cubic and face–centered cubic forms of iron are designated α and γ respectively.

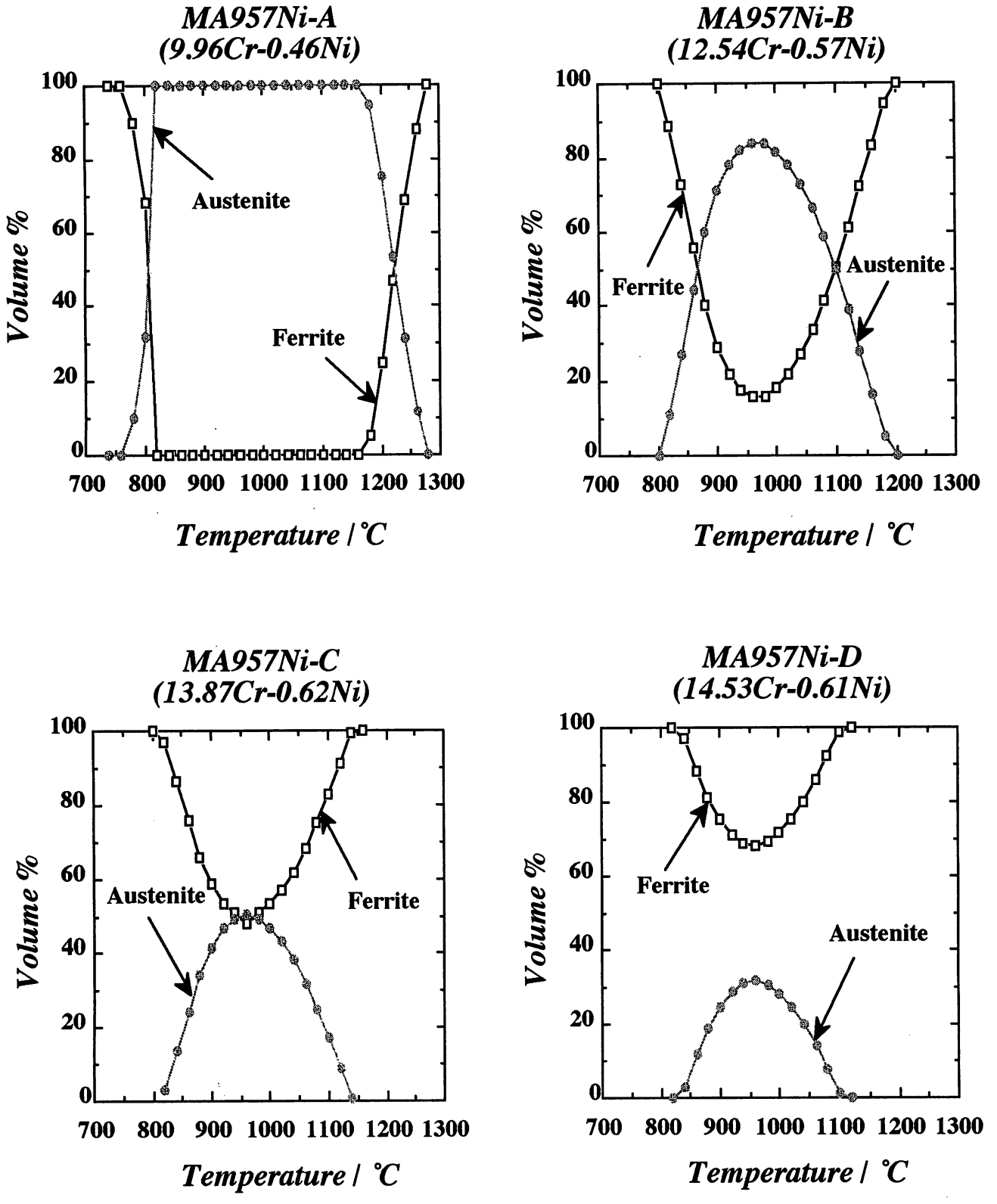

Figure 8.2: The change of α and γ volume fractions with temperature of modified *MA957-Ni* steels.

Alloy	Hardness HVN (20kg)	Average
MA957	381, 379, 383, 379	381.3
MA957-Ni-A	293, 294, 289, 292	292.0
MA957-Ni-B	339, 335, 341, 352	342.0
MA957-Ni-C	453, 450, 434, 442	444.8
MA957-Ni-D	391, 387, 391, 391	390.0

Table 8.6 Vicker's hardness data for as–received *MA957* and *MA957–Ni* steels.

8.3.2 As–Received Microstructures

Hardness measurements were carried out before the observations of the microstructures of as-received *MA957–Ni* steels. Table 8.6 shows the hardness of the nickel modified alloys against with the conventional *MA957* steel. It is clear that as-received *MA957-Ni-A* and *MA957-Ni-B* have lower hardness values than conventional *MA957* in the as-received state. The significantly low hardness of as-received *MA957-Ni-A* is found to be similar with that of preannealed *MA957* (Chapter 5). On the other hand, the as-received *MA957-Ni-C* and *MA957-Ni-D* have higher hardness than *MA957*. Particularly high hardness values were found for as-received *MA957-Ni-C*. These results will be discussed later.

Figure 8.3 shows optical micrographs of the as–received *MA957–Ni* steels. On this optical scale, Figure 8.3 shows that some relatively coarse grained microstructures occur in both *MA957-Ni-A* and *MA957-Ni-B* steels. On the other hand, *MA957-Ni-C* and *MA957-Ni-D* show a very fine grained microstructure similar to the as-received *MA957* steel.

Since the microstructures are produced by a combination of deformation and phase transformation in these transformable alloys, it is obvious that at the extrusion temperature, *MA957-Ni-A* and *MA957-Ni-B* alloys will contain a lot of austenite which will then transform on cooling. This should give a bimodal microstructure consisting of ferrite deformed at high temperatures and softer ferrite formed by the transformation of austenite.

Further confirmatory metallography by transmission electron microscopy shows that as-received *MA957-Ni-A* does indeed have a bimodal grain structure (Figure 8.4). The equiaxed grains with diameter up to 5 μm and with a low dislocation density are due to transformation from the deformed austenite. The banded submicrometre grains are like those found in as-received *MA957*. A similar microstructure like *MA957-Ni-A* was found in as-received *MA957-Ni-B* steel (Figure 8.5), since both of these two steels have a high austenite volume fraction at the extrusion temperature. The austenite volume percentages at the extrusion temperature

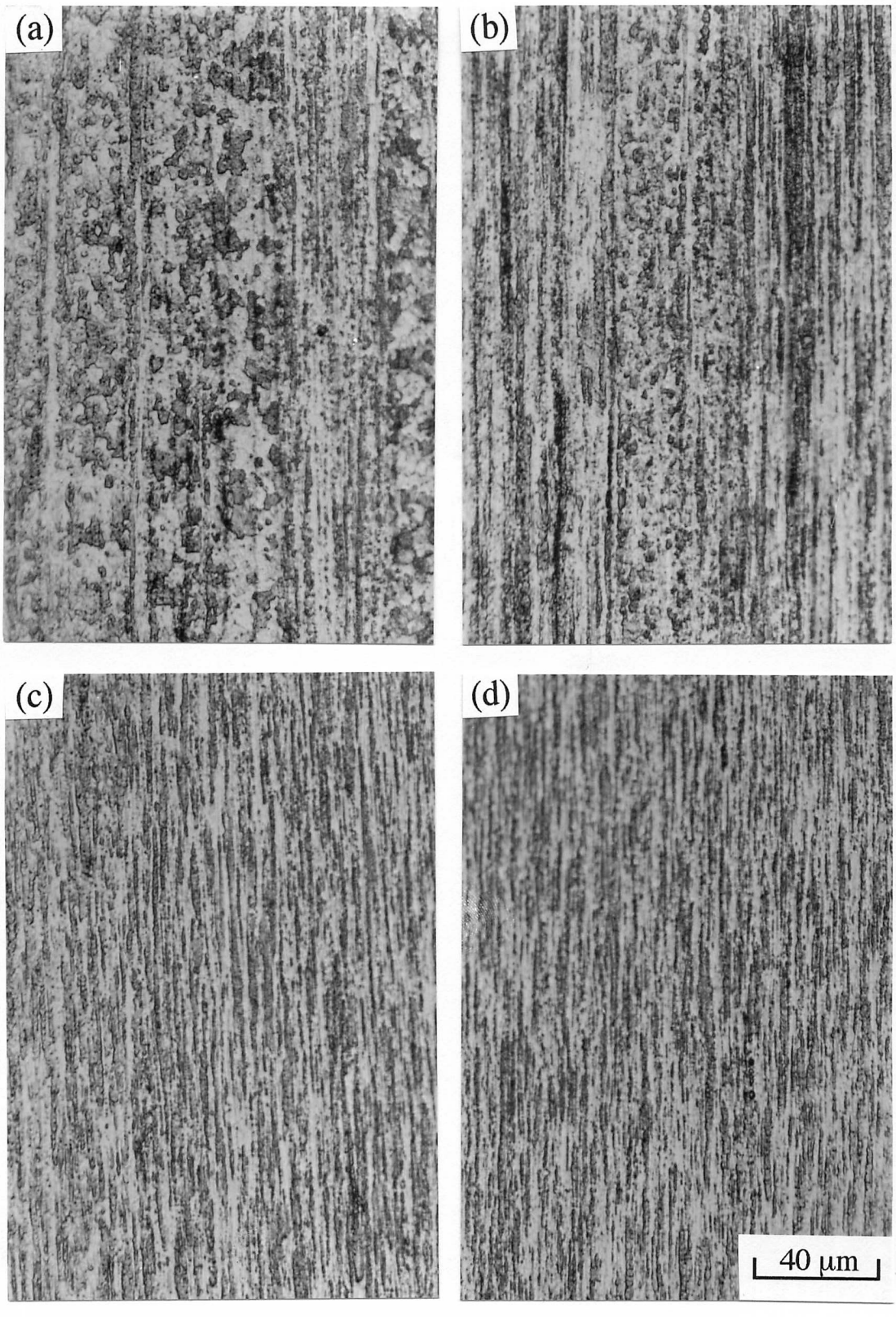

Figure 8.3: Set of micrographs illustrating the optical microstructures of as–received *MA957–Ni* steels, (a) *MA957-Ni-A*, (b) *MA957-Ni-B*, (c) *MA957-Ni-C*, and (d) *MA957-Ni-D*.

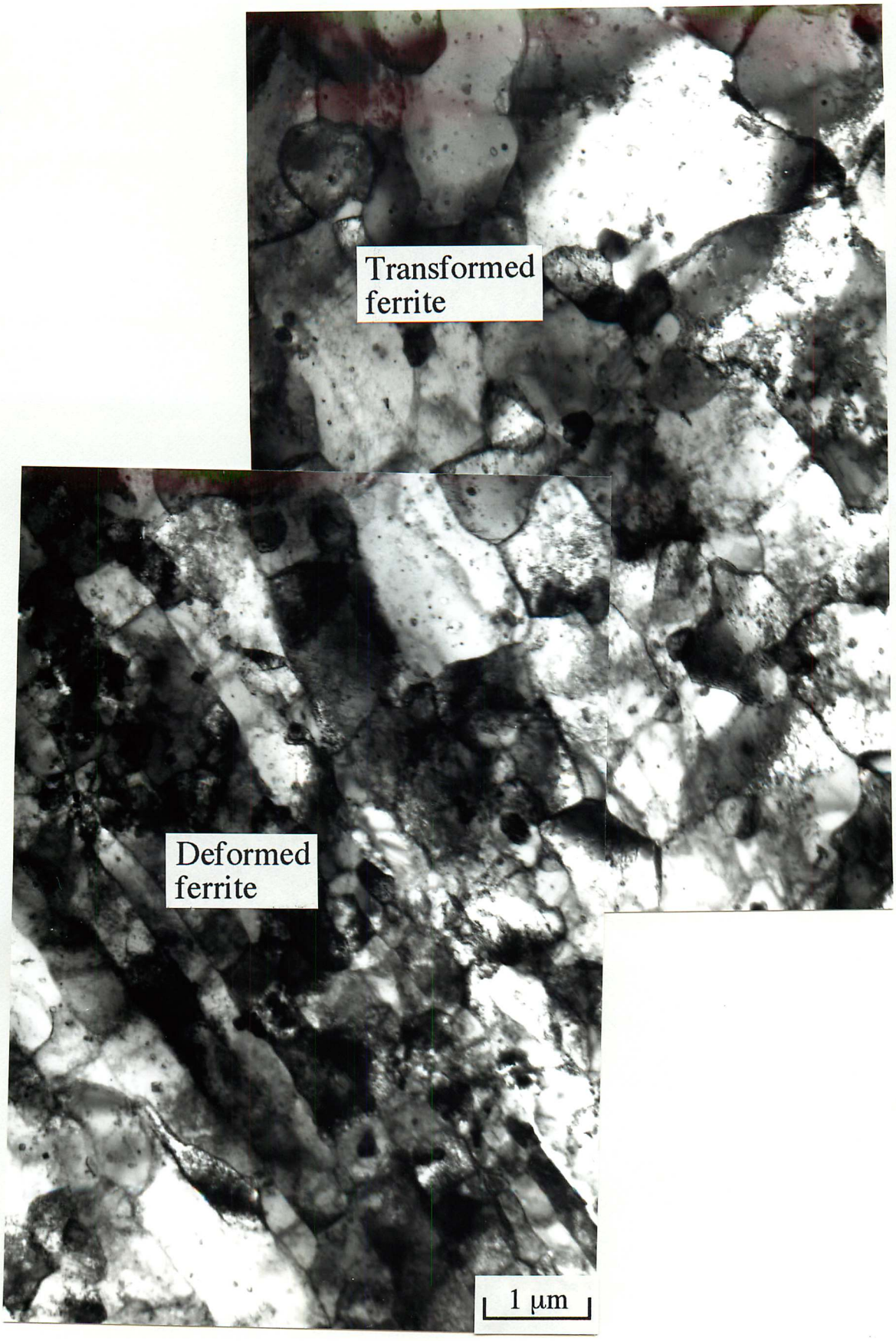

Figure 8.4: Transmission electron micrograph shows the bimodal microstructure of *MA957-Ni-A* steels in as–received condition.

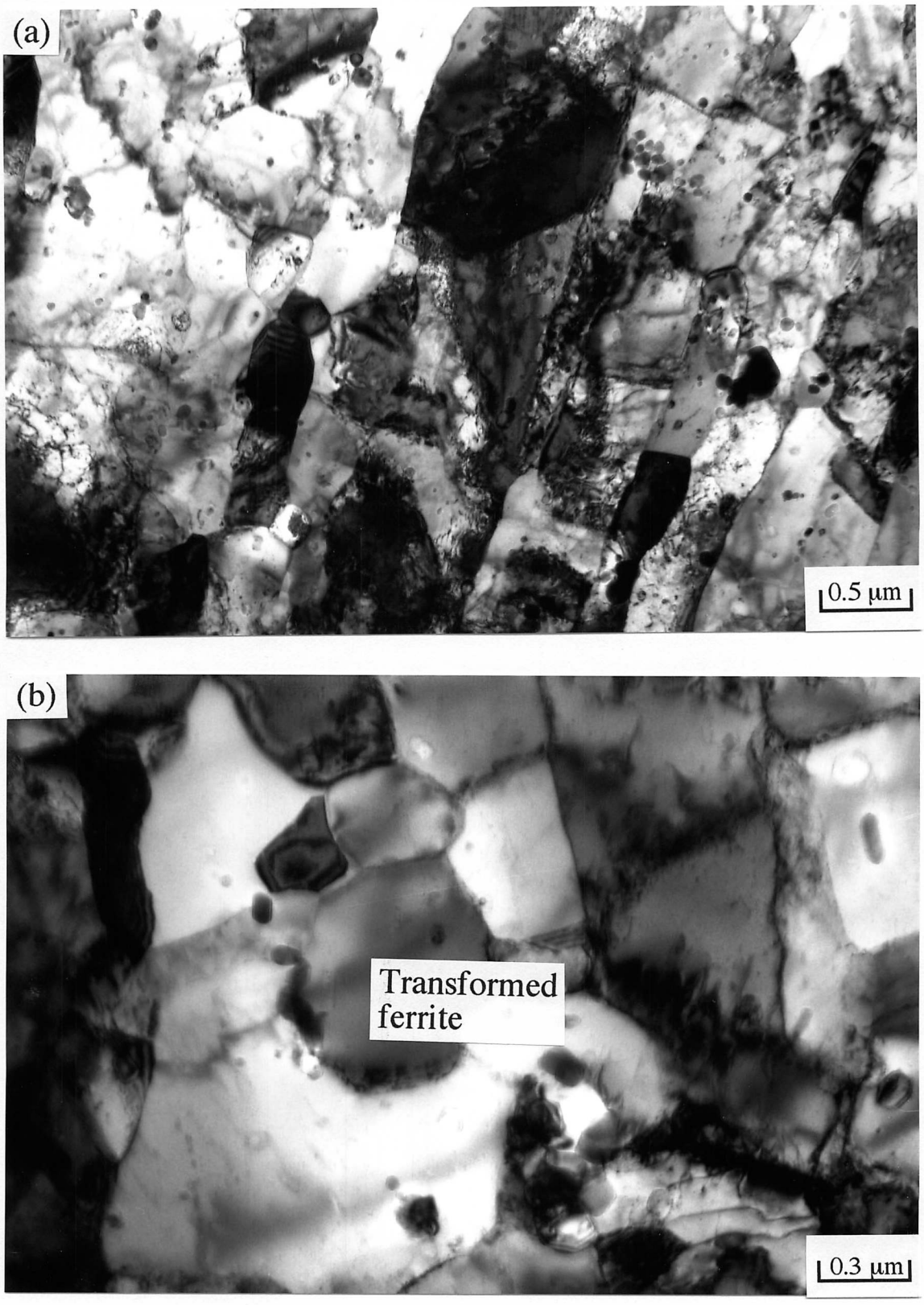

Figure 8.5: Transmission electron micrograph of as-received *MA957-Ni-B* steel. (a) bimodal grain structure, (b) transformed ferrite grains with low dislocation density.

(1070 °C) are about 95% and 65% for *MA957-Ni-A* and *MA957-Ni-B*, respectively (Table 8.2, 8.3). Due to the lower austenite content of *MA957-Ni-B*, more bands of deformed ferrite were apparent than in *MA957-Ni-A* (Figure 8.2). Therefore, *MA957-Ni-B* naturally shows a higher hardness (Table 8.6).

MA957-Ni-C should contain only 30% of austenite at the extrusion temperature. The correspondingly large content of deformed ferrite bands and the fact that its high hardenability austenite transforms to martensite on cooling (Figure 8.6) gives this alloy a particularly high hardness. It is worth noting that the martensite makes *MA957-Ni-C* even harder than conventional *MA957* (Table 8.6). On the other hand, *MA957-Ni-D* (Figure 8.7) is almost like *MA957* because at the extrusion temperature (1070 °C) the amount of austenite is negligible. Hence, its hardness is nearly the same as that of *MA957* although the detailed microstructures are different because no hot rolling process had been applied to the modified alloys.

8.3.3 Dilatometry

The occurrence of austenite in the modified *MA957–Ni* steels was further confirmed using dilatometry. These measurements were carried out on the steels after heat treatment at 1350 °C, the recrystallisation temperature of conventional *MA957* steel, for 1 hour. Figures 8.8 and 8.9 show the data for *MA957-Ni-A* and *MA957-Ni-B*, respectively. Transformation of ferrite to austenite and *vice versa* was detected from both *MA957-Ni-A* and *MA957-Ni-B* steels. However, no clear transformation could be observed in *MA957*, *MA957-Ni-C* and *MA957-Ni-D* steels (Figure 8.10) presumably because of the small fractions of austenite involved, which are stable only over relatively narrow temperature ranges (Figure 8.2). The problem therefore is one of sensitivity. The heating rate used is not expected to give the equilibrium fraction of austenite since that would involve a long range redistribution of substitutional atoms like nickel and chromium. The actual maximum fraction of austenite that forms will therefore be less than indicated by the phase diagram.

8.3.4 DSC Measurement

Figure 8.11 shows the DSC curves recorded from mild steel (carbon < 0.1 wt.%) as a comparison standard. There are three peaks both during heating and cooling tests. The first one, at temperature around 700 °C, is attributed to the changes in heat capacity accompanying the Curie transition in ferrite. Whether this peak points upwards or downwards depends on the relative weights of the reference and sample. The second peak (880 to 910 °C) is due to the ferrite to austenite ($\alpha \rightarrow \gamma$) transformation peak. The third (1380 to 1400 °C) is attributed to

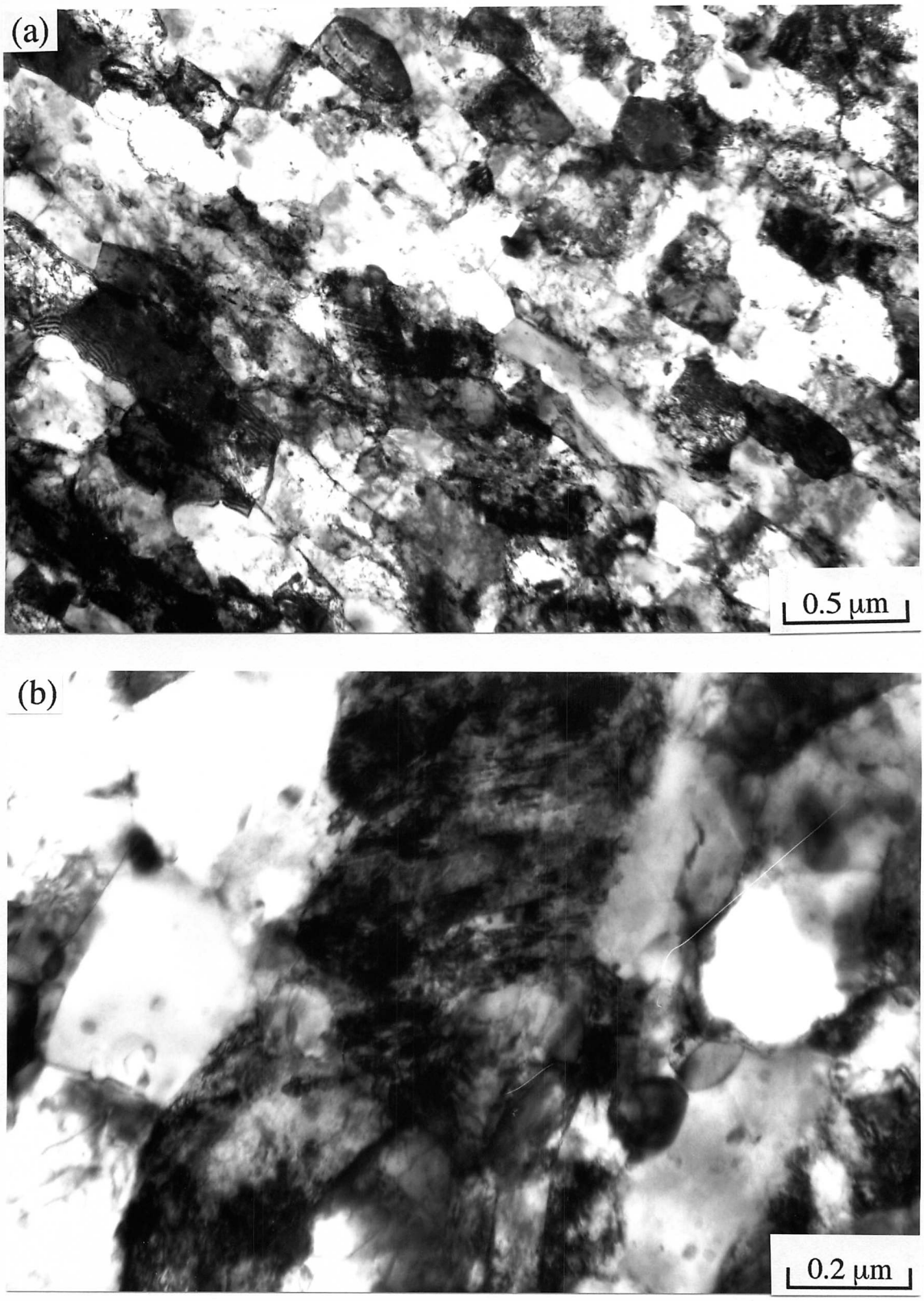

Figure 8.6: Transmission electron micrograph of as-received *MA957-Ni-C* steel, (a) finer subgrain structure, (b) martensite phase.

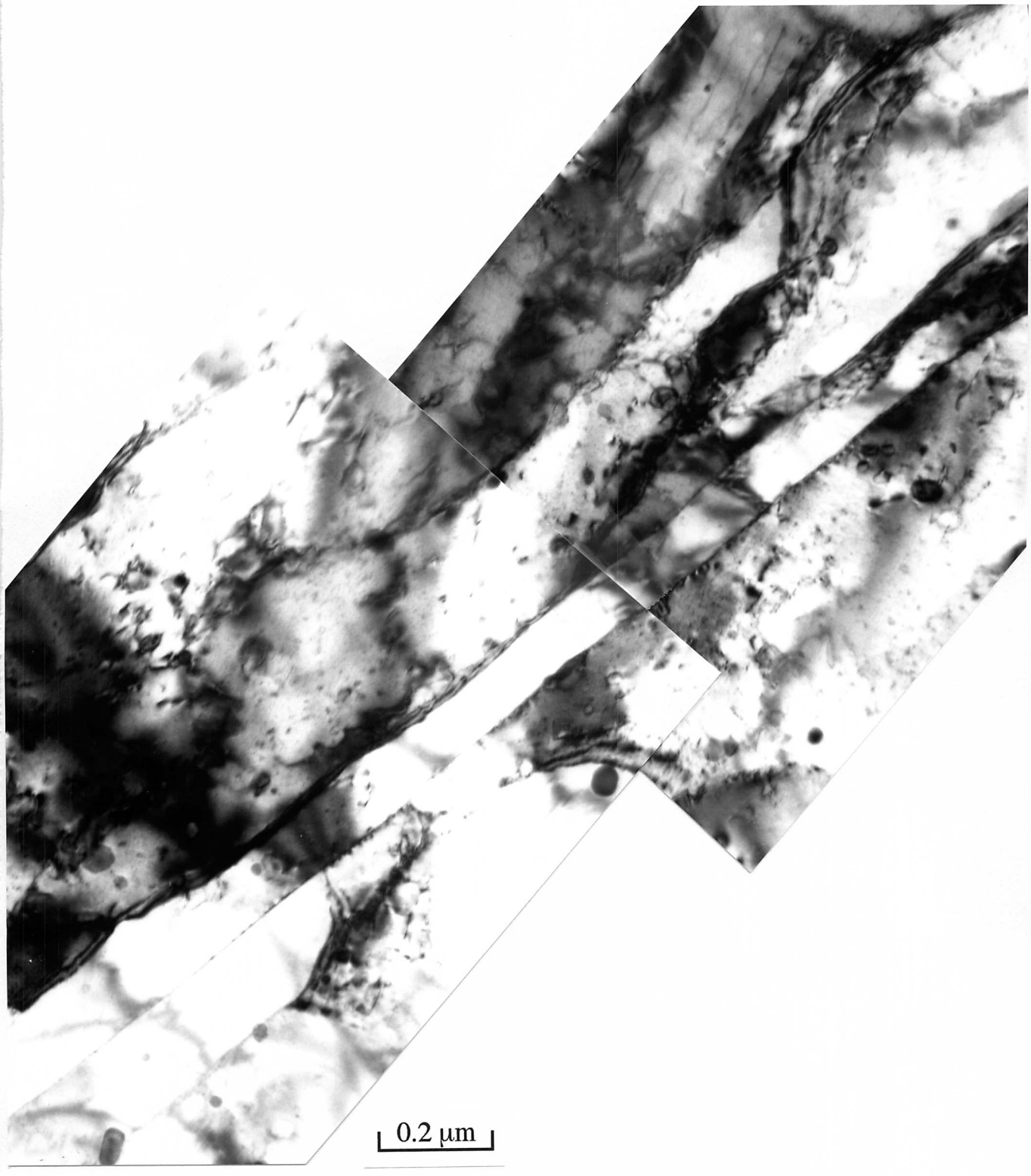

Figure 8.7: Transmission electron micrograph of as-received *MA957-Ni-D* steel illustrating the elongated grain structure.

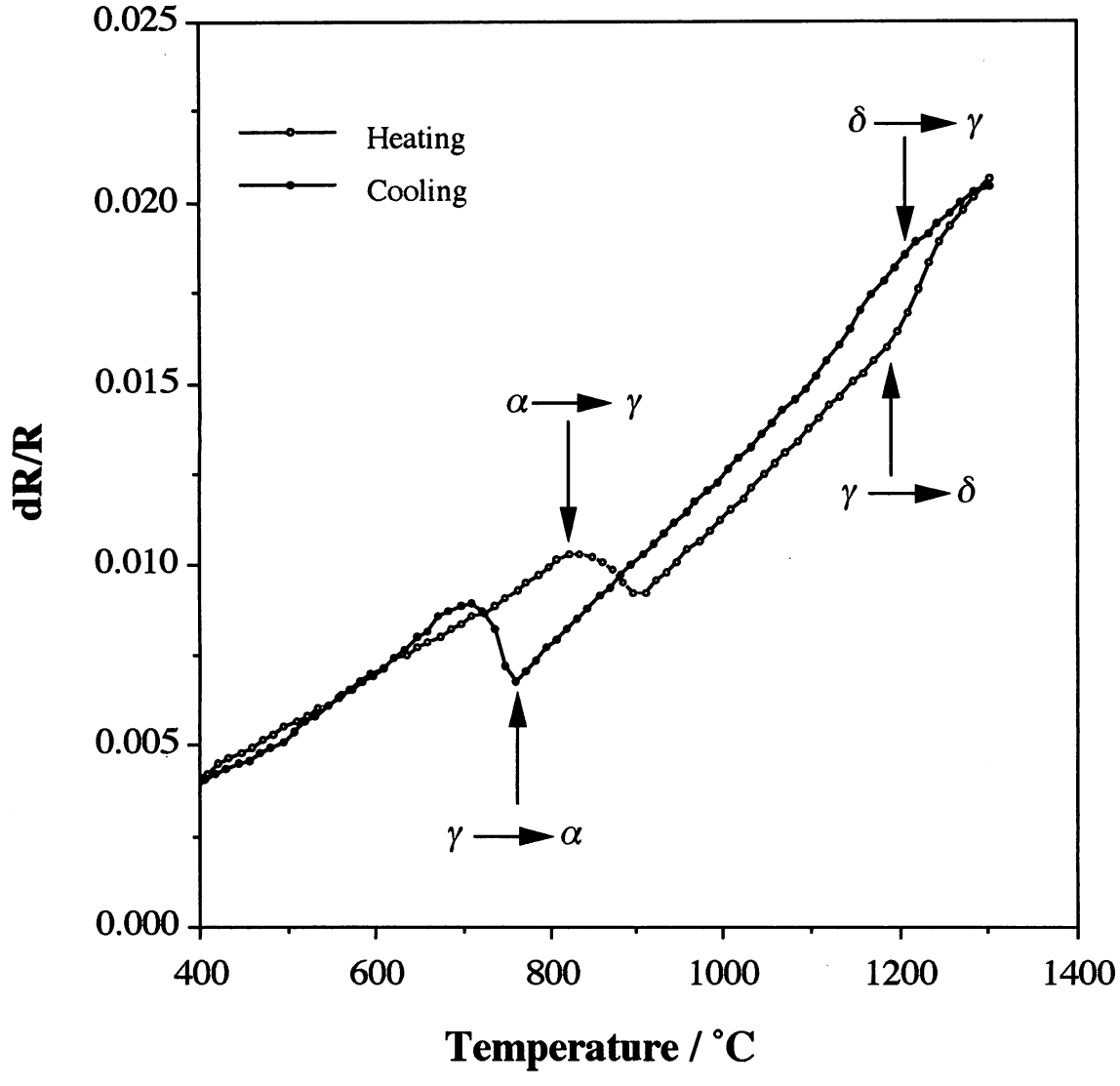

Figure 8.8: Dilatometry curves of *MA957-Ni-A* steel heated and cooled at rate of 1 °C s^{-1}.

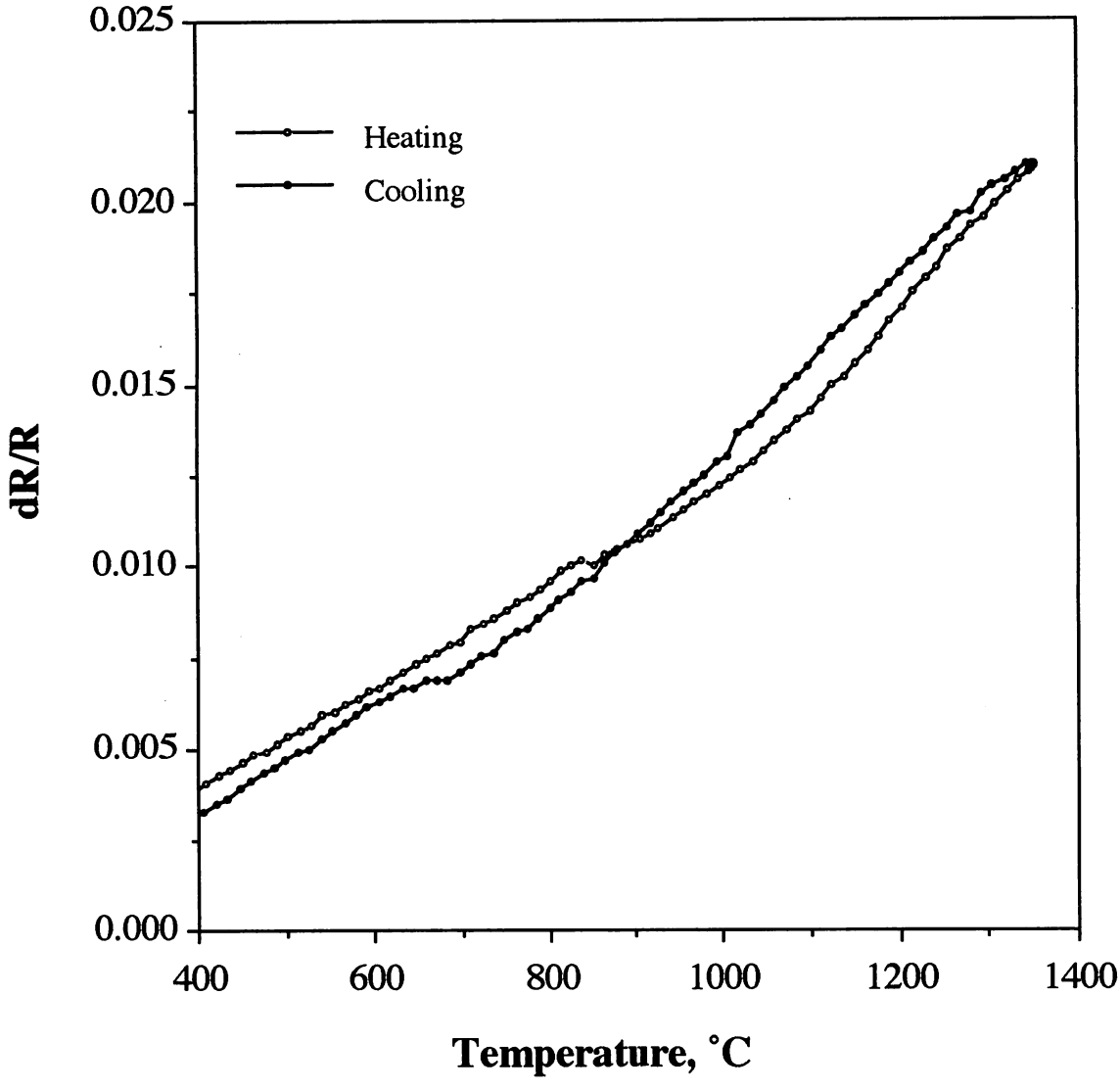

Figure 8.9: Dilatometry curves of *MA957-Ni-B* steel heated and cooled at rate of 1 °C s^{-1}.

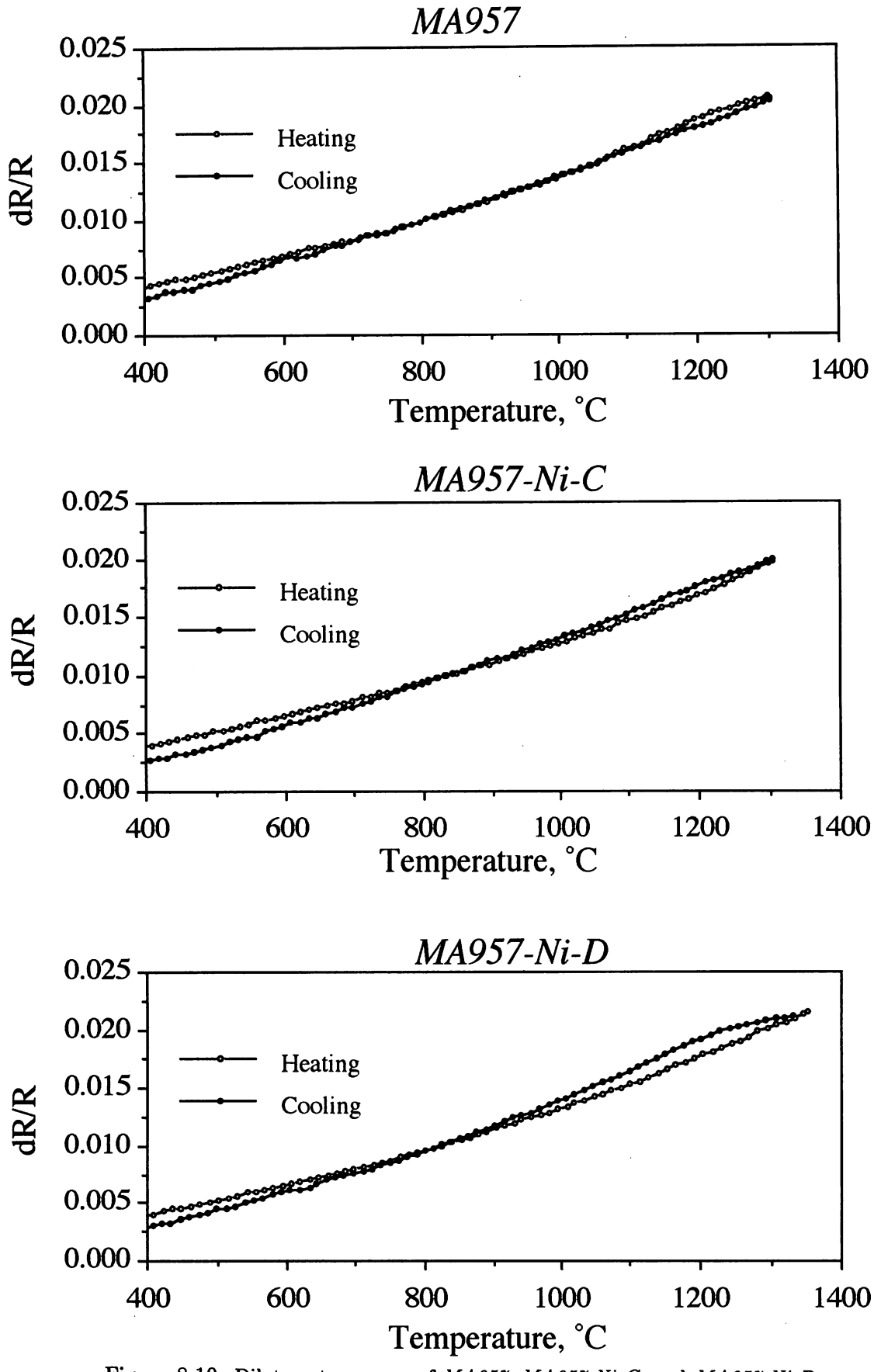

Figure 8.10: Dilatometry curves of *MA957*, *MA957-Ni-C*, and *MA957-Ni-D* steels heated and cooled at rate of 1 °C s^{-1}.

the austenite to delta ($\gamma \rightarrow \delta$) transformation on heating. These measurements are consistent with the Fe-C phase diagram (Reed-Hill and Abbaschian, 1992). On cooling, the recorded DSC peaks are $\delta \rightarrow \gamma$, $\gamma \rightarrow \alpha$ and Curie point in that order. The phase transformation peaks are slightly depressed to lower temperature ranges. In addition, the transformation peaks during cooling are of opposite sign to those during heating.

Figure 8.12 illustrates the DSC curves of *MA957-Ni-A* steel. There are three peaks recorded on heating for the first run. The first peak located around 730 °C is the Curie peak as mentioned before. The second peak, although it is not very clear, located at the temperature around 900 °C is attributed to the $\alpha \rightarrow \gamma$ transformation. The significant third peak located around 1300 °C is due to the $\gamma \rightarrow \delta$ transformation. On cooling (first run), the recorded DSC peaks are $\delta \rightarrow \gamma$, $\gamma \rightarrow \alpha$ and Curie point in that order like the finding in mild steel. Similar DSC peaks were obtained for the second test run. However, it is found that the $\alpha \rightarrow \gamma$ peak is more significant than that for the first test run, and the $\gamma \rightarrow \delta$ transformation occurs at somewhat lower temperature compared with the first test run on heating, whereas no difference occurred during cooling between these two tests.

It is considered that the difference in transformation peaks on heating may come from the unrecrystallised structure, which masks the occurrence of phase transformation during heating for the first run.

As demonstrated earlier (Figure 8.4) the as-received microstructure of *MA957-Ni-A* consists of deformed ferrite and softer equiaxed ferrite. The enthalpy change during the formation of austenite below about 1360 K is positive, *i.e.*, the $\alpha \rightarrow \gamma$ transformation by an absorption of heat (Kaufman *et al.*, 1963). The deformed ferrite on the other hand releases stored energy on heating to elevated temperatures and those phenomena therefore oppose each other. It is not then surprising that on the first run only, the $\alpha \rightarrow \gamma$ transformation peak is masked.

Figure 8.13 shows the DSC curves for *MA957-Ni-B* steel. The results are similar to those of *MA957-Ni-A* although the peaks are less obvious because of smaller tendency to form austenite. DSC measurements on *MA957-Ni-C* and *MA957-Ni-D* steels failed to detect the transformation peaks (Figure 8.14, Figure 8.15), consistent with the dilatometry tests.

As summaried the transformation temperatures by *MTDATA* calculations, Dilatometry test, and DSC measurement, a good consistence among these transformation temperatures is obtained, as shown in Table 8.7 for *MA957-Ni-A* and in Table 8.8 for *MA957-Ni-B* steels, respectively.

(a) First run

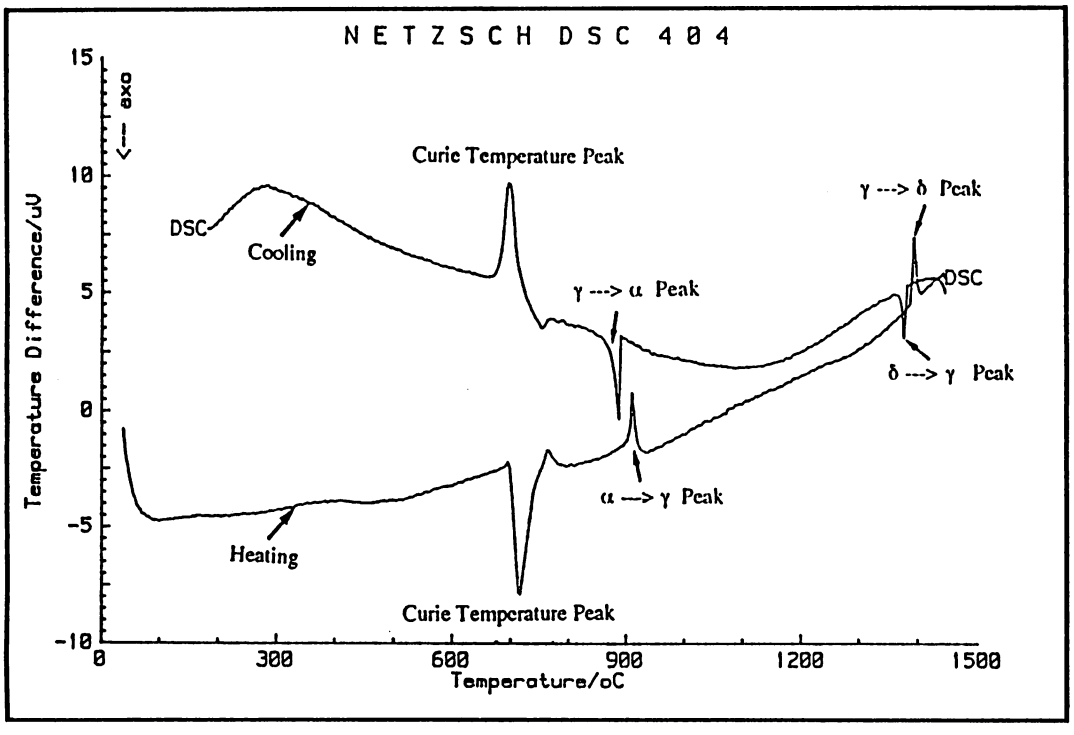

(b) Second run

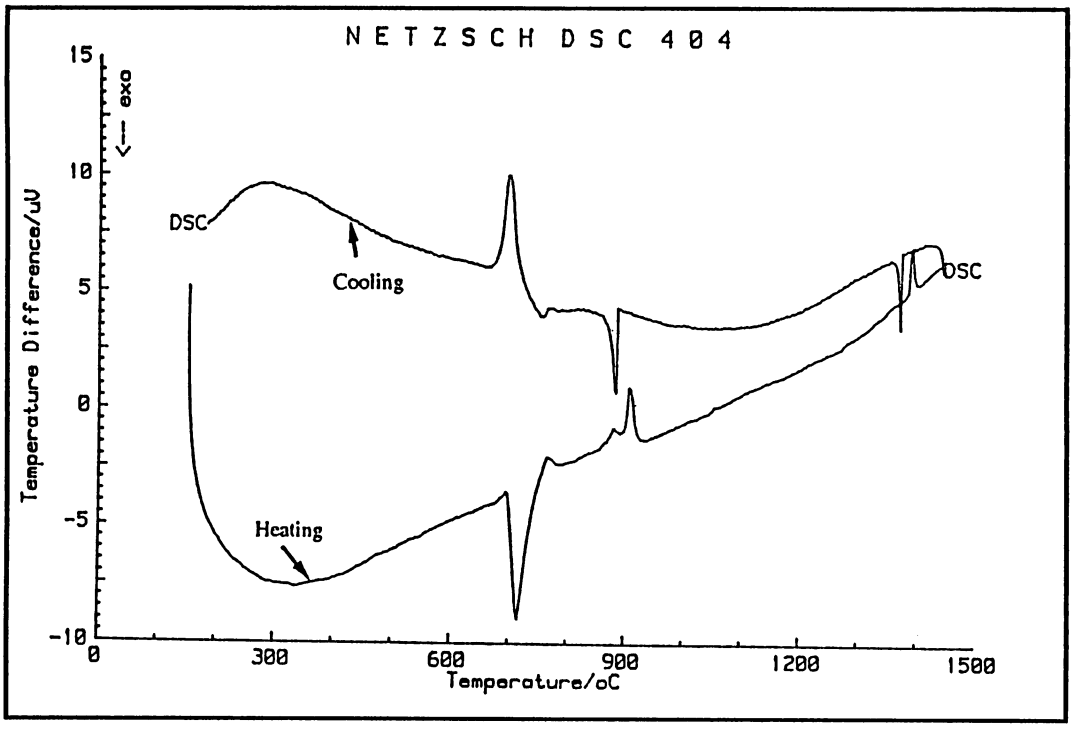

Figure 8.11: DSC curves of conventional mild steel to clarify the transformation peaks for the on going DSC measurements on *MA957Ni* steels (heated and cooled at the rate of 20 °C min^{-1}).

(a) First run

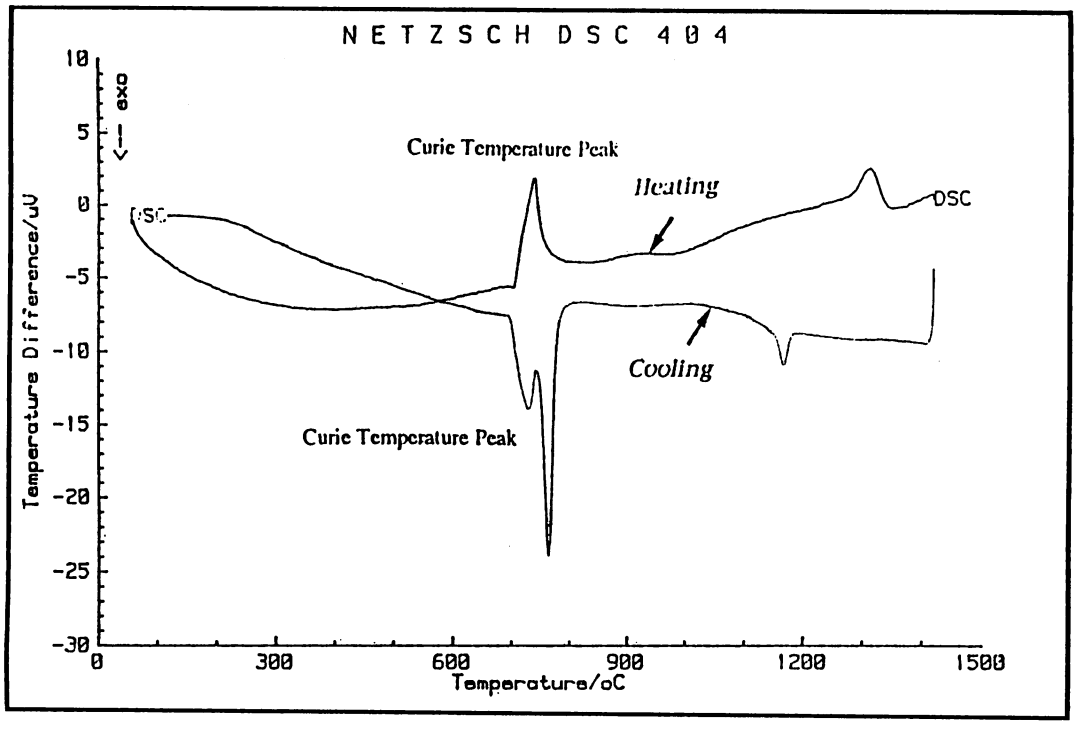

(b) Second run

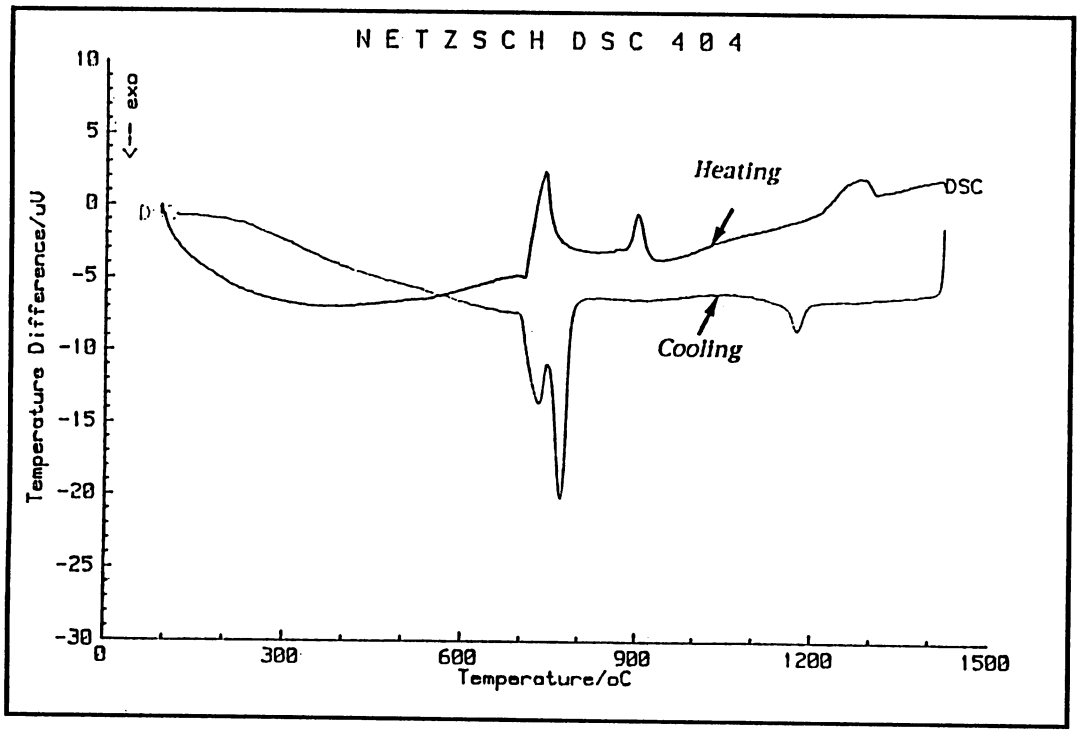

Figure 8.12: DSC curves of *MA957-Ni-A* steel heated and cooled at the rate of 20 °C min^{-1}.

(a) First run

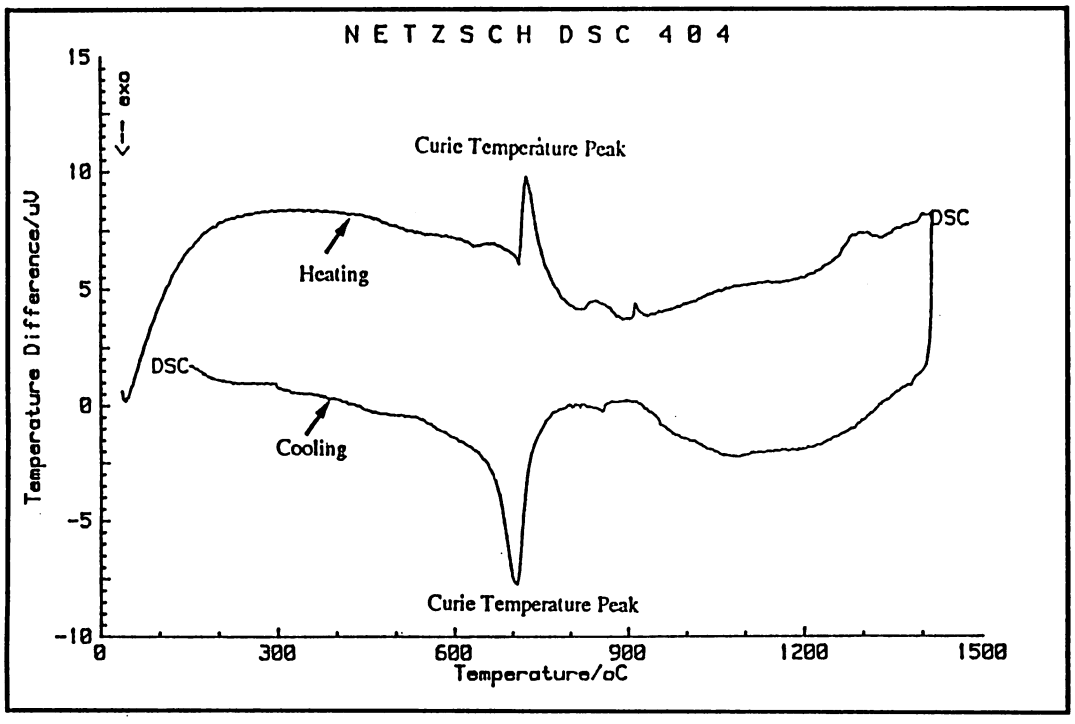

(b) Second run

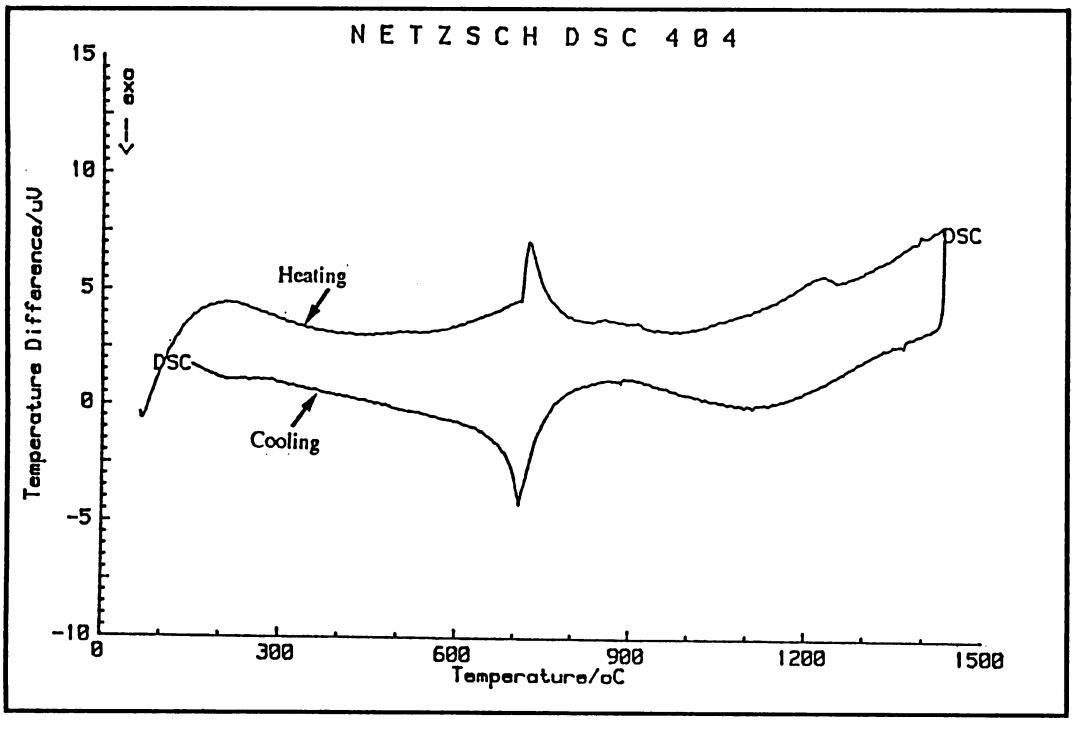

Figure 8.13 DSC curves of *MA957-Ni-B* steel heated and cooled at the rate of 20 °C min^{-1}.

(a) First run

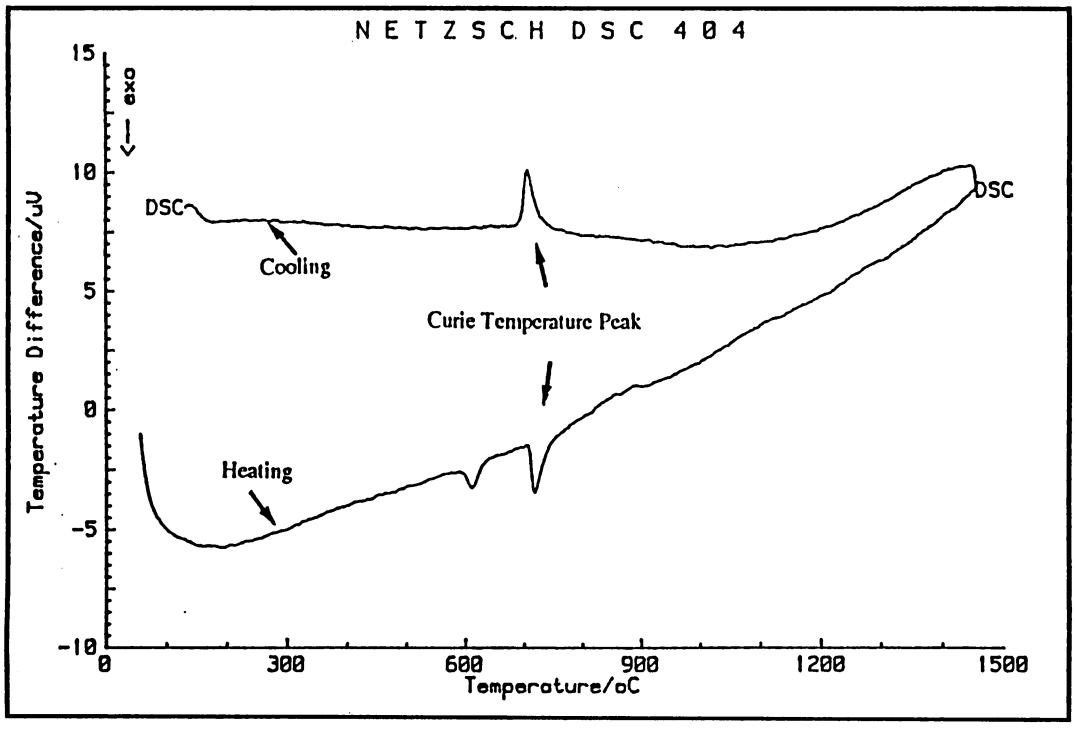

(b) Second run

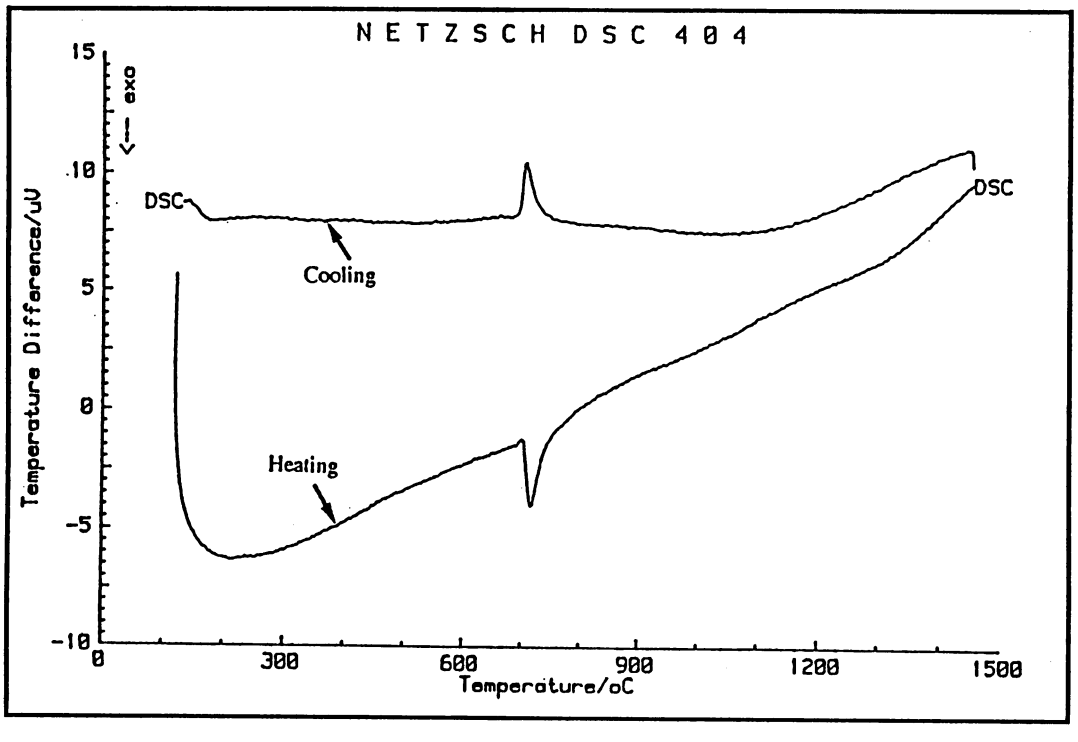

Figure 8.14 DSC curves of *MA957-Ni-C* steel heated and cooled at the rate of 20 °C min^{-1}.

(a) First run

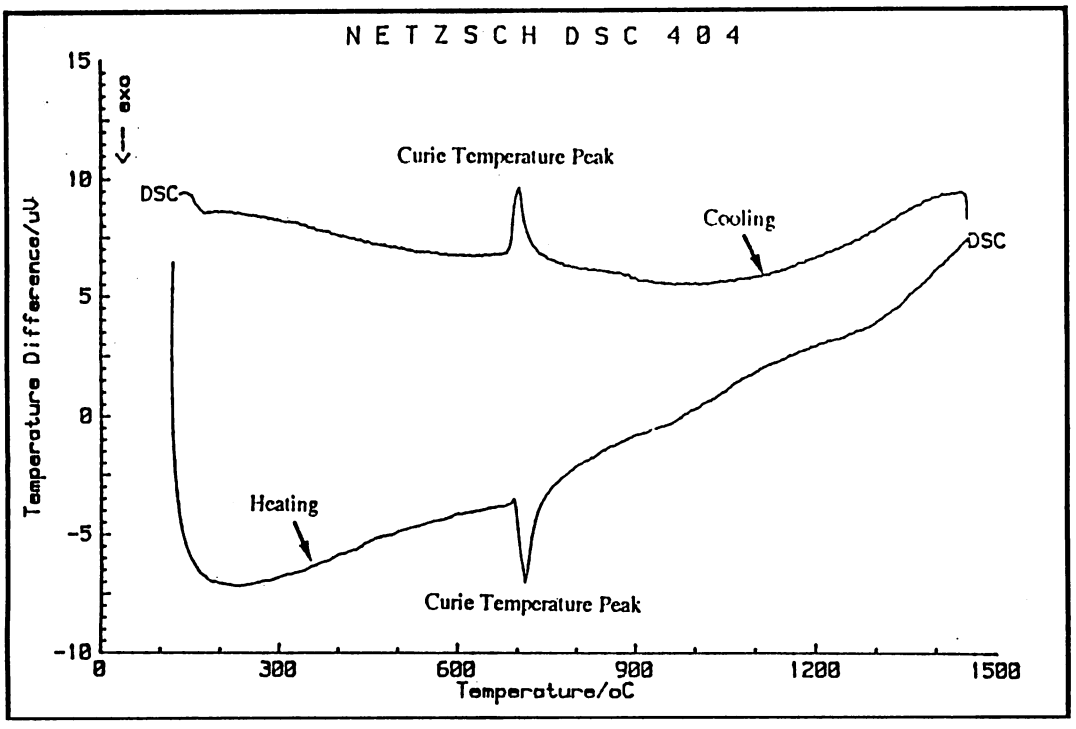

(b) Second run

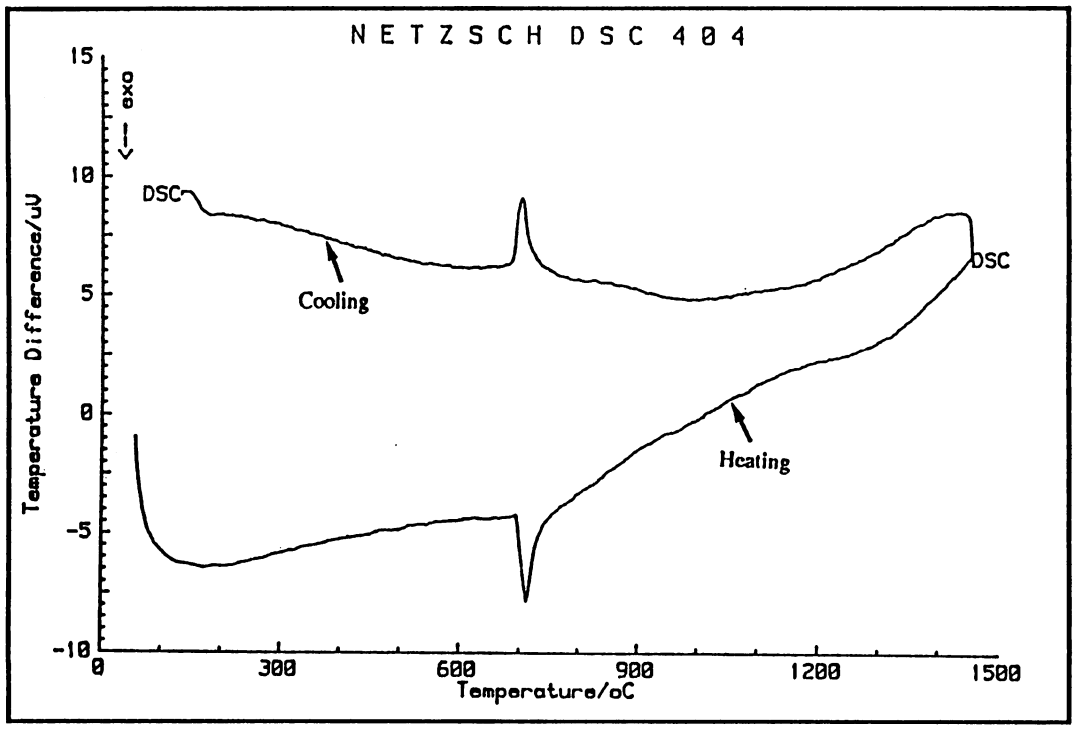

Figure 8.15 DSC curves of *MA957-Ni-D* steel heated and cooled at the rate of 20 °C min^{-1}.

Temperature °C		T_{s_1}	T_{f_1}	T_{s_2}	T_{f_2}
MTDATA Calculations		790	860	1170	1270
Dilatometer Test	Heating	820	880	1167	1230
DSC Measurement	Heating (first run)	830	–	1270	1350
	Heating (second run)	830	910	1200	1270

Table 8.7 Comparison of transformation temperatures among *MTDATA* calculations, dilatometry test, and DSC measurement in *MA957-Ni-A* steel. For first run results, the lower temperature phase transformation peak couldn't be detected. T_{s_1}: the start of $\alpha \rightarrow \gamma$ transformation, T_{f_1}: the finish of $\alpha \rightarrow \gamma$ transformation, T_{s_2}: the start of $\gamma \rightarrow \delta$ transformation, and T_{f_2}: the finish of $\gamma \rightarrow \delta$ transformation.

Temperature °C		T_{s_1}	T_t	T_{f_2}
MTDATA Calculations		800	960	1200
Dilatometer Test	Heating	820	950	1180
DSC Measurement	Heating (first run)	830	–	1320
	Heating (second run)	830	960	1250

Table 8.8 Comparison of transformation temperatures among *MTDATA* calculations, dilatometry test, and DSC measurement in *MA957-Ni-B* steel. At first run results, the lower temperature phase transformation peak couldn't be detected. T_{s_1}: the start of $\alpha \rightarrow \gamma$ transformation, T_t: the transition from the $\alpha \rightarrow \gamma$ to $\gamma \rightarrow \delta$ transformation, and T_{f_2}: the finish of $\gamma \rightarrow \delta$ transformation.

8.3.5 Crystallographic Texture

{2 0 0} and {1 1 0} partial pole figures were measured to evaluate the effect of austenite phase on the deformation texture. Figures 8.16 and 8.17 illustrate the relative pole figures of the steels. All of the steels have a < 110 >-fibre, and the intensity of the fibre increases with decreasing austenite volume fraction at the deformation temperature, except that for *MA957-Ni-C* steel. Since *MA957-Ni-C* alone contains significant amount of martensite, the complex crystallographic variants should lead to a more random texture. Figure 8.18 shows a condensed analysis on the "α-fibre" of as-received *MA957-Ni* steels. For *MA957Ni-A* steel which has a fully austenitic structure during the hot-working temperature range results in the weakest fibre intensity. A stronger fibre intensity is recorded in *MA957-Ni-D* steel, which has the lowest of austenite contents at the deformation temperature.

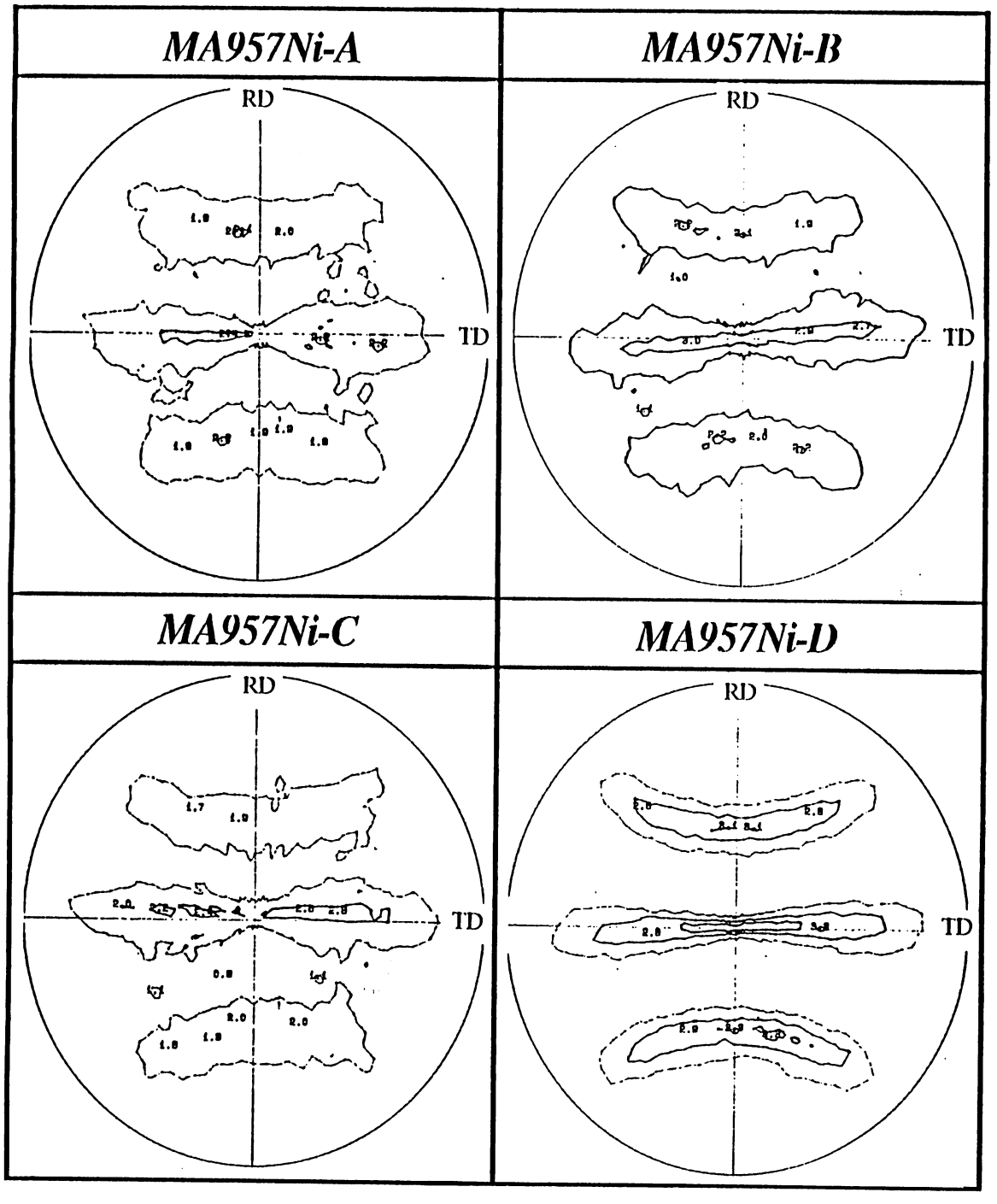

Figure 8.16: The {2 0 0} partial pole figures of as-received *MA957-Ni* steels.

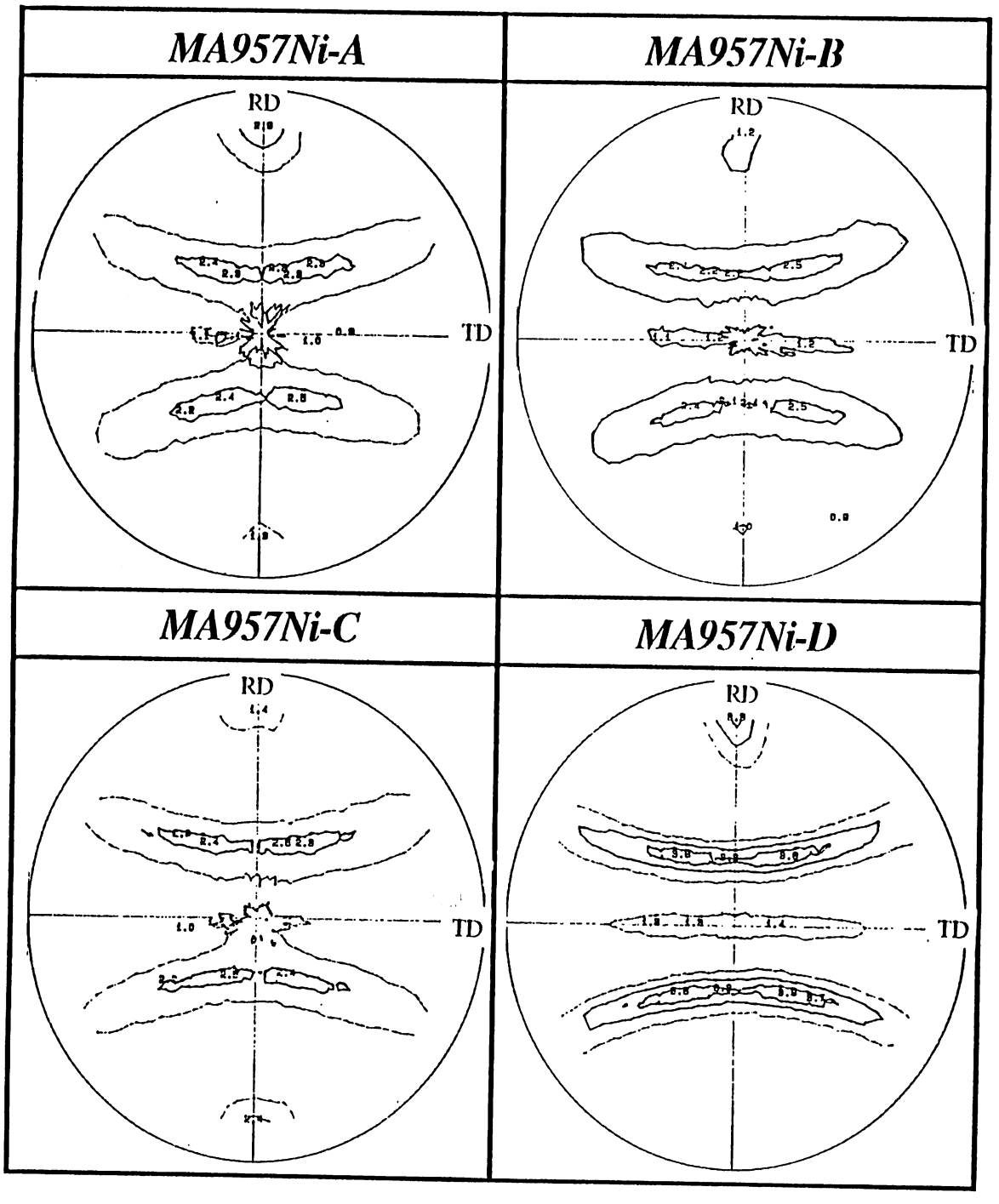

Figure 8.17: The {1 1 0} partial pole figures of as-received *MA957-Ni* steels.

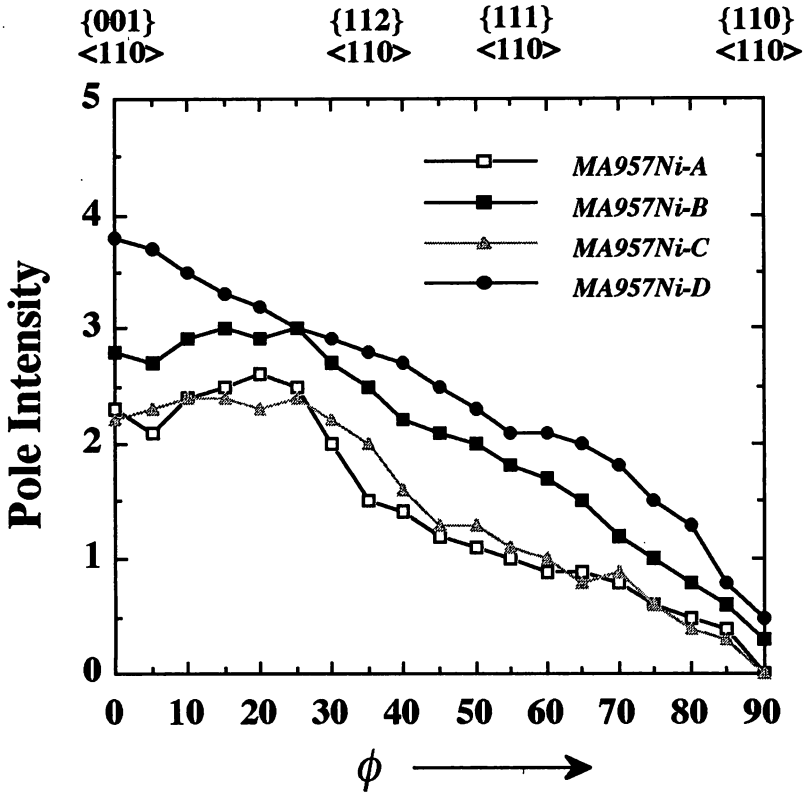

Figure 8.18: The analysis of α-fibre on as-received *MA957-Ni* steels.

When compared with the relatives of conventional *MA956* and *MA957* steels (Chapter 4), a stronger γ–fibre can never be found either in *MA957* or modified *MA957-Ni* steels. It is also noticed that the texture of modified *MA957-Ni-D* is similar to *MA957*, except a stronger $\{001\} < 110 >$ component in *MA957-Ni-D*, which is attributed to the transformation product from the $\{001\} < 100 >$ cube component of deformed austenite at extrusion temperature into ferrite on cooling.

8.4 CONCLUSIONS

The microstructures and transformation behaviours of modified *MA957–Ni* steels have been investigated. It is found that the generation of austenite can be promoted by adding half a weight percent of nickel and further enhanced by decreasing the chromium content. The generation of austenite at the hot-working temperature significantly affects the microstructure obtained at room temperature. Equiaxed ferrite grains with the grain diameter up to 5 μm and with a low dislocation density due to transformation of austenite associated with bands of deformed ferrite. Martensite forms from austenite in *MA957-Ni-C*, consistent with its high hardness in the as-received state. *MA957-Ni-D* shows an elongated deformed ferrite which is like that of conventional *MA957*.

These interpretations are based on a consistent set of data generated using microscopy, dilatometry, differential scanning calorimetry and crystallographic texture data. Further work is needed to study the properties of the new alloys.

CHAPTER NINE

METAL-METAL-COMPOSITE AND THE EFFECT OF PREANNEALING *MA956* STEEL

9.1 INTRODUCTION

MA956 is so heavily alloyed with chromium and aluminum that austenite formation cannot be induced by small compositional modifications, as was done for *MA957* (Chapter 8). One way of overcoming this difficulty would be to make a composite metal, fabricated by extruding a mechanical mixture of *MA956* and *MA957-Ni* powders, each of which is produced seperatedly by mechanical alloying. This metal-metal-composite (MeMeC) would then be inhomogeneous, some regions (*MA957-Ni*) being transformable to austenite. These regions could then be exploited as a means to control the grain structure; this idea forms the basis of the present Chapter.

In addition, preannealing experiments aimed at refining the recrystallised grain structure of conventional *MA956* steel are also reported.

9.2 EXPERIMENTAL PROCEDURE

The composite alloy, "MeMeC", was prepared by blending 80 wt.% of standard *MA956* powder with 20 wt.% of modified *MA957-Ni-B* powder. The compositions of these two steels are given in Table 3.1 and Table 8.1 respectively. The mixture of powders were then canned in mild steel and reduced by extrusion from 2-inch diameter to half inch diameter at 1070 °C. Unlike conventional *MA956* and *MA957*, the "MeMeC" was not further hot-rolled after extrusion.

To study the recrystallisation behaviour, samples 3 mm square by 10 mm long were cut from the as-received rod and sealed in quartz tubes containing argon for heat treatment in a programmable induction furnace. After isothermal annealing at high temperatures the fully recrystallised "MeMeC" sample was cooled into the $\delta + \gamma$ phase region to form some austenite in order to induce grain refinement by phase transformation. An alternative heat treatment route involved a preanneal (without recrystallisation) followed by elevated temperature heat treatment to induce recrystallisation.

Optical microscopy was used to observe the microstructures both of the as-received and heat treated specimens. The etchant used was 2g $CuCl_2$, 40 ml HCl, and 40 to 80 ml ethanol. Transmission electron microscopy was carried out using a *Philips EM400* microscope operated at 120 kV.

A *Siemens 200* X–ray diffractometer with a pole figure goniometer was employed to measure the bulk textures by recording the {2 0 0} and {1 1 0} pole figures from longitudinal sections. Transmission electron microscopy and electron diffraction were used to carry out the microtexture analysis.

9.3 RESULTS AND DISCUSSION

9.3.1 MeMeC Effect

9.3.1.1 As-Received Microstructure

Figure 9.1 shows the longitudinal and transverse sections of the extruded "MeMeC" steel along with the parent steels *MA956* and *MA957-Ni-B*. It is found that significant difference on the contrast existed in the as-received "MeMeC" steel in comparison with the as-received structures of parent steels, *MA956* and *MA957-Ni-B*. In spite of the differences in etching contrast, the microhardness (Table 9.1) was found to be virtually identical throughout the "MeMeC" sample. The white contrast regions were investigated further using transmission electron microscopy. Samples were sliced from the extruded "MeMeC" rod parallel with the longitudinal direction. The slice was etched to reveal the different contrast features, and the white region was punched out for TEM study. Figure 9.2 illustrates the submicron cold-deformed grain structure revealed by transmission electron microscopy. The observed microstructure is consistent with the hardness data in that there is evidence for heavy deformation in the white-etching regions, which are as hard as the dark-etching regions.

Microanalysis using scanning electron microscopy showed that the dark-etching regions had a composition consistent with *MA956* (Table 9.2), whereas the white regions approximated the composition of *MA957-Ni-B*. The detailed compositions showed some mixing between the two powders, although this is probably not interdiffusion but simply mechanical mixing due to extrusion.

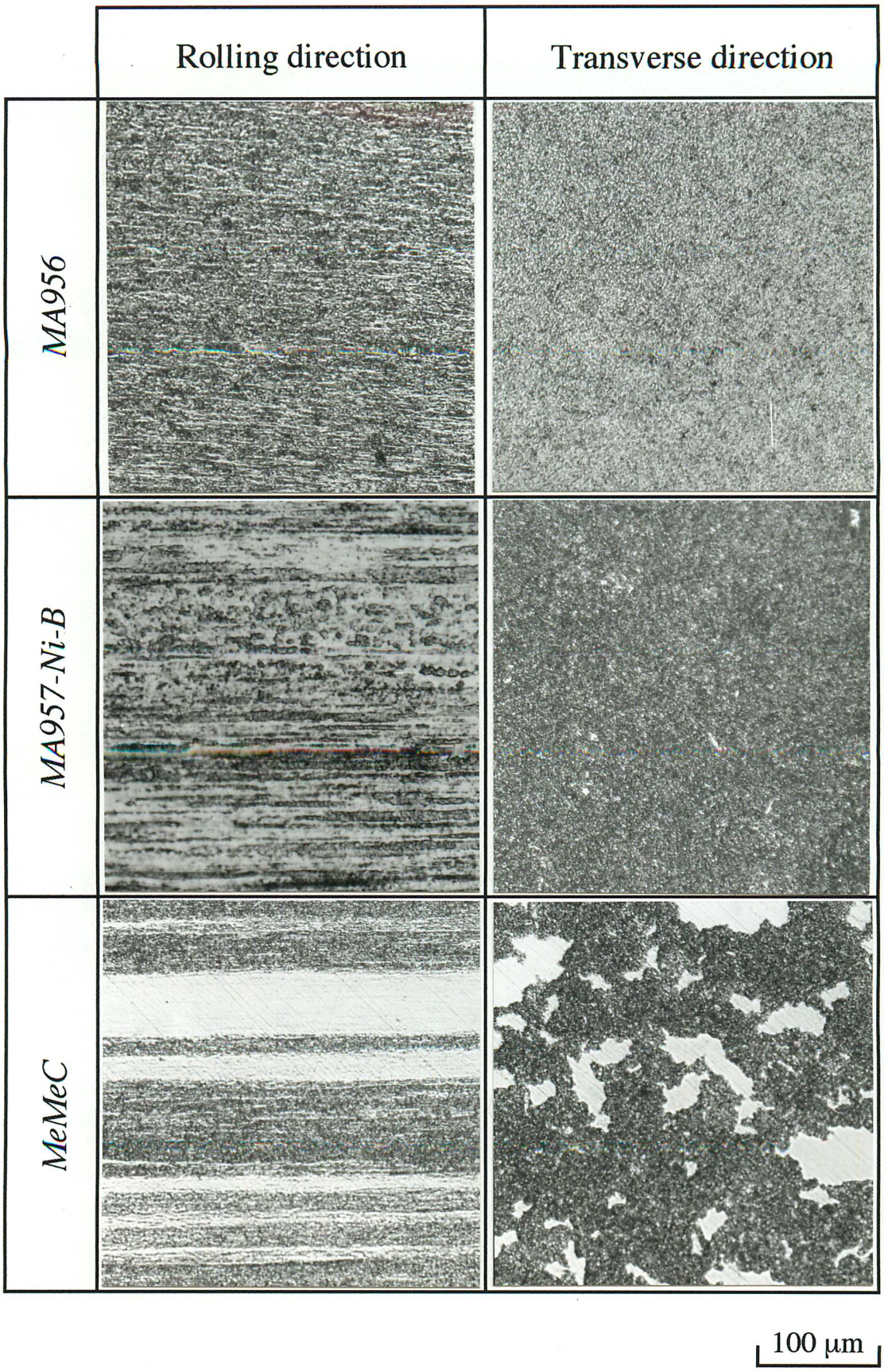

Figure 9.1: Set of optical micrographs illustrating the parent steels and the inhomogeneous microstructure of "MeMeC" in the as-received state.

Figure 9.2: Transmission electron micrograph showing the submicron grain structure taken from the white-etching region of as-received "MeMeC" illustrated in Figure 9.1.

	White Region	Dark Region
Micro-hardness (HV/ 0.5N)	453	490
	480	501
	494	463
	494	497
	490	494
Average	482	489

Table 9.1 Microhardness recorded from white and dark regions on as-received "MeMeC" steel (The hardness values recorded by microhardness test are higher than those by macrohardness test.

Alloy	Cr	Ti	Mo	Ni
MA956	20.0	0.50	–	–
MA957-Ni-B	12.54	0.99	0.26	0.57
MeMeC White-region	15.72 $\pm$ 0.25	0.98 $\pm$ 0.10	NA	0.57 $\pm$ 0.15
MeMeC Dark-region	21.67 $\pm$ 0.27	0.47 $\pm$ 0.09	NA	0.20 $\pm$ 0.14

Table 9.2 Chemical compositions, wt.%

9.3.2 Recrystallised Microstructure

To induce recrystallisation, the composite was heat treatment at 1250 °C, the temperature at which *MA956* normally recrystallises. However, optical metallography showed that the heat-treated sample remained unrecrystallised (Figure 9.3a). Annealing at 1300 °C for one hour still failed to produce a recrystallised microstructure (Figure 9.3b). The hardness data listed in Table 9.3 indicated that recrystallisation did finally occur after heat treatment at 1350 °C and this was confirmed metallographically, as illustrated in Figure 9.4.

Heat Treatment Temperature, °C	As-received	1250	1300	1350
Hardness, HVN 20kg	360	301	293	225

Table 9.3 Hardness data for MeMeC in a variety of conditions. The samples were heat-treated at the temperatures indicated for an hour in each case.

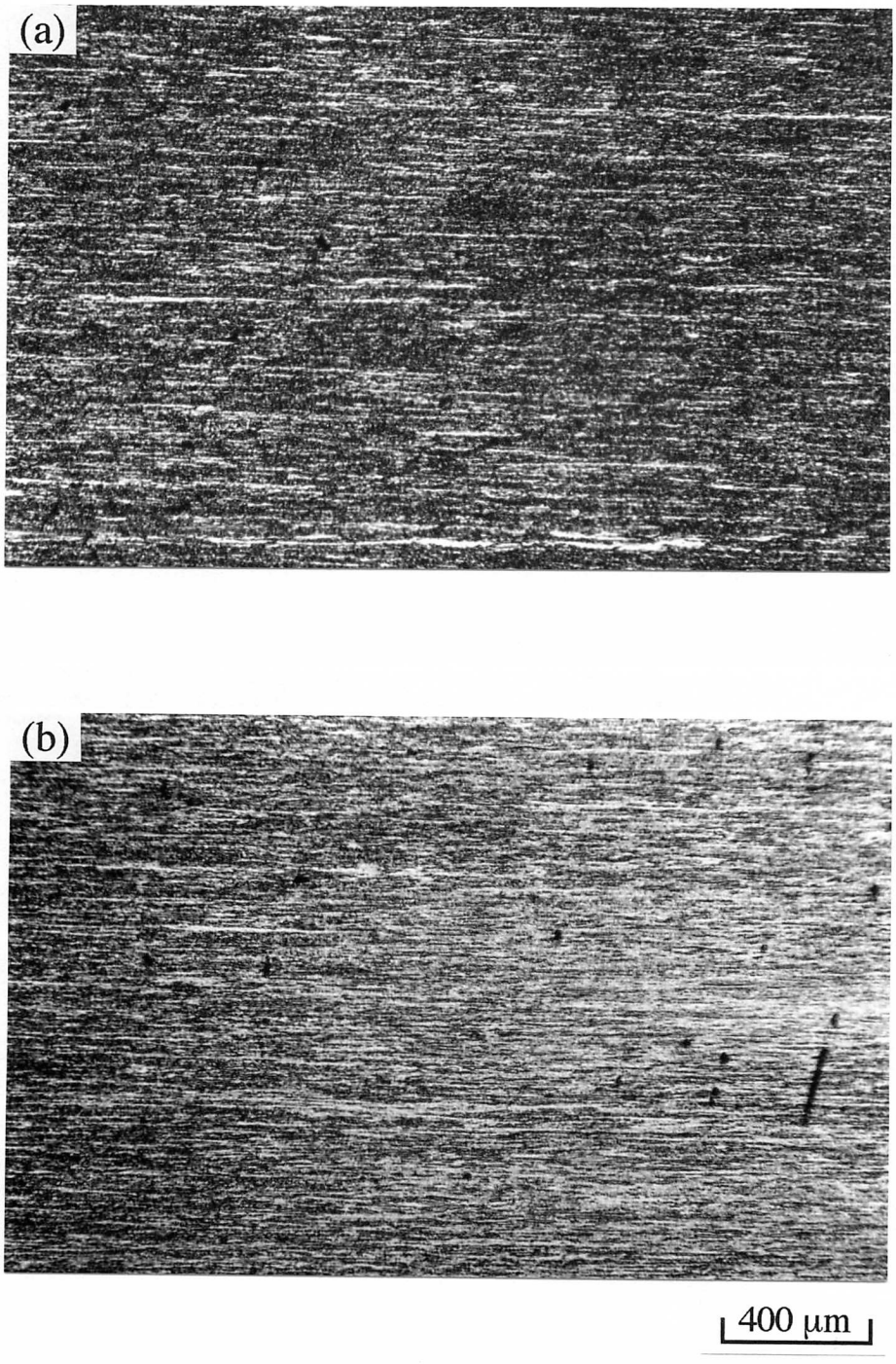

Figure 9.3: Optical microstructures of MeMeC steel isothermally annealed at (a) 1250, and (b) 1325 °C for one hour.

Figure 9.4: Recrystallised grain structure of MeMeC steel as-annealed at 1350 °C for one hour.

Figure 9.5 illustrates the DSC curve of MeMeC steel. It confirms that recrystallisation occurs at temperature in excess of 1315 °C, which is higher than the temperature 1250 °C associated with *MA956*. Moreover, the measured stored energy (0.28 J g^{-1}) is lower than that of *MA956* steel (around 0.4 J g^{-1}). This may be because the *MA957-Ni-B* regions lose their stored energy on transformation during heating to the recrystallisation temperature. In addition the deformation texture (Figure 9.6) shows that unlike the strong $\{1\ \bar{1}\ 1\} < 1\ 1\ 0 >$ component in as-received *MA956*, the MeMeC contains two major components $\{1\ \bar{1}\ 5\} < 1\ 1\ 0 >$ and $\{1\ \bar{1}\ 2\} < 1\ 1\ 0 >$. These are expected to have a relatively lower energy state (Dillamore *et al.*, 1974).

Figure 9.7 illustrates the microstructure of MeMeC steel after recrystallisation at 1350 °C followed by annealing at 1000 °C for 1 hour. The Widmanstätten ferrite observed in the recrystallised sample is believed to be the product of austenite phase generated during duplex phase annealing.

However, this transformation refinement was found not to be reproducible. Instead of the refined recrystallised grain microstructure, an elongated grain structure was obtained when the experiment was repeated (Figure 9.8). The grain boundary topology of these heat treated steels is different from that of conventional recrystallised *MA956* steel. Ragged grain boundaries are found in recrystallised "MeMeC" steel whereas smooth grain boundaries occur in the recrystallised *MA956* steel (Chapter 4). The indications are that ragged boundaries lead to better mechanical properties, particularly creep resistance (Tanaka *et al.*, 1988).

As mentioned before, the as-received "MeMeC" steel showed an inhomogeneous microstru -cture. The blending state of the powders before extrusion should dominate the development of the recrystallised structure. It has also been mentioned earlier (Chapter 8) that instead of the master alloyed powders used in the making of conventional mechanically alloyed steels, ferrometal powders were used in the fabrication of modified *MA957-Ni* steels.

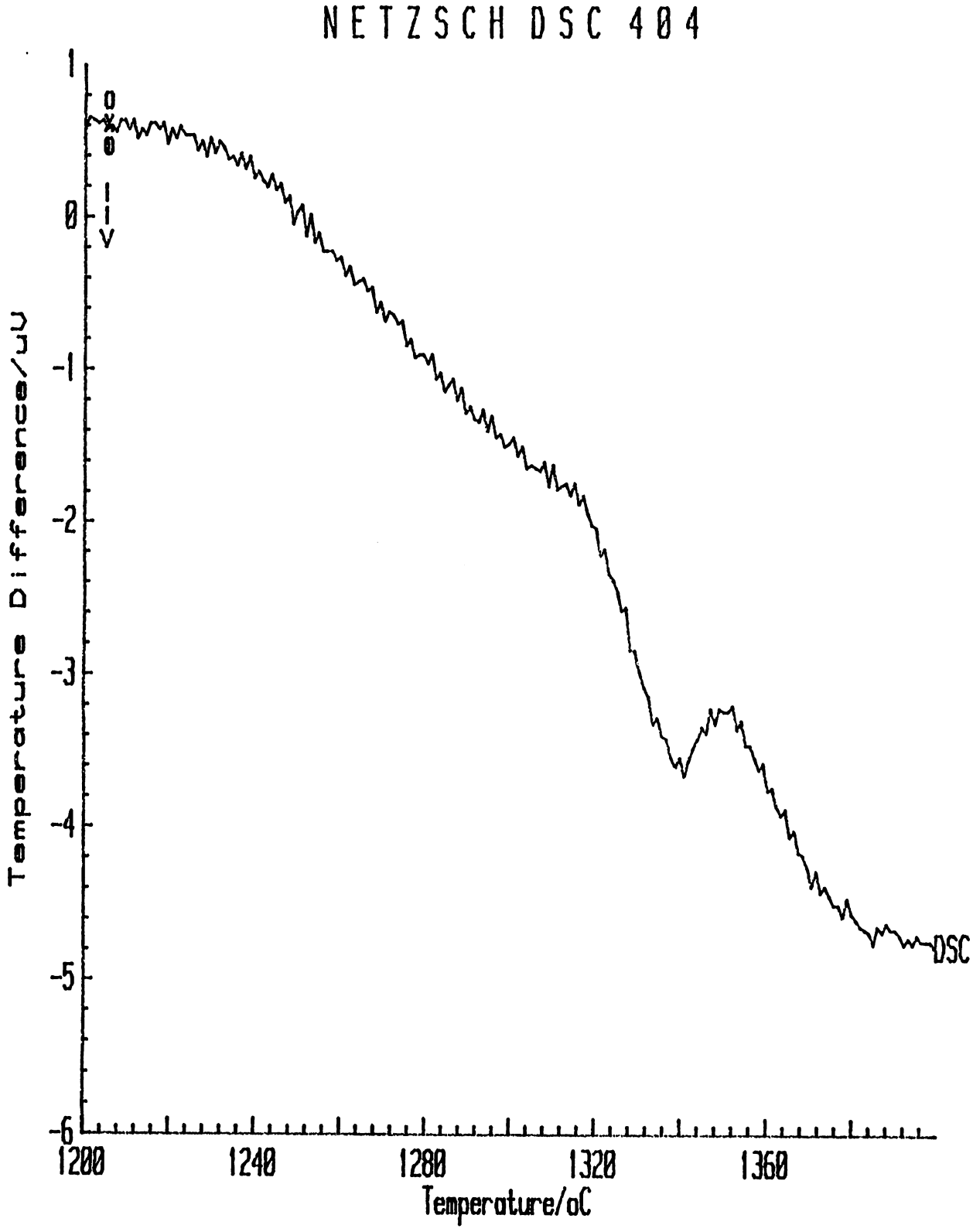

Figure 9.5: DSC curves recorded for MeMeC steel at the rate 20 K min^{-1}.

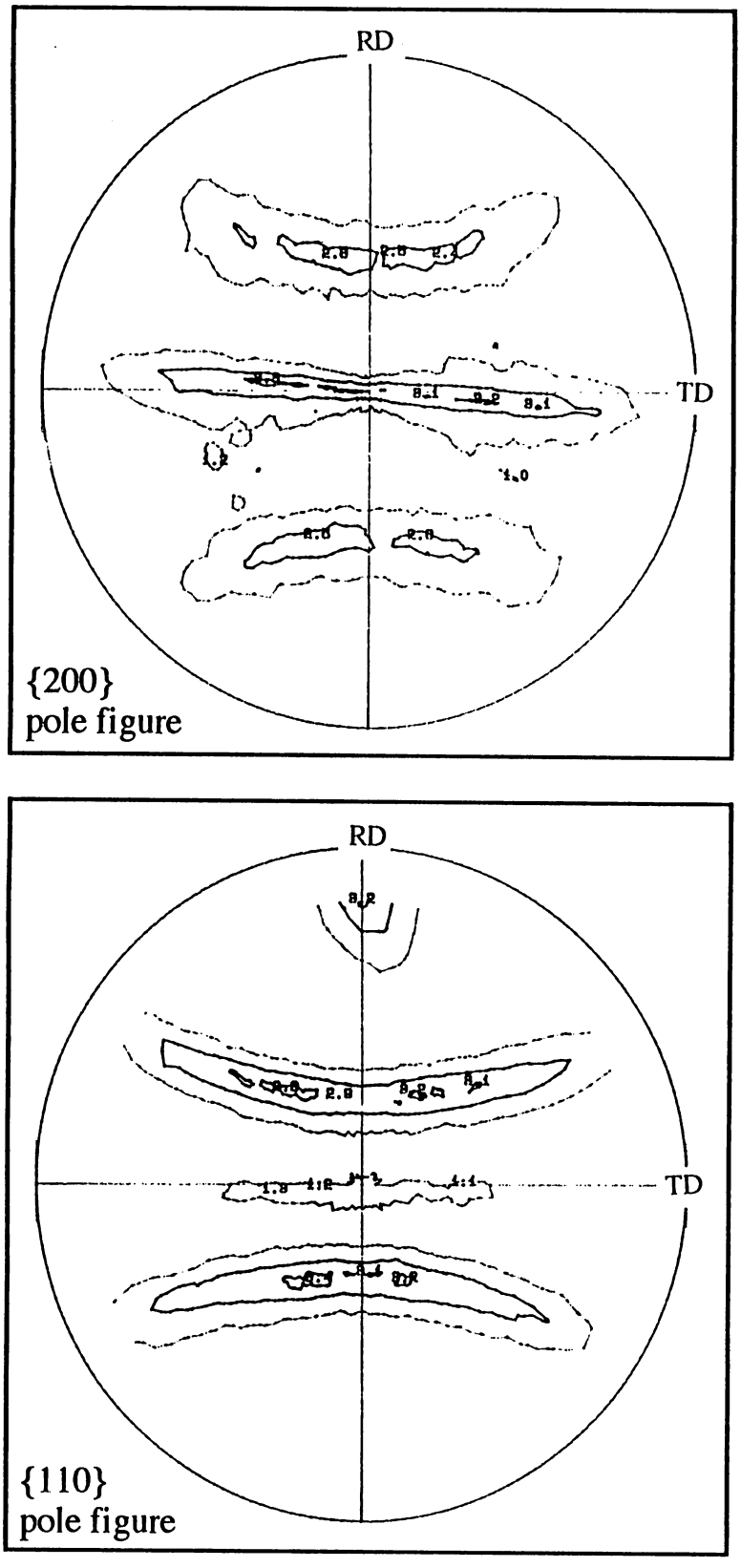

Figure 9.6: The {200} and {110} partial pole figures for "MeMeC" steel (as-received).

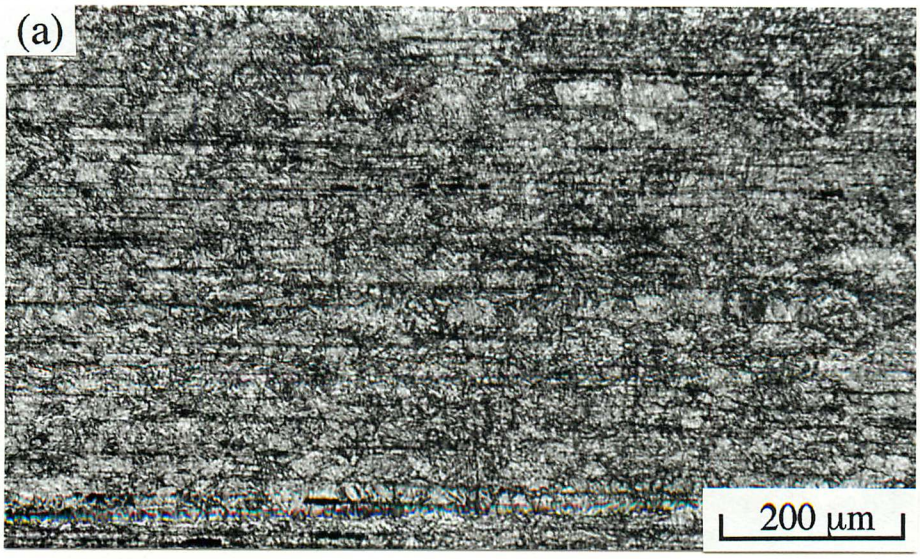

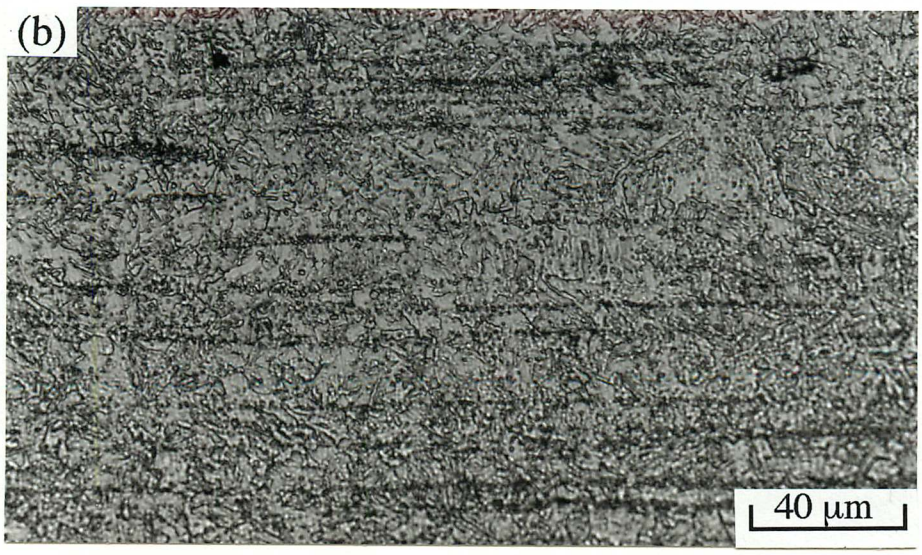

Figure 9.7: Refined grain structure of MeMeC steel, (a) annealed at 1350 °C for one hour, followed by 1000 °C for one hour, (b) as (a) in a larger magnification.

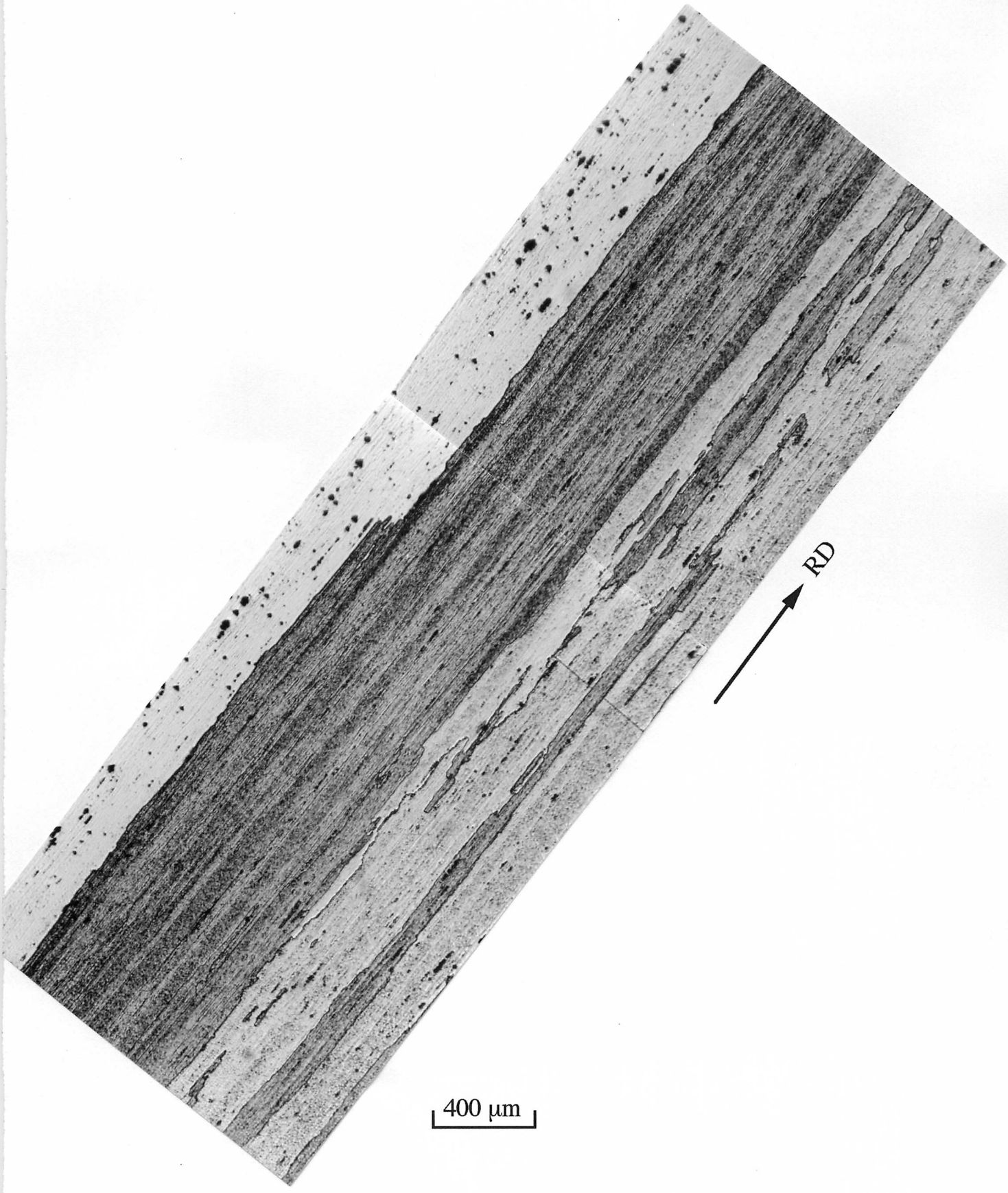

Figure 9.8: The elongated structure of MeMeC steel after repeating the heat treatment illustrated in Figure 9.7.

9.3.2 Preannealing of Conventional MA956

Samples of *MA956* steel were isothermally annealed below the recrystallisation temperature. At first, the preannealing conditions established to refine the recrystallisation structure of *MA957* steel were applied, *i.e.* 1150 °C for more than 160 hours (Chapter 5). However this failed to produce the desired fine grain structure in *MA956* steel. The sample of *MA956* became fully recrystallised after heat treatment at 1150 °C for more than 160 hours (Figure 9.9). The samples also revealed porosity whose origin is not clear.

The results obtained by preannealing at the lower temperature of 1050 °C for a variety of time intervals with a various of holding time are shown in Figures 9.10 and 9.11. Figure 9.10 shows the preannealed microstructures, whilst Figure 9.11 reveals the effect of preannealing followed by recrystallisation at 1250 °C for one hour. It is clear that preannealing leads to a significant change in the recrystallisation microstructure. The grain size and aspect ratio can be controlled by preannealing prior to recrystallisation.

Figure 9.12 – 9.14 illustrate the progress of recrystallisation front during recrystallisation treatment on the samples with and without preannealing. Obviously, the preanneal treatment tends to promote the onset of recrystallisation. A higher recrystallisation fraction is obtained for the samples with preannealing than those without.

These observations are consistent with the behaviour of preannealed *MA957* reported in Chapter 5. The stored energies of both steels decreases during preannealing, whereas the ease with which recrystallisation occurs is enhanced. Therefore, factors other than stored energy alone determine the nucleation sequence. Perhaps the stored energy affects the grain growth rate. Although the as-received samples show a relatively late onset of recrystallisation, the process is completed within a short time as clearly shown in the sequence Figures 9.12 – 9.14.

After extensive studies, the optimum condition for a refined recrystallised grain structure for *MA956* was found to be a recovery treatment at 1050 °C for 10 days followed by recrystallisation at 1250 °C for 20 minutes. A refined grain microstructure with a grain diameter around 50 μm can be obtained as shown in Figure 9.15. Instead of the equiaxed fine grain structure obtained in preannealed plus recrystallised *MA957* steel, the fine grains in *MA956* are elongated. The difference on *MA956* and *MA957* is attributed to the higher yttria content of *MA956*.

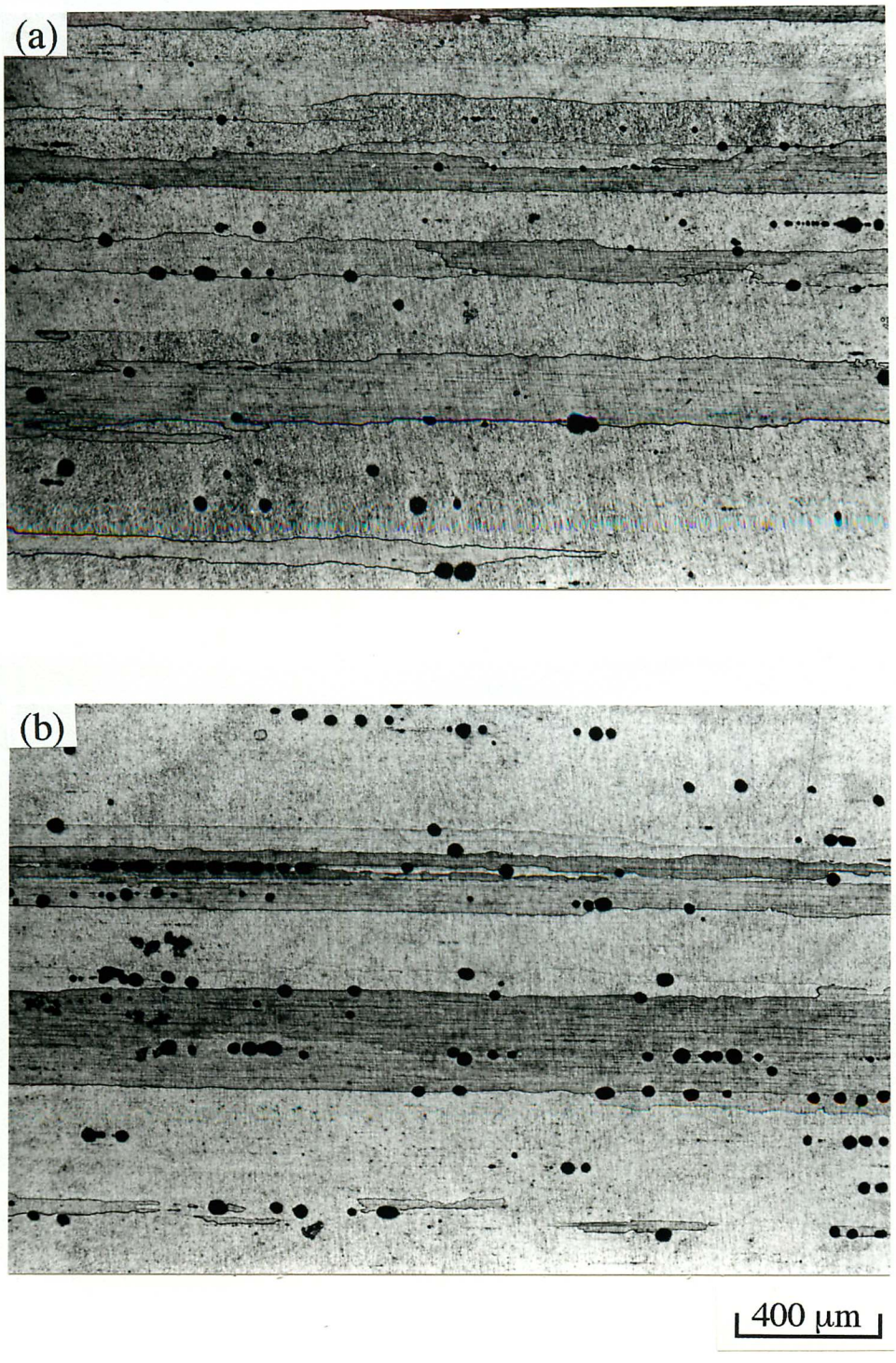

Figure 9.9: Optical micrographs illustrating the fully recrystallised structure of *MA956* steel after isothermal annealing at 1150 °C for (a) 160 , (b) 240 hours.

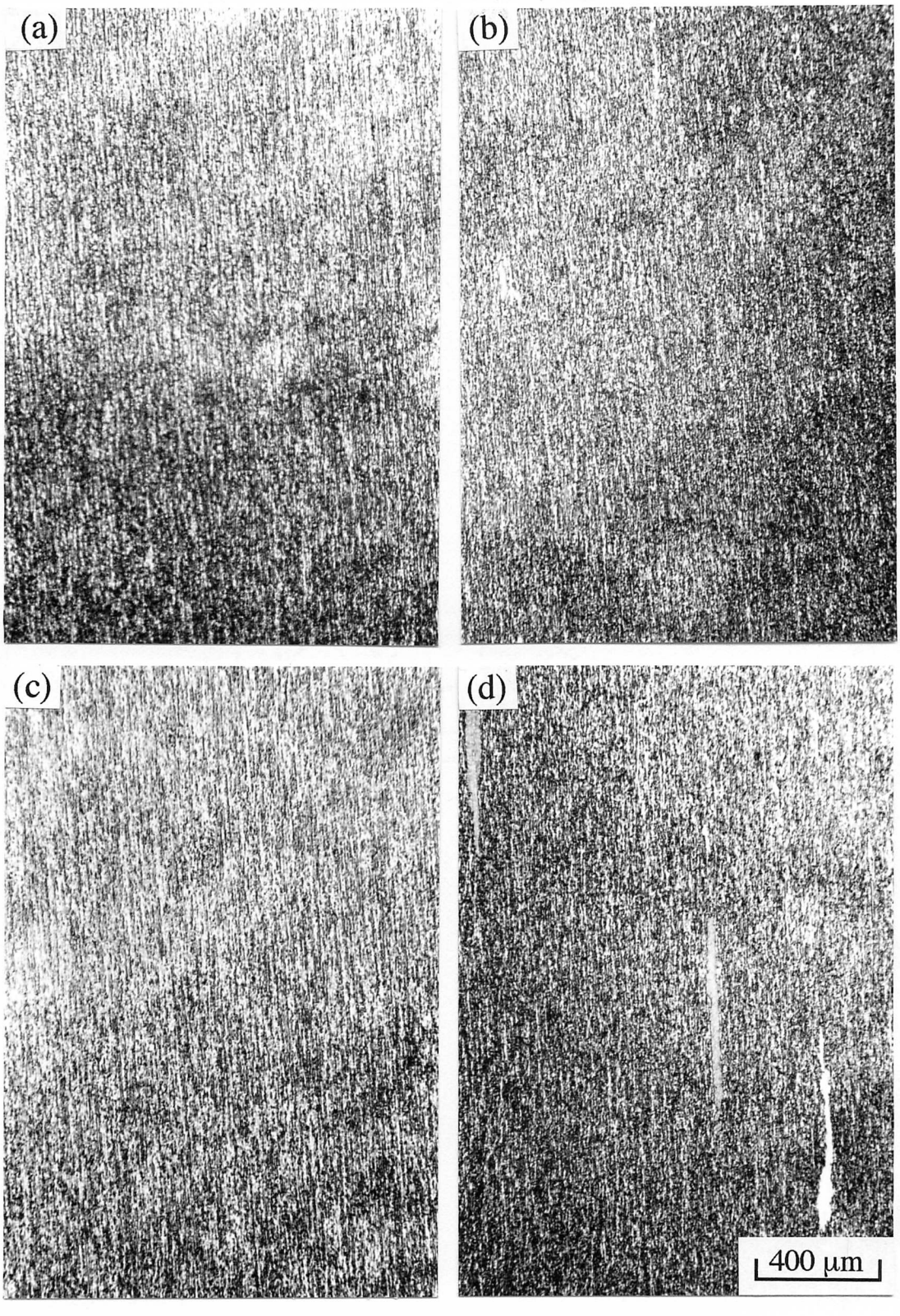

Figure 9.10: Micrographs illustrating *MA956* steel preannealed at 1050 °C for (a) 15, (b) 60, (c) 72, and (d) 120 hours.

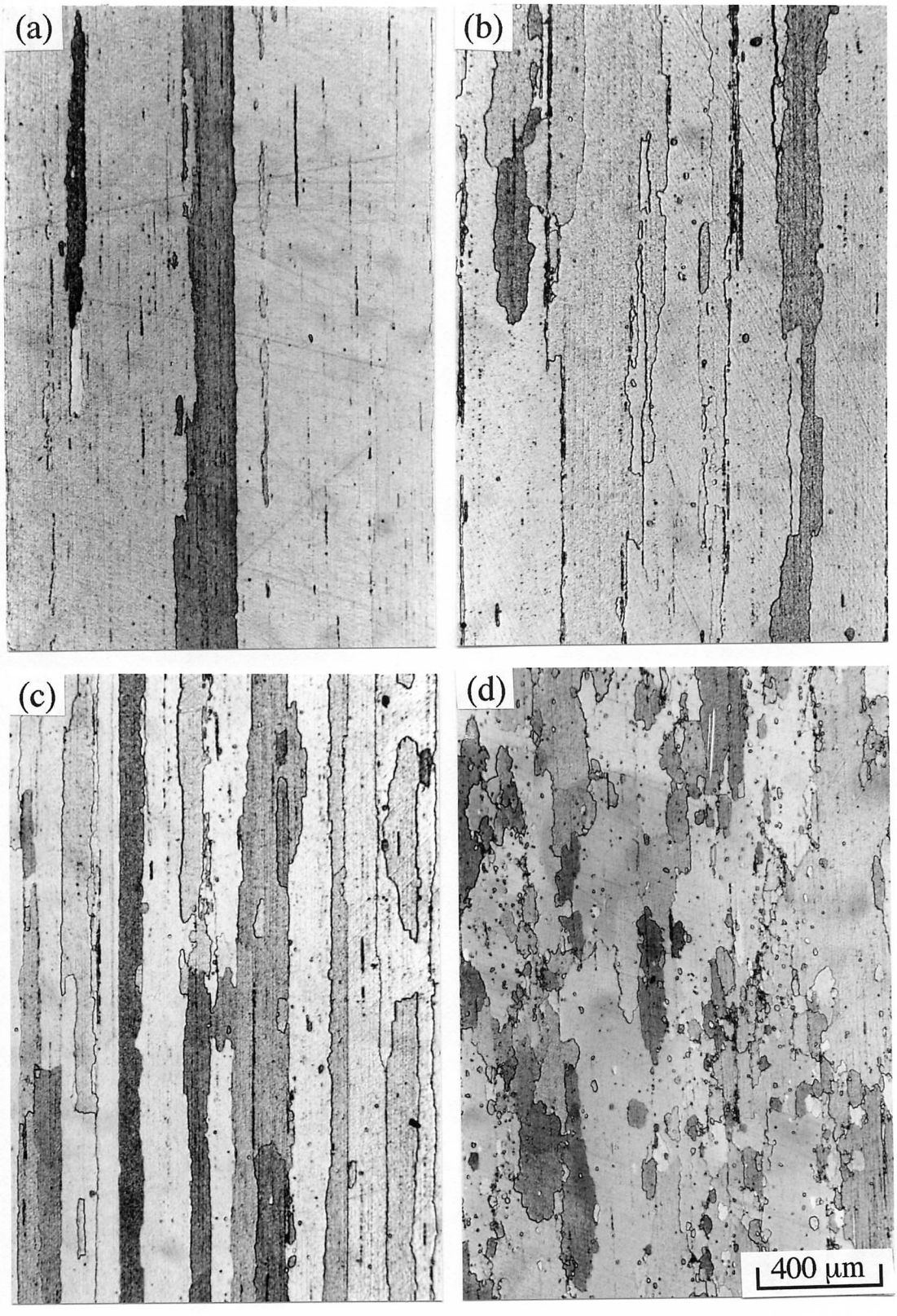

Figure 9.11: Optical micrographs illustrating the recrystallised microstructures of the preannealed samples shown in Figure 9.10.

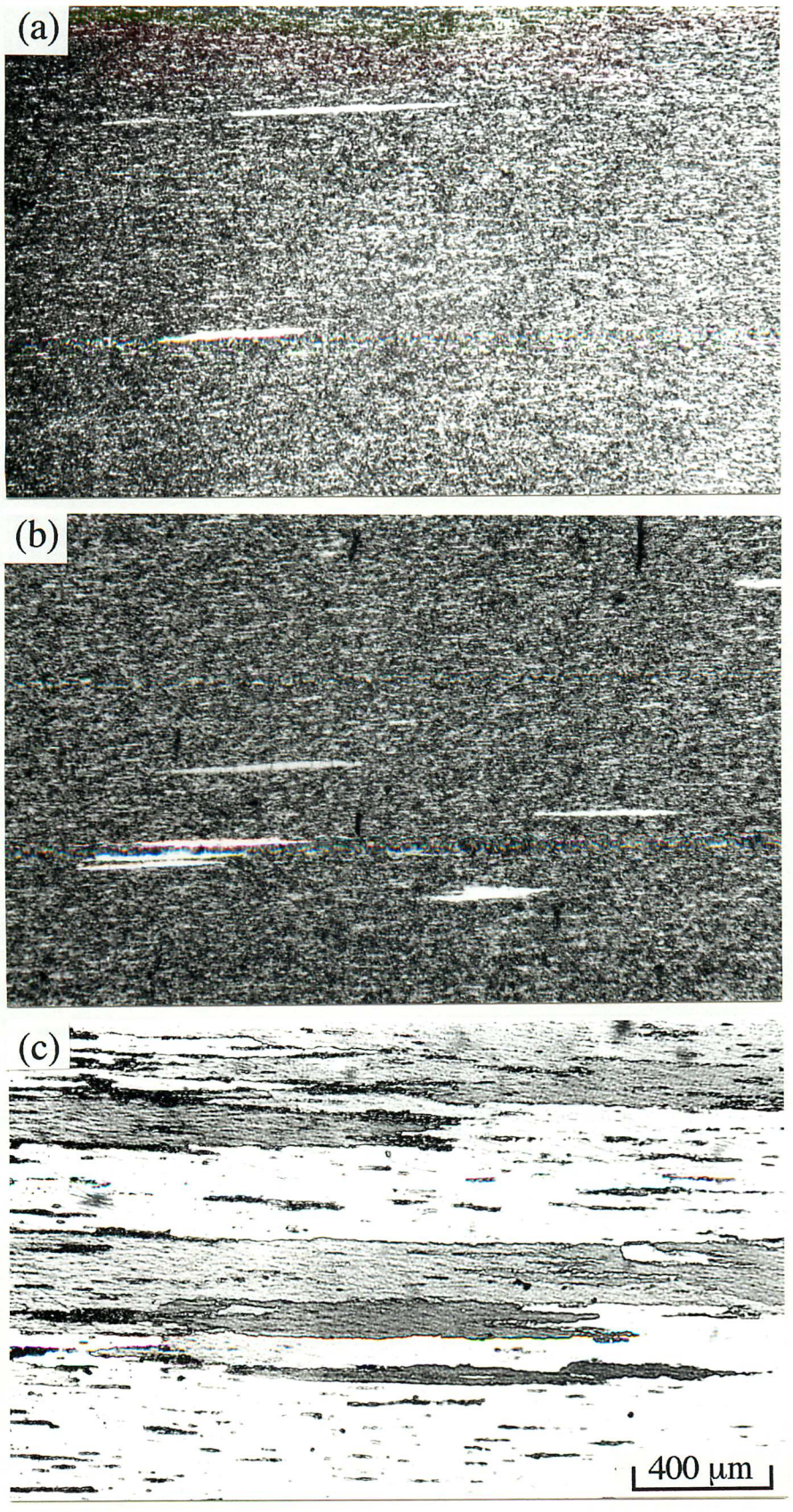

Figure 9.12: Optical micrographs showing the progress of recrystallisation front in as–received *MA956* recrystallised at 1250 °C for (a) 3, (b) 6, and (c) 15 minutes.

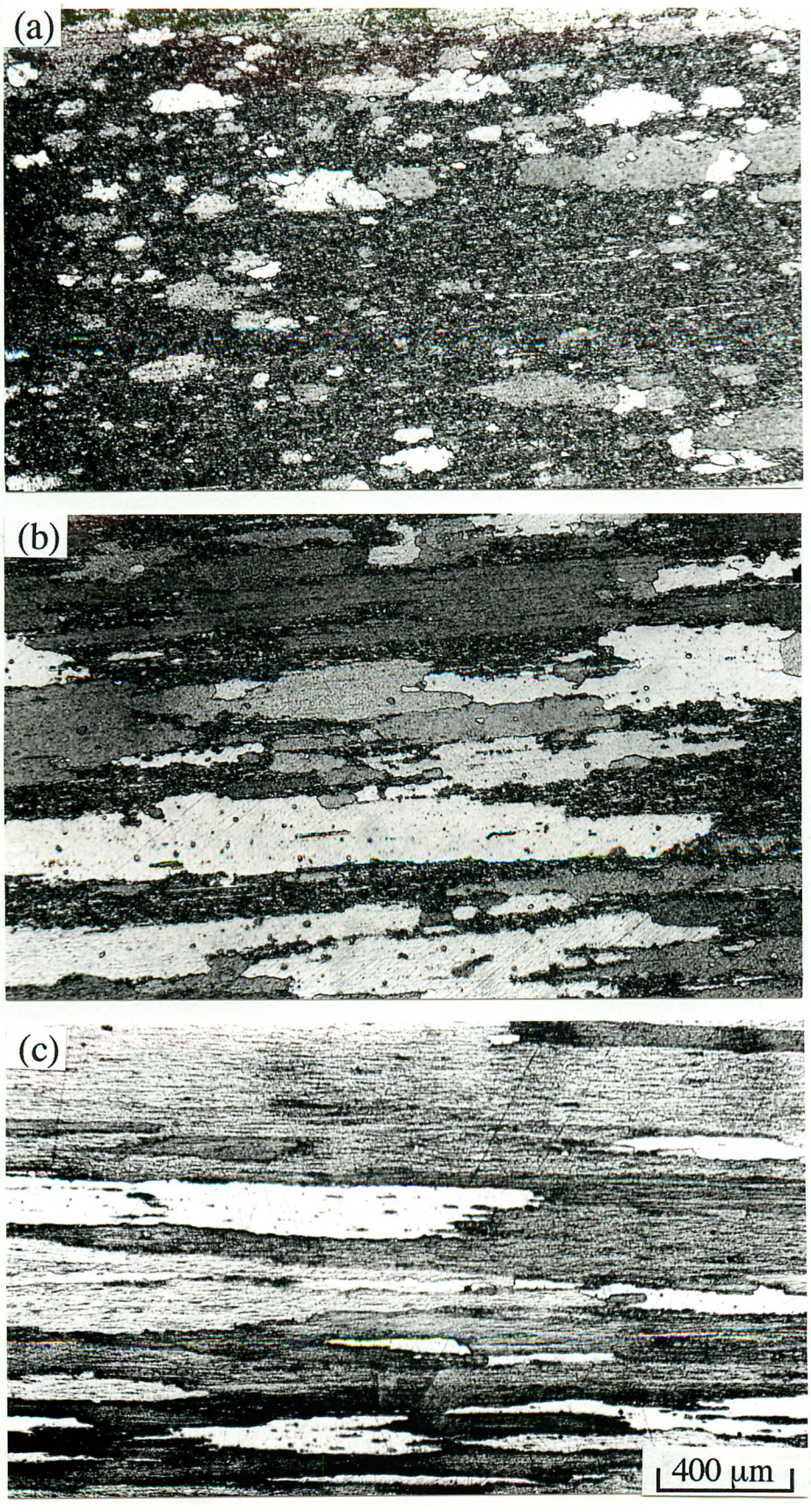

Figure 9.13: Optical micrographs showing the progress of recrystallisation front in *MA956* preannealed at 1050 °C for 60 hours then recrystallised at 1250 °C for (a) 3, (b) 6, and (c) 15 minutes.

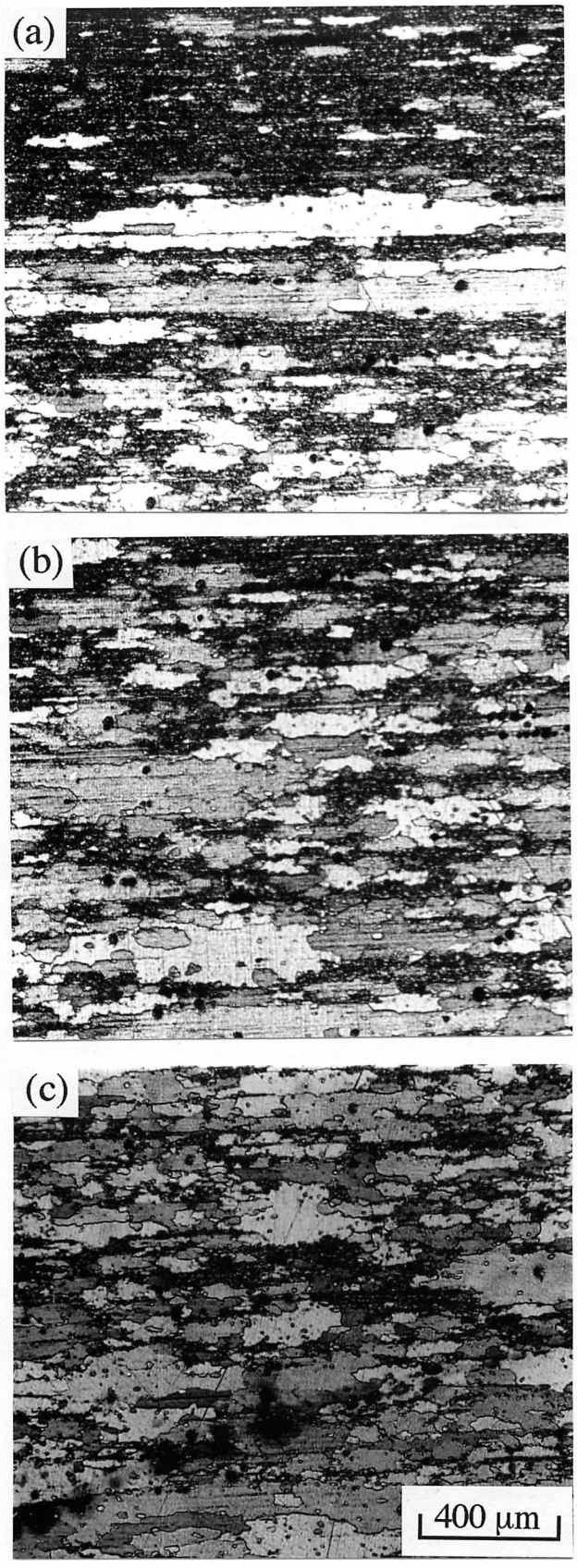

Figure 9.14: Optical micrographs showing the progress of recrystallisation front in *MA956* preannealed at 1050 °C for 120 hours then recrystallised at 1250 °C for (a) 3, (b) 6, and (c) 15 minutes.

Figure 9.15: Fine recrystallisation grain structure of *MA956* steel preannealed at 1050 °C for 240 hours then recrystallised at 1250 °C for 20 minutes.

9.5 CONCLUSIONS

A novel composite steel made from a mechanical mixture of conventional *MA956* and modified *MA957-Ni-B* to form a metal-metal-composite has been investigated and found to give some interesting microstructures whose properties remain to be determined.

In principle, a refined grain structure can be obtained from the transformation of the *MA957-Ni* component of the composite. However, this is found not to be highly reproducible. Detailed investigations of interdiffusion and homogenisation are needed before further progress is possible with the concept of a composite alloy.

Preannealing heat treatments have been demonstrated to be capable of leading to a significant refinement in the recrystallised microstructure of *MA956*. Although refined, the grain structure remains somewhat anisotropic, the long dimensions being parallel to the extrusion direction. This is unlike similarly treated *MA957* in which equiaxed grain structures are obtained, probably because *MA956* has a larger yttria content.

CHAPTER TEN

RECRYSTALLISATION TEMPERATURES IN MECHANICALLY ALLOYED OXIDE DISPERSION STRENGTHENED *MA956* AND *MA957* STEELS

10.1 INTRODUCTION

Before heat–treatment, the mechanically alloyed steels *MA956* and *MA957* have microstructures consisting of sub–micrometre size grains in the cold–deformed condition (Baloch, 1989). Subsequent heating leads to directional recrystallisation at very high temperatures ($\approx$ 0.9 T_m).

Alloy *MA957* recrystallises at a significantly higher temperature than *MA956*, in spite of the fact that it contains a larger stored energy prior to recrystallisation. It has been shown in Chapter 4 that the crystallographic textures of the two alloys, prior to recrystallisation, are quite different. The purpose of the work presented here was to investigate whether this difference can also explain the discrepancies in their recrystallisation behaviours.

10.2 EXPERIMENTAL PROCEDURE

To measure the recrystallisation temperatures and the release of stored energy, differential scanning calorimetry (DSC) was carried out using a Netzsch DSC 404/3/413/D machine. The DSC experiments involved continuous heating at rates ranging from 5 to 30 K min^{-1}.

A *Siemens 200* X–ray diffractometer with a pole figure goniometer was employed to measure the bulk textures by recording the {2 0 0} and {1 1 0} pole figures from longitudinal sections. Transmission electron microscopy and electron diffraction were used to carry out the microtexture analysis.

10.3 RESULTS AND DISCUSSION

10.3.1 DSC Measurements

Figure 10.1 illustrates the effect of heating rate on the recrystallisation temperatures of *MA956* steel. It is found that recrystallisation occurs over a range of temperatures. As expected in any thermally activated process, the onset of recrystallisation is retarded to higher

temperatures with increasing heating rate. The stored energy released by recrystallisation was found to be 0.4 J g^{-1}, the measurement being made at a heating rate of 10 K min^{-1}.

Figure 10.2 illustrates the DSC curves for *MA957*. The energy released, 1.0 J g^{-1} (at 10 K min^{-1}), is higher than that of *MA956* steel. The start–temperature for recrystallisation is found to be about 100 °C higher in *MA957* steel when compared with *MA956* steel. This is at first sight surprising since the higher stored energy of *MA957* should cause it to recrystallise more readily. It is notable also that the yttria content of *MA957* is *lower* so that the dispersoids are not the cause of the relatively high recrystallisation temperature of *MA957*.

10.3.2 Crystallographic Texture

A possible reason why the recrystallisation temperature for *MA957* is higher than that of *MA956*, in spite of its higher stored energy and lower dispersoid content, could be related to differences in the initial crystallographic texture.

The deformation textures in as-received *MA956* and *MA957* are certainly different (Chapter 4). Although both steels in bar form have a $< 1\ 1\ 0 >$ fibre texture, the texture is more intense in *MA956* steel, which has pronounced $\{0\ 0\ 1\} < 1\ 1\ 0 >$ and $\{1\ \bar{1}\ 1\} < 1\ 1\ 0 >$ components.

Experiments were conducted in an effort to see whether the texture of *MA957* could be manipulated by a "pre–annealing" heat–treatment, *i.e.* heat treatment which is not potent enough to induce recrystallisation but which can allow some changes in the sub–micron microstructure. Figure 10.3 illustrates the texture of *MA957* steel which has been "preannealed" at 1150 °C for 160 hours. This heat treatment is not capable of inducing recrystallisation, which occurs at a much higher temperature (Chapter 5). A $< 1\ 1\ 0 >$ fibre texture with a sharpened $\{1\ \bar{1}\ 1\} < 1\ 1\ 0 >$ component is revealed. The results using fibre analysis are summarised in Figure 10.4, which shows that the preannealed *MA957* steel has a remarkably similar texture to the as-received *MA956*.

The measured recrystallisation characteristics of all samples, including the one which was preannealed, are summarised in Table 10.1; the textures of as–received *MA956* and *MA957* have been reported previously (Chapter 4). It is evident that a strong $\{1\ \bar{1}\ 1\} < 1\ 1\ 0 >$ component is associated with a lower recrystallisation temperature, in spite of the overall lower stored energy.

Published data on the correlation between crystallographic texture and recrystallisation indicate that when the cold–deformed texture is random, certain texture components grow at the expense of others during the course of recrystallisation (Higgins, 1974). This process

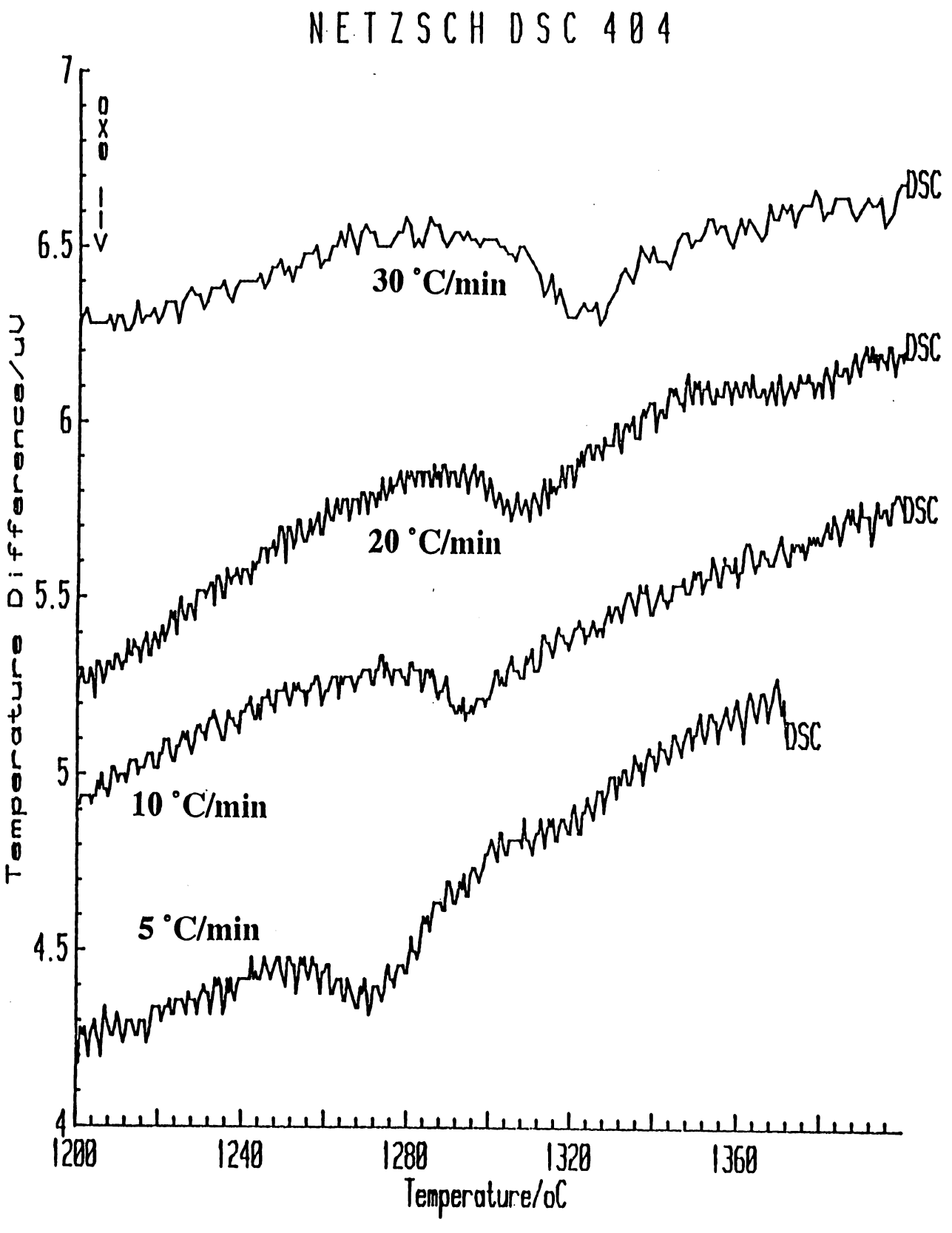

Figure 10.1: DSC curves for as-received *MA956* steel, obtained using a variety of heating rates.

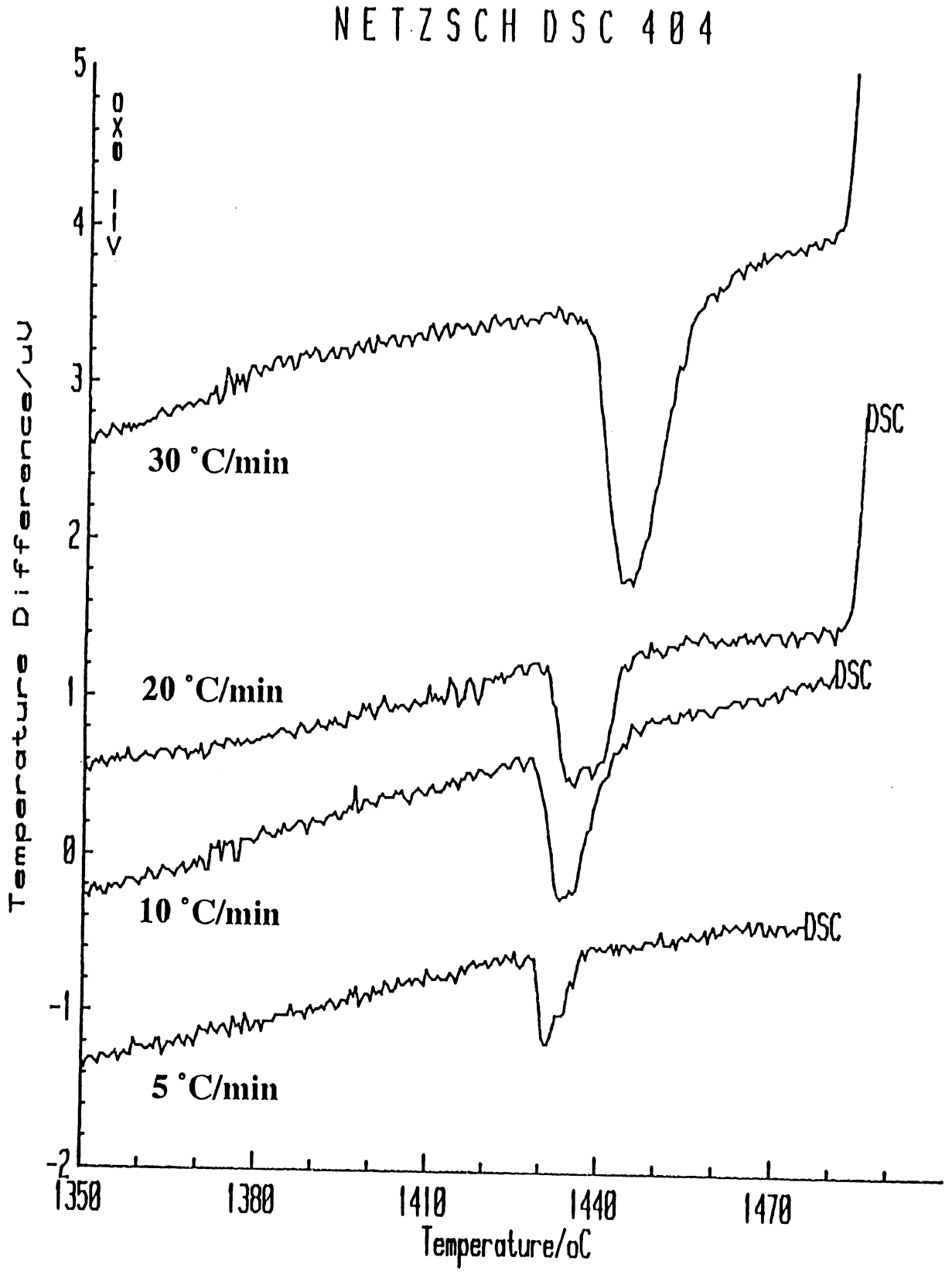

Figure 10.2: DSC curves for as-received *MA957* steel, obtained using a variety of heating rates.

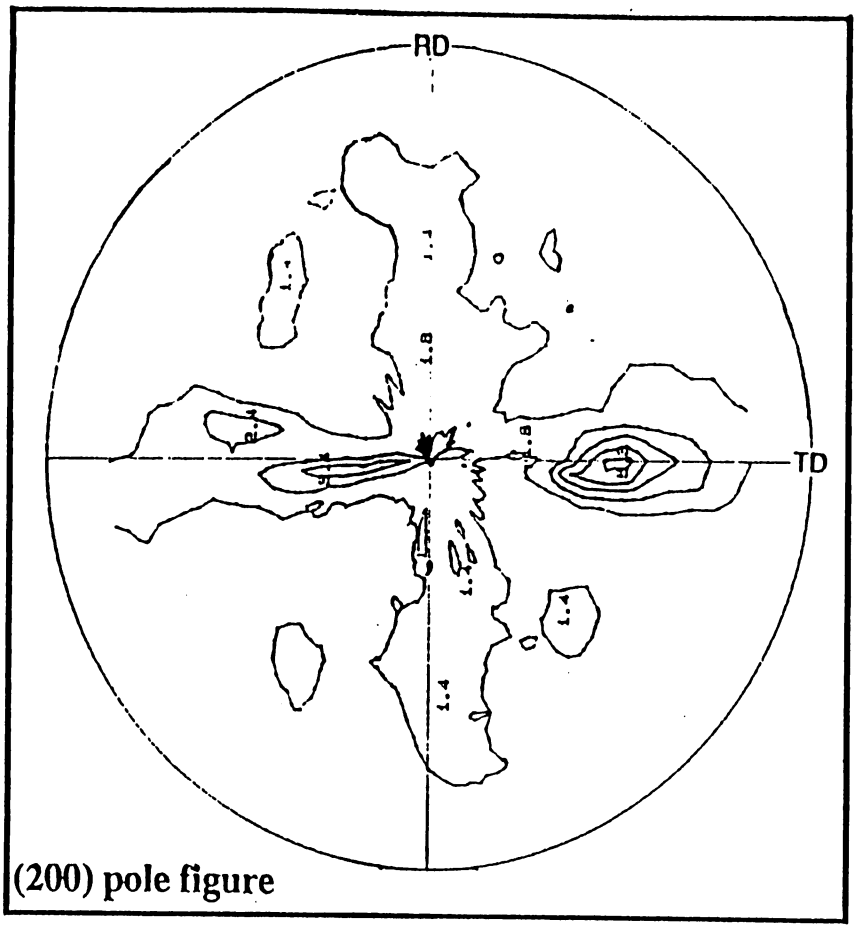

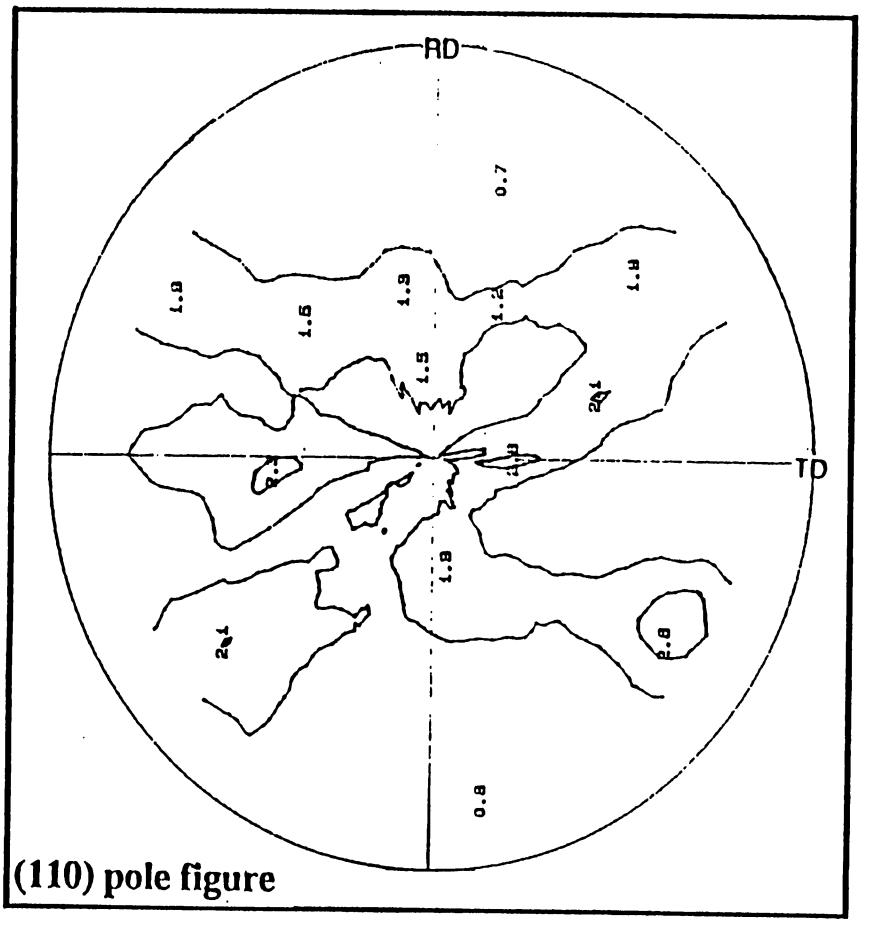

Figure 10.3: The {200} and {110} partial pole figures for *MA957* steel pre-annealed at 1150°C for 160 hours.

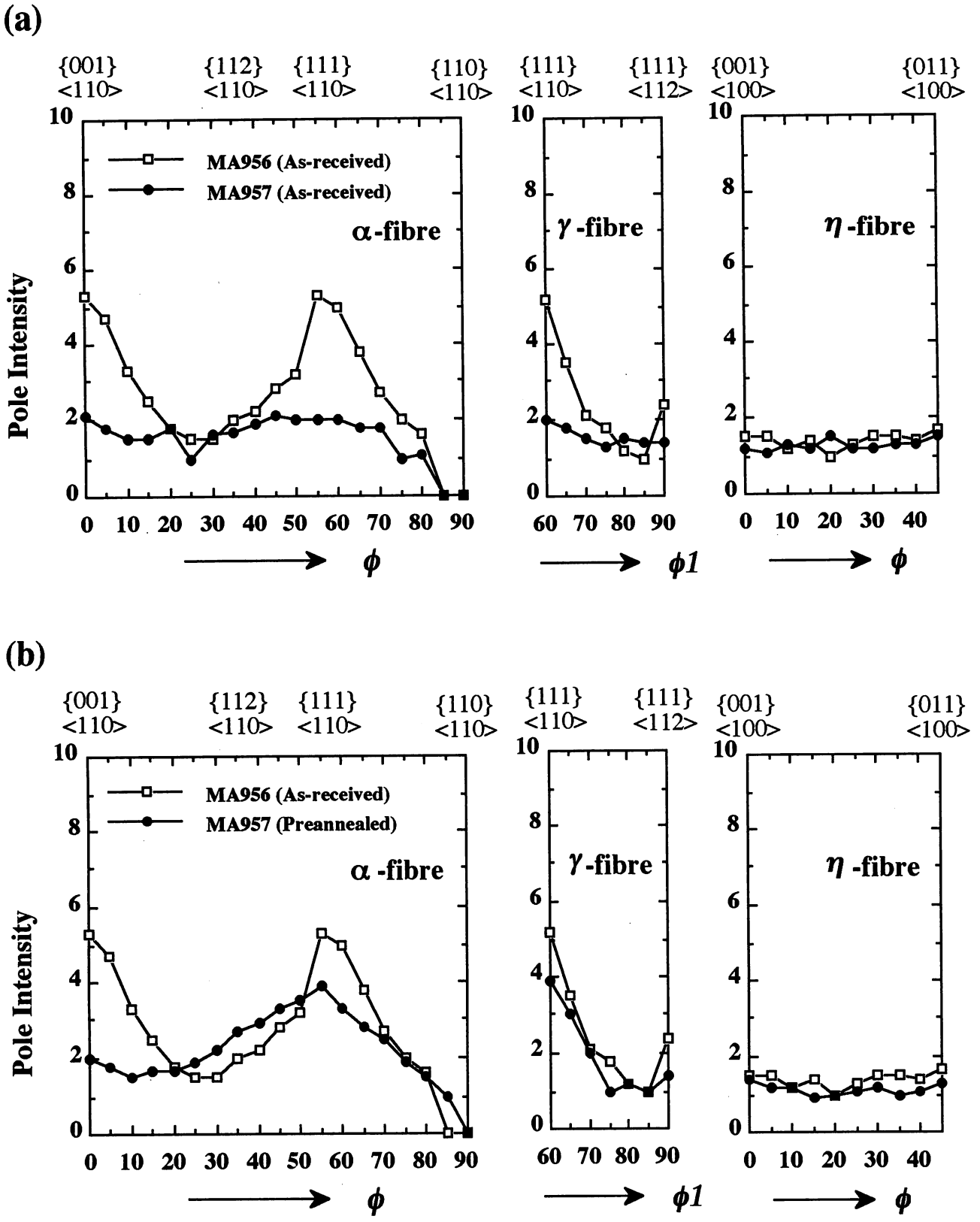

Figure 10.4: Fibres of deformation texture of (a) as-received *MA956* and as-received *MA957*, (b) as-received *MA956* and preannealed *MA957*.

Alloy	*As-received* *MA956*	*As-received* *MA957*	*Preannealed* *MA957*
Stored energy, J g^{-1}	0.40	1.00	0.70
Recrystallisation Temperature* (T_s,T_f), °C	1273, 1334	1429, 1447	1362, 1382
Texture	< 110 > fiber with stronger {001} < 110 >, {1$\bar{1}$1} < 110 > components	very weak < 110 > fiber	< 110 > fiber with sharpened {1$\bar{1}$1} < 110 > component
Recrystallised Grain Structure	Elongated grains, high grain aspect ratio	Coarse grains, low grain aspect ratio	Equiaxed fine grain

Table 10.1 Relationship between the recrystallisation behaviour and crystallographic texture of mechanically alloyed steels. T_s, T_f are the start and finish temperatures for recrystallisation respectively. * : DSC measurement at 20 K min^{-1}.

is similar to directional solidification, in which the fastest growing orientations are selected preferentially in the final microstructure. It is found that during the recrystallisation of cold deformed ferritic steels, the {1 1 1} texture component grows preferentially (Higgins, 1974), and a reasonable explanation for this could be that the boundary-mobility of grains contributing to this particular component is relatively high. Hence, it follows that at a given value of stored energy, a sample with a stronger {1 1 1} texture should recrystallise more readily.

For the present purposes it is clear that a stronger {1 $\bar{1}$ 1} < 1 1 0 > texture leads to easier recrystallisation (Table 10.1); the {1 1 0} component is relatively weak and its role might be neglected as a first approximation. As-received *MA957* has a higher stored energy, but because of its nearly random fibre texture, the {1 1 1} component is less developed when compared with *MA956*. It is therefore expected that as–received *MA957* should find it more difficult to recrystallise. The preanneal obviously intensifies the {1 1 1} component with a consequent reduction in the recrystallisation temperature. To summarise, the results establish a clear link between the nature of the crystallographic texture and the recrystallisation behaviour and explain some of the observed differences between *MA956* and *MA957*.

Some recently published results by Alamo *et al.* (1992) can also interpreted in the manner discussed above. They were able, using severe cold–deformation, to dramatically reduce the subsequent recrystallisation temperatures of both *MA956* (1350 → 750 °C) and *MA957* (1450 → 1250 °C). There is evidence in the literature (Hölscher *et al.*, 1991) that cold–deformation of a Fe–16Cr wt.% alloy leads to the sharpening of the γ–fibre, the {1 1 1} texture. These results of Alamo *et al.* (1992) are in this sense consistent with the work presented here.

10.3.3 Microtexture Data

A stronger {111} texture component seems to lead to lower recrystallisation temperatures as revealed by bulk texture data mentioned above. This was investigated further using some microtextural data compiled by transmission electron microscopy and electron diffraction.

For the microtexture analysis, the orientation relationship between a pair of like crystals, the crystallographic bases of which are defined from a common origin, can be described using an axis-angle pair. From this it can be inferred that if one of the crystals is rigidly rotated about the specified axis which passes through the origin, through a right-handed angle of rotation θ, its orientation coincides with that of the other (Christian, 1975c; Bhadeshia, 1987).

Accurate measurement of orientation relationships is best carried out using Kikuchi lines, but this proved difficult in the present work, since the high dislocation density of the as-received mechanically alloyed steels makes the Kikuchi lines rather diffuse. Therefore, the more approximate conventional selected area electron diffraction method was used, which is based on the analysis of the reciprocal lattice vectors. The method to calculate the coincidence site lattice (sigma value) was mentioned briefly in Chapter 3.

Figure 10.5 illustrates the distribution of sigma value in as-received *MA956* and *MA957* steels. It is found that strongly textured *MA956* steel has a high percentage of low misorientation boundaries, whereas a high percentage of high misorientation grain boundaries could be observed in as-received *MA957* steel. The frequency of low misorientation boundaries should increase with the strength of crystallographic texture (Watanabe, 1992). In addition, the analysis illustrates a high percentage of grains with a $< 111 >$ direction parallel to the extrusion direction in as-received *MA956* steel (Figure 10.6). These microtexture observations are consistent with the macrotexture data reported in Chapter 4.

Figure 10.7 shows that there is often a tendency for adjacent grains to be similarly oriented, *i.e.*, there are really clusters of subgrains with misorientations close to $\Sigma = 1$. This effect is stronger for *MA956*, consistent with its lower stored energy relative to *MA957* in which the elongated grains are more frequently randomly oriented with respect to their neighbours.

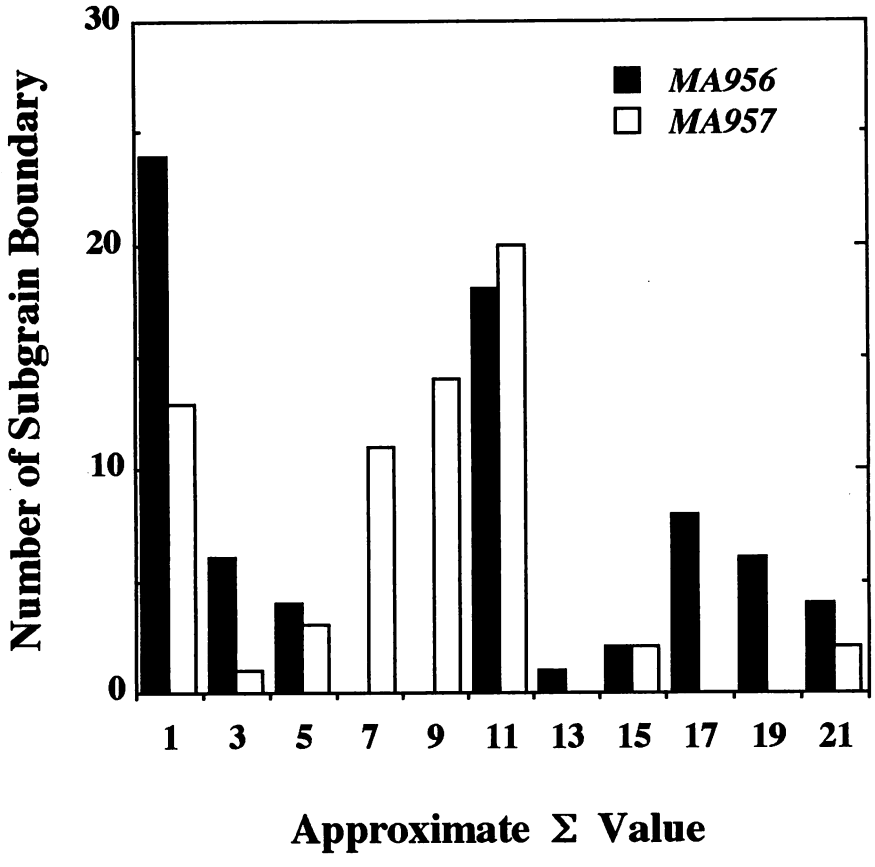

Figure 10.5: Distribution of Σ values in as-received *MA956* and *MA957* steels.

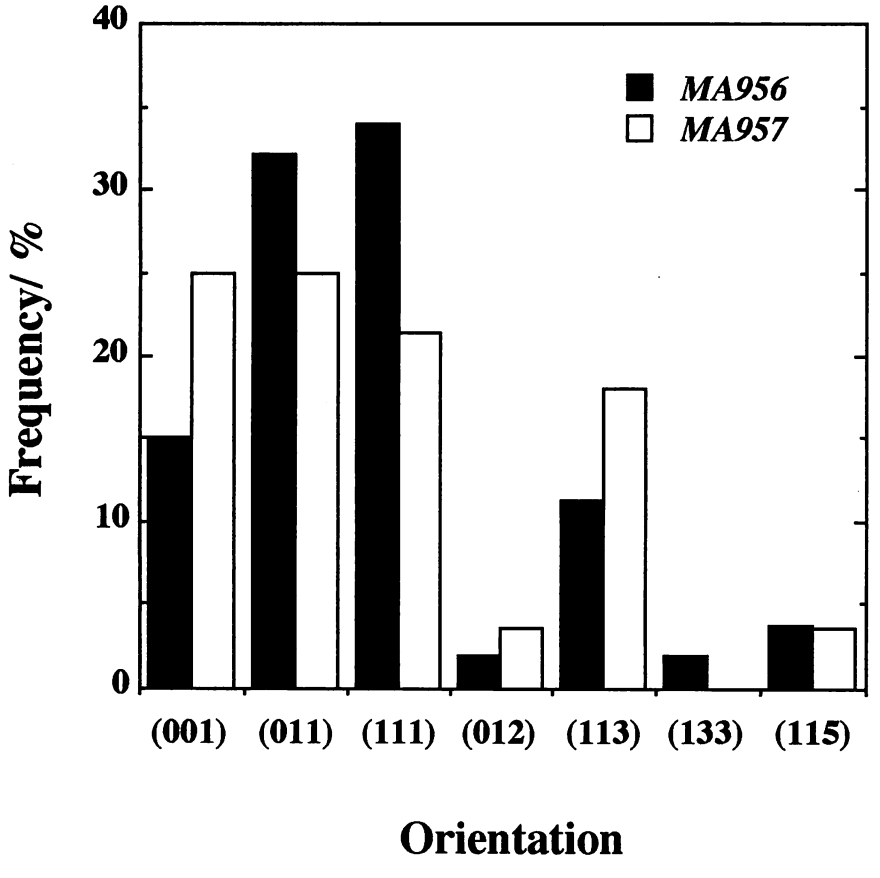

Figure 10.6: Distribution of subgrain orientations in as-received *MA956* and *MA957* steels.

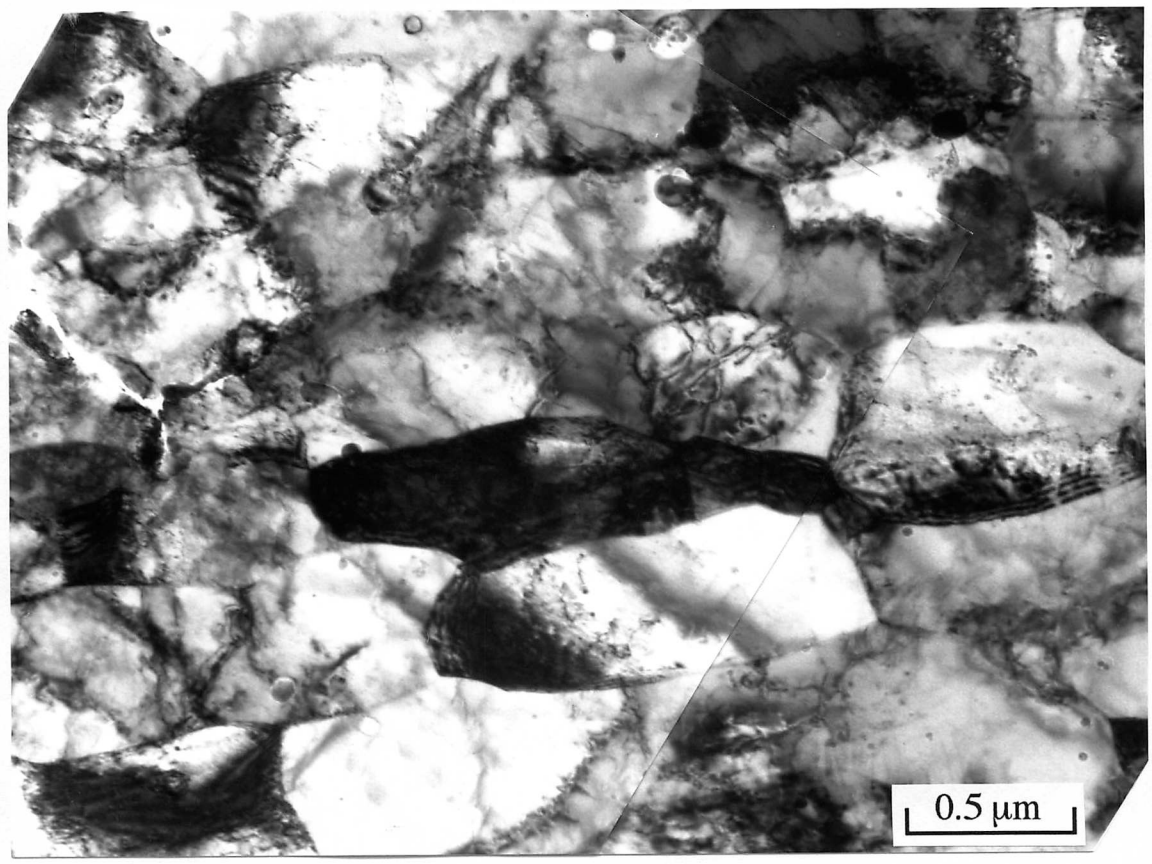

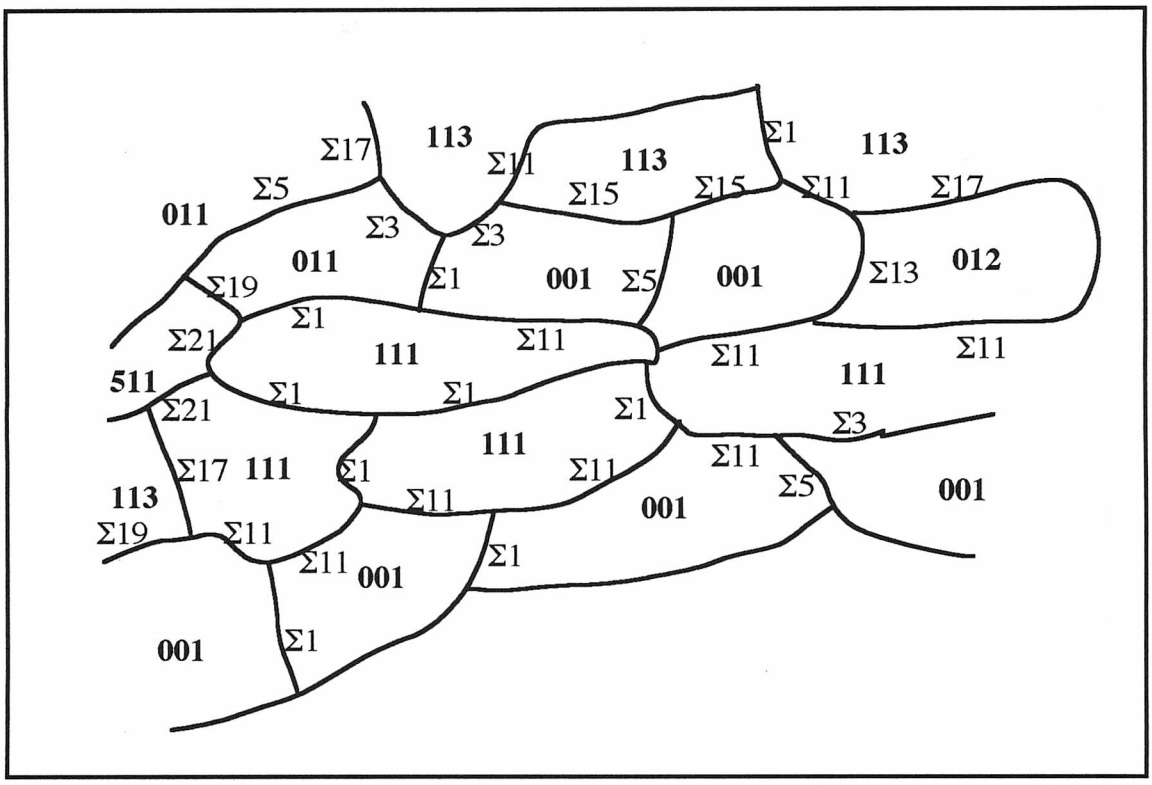

Figure 10.7: Distribution of grain orientations in as-received *MA956* steel.

The microtexture and recrystallisation data also consistent with the fact that nucleation of recrystallisation has been reported to occur at a lower temperature when there is a stronger {111} component to the texture (Abe, 1992).

10.4 CONCLUSIONS

It appears that the higher recrystallisation temperature of alloy *MA957* when compared with *MA956*, can be attributed to the fact that the crystallographic texture (measured both macroscopically and using TEM) of the two alloys prior to recrystallisation are significantly different. In particular, the presence of a strong "γ–fibre" or {1 1 1} component seems conducive to easier recrystallisation.

CHAPTER ELEVEN

SUMMARY AND SUGGESTIONS FOR FUTURE WORK

11.1 SUMMARY

The factors which affect the recrystallisation behaviour of mechanically alloyed oxide dispersion strengthened *MA956* and *MA957* stainless steels have been investigated systematically. The microstructures prior to recrystallisation consist of incredibly fine grains which are in a heavily deformed state. This accounts for the large stored energy in the materials immediately after consolidation and extrusion. Indeed, the deformation during mechanical alloying, and the subsequent fabrication, has been found to be sufficient to randomise the distribution of different atoms in the ferritic matrix. This is in spite of the fact that there should be a tendency for atomic clustering when the alloys are in thermodynamic equilibrium.

Mechanically alloyed steels tend to recrystallise into extremely coarse columnar grained microstructures. Such microstructures are good for some applications which require creep resistance, but not for others which call for more isotropic properties. Two new methods have emerged for the control of the recrystallised grain structures. Grain refinement has been achieved by adjusting the stored energy and by modifying the crystallographic texture. The grain boundary velocities are then reduced to a level which allows nucleation to develop at many sites in both the high chromium content *MA956* and low chromium content *MA957* steels. Although equiaxed, fine recrystallised grains could be generated in *MA957*, the refined grains in *MA956* remained somewhat anisotropic, probably because of its larger yttria content. The yttria particles are aligned along the fabrication direction and this is what seems to be the main feature responsible for grain anisotropy when the steels are either isothermally or otherwise annealed.

The second method follows from the discovery of austenite in alloy *MA957*. This opens up the possibility of grain refinement *via* a phase transformation from austenite to ferrite. It is found that *MA957* can be modified with the addition of a small amount of nickel because the alloy chemistry is quite close to the γ-loop in the phase diagram. This cannot be done with the more heavily alloyed *MA956*. On the other hand, the grain refinement can in principle be achieved by mixing powders of *MA956* with transformable "*MA957-Ni*" to make a metal-

metal-composite (MeMeC). However, the refining effect depends on the blending process, and further work is necessary to optimise the composite microstructure.

A good deal of work has been done to investigate the relationship between the recrystallisation behaviour and crystallographic texture. It is found that crystallographic texture has a significant effect on the recrystallisation temperatures. A sharpened $\{1\ \bar{1}\ 1\} < 1\ 1\ 0 >$ component in the unrecrystallised steel favours easy recrystallisation and this can be interpreted in terms of nucleation. Remarkably, the level of stored energy has a much less pronounced influence on the onset of recrystallisation.

A study of the hot-deformation behaviour has revealed that dynamic recrystallisation occurs during the hot-deformation of *MA956* and *MA957*, at temperatures far below the normal recrystallisation temperatures. The occurrence of dynamic recrystallisation is attributed to the high stored energy in the as–received state. Stress appears to assist the migration of the glissile components of subgrain or grains boundaries, thereby permitting easier recrystallisation.

11.2 SUGGESTIONS FOR FUTURE WORK

The most exciting future work should include more detailed field-ion microscopy and atom probe measurements to look at the long term stability of the solutions formed by mechanical alloying, and to examine fine scale changes in the dispersoid and precipitation characteristics. The idea of the metal-metal-composite also needs to be pursued with the fabrication of new combinations of powders and processing prior to consolidation. Detailed studies of the factors which influence the development of crystallographic texture also need to be investigated. A problem is that such work requires a dedicated commitment of industrial scale extrusion and fabrication facilities.

REFERENCES

Abe, H.: *Testu to Hagane* **52** (1966) 882–898.

Abe, M.: *Constitution and Properties of Steels, Materials Science and Technology, VCH Publishers Inc., New York, USA* **7** (1992) 285–333.

Alamo, A., Decours, J., Pigoury, M. and Foucher, C.: *Structural Applications of Mechanical Alloying Proceedings of an ASM International Conference, South Carolina* (1990) 89–98.

Alamo, A., Regle, H. and Bechade, J. L.: *The 8th International Conference on Heat Treatment of Materials, Kyoto, Japan* (1992) 277–280.

Alberry, P. J. and Jones, W. K. C.: *Metals Technology* **4** (1977) 557–566.

Alberry, P. J. and Jones, W. K. C.: *A computer model for the prediction of heat-affected zone microstructure in steel welds, Internal Report R/M/R282, Central Electricity Research Laboratories, Leatherhead* (1979)

Alberry, P. J., Brunnstrom, R. R. L. and Jones, W. K. C.: *Metals Technology* **10** (1983) 28–38.

Asano, K., Kohno, Y., Kohyama, A., Suzuki, T. and Kusanagi, H.: *Journal of Nuclear Materials* **155** (1988) 928–934.

Ashby, M. F. and Easterling, K. E.: *Acta Metallurgica* **30** (1982) 1969–1978.

Bailey, J. E.: *Philosophical Magazine* **5** (1960) 833–842.

Bailey, J. E. and Hirsch, P. B.: *Proceedings of Royal Society* **267A** (1962) 11–30.

Bailey, J. E.: *Electron Microscopy and Strength of Crystals, ed. G. Thomas and G. Washburn, Interscience, New YorK* (1963) 131–145.

Baloch, M. M.: *Ph.D. Thesis,* University of Cambridge (1989)

Baloch, M. M. and Bhadeshia, H. K. D. H.: *Materials Science & Technology* **6** (1990) 1236–1246.

Beck, P. A., Holzworth, M. L. and Sperry, P. R.: *Transactions AIME* **180** (1949) 163–192.

Beck, P. A. and Sperry, P. R.: *Journal of Applied Physics* **21** (1950) 150–152.

Benjamin, J. S.: *Metallurgical Transactions* **1** (1970) 2943–2951.

Benjamin, J. S. and Bomford, M. J.: *Metallurgical Transactions* **5** (1974) 615–621.

Benjamin J. S. and Volin, T. E.: *Metallurgical Transactions* **5** (1974) 1929–1934

Benjamin J. S.: *Scientific American* **234** (1976) 40–48.

Bhadeshia, H. K. D. H.: *Working Examples in Geometry of Crystals, Institute of Metals, London* (1987)

Blavette, D., Bostel, A. and Sarrau, J. M.: *Journal of Physics (Orsay)* **C2** (1986) 473–477.

Bleck, W., Groβterlinden, R., Lotter, U. and Reip, C.: *Steel Research* **12** (1991) 580–586.

Burke, J. E. and Turnbull, D.: *Progress in Metal Physics* **3** (1952) 220–292.

Burton, C. J., Baranow, S. and Tien, J. K.: *Metallurgical Transactions A* **10** (1979) 1297–1302.

Cahn, R. W.: *Proceedings of Physical Society (London)* **A60** (1950) 323–336.

Cairns, R. C., Curwick, L. R. and Benjamin, J. S.: *Metallurgical Transactions A* **6** (1975) 179–188.

Christian, J. W.: *Theory of Transformations in Metals and Alloys, part I, 2nd edition, Pergamon Press, Oxford* (1975) 479.

Christian, J. W.: *Theory of Transformations in Metals and Alloys, part I, 2nd edition, Pergamon Press, Oxford* (1975) 545.

Christian, J. W.: *Theory of Transformations in Metals and Alloys, part I, 2nd edition, Pergamon Press, Oxford* (1975) 346.

Clarebrough, L. M., Hargreaves, M. E. and West, G. W.: *Proc. Roy. Soc.* **A232** (1955) 252.

Cotterill, P and Mould, P. R.: *Recrystallisation and Grain Growth in Metals, International Textbook Company Limited, Surrey* (1976) 180.

Countney, T. H.: *Mechanical Behavior of Materials, McGRAW-HILL Int., New York* (1990) 263–324.

Dieter, G. E., Mullin, J. V. and Shapiro, E.: *Deformation under Hot Working Conditions, Iron Steel Inst., London* (1968) 7–13.

Dieter, G. E.: *Mechanical Metallurgy, 2nd Edition, McGrav-Hill-Kogakusha, Tokyo* (1976)

Dillamore, I. L. and Katoh, H.: *Metal Science* **8** (1974) 73–83.

Dillamore, I. L., Morris, P. L., Smith, C. J. E. and Hutchinson, W. B.: *Proceedings of the Royal Society* **329A** (1972) 405–420.

Doherty, R. D. and Martin, J. W.: *Journal of Institute of Metals* **91** (1963) 332–338.

Evans, P. J. and Martin, J. W.: *Materials Science Forum* **94** (1992) 643–648.

Fischer, J. J., Astley, I, and Morse, J. P.: *Proc. 3rd Int. Symp. on Superalloys–Metallurgy and Manufacture* (1977) 361.

Fleetwood, M. J.: *Materials Science and Technology* **2** (1986) 1176–1182.

Fraser, R. W. and Evans, D. J. I.: *Oxide Dispersion Strengthening,* Gordon and Breach, New York (1968) 375–403.

Fridberg, L–E Törndahl and Hillert, M.: *Jernkonotorets Ann.* **153** (1969) 263.

Fujita, H.: *Journal of Physical Society, Japan* **16** (1961) 397–406.

Gessinger, G. H.: *Metallurgical Transactions A* **6A** (1976) 1203–1209.

Gessinger, G. H.: *Powder Metallurgy of Superalloy, Butterworth and Co., London* (1984) 213–292.

Gilmann, P. S. and Benjamin, J. S.: *Annual Review of Materials Science* **13** (1983) 279–300.

Grundy, E. and Patton, W. H.: *High Temperature Alloys, ed. J. B. Marriott, M. Merz, J. Nihoul and J. Ward, Elsevier Applied Science, London* (1985) 327–335.

Hack, G. A. J.: *Powder Metallurgy* **27** (1984) 73–79.

Hansen, N. and Bay, B.: *Acta Metallurgica* **29** (1981) 65–77.

Hatherley, M. and Hutchinson, W. B.: *Introduction to Textures in Metals,* Institution of Metallurgists, London (1979.)

Heckelmann, I., Abbruzzese, G. and Lücke, K.: *Materials Science Forum* **94–96** (1992) 391–398.

Higgins, G. T.: *Metal Science* **8** (1974) 143–150.

Hollomon, J. H. and Jaffe, L. D.: *Transactions AIME* **162** (1945) 223–249.

Hölscher, M., Raabe, D. and Lücke, K.: *Steel Research* **12** (1991) 567–579.

Hotzler, R. K. and Glasgow, T. K.: *Metallurgical Transactions A* **13A** (1982) 1665–1674.

Hu, H.: *Transactions AIME* **162** (1959) 320–326.

Hu, H.: *Acta Metallurgica* **10** (1962) 1112–1116.

Hu, H.: *Recovery and Recrystallisation of Metals., (ed. L. Himmel) New York* (1963) 311–362.

Huet, J. J. and Leory, V.: *Nuclear Technology* **24** (1974) 216–224.

Hughes, I. F. and Page, E. W.: *Metallurgical Transactions* **2** (1971) 2067–2075.

Humphreys, F. J.: *Recrystallisation and Grain growth of Multiphase and Particle Containing Materials,* ed. Harsen, N., Jones, A.R., and Leffers, T., Risϕ National Laboratory, Roskilde, Denmark (1980) 35.

Humphreys, F. J.: *Materials Science and Technology* **15** (1991) 371–428.

Hutchinson, W. B.: *Metal Science* **8** (1974) 185–196.

Inagaki, H.: *Proceedings of the 6th International Conference on Textures of Materials,* The Iron and Steel Institute of Japan, Tokyo, Japan (1981) 149–163.

Kane, R. H., McColvin, E. M. Kelly, T. J., and Davidson, J. M.: *Proc. Conf. "Corrosion 84",* New Orle ans, La, USA, National Association of Corrosion Engineers, paper 12. (1984)

Kim, Y. G. and Merrick, H. F.: *NASA CR159-493,* Lewis Research Center (1979)

Koch, C. C.: *Structural Applications of Mechanical Alloying,* Froes, F. H., de Barbadillo, J. J. (eds), Materials Park (OH) : ASM Int. (1990) 193–245.

Koch, C. C.: *Phase Transformations in Materials, Materials Science and Technology, VCH Publishers Inc., New York, USA* **5** (1992) 193–245.

Kramer, K. H.: *Powder Metallurgy Int.* **9** (1977) 105.

Landau, L. D. and Lifshitz, E. M.: *Statistical Physics, Pergamon Press, London* (1958) 344.

Li, J. C. M.: *Journal of Applied Physics.* **33** (1962) 2958–2966.

Little, E. A., Mazey, D. J. and Hanks, W.: *Scripta Metall. Mater.* **25** (1991) 1115–1118.

Luton, M. J. and Sellars, C. M.: *Acta Metallurgica* **17** (1969) 1033–1043.

Lytton, J. L., Westmacott, K. H. and Potter, L. C.: *Transactions AIME* **233** (1965) 1755–1765.

Martin, J. W.: *Metellurgia* **56** (1957) 161.

MacKay, R. A., Dreshfield, R. L. and Maier, R. D.: *Superalloys 1980, J. K. Tien et al. ed., ASM, Metals Park, Ohio* (1980) 385.

McGolvin, G. M. and Smith, G.D.: *High Temperarure Alloys,* Elsevier Applied Science, *Essex* (1987) 139–153.

McQueen, H. J. and Jonas J. J.: *Recovery and Recrystallisation During High Temperature Deformation, Treatise Matls. Sci. and Tech., ed R. J. Arsenault* **6** (1975) 393–493.

McQueen, H. J., Chia, H. and Starke, E. H.: *Microstructural Control in Aluminium Alloys : Deformation, Recovery and Recrystallisation* (1985) 1–18.

Miller, M. K., Beaven, P. A. and Smith, G. D. W.: *Metallurgical Transactions A* **12A** (1981) 1197–1204.

Miller, M. K.: *International Materials Review* **32** (1987) 221–240.

Miller, M. K.: *Phase Transformations '87, ed. G. W. Lorimer, Institute of Metals, London* (1988) 39–43.

Miller, M. K. and Smith, G. D. W.: *Atom Probe Microanalysis: Principles and Applications to Materials Problems, Materials Research Society* (1989)

Mino, K., Nagakawa, Y. G. and Glasgow, T. K.: *Metallurgical Transactions A* **13A** (1982) 1665–1674.

Mino, K., Nagagawa, Y. G. and Ohtomo, A.: *Metallurgical Transactions* **18A** (1987) 777–784.

Mino, K., Harada, H. and Bhadeshia, H. K. D. H.: *Materials Science Forum* **88–90** (1991) 777–784.

Morse, J. P. and Benjamin, J. S.: *New Trends in Materials Processing, Americal Society for Metals, Metals Park, Ohio* (1976) 165.

Mould, P. R. and Cotterill, C.: *Journal of Materials Science* **2** (1967) 241–255.

MTDATA: Metallurgical and Inorganic Thermodynamic Bank, National Physical Laboratory, Teddington, U K, (1992.)

Murakami, K., Mino, K., Harada, H. and Bhadeshia, H. K. D. H.: *Metallurgical Transactions A* **24A** (1993) 1049–1055.

Murakami, K.: *Ph.D. Thesis,* University of Cambridge (1993)

Nardone, V. C., Matejczyk, D. E. and Tien, J. K.: *Metallurgical Transactions A* **14** (1983) 1435–1441.

Nielsen, J. P.: *Transactions AIME* **200** (1954) 1084–1088.

Pickering, F. B.: *Constitution and Properties of Steels, Materials Science and Technology, VCH Publishers Inc., New York, USA* **7** (1992) 41–94.

Ralph, B., Shim, K. B., Huda, Z., Furley, J. and Edirisinghe, M.: *Materials Science Forum* **94–96** (1992) 129–140.

Ray, R. K. and Jonas, J. J.: *International Materials Reviews* **35** (1990) 1–36.

Reed–Hill, R. E. and R. Abbaschian: *Physical Metallurgy Principles, 3rd Edition, PWS-KENT, Boston* (1992) 590.

Regle, H. and Alamo, A.: *EUROMAT 93, Paris* (1993)

Reynolds, R. A. and Tegart, W. J. McG.: *Journal of Iron and Steel Institute* **200** (1962) 1044–1059.

Rickert, T. J., Salsgiver, J. A. and Washko, S. D.: *Proc. Int. Conf. on Stainless Steels, Chiba, Japan, ISIJ* (1991) 877–884.

Rossard, C.: *Proc. Int. Conf. Strength Metals Alloys, 3rd* **2** (1973) 175–203.

Russell, K. C.: *Metallurgical Transactions* **2** (1971) 5–12.

Salsgiver, J. A., Shen, T. H., Washko, S. D. and Lücke, K.: *Proc. Int. Conf. on Textures of Materials, ICOTOM 8, Santa Fe, NM* (1988) 1065–1070.

Schlippenbach, U. V., Emren, F. and Lücke, K.: *Steel Reviews* **12** (1991) 1289–1301.

Singer, R. F. and Gessinger, G. H.: *Metallurgical Transactions A* **13A** (1982) 1463–1470.

Sundaresan, R. and Froes, F. H.: *Journal of Metals* **39** (1987) 22–27.

Tanaka, M., Iizuka, H. and Ashihara, F.: *Transactions of Iron and Steel Institute, Japan* **28** (1988) 129.

Tegart, W. J. McG.: *Ductility, Amer. Soc. Metals, Metals Park, Ohio* (1968) 133–177.

Towner, R. J. and Berger, J. A.: *Transactions AIME* **218** (1960) 611–617.

Ubhi, H. S. Hughs, T. A. and Nutting, J.: *Proc. Conf. on Fourtiers of High Temperature Materials,* New York (1981) 33–49.

Uemori, R., Mukai, T. and Tanino, M.: *Phase Transformations '87, ed. G. W. Lorimer, Institute of Metals, London* (1988) 44–46.

Vandermeulen, W. and Coheur, L.: *Powder Metallurgy* **3** (1981) 141–145.

Watanabe, T., Oikawa, H. and Arai, K–I: *Acta Metallurgica* **37** (1989) 941–952.

Watanabe, T.: *Materials Science Forum* **94–96** (1992) 209–220.

Whittenberger, J. D.: *Metallurgical Transactions A* **12A** (1981) 845–851.

Wilcox, B. A. and Clauer, A. H.: *Acta Metallurgica* **20** (1972) 747–757.

Yamazaki, M., Kawasaki, Y. and Kusumoki, K.: *ASM Internationa Conference on Structure and Application of Mechanically Alloying,* Myrtle Beach (SC) (1990) 33.

Zener, C.: *Transactions AIME* **175** (1948) 15–51.

APPENDIX ONE

TEXTURE ANALYSIS

EXPERIMENTAL DETERMINATION OF TEXTURE

The vast majority of texture determinations are done using the well established principle of X-ray diffraction from polycrystals. This method uses a monochromatic beam of radiation with the Bragg condition satisfied for a single set of reflecting planes and maintained throughout the determination of the pole figure. Under these conditions the normal ($\underline{k}$) to the diffracting planes {hkl} remains fixed in space and the specimen is rotated over a wide range of angles to achieve coincidence with the diffracting normal. Whenever a crystal becomes so oriented that the normal to any one set of the prescribed {hkl} planes coincides with the fixed normal, $\underline{k}$, a diffracted intensity will be measured from that grain. The total diffracted intensity at any instant is then proportional to the volume of the specimen in which the {hkl} planes are so oriented. In other words, the measured intensity at a given time is directly proportional to the pole density on the pole figure under investigation. The proportionality between the diffracted intensity and pole figure density is usually quantified relative to a "random intensity", or the density which is observed when a textureless sample is examined under precisely the same conditions. The pole figure is then plotted out with contour levels which correspond to 1/2, 1, 2, 3, ...× random intensity. This provides a sensible basis on which the sharpness of the texture may be assessed and allows a comparison to be made between results obtained in different laboratories and using different experimental methods. When using X-ray diffraction methods, consideration has to be given to the choice of the most suitable characteristic radiation, correct filter and optimum detector conditions.

Many techniques and variations have been proposed over the years for determining preferred orientation. For an accurate, quantitative description of the texture of a metal it is clearly desirable to have information concerning all possible directions in the specimen or, in other words, a complete pole figure. This can be achieved by some of the more elaborate methods, but pole figures are most commonly determined in an incomplete form by the use of the Schulz reflection method (Hatherley *et al.*, 1979).

The specimen used in Schulz method is typically a piece of sheet about 25 mm square

with a flat surface that has been prepared by chemical polishing or etching. The X-ray must not been transmitted through the specimen so the thickness should normally be greater than 0.2 mm. The upper limit to thickness is determined only by the design of the specimen holder and is usually about 5 mm. when mounted on the goniometer the specimen is subjected to three types of movement. These are :

(i) simple translation to and fro which improves the statistical averaging of the texture measurement by increasing the number of grains that are sampled.
(ii) rotation about an axis perpendicular to the sheet surface (angle ϕ), and
(iii) rotation about an rotational axis through an angle ϕ.

Figure 1a shows a commercial texture goniometer with a specimen in position. A schematic diagram which explains the geometrical arrangement is shown in Figure 1b, and the corresponding sterographic projection is given in Figure 1c. An X-ray beam from the source (1) is restricted by divergence slits (2) and subsequently passes through a narrow horizontal slit (3) to the specimen (4). The major circle of the goniometer (5) is set so that its axis makes Bragg angle, θ, with the central ray of the incident beam. The required diffraction condition is chosen by moving the arm holding the receiving slits (6) and counter (7) to the angle 2θ. In practice, the angle θ is not critical and is simply set to the calculated value. The counter position 2θ requires fine adjustment, in order to maximise the measured intensity of the diffracted beam.

When the specimen is arranged with its rolling direction pointing vertically. The normal direction to the sheet now bisects the angle between the incident and diffracted beams and so coincides precisely with the diffracting vector, $\underline{k}$, which is labelled (8). The measured intensity therefore comes from the planes {hkl} which are parallel to the sheet plane. In other words, we measure the intensity at the center of the pole figure (Figure 1c). If we now rotate the specimen in the major arc of goniometer (angle ψ) through 90 ° we bring the rolling direction parallel to the diffracting normal, and so the measured intensity corresponds to the position RD on the pole figure. By this rotation "radial scan" is made of the pole figure, sampling the diffracted intensity along the great circle from ND to RD. Next, when rotating the specimen about the normal to its surface, angle ψ. After 90 ° rotation the transverse direction will coincide with the diffracting normal. The rotation, therefore, allows the diffracted intensity to be sampled through the angle ψ with a slow rotation through the angle ϕ, determining the diffracted intensity along a spiral trace as indicated in Figure 1d.

Typically, the radial angle ϕ is changed by 5 ° during a complete revolution around the ψ axis. Positions of high measured intensity on sequential dial laps of the spiral track are then

used to locate regions of high pole density on the pole figure, with points of equal intensity being joined together along contour lines.

REPRESENTATION OF TEXTURE COMPONENT

The orientations of grains are defined by the pole figure and expressed as a tendency of particular planes and directions $\{hkl\} < uvw >$ being parallel to significant directions of the specimen (such as the normal and rolling directions). It is also possible to express the texture differently, by plotting the rolling direction etc. relative to the crystallographic axes.

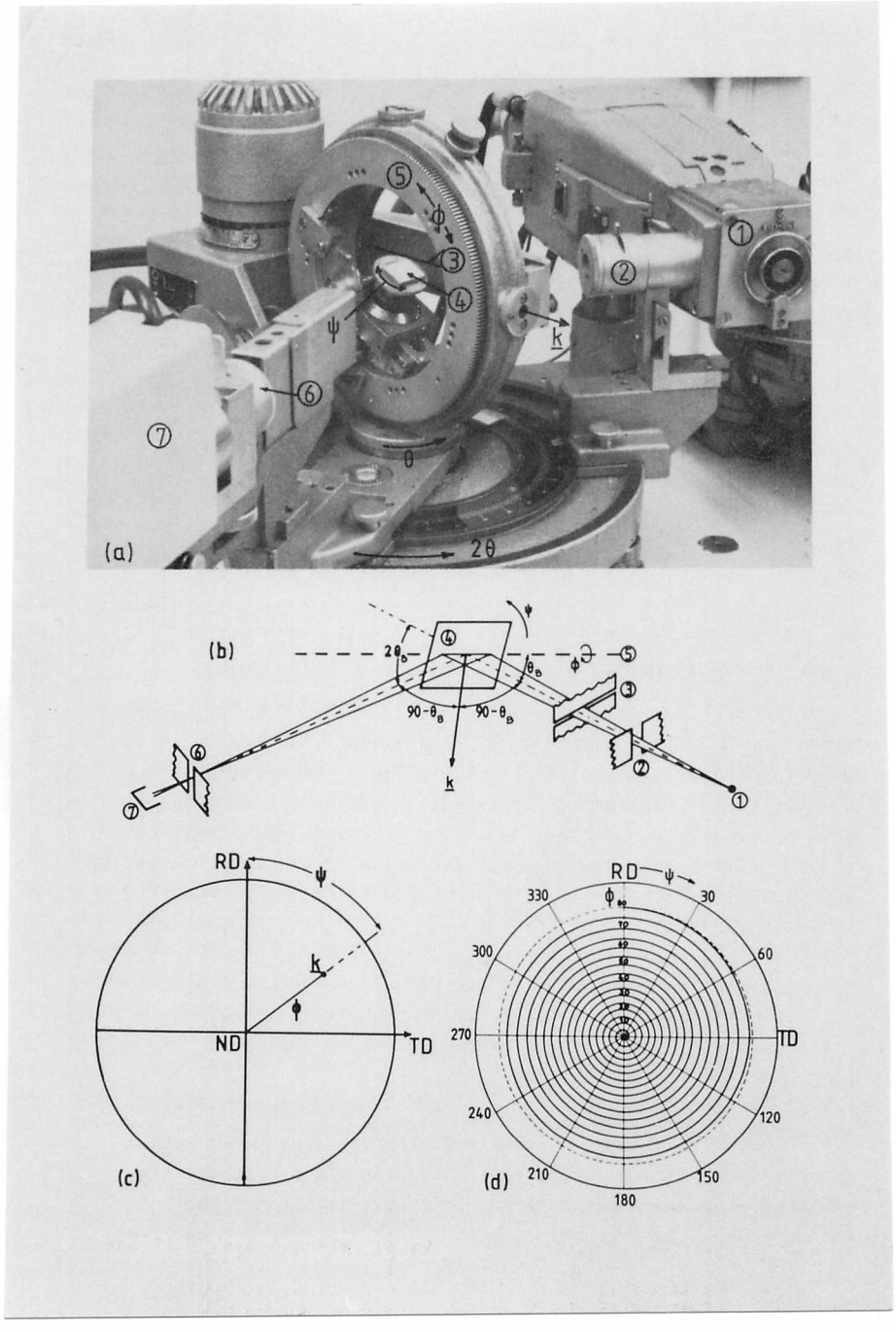

Figure 1: (a) Experimental texture goniometer, (b) schematic diagram of (a), (c) projection showing the diffracting vector $\underline{k}$, (d) spiral path of the diffracting vector.

APPENDIX TWO

EFFECT OF COLD-DEFORMATION ON THE RECRYSTALLISATION BEHAVIOUR OF *MA957* STEEL

Regle and Alamo (1993) have conducted extensive studies on the recrystallisation behaviour of *MA956* and *MA957*, for samples which were cold-deformed after extrusion. Two deformation processes were used, swaging and drawing, with reductions ranging from 10 → 60%.

Swaging and drawing led to quite different changes in crystallographic texture, and indeed to the subsequent recrystallisation behaviour. In all cases, deformation led to a reduction in the recrystallisation temperature (Regle and Alamo, 1993), the change being largest for the cold-drawn samples. For *MA957*, the maximum reduction in the recrystallisation temperature was found to be about 200 °C from 1450 → 1250 °C . The corresponding maximum reduction for *MA956* was for the cold-drawn samples, where the recrystallisation temperature could be reduced from 1350 → 750 °C .

Their samples of *MA957* were studied using differential scanning calorimeter to establish any changes in stored energy as a function of deformation. Fig. 1 illustrates a DSC curve recorded from as-received *MA957* steel at heating rate of 20 K min^{-1}. A recerystallisation temperature range was from 1370 to 1412 °C with a stored energy of 0.93 J g^{-1} released during recrystallisation. This result is consistent with the results of Chapter 5. The corresponding data for cold-drawn samples are in Fig. 2. The recrystallisation temperature deceases with increasing cold deformation. In addition, it is found that the deformation leads to a reduction in stored energy (Table 1).

There is no clear explanation of the results, but it is possible that the cold deformation modifies the crystallographic texture. It is conceivable that the texture change both leads to a reduction in the stored energy, and at the same time, a reduction in the recrystallisation temperature. The texture could, for example, lead to the clustering of adjacent grains into similar orientations (Watanabe, 1992). This would lead to an increase in the effective grain size, thereby making the nucleation of recrystallisation more easy.

There are some other elegant results presented by Regle and Alamo (1993), which are

MA957 Steel	T_s, °C	T_f, °C	Stored Energy, J g^{-1}
AS-received	1370	1412	0.93
30% Cold-drawn	1018	1093	0.78
40% Cold-drawn	998	1056	0.70
50% Cold-drawn	989	1041	0.69
60% Cold-drawn	980	1027	0.65

Table 1. Effect of cold-deformation on the recrystallisation behaviours of *MA957* steels. T_s, T_f are the start and finish temperatures for recrystallisation respectively. DSC measurements at 20 $K\ min^{-1}$.

consistent with this interpretation. A sample which was necked by deformation (and hence contained a controlled deformation gradient), was subjected to a recrystallisation heat treatment. It was vividly demonstrated that the anisotropic recrystallisation grain structure become refined with the extent of deformation. This is in spite of the fact that the stored energy actually decreased. Thus, deformation must enhance the nucleation rate of recrystallisation, perhaps by the texture mechanism discussed above.

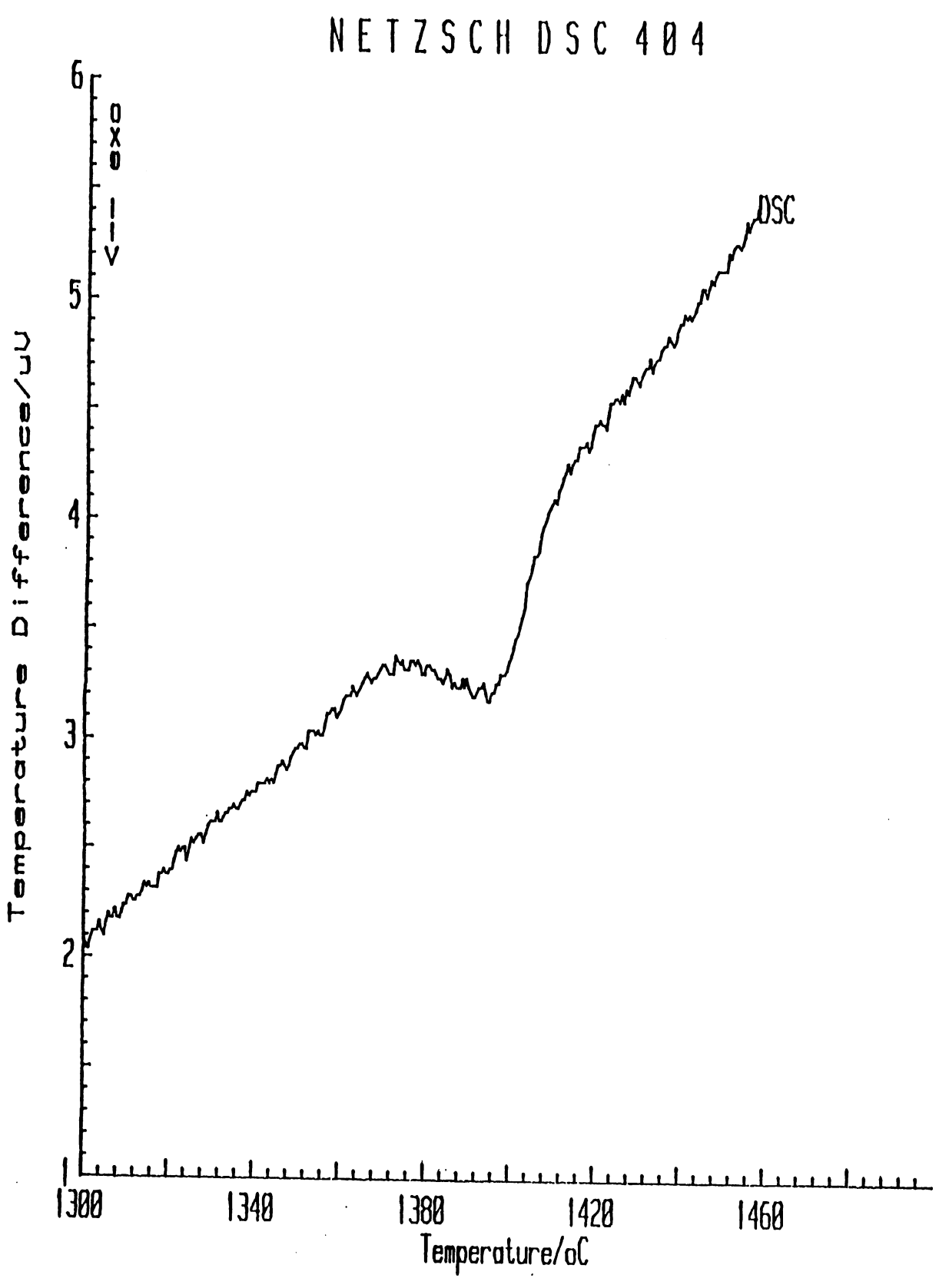

Figure 1: DSC curve recorded from as-received *MA957* steel (25 mm diameter bar).

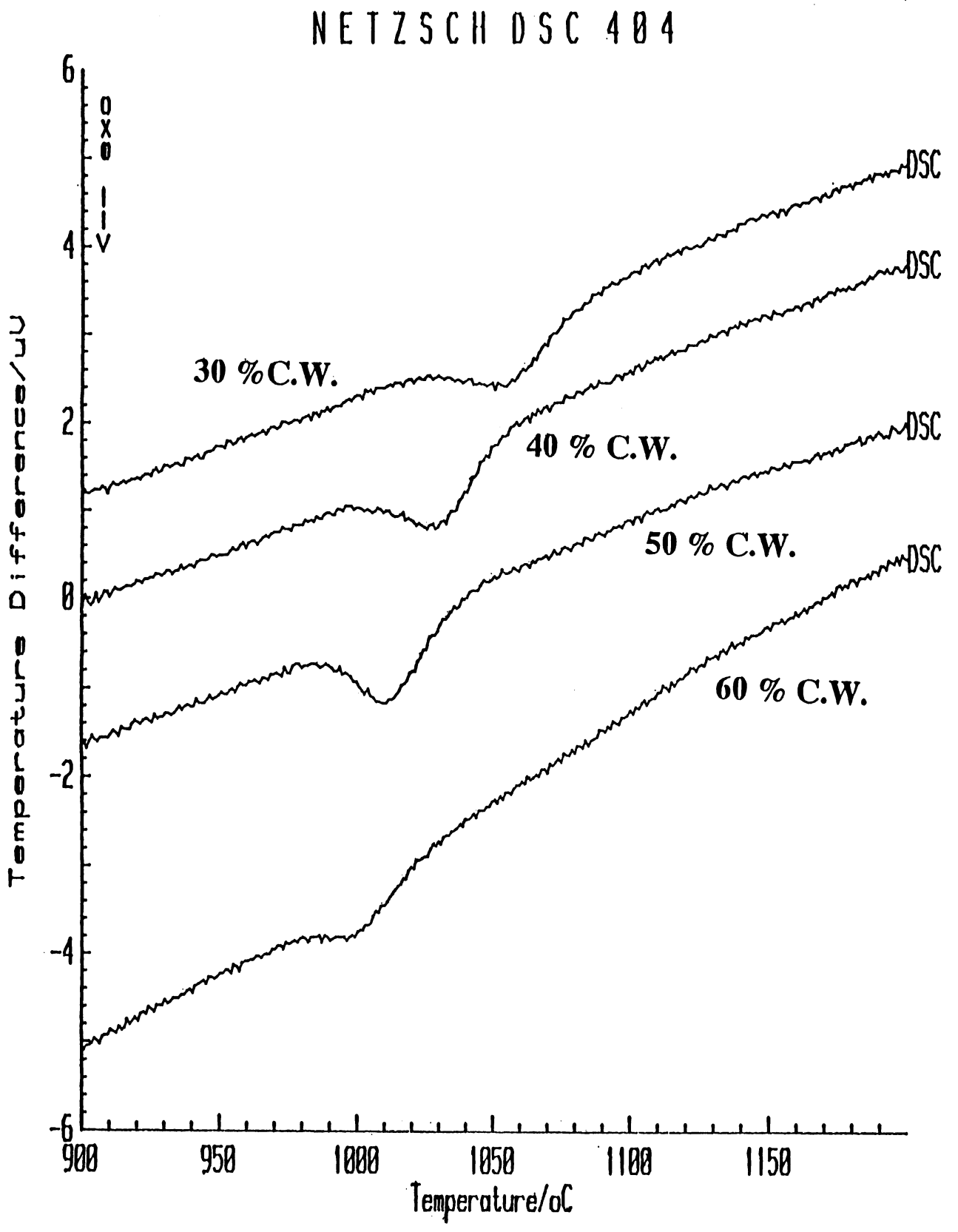

Figure 2: DSC curves recorded from cold-drawn *MA957* steel. The drawing ratio ranging from 30 to 60%.